THE UNIVERSITY
of EDINBURGH

Post-caldera eruptions and pyroclastic density current hazard in the Main Ethiopian Rift

Benjamin A. Clarke

Submitted for the degree of Doctor of Philosophy
The University of Edinburgh

2019

Abstract

The eruption of a peralkaline rhyolite magma has never been observed, yet these eruptions are amongst the most common in the Main Ethiopian Rift Valley since 1 Ma and dominate the eruption record of volcanoes that have undergone caldera collapse. The unusual rheological properties of peralkaline rhyolites, in combination with the lack of direct observations of eruptions, means that the style and hazards associated with them is essentially unknown. With 1 million people living within 10 km of a volcano in Ethiopia, and numerous geothermal power stations being built directly on these volcanoes, understanding their eruptive style and hazards is timely, and essential to robustly assess risk. This thesis aims to evaluate the eruptive styles and pyroclastic density current (PDC) hazards of post-caldera peralkaline rhyolite eruptions. I focus on Aluto volcano, a restless caldera system which has seen a multitude of peralkaline rhyolite eruptions over at least the past 16 Ka. By studying the deposits from these eruptions, I attempt to evaluate the styles of eruptive activity these magmas undergo; whether they generate PDCs, how these PDCs are generated, and how mobile they might be. I find that eruptions at Aluto occur across the edifice, akin to a monogenetic field, and that each eruption tends to undergo a very similar eruption sequence, albeit over a range of magnitudes. Eruptions typically begin with the formation of an eruption column, generating tephra fall deposits. Whilst investigating these deposits we have discovered, described and investigated a largely unrecognised type of pyroclast which I term a 'pumiceous achnelith'. Thermal and ballistic modelling of these pumiceous achneliths indicates that pumice cones are generated by pyroclastic material falling from the sides of these columns, accumulating around the vent. Towards the end of the eruption, the eruption-column becomes unsteady, repeatedly collapsing and re-establishing, generating multiple PDCs. These PDCs usually have a high particle-concentration at their base, and tend to be confined to drainages. In most cases, the final stage of the eruption is marked by the effusion of a silicic lava flow, though it is uncertain how explosive this phase is. Using these insights, I have selected analogue PDC data, combined with modelled collapse heights and a kernel-density vent-susceptibility model, to inform a simple energy-cone model which estimates the inundation footprints of hypothetical PDCs. I employ a Monte-Carlo approach to evaluate a full range of probable

eruption scenarios, and I find that the caldera, and its NW, N, and SE flanks, are particularly prone to inundation by PDCs. I combine this with geospatial data of people and infrastructure around Aluto to evaluate the collective risk, and the risk to individuals posed by PDCs. In terms of collective risk, I find that although most PDCs are constrained to within a few kilometers of the edifice, though it is still possible for more distal settlements to be inundated during rarer high-magnitude events. The population of these distal settlements is much denser than in local settlements, meaning that the collective risk is often similar between proximal and distal locations. For the individual, PDC risk is much higher closer to the edifice. I frame this risk amongst 'everyday' risks experienced by individuals in Ethiopia, and establish that for residents on the volcano, the time-averaged yearly risk of death by PDC is comparable to that of death by malaria, house-fire, malnutrition or road traffic accident. Using current best-practices, I have produced PDC hazard maps for different stakeholder groups at Aluto. Though there is still great uncertainty surrounding the styles and hazards associated with peralkaline rhyolites globally, this work shows that they're capable of producing intense eruptions (intensity 7-10); generating moderate to tall eruption columns (3-16 km), which can collapse to form pyroclastic density currents with the potential to devastate local settlements and infrastructure.

Lay Summary

Volcanoes around the world vary considerably in how they erupt; at Kilauea volcano in Hawaii, molten rock is liable to trickle out, or produce short fountains which form lava flows that travel relatively slowly down-slope. By comparison, in 1980, Mt. St Helens erupted explosively producing a tall column of pulverised rock, and a fast-moving avalanche of super-hot volcanic debris called a pyroclastic density current, or 'PDC' for short. Such volcanoes pose very different hazards to those who live around them; whilst a resident in Hawaii may be able to walk away from an oncoming lava flow, anyone within the path of a PDC from Mt. St. Helens had no chance of escape and was killed. Much of the variation in eruption-style is a result of the chemical and physical make-up of the magma, and broadly speaking, volcanoes with similar types of magma erupt in similar ways. However, volcanoes in the Ethiopian Rift Valley comprise unusual magmas. These volcanoes haven't erupted in the view of scientific observers, and so we have very little idea about what a future eruption from one of these volcanoes will be like: will it be a Kilauea, or a Mt. St. Helens? The answer to this question is essential in order to protect people and assets from volcanic eruptions in Ethiopia. Although Ethiopia is not often associated with volcanoes, it hosts one of the highest densities of them on Earth, with 1 million people living close-by an active volcano, and several power stations using the volcanoes' heat to generate electricity. In order to develop plans for what to do if one of these volcanoes shows signs of imminent eruption, or to decide where is most sensible to build new houses or infrastructure near these volcanoes, we need to know what a future eruption is going to be like. By studying the rocks left-behind by previous eruptions at Aluto (an Ethiopian volcano that has erupted many times over the past 16 thousand years, and is likely to erupt again in the future), I have reconstructed what past eruptions looked like. I have discovered that eruptions at Aluto are more similar to Mt. St. Helens than Kilauea, albeit a little smaller. PDCs are usually produced during these eruptions, which have the potential to destroy anything in their path. To understand where around the volcano is most likely to be hit by a PDC, I ran computer simulations of many eruptions within the range of what has happened at Aluto in the past, each time recording where PDCs hit. Using these data, and maps of where people live around the volcano, I have produced analyses and maps showing the

most risky places near Aluto. These results are useful specifically for Aluto volcano, but by understanding the style of the eruptions from these unusual magmas helps us to understand the eruptions from similar volcanoes in Ethiopia and around the world.

Declaration

I declare that this thesis was composed by myself, that the work contained herein is my own except where explicitly stated otherwise in the text, or where work which has formed part of jointly-authored publications has been included. My contribution and those of the other authors to this work have been explicitly indicated below. I confirm that appropriate credit has been given within this thesis, where reference has been made to the work of others. This work has not been submitted for any other degree or professional qualification.

The work presented in Chapter 2 was previously published in *Nature Communications* as *Fluidal pyroclasts reveal the intensity of peralkaline rhyolite pumice cone eruptions* by *Ben Clarke* (student), *Eliza Calder* (supervisor), *Firawalin Dessalegn*, *Karen Fontijn*, *Joaquín Cortés*, *Mark Naylor*, *Ian Butler*, *William Hutchison* and *Gezahegn Yirgu*. This study was conceived by all of the authors. I, Ben Clarke, authored the manuscript, lead the investigation, undertook the supporting fieldwork, carried out all analyses, characterised the thermal behaviour, parameterised and coded the thermal and ballistic models and developed, under supervision, the key ideas and processes presented in the paper.

Benjamin Andrew Clarke, August 2019

Acknowledgements

This work is the culmination of 4 years of considerable effort, bouts of typhoid, being chased by men with spears, coughing on volcanic ash, dodging baboons, cursing at computers and numerous other activities which have caused my wife great anxiety. Therefore it seems appropriate for my first acknowledgement to go to her: Eleri, the best wife I could have asked for; who, despite battling a PhD herself, not only put up with my struggles and bad mood, but actively worked through them with me. I would not have completed this PhD without you.

Throughout my PhD there have been a few individuals who have been particularly important; they form my (extended) supervisory team. Eliza Calder: who showed me the ropes, provided me with a wealth of opportunities, and taught me why we study volcanoes. Karen Fontijn: who was always there for advice, and opened up a new continent to me. Pablo Tierz: who taught me that statistics isn't boring, and was always up for beer and darts. Joaquin Cortés: who was a diligent teacher, and always provided encouragement. Julia Crummy: who was there when I needed her. And Mark Naylor: who taught me that there is more to Python than snakes. Thank you all. Thanks must also go to those who developed the RiftVolc consortium to which this work contributes.

This work wouldn't have been possible without our Ethiopian partners, who navigated us through the joys and challenges of working in one of the most spectacular, varied, and exciting countries I've had the opportunity to visit. Thank you to our facilitator and co-author: Gezahegn Yirgu. To our colleagues, field assistants and interpreters: Amde Zafu, Firawalin Desalegn and Ermias Gebru. To our drivers and guides, who need to update their music library, but made field work so much fun: Solomon Getachew and Zelalem Mandefro *"Another day another dollar, another day in paradise"*. I'd especially like to thank the countless residents around Aluto who helped us in the field, and so graciously allowed us onto their land. Particular thanks go to the crack team who helped us sieve and sort our rocks - especially Daniel, who showed us around for multiple days, so that he could bring some money back to support his newly grown family. And to Gemedo, who

I'm pretty sure was just in it for the free lunch, but guided us wonderfully around Aluto's southern flank. Galatoomi!

The ideas developed through this thesis are the product of hundreds of conversations, presentations, posters and questions from a great number of people I've had the privilege to meet over the last 4 years. I wish I could list each of them, but in the interest of space, I would particularly like to thank Will Hutchison, David Pyle, Viki Smith, Sam Engwell, Donald Dingwell, Kai-Uwe Hess, Mike Branney, Hugh Tuffen, Sue Loughlin, Greg Valentine, Keri McNamara, Ian Butler, Geoff Kilgour, Brian Upton, Jonathan Fink, Colin Wilson, Ulrich Kueppers and Marie Edmonds; from whom I've learnt a great deal, and to whom I'm greatly indebted.

I often consider where would I be without the wonderful people of the Grant PhD attic? Wherever that might be, I'd probably have a healthier liver, but I'd be far poorer for the lack of parties, coffee times, pub trips, runs and hikes. Thank you all! In particular, I thank Ashley Smith and Roseanne Clement, without whom much of my code wouldn't have worked, and to Kirsty Bayliss, the provider of motivational citrus fruit and statistical knowledge. My academic sisters, Amelia Bain and Isla Simmons put up with me for a considerable period of time, and for that you have my gratitude. I'd also like to thank Sophie Butcher, James Scott, Davide Foffa, Hannah Rogers and Berit Schwichtenberg for keeping mine and everyone's spirits up with running, prosecco and general gaeity. Finally, I'd like to thank my family: my parents for encouraging me to pursue my interests, and my whole family for supporting me, notwithstanding my poor communication and the occasional forgotten birthday.


Ermias
Firawalin
Amde
Karen
Eliza
Daniel
Sam
Pablo
Karen
Zelalem
Solomon
Firawalin
Pablo
Ermias
Viki
Me

Contents

Chapter 1

Introduction

1.1 Volcanism and exposure in the Ethiopian Rift Valley

The Ethiopian Rift Valley forms a northerly segment of the East African Rift, south of the Afar triangle, and hosts a great number of volcanoes along its length. Of these volcanoes a large proportion are classified as 'high uncertainty' in terms of their eruptive history and eruption style. This makes Ethiopia the second most volcanically threatened country on Earth after Indonesia (Aspinall et al., 2011), and a country for which volcanic risks are poorly constrained (Figure 1.1).

There is also considerable exposure to volcanic hazards in Ethiopia, with 1 million people living within 10 km of a volcano in 2011 (Aspinall et al., 2011), and a series of geothermal power plants situated, or planned to be situated, on volcanic edifices. Ethiopia is a fast developing African nation, with rapid industrialisation and an increasing population (UNDP, 2018). Thus, there is a large and increasing exposure to volcanic hazards (Vye-Brown et al., 2016). Such development and growth is leading to an increasing demand on energy. In fact, according to the International Energy Agency, as of 2015, Africa as a whole must generate enough power to supply an economy three times its current size and with an 80% larger population by 2040 (International Energy Agency, 2015). As a result, a US$218 million project has been funded by the World Bank to develop Ethiopia's abundant geothermal resources (World Bank, 2016). The project consists of a 7 MW (with plans to extend to a 80 MW capacity) geothermal power station on Aluto volcano, the development of a 1000 MW power station on Corbetti volcano and a further four prospective

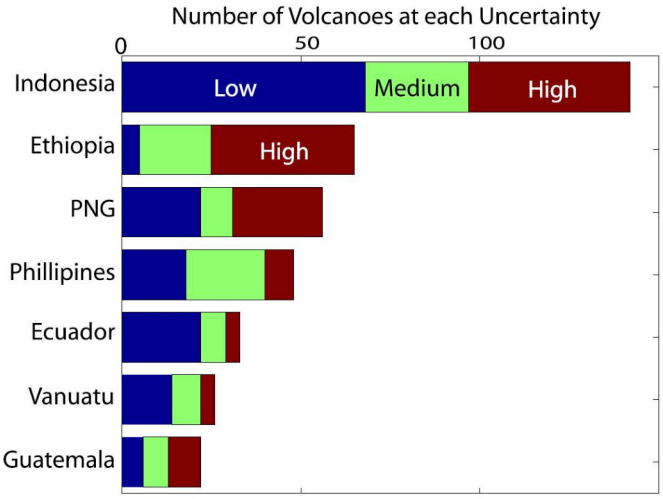

Figure 1.1: *A comparison of volcanoes at each uncertainty by country from Aspinall et al. (2011). Ethiopia stands as the second greatest volcanically threatened country on Earth, with a large proportion of its volcanoes in the high uncertainty category.*

geothermal sites along the Ethiopian rift valley (Teklemariam and Kebede, 2010).

However, volcanoes in Ethiopia have been the subject of relatively little investigation and as a result the risk posed by these volcanoes is largely unknown. There is a paucity of knowledge surrounding the eruptive history of many of these volcanoes, and the rarity of contemporary eruptions means there is great uncertainty surrounding the style and frequency of activity. To compound this, many of the volcanoes in the Ethiopian rift erupt peralkaline rhyolite magmas, for which there have been no observed contemporary eruptions anywhere on Earth, meaning that there are no clear analogues on which to base eruption scenarios. Without a clear idea of what the eruption of a peralkaline rhyolite volcano 'looks like', in terms of explosivity, mass eruption rate, processes, volume, frequency or duration, it is impossible to provide reliable insights on the potential impacts of these eruptions. Without a quantifiable impetus, it's hard to justify any efforts into mitigating this volcanic risk for the benefit of the country and its inhabitants. To date, there has been little awareness of volcanic hazards amongst decision makers in Ethiopia, exemplified by the lack of a permanent volcanic monitoring network, and no formal policy on the management of volcanic crises (Vye-Brown et al., 2016). However, the recent development of an Ethiopian governmental working group on geological hazards marks a step in the

right direction. The potential benefits of understanding Ethiopian volcanism are large, as they would allow informed planning of future settlements and infrastructure to minimise exposure to volcanic hazards. Using this information, action-plans and policies might also be developed to minimise the impact of a future eruption or volcanic crisis. Not only might this save lives, but also protect essential energy infrastructure that supports critical systems and economic centres throughout Ethiopia.

1.2 Project Aims

In order to understand the level of volcanic risk to people and infrastructure in Ethiopia, we first need to understand the nature of the volcanism. Distinct eruptive styles pose quite distinct hazards on a wide range of spatial scales relative to the vent (meters to 100s of km), and a wide range of temporal scales (minutes to years). Not only do we need to understand what hazards an eruption might pose, we must also understand where and when an eruption is most likely to occur. These primary questions of 'What?', 'Where?' and 'When?' form the crucial variables in understanding the *hazards* volcanoes pose. However, to understand the *risk* we must also understand the 'Who?'. Initially this is a case of characterising the spatial density distribution of people, cultural assets and infrastructure, and how this relates to the footprint of potential hazards. However, to gain a true understanding of the impact of volcanic eruptions, one must understand the varied and nuanced vulnerabilities of these populations and assets. For example: What times of day/year are people most likely to be around the volcano? Are there particular assets of greater importance to residents/decision makers/businesses? Are there distinct racial/cultural/-gender/economic/political considerations that need to be made? How effective will any hazard mitigation method be for different stakeholders, and how will this impact different stakeholders on a day-to-day basis?

The work presented in this thesis aims to understand the What?, the Where? and the initial stage of Who?, with a particular focus on pyroclastic density currents (PDCs). More specifically, in this thesis I attempt to:

1. Understand the eruptive styles and processes of Quaternary peralkaline rhyolite volcanoes in the Main Ethiopian Rift valley

2. Characterise the extent to which, and how, PDCs are produced during these eruptions, evaluating the style and mobility of the flows

3. Identify the likely source-locations of future eruptions

4. Use this information to physically and statistically model PDCs, to probabilistically assess the PDC hazard

5. Combine this probabilistic analysis with data of the spatial density of exposure, to identify key areas currently at risk

6. Develop PDC hazard maps to effectively communicate this information to a range of stakeholders

These aims are ambitious, and as such I will focus on the PDC hazard of one particular volcano: Aluto, for which some research has already been conducted.

This work contributes to RiftVolc, a NERC large grant-funded project initiated in 2014. As a whole, RiftVolc aims to understand past, present and future volcanism in the Ethiopian rift valley. The project consists of teams from the universities of Edinburgh, Oxford, Cambridge, Bristol, Southampton, Leeds, Addis Ababa and the British Geological Survey. Covering a wide range of disciplines, the project explores aspects of rifting processes, magma generation, migration and storage, eruption magnitudes and frequencies, eruptive styles and probabilistic tephra fall and pyroclastic density current hazards. This is in addition to improving awareness and initiating actionable steps to increase Ethiopia's resilience to volcanic hazards. Much of the work referenced in this thesis is the product of earlier phases of the RiftVolc project; in particular, the PhD thesis and associated papers of William Hutchison concerning Aluto volcano.

1.3 Background: Volcanism and the Main Ethiopian Rift

1.3.1 A geological history of the Main Ethiopian Rift

The main Ethiopian Rift (MER) is a northerly segment of the East African Rift System (EARS) where the Somalian and Nubian plates diverge at around 6.5 mm/year (Stamps et al., 2008) forming a NE/SW trending valley (Figure 1.2). The MER can be divided into three geomorphologically and geologically distinct sections: the Northern MER (NMER), Central MER (CMER) and the Southern MER (SMER) (Figure 1.2). The evolution of the MER is thought to result from a strong feedback between magmatic and tectonic forcings. Initially plume-related flood basalts resulted in doming of the crust at around 30 Ma (Hofmann et al., 1997) to produce the Ethiopian and Somalian plateaus (Ferguson et al., 2013; Rychert et al., 2012; Pik et al., 1998) and the presence of pre-existing crustal weaknesses localised strain accumulation along the future MER. Rifting in the MER initiated in the SMER (18 Ma) and the NMER (11.5 Ma), stalled at the NMER-CMER boundary and then continued in the CMER from 5-6 Ma (Keranen and Klemperer, 2008). Extension of the crust at the MER results in crustal thinning, and the associated reduction in pressure in the underlying mantle has lowered the solidus temperature below the geotherm, eliciting mantle melting (Ebinger, 2005) (Figure 1.3). This initially resulted in diffuse silicic magmatism across the rift. As the extension progressed, faulting moved towards the rift axis, and as the crust continued to thin, prodigious decompression melting resulted in continued volcanism; leading to more extension through intrusion of magma into the rift (Kendall et al., 2005) where basaltic fissure eruptions became dominant (Lahitte et al., 2003; Hutchison, 2015). This can be seen today in Afar; where the most mature northerly section of the East African Rift meets the Red Sea Rift. The CMER, being the least mature portion of the MER, appears to be at an intermediate stage in this process, where volcanism is dominated by diffuse, large silicic calderas (Fontijn et al., 2018).

The silicic calderas of the region, from north to south are Fentale, Kone, Boset-Bericha, Gedemsa, Bora-Bericha, Aluto, Shala and Corbetti (Figure 1.2). Many of these volcanoes first developed as trachytic shields, and subsequently underwent large caldera-forming eruptions (Hutchison et al., 2016b). Corbetti, Shala, Gedemsa and Aluto underwent these large

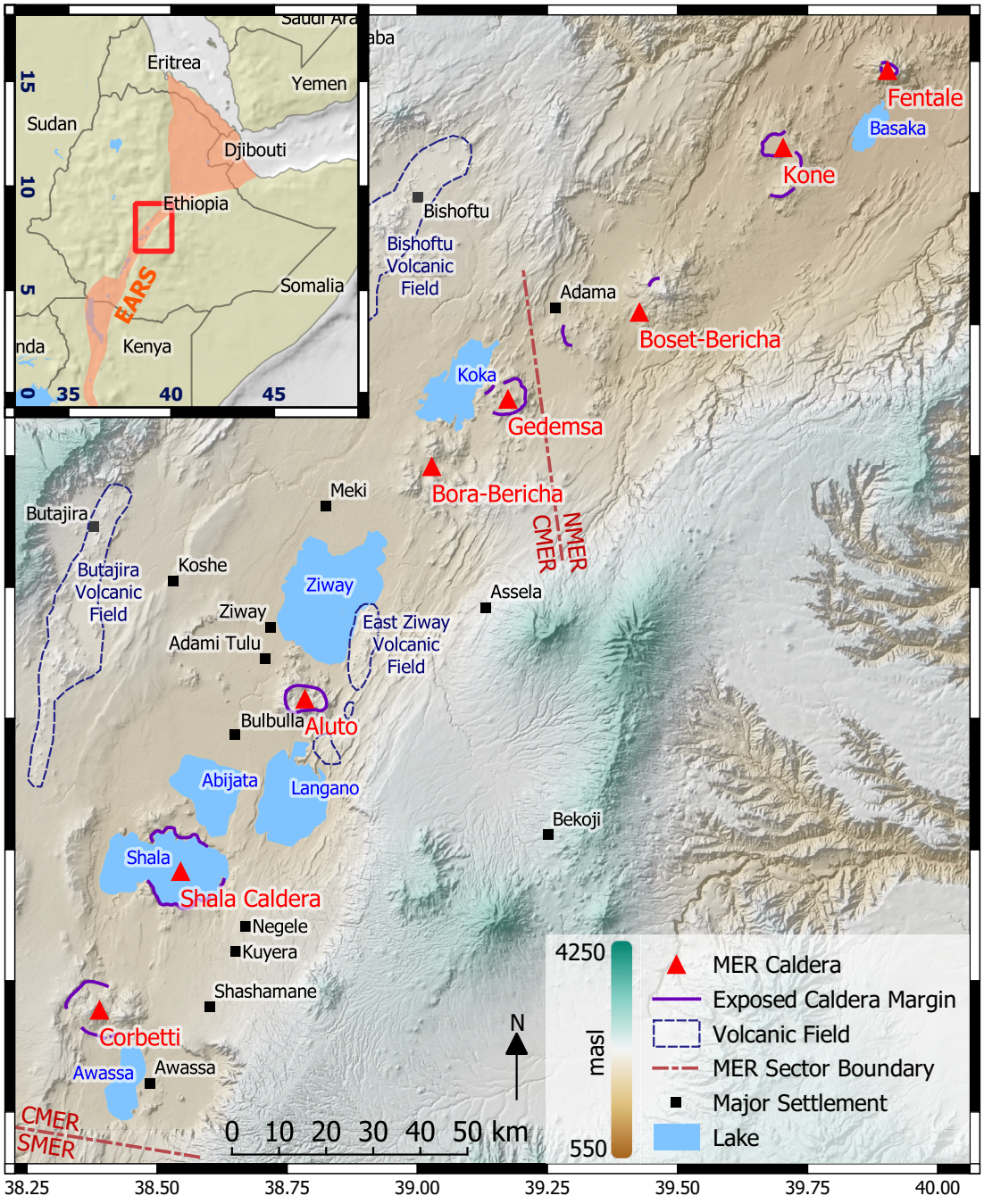

Figure 1.2: *An overview of the Main Ethiopian Rift: its location, topography, volcanoes, volcanic fields, major lakes and major settlements. EARS = East African Rift System, MER = Main Ethiopian Rift, NMER = Northern MER, CMER = Central MER, SMER = Southern MER. WGS84 coordinates. Topography: (NASA, 2014), Lakes: (RCMRD, 2015), Major Settlements: (OpenStreetMap, 2019), Calderas, margins and volcanic fields: (Fontijn et al., 2018), MER sector boundaries: (Corti, 2009).*

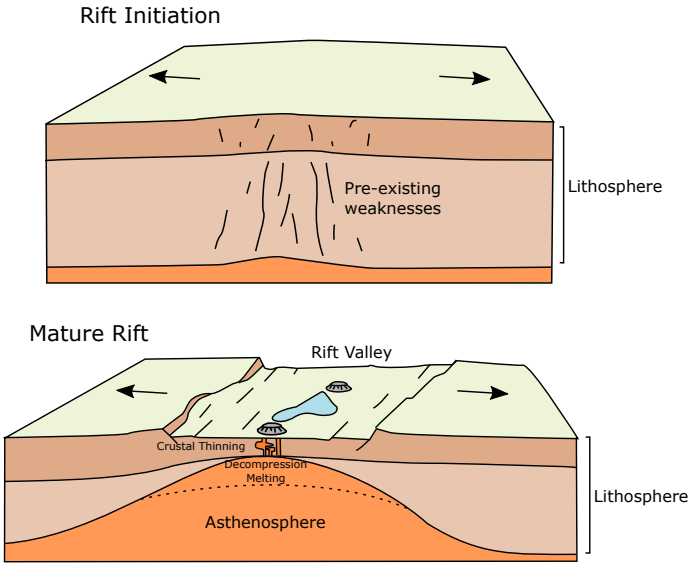

Figure 1.3: *Schematic block diagram illustrating the initiation and development of the East African Rift System. Crustal thinning leads to decompression melting, resulting in volcanism.*

eruptions over a relatively short temporal window between 316 and 270 Ka, in what is proposed as an 'ignimbrite flare-up' in the MER (Hutchison et al., 2016b). Since these large caldera-forming eruptions, most volcanic activity has been limited to smaller scale silicic eruptions at these centres (Fontijn et al., 2018), and monogenetic basaltic volcanism at the numerous fault-controlled volcanic fields along the MER (Figure 1.2) (Abebe et al., 2007; Mazzarini et al., 2016).

The lakes of the MER have undergone dramatic changes over their history as a result of climatic, tectonic and volcanic forcings (Le Turdu et al., 1999). Lakes Shala, Longano, Abijata and Ziway lie within the Shala lakes basin which has had a complex history of water-level fluctuation and interconnection since the early Pleistocene, and at times have formed a single megalake (Benvenuti et al., 2002a). This basin has collected the deposits of many eruptions from MER volcanoes, providing a record of the larger eruptions, where tephra has reached the lakes in sufficient volume to not be completely eroded or reworked. Recent work studying lake sediment cores from Langano and Abijata has helped to develop a teprhastratigraphy for this portion of the CMER between 13.4 and 1.7 cal.Ka BP (McNamara et al., 2018). The tephras in these cores are attributed to at least 24 distinct eruptions, mostly from Aluto, but two from Corbetti (McNamara et al., 2018). The

tephras from Aluto are thickest in the lake Abijata core, consistent with the present-day dominant wind direction (towards the west) at Aluto since at least 1990 (Mastin, 2017). Eruptions from Aluto appear to have occurred in temporal clusters at 11, 6.1 and 3.5 Ka, and are tentatively described to range from vulcanian to sub-plinian in magnitude and style (McNamara et al., 2018).

The most recent signs of volcanic unrest at MER calderas have been InSAR-measured ground inflation and deflation events at Corbetti, Aluto, Bora-Bericha and Haledebi (to the far north) (Biggs et al., 2011; Lloyd et al., 2018). These have been attributed to repeated replenishment of magma to depths shallower than 10 km beneath the respective volcanic edifices (Biggs et al., 2011; Hutchison et al., 2016a). Due to their unrest, recent history of explosive eruptions, and proximity to large population centres and geothermal infrastructure, Aluto and Corbetti have been identified as of particular concern for volcanic hazards in Ethiopia.

1.3.2 Aluto Volcano

Context and Geology

This work concentrates on Aluto volcano; a 12 km wide caldera within the CMER between the lakes Ziway and Langano, forming an irregular prominence of around 700 m from the surrounding flat plains. The towns of Adami Tulu and Ziway lie to the NW, and Bulbulla to the SW, with many other diffuse or smaller settlements on and surrounding the edifice. There are numerous important assets within the caldera itself, including a school, multiple settlements and a US$126 million 7 MW pilot geothermal power station, with a US$76.8 million contract to expand to an 80 MW capacity (Tedesse, 2018; Richter, 2019). In additional to field work and remote sensing data, borehole data from this geothermal project was analysed by Hutchison et al. (2016c) (Figure 1.4) in order to develop a broad stratigraphy and geological history of Aluto. Their geological map is presented in Figure 1.5.

The oldest rocks attributed to Aluto volcano are dated to around 570 Ka, and are trachytic lavas and tuffs forming a shield volcano (Hutchison et al., 2016c). This shield volcano must have been relatively low relief, allowing the deposition of lacustrine sediments over part of the edifice (Figure 1.4). The trachytic shield sat atop the rift floor composed of Neogene ignimbrites and the Bofa basalt formation (Figure 1.4). At between 300-320 Ka, Aluto underwent dera imbrites (Hutchison et al., 2016c; Fontijn et al., 2018), and leaving behind the outer flanks of the trachyte shield and a section of caldera fault scarp in the NE sector of the caldera. Since at least 60 Ka, Auto has undergone numerous smaller volume silicic eruptions across the edifice which have buried much of the older stratigraphy. These eruptions typically produce pumice cones and obsidian lava flows or couleés, and distal tephra fall deposits within the surrounding lakes, some to a distance of at least 25 km (Hutchison et al., 2016c; McNamara et al., 2018; Fontijn et al., 2018). These eruptions have emanated from the caldera ring-fault, and numerous NE/SW cross cutting regional Wonji faults (Hutchison et al., 2015). These faults provide structural pathways to allow magma ascent, and are marked today by localised high CO_2 fluxes (Hutchison et al., 2015), a feature also recognised on a rift-scale (Hunt et al., 2017). The youngest eruptive products from Aluto that have been dated are around 400 $\pm$ 50 years old (Hutchison et al., 2016c), and first-order estimates of average recurrence rates from lake tephras indicate a frequency of between 2 and 3 eruptions per millennium (Fontijn et al., 2018). However, recent studies of Lake tephras indicate eruptions have a average return period of around 250 years, but have been concentrated in temporal clusters at 3, 6.5 and 11 Ka, where eruptions occur every 100 years or so (McNamara et al., 2018). Unfortunately, as only two lake cores exist, it is challenging to extract quantitative estimates on the volume of erupted material or invert deposit data for column heights. However, by comparisons with thickness grain-size distance relationships for fall deposits elsewhere, McNamara et al. (2018) tentatively suggest these eruptions range in intensity, style and magnitude from vulcanian to sub-plinian, and that plinian eruptions are absent in the Holocene record of Aluto.

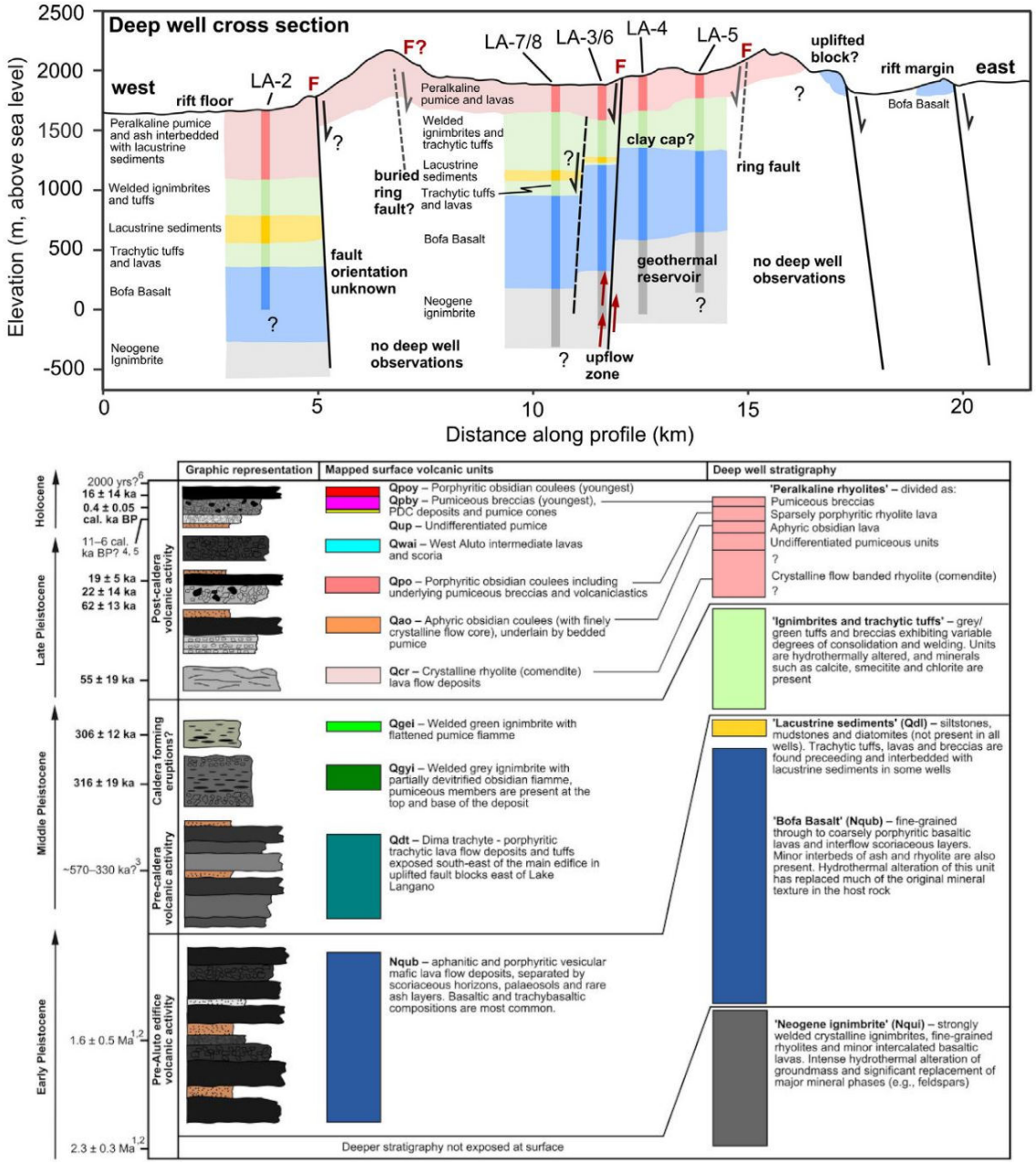

Figure 1.4: *A cross section and stratigraphy of Aluto and its flanks based on borehole and field data, displaying the main rock units that form Aluto's stratigraphy (Figures 2 and 3 from Hutchison et al. (2016c).*

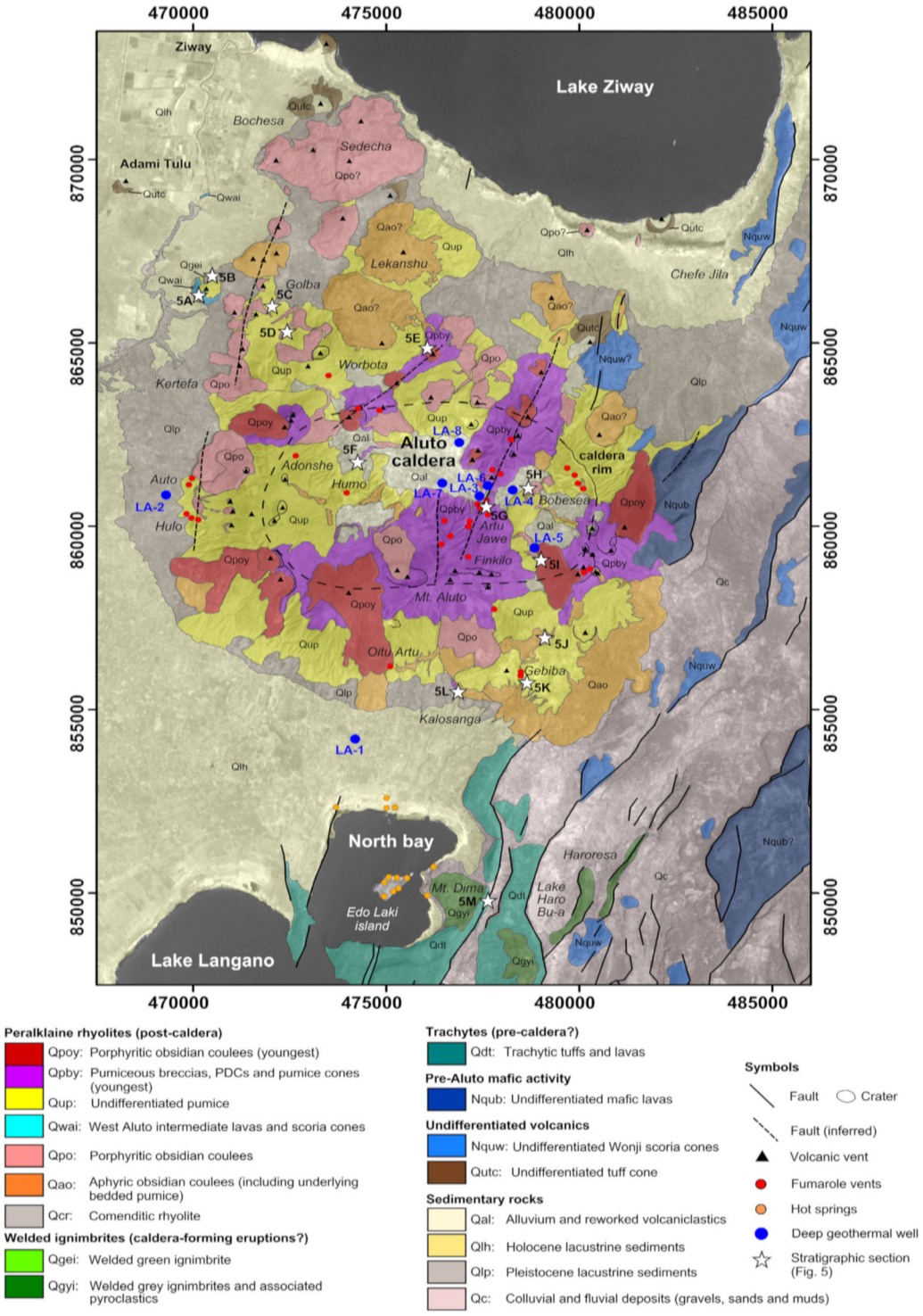

Figure 1.5: *A geological map of Aluto caldera from (Hutchison et al., 2016c), showing the major rock units, faults and geothermal areas of Aluto volcano.*

Melt Generation and storage

In the MER today, magmatism tends to be focussed around two points: the Wonji and Silti-Debre Zeyit fault zones, the former hosting Aluto and Corbetti volcanoes (Rooney et al., 2012). Volcanism at these sites is dominated by alkali-rich magmas, ranging from alkaline basalts through to peralkaline rhyolites with a marked paucity of intermediate compositions (Peccerillo et al., 2007; Hutchison et al., 2016c). Peralkaline magmas are defined by their molar excess of K and Na (molar $Na_2O + K_2O$ / $Al_2O_3 \geq 1$). Peralkaline rhyolites can be further subdivided into pantellerites and comendites, defined by their ratio of Al_2O_3 to FeO, with pantellerites being relatively iron rich and aluminium poor. The peralkaline rhyolites at Aluto are almost exclusively pantellerites (Hutchison et al., 2016c; Gleeson et al., 2017). Peralkaline rhyolites are generated throughout the East African rift and the Red Sea rift, attributed to prodigious fractional crystallisation of plagioclase with minor crustal assimilation of a mafic parent (Rooney et al., 2012; Peccerillo et al., 2007, 2003; Field et al., 2012, 2013; Barberi et al., 1974; Hutchison et al., 2016c). Based on major and trace element modelling, the process is also thought to be responsible for the peralkaline rhyolites at Aluto (Hutchison et al., 2016c; Gleeson et al., 2017). Such extensive fractional crystallisation is also invoked as the driving force behind the very high concentrations of other incompatible high field strength elements, halogens and large ion lithophile elements in peralkaline magmas (Harris, 1981; Field et al., 2012, 2013; Aiuppa et al., 2009). Alternatively, some workers suggest these geochemical features are a result of open system crustal assimilation processes (Bailey and Macdonald, 1975; Macdonald et al., 1987). However, trace element ratios (La/Y and Rb/Nb) do not vary significantly and are much lower than would be expected for assimilation of the pre-cambrian crustal rocks beneath Aluto (Peccerillo et al., 2003; Hutchison, 2015).

The more recent eruptions at Aluto have been dominated by remarkably geochemically homogeneous peralkaline rhyolites. Apart from occasionally abundant feldspar microlites, many of the eruptive products are aphyric, especially the tephras. However, some obsidian lavas contain considerable phenocryst cargoes, often exceeding 20 vol%, with a typical mineral assemblage of Quartz + K-feldspar ± aegerine ± aenigmatite. Quartz and k-feldspar

often exist as subhedral granophyric masses surrounding a crystallising core of either phase (Hutchison et al., 2016c; Gleeson et al., 2017). Gleeson et al. (2017) investigated the magma storage conditions of peralkaline rhyolites at Aluto using rhyolite-MELTS, a thermodynamic and empirically constrained model of magmatic melting, crystallisation and differentiation (Gualda et al., 2012). Gleeson et al. (2017) found that peralkaline rhyolites at Aluto were most likely to have been stored at low pressure (150 MPa), corresponding to depths of around 5.6 km, with an oxygen fugacity near the Quartz-Fayalite-Magnetite (QFM) buffer. Unfortunately, peralkaline systems are relatively understudied, and so there is a lack of experimental data on the stability of phases such as aenigmatite. This means that the rhyolites-MELTS model is poorly parameterised for these magmas. Despite this, the depths of storage suggested by this modelling are somewhat consistent with the depths of contemporary magma storage inferred from ground deformation (Hutchison et al., 2016a; Biggs et al., 2011) and seismicity (Wilks et al., 2017). Oddly, magnetotelluric studies (Samrock et al., 2015; Hübert et al., 2018) have shown that there is no conductor at 5 km depth under Aluto, as might be expected with the presence of a magma body, but Hübert et al. (2018) conclude this is due to poor melt connectivity and perhaps low (<4 wt%) water concentrations. This would suggest magma under Aluto is stored as a high crystal-fraction mush, containing small lenses of melt. This is supported by petrological studies of Aluto, suggesting that magma storage is dominated by repose periods of unconnected peralkaline rhyolite mush, with relatively rapid assembly of eruptable magma [months to decades] prior to eruptions (Iddon et al., 2019).

1.3.3 The rheology of peralkaline rhyolites

The composition of a silicate melt has a significant influence on its physical properties (e.g. Giordano et al., 2008), which in part influences the style and hazards of any given eruption. Peralkaline melts are packed with a high proportion of network modifiers: excess (free) ions of Na and K, and high water and F concentrations. This has the effect of de-polymerising the melt and lowering its viscosity (Baasner et al., 2013; Di Genova et al., 2013; Dingwell et al., 1998; Hess et al., 1995). Despite their relatively low temperatures

(around 750^{o}C at Aluto (Gleeson et al., 2017)), peralkaline rhyolites are still lower viscosity than non-peralkaline melts of equivalent silica enrichment.

Experimental studies have already indicated the particularly strong influence of water on lowering the viscosity of peralkaline rhyolites (Hess et al., 1995; Dingwell et al., 1998), but fluorine also plays a important role, with the addition of fluorine having a similar influence on the viscosity as water on a weight percent basis (Giordano et al., 2004; Zimova and Webb, 2007). Peralkaline rhyolites are often hydrous melts due to concentration through fractional cyrstallisation. They typically possess water concentrations between 2.5 and 5 wt% (Field et al., 2013; Neave et al., 2012), though water concentrations above this are still relatively common. There are currently no published data on the water concentrations measured in melt inclusions at Aluto, but in the absence of data, we assume that the water contents of Aluto melts lie within the range of peralkaline rhyolites elsewhere (Figure 1.6). Fluorine contents measured in peralkaline rhyolite glasses from Aluto are also high, at around 0.5 wt% (Clarke et al., 2019). The combined effect of excess alkalis, and high water and fluorine concentrations makes melts at Aluto particularly low viscosity considering the high degree of silica enrichment. In fact, at eruption temperatures, hydrous peralkaline rhyolites possess similar melt viscosities to basalts (Figure 1.7) (Clarke et al., 2019). This is liable to influence the eruptive style at Aluto and in turn the hazards posed to local stakeholders.

1.3.4 Previous studies on the eruptive style of peralkaline rhyolites

Due to its relative rarity on Earth, peralkaline rhyolite volcanism has been understudied compared to volcanism associated with more common melt compositions. This may also be a result of no eruption of a peralkaline rhyolite being observed and recorded. The fact that peralkaline melts possess a peculiar rheology means that it is questionable to assume similarity in eruptive style to any other composition. The most studied peralkaline rhyolite eruptions are caldera-forming (Mahood, 1984; Schmincke, 1975b), but relatively few investigations have taken place to study smaller scale eruptions that typically occur after

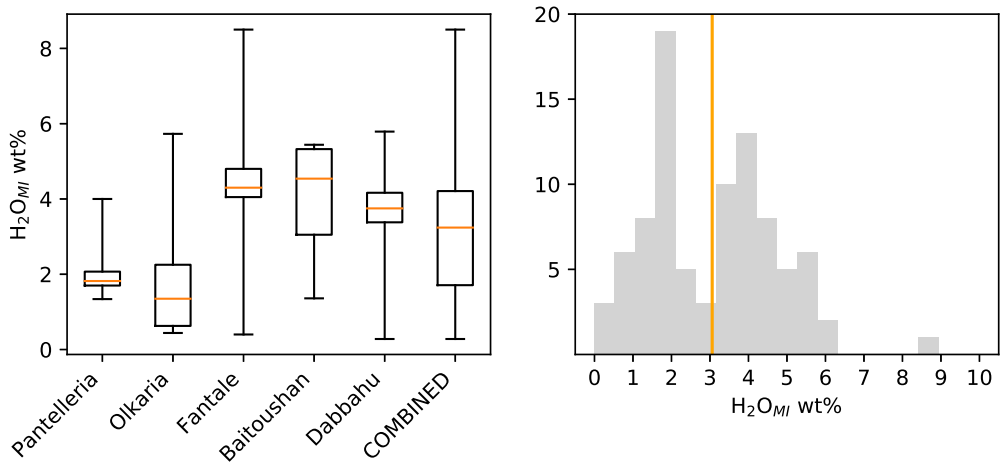

Figure 1.6: *Ranges of published melt-inclusion derived water concentrations in peralkaline rhyolites from volcanoes worldwide. Data are from from quartz and plagioclase-hosted melt inclusions. On the left: Whiskers show the range, the boxes span the upper and lower quartiles of the data. The orange centre-lines show the mean for each volcano. On the right: a histogram of all combined H_2O melt inclusion data, the vertical orange line marks the mean at 3.1 wt%. Overall, most pantellerites have water contents between 2 and 4.5 wt%, but span a range between 0.5 and 8 wt%. Data sources: Pantelleria (Lowenstern and Mahood, 1991; Lanzo et al., 2013), Olkaria (Wilding et al., 1993), Fantale (Webster et al., 1993), Baitoushan (Horn and Schmincke, 2000), Dabbahu (Field et al., 2012).*

caldera formation. Such eruptions may be the most pertinent for contemporary volcanic hazards in places such as the MER, where caldera formation is infrequent, and has already taken place at many silicic centres, including the potential 'high risk' volcanoes Aluto and Corbetti (Hutchison et al., 2016b).

Post-caldera volcanism at peralkaline rhyolite volcanoes is characterised by pumice cones (Mahood, 1984; Houghton and Wilson, 1989; Houghton et al., 1985; Orsi et al., 1989); enigmatic scoria-cone-like structures comprising rhyolitic pumice rather than basaltic scoria. Prior to the RiftVolc project, two main works explored the nature of pumice cone formation during post-caldera eruptions of peralkaline rhyolite volcanoes. Orsi et al. (1989) investigated deposits from the pumice-cone-forming 8 Ka Serra della Fastuca eruption on Pantelleria, and concluded from inversions of isopleth and isopach data, that the eruption was strombolian in style and magnitude. They also conclude that no stable column was generated, and that plumes did not collapse to form pyroclastic density currents. This paints a picture of eruptions dynamically similar to basaltic scoria cone eruptions, where

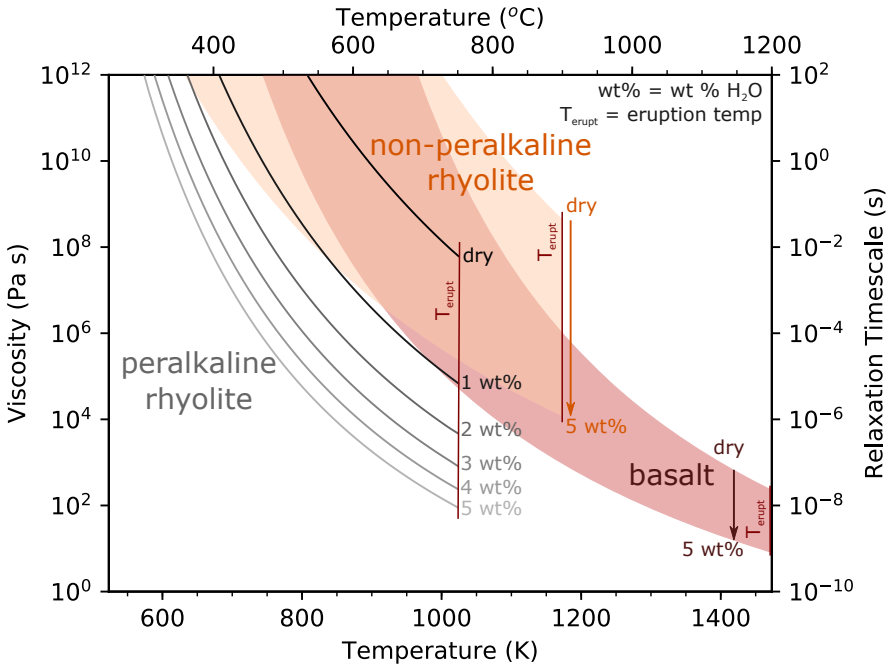

Figure 1.7: *Viscosity-temperature relationship for peralkaline rhyolite melt with varying water concentration based on the model of Di Genova et al. (2013). Pantellerites typically contain between 2.5 and 5 wt % H_2O prior to eruptive degassing (Field et al., 2012; Neave et al., 2012). For comparison, the viscosity-temperature relationship calculated by the VFT equation (Giordano et al., 2008) is shown for a typical, non-peralkaline (in this case peraluminous), rhyolitic melt (Rhyolite Glass Mountain - 1 standard) and basaltic melt (Basalt Hawaii Volcanic Observatory - 1 standard). Note that at eruption temperature, hydrous Aluto peralkaline rhyolites have a similar viscosity to basalts, and possess exceptionally low glass transition temperatures (temperature at which viscosity = 10^{12} Pa s). Figure 6 in (Clarke et al., 2019).*

the main depositional regime is ballistic, producing localised cones of material with limited lateral tephra dispersal. A similar conclusion was reached by Houghton et al. (1985), who studied pumice cone forming eruption deposits on Mayor Island, New Zealand. In both cases, they cite the comparatively low viscosity of peralkaline rhyolite to allow decoupling of the melt and gas phase during magma ascent, thus efficiently degassing the system without producing an intense explosive eruption. However, in the MER, larger eruptions (vulcanian to sub-plinian, in terms of volume and style) are typical for post-caldera activity at peralkaline rhyolite volcanoes (Fontijn et al., 2018), and pyroclastic density current deposits are very commonly preserved (Hutchison et al., 2016c). Investigations of distal lake cores have linked tephras to pumice cone forming eruptions (McNamara et al., 2018), suggesting in the MER at least, pumice cones may be associated with eruptions of greater volume and intensity than those studied elsewhere.

1.4 A brief note on style and structure

This project begins from first-principles, with little knowledge of the specific volcano, the style of volcanism, frequency of eruptive events or the exposure to volcanic hazards. The ultimate aim is to produce a probabilistic PDC hazard and risk evaluation. Such hazard analyses aren't common, even for some of the world's most studied volcanoes, and so this project aims to cover a lot of ground in the space of a single PhD. The primary purpose of this PhD is thus not only to develop a greater understanding of peralkaline rhyolite volcanism in the MER, but to attempt to develop a probabilistic PDC hazard and risk assessment from a point of near-zero knowledge surrounding a volcanic system, with limited time and resources.

In order to do this, my thesis employs a very broad range of techniques and approaches. Such material doesn't lend itself to a single *'Review, Methods, Results, Discussion, Conclusions'* structure. Instead, I have chosen to divide the chapters by technique and approach, where each chapter includes an introduction, methods, results and discussion section, and is consistent in its theme, aims and approach. Each chapter builds upon the last, using

inferences and conclusions from earlier chapters to inform and direct the techniques and approaches used later. In the end, I tie the work together in a final summary and conclusions chapter. I have also chosen to use the first-person on occasion, for greater clarity (Schultz, 2009), though where the work I am discussing involves collaborators, I acknowledge their contribution. In Chapter 2, the text is sourced from collaborative published work, and so my use of language and perspective changes for this section of the thesis.

Chapter 2

Pumiceous Achneliths: New clues to the style and intensity of pumice cone-forming eruptions

"The precision of naming diminishes the uniqueness of seeing"

Pierre Bonnard

2.1 Introduction

As I have established in the introductory chapter, pumice cones are a primary volcanic feature typically produced during non-caldera-forming peralkaline rhyolite eruptions. Despite this, no peralkaline rhyolite eruptions have been directly recorded, and non-caldera-forming peralkaline rhyolite eruptions have been the subject of little scientific investigation. Consequently their eruptive style and associated hazards are very poorly understood. Aluto volcano in Ethiopia possesses a large number of pumice cones produced during multiple post-caldera eruptions. It therefore provides an opportune location to investigate the style of these enigmatic eruptions. During the first preliminary field campaign in November 2015, we investigated the deposits of numerous pumice cones at Aluto. In the NE sector of the volcano, we found some rather unusual pyroclasts, which we term 'pumiceous achneliths', within the deposits of two separate pumice cones. Some appeared to have 'inflated' into their void space in deposit, whilst others had developed aerodynamic shapes similar to Pele's tears that are sometimes produced during basaltic eruptions (Walker and Croasdale,

1971; Porritt et al., 2012). The presence of these pyroclasts amongst seemingly contemporaneous, 'normal'-looking rhyolitic pumice raised questions of how these pyroclasts were generated and what they may tell us about the nature of pumice cone eruptions. In the following paper (Clarke et al., 2019), published in *Nature Communications, May 2019*, we use a combination of field-observations, geochemistry, x-ray computed microtomography (XCT) and thermal-modelling to investigate how these pyroclasts are formed. We find that they deform during flight and, depending on size, quench prior to deposition or continue to inflate then quench in-situ. These findings reveal important characteristics of the eruptions that gave rise to them: that despite the relatively low viscosity of these magmas, and similarities to basaltic scoria-cone deposits, moderate to intense, unstable, eruption columns are developed; meaning that such eruptions can generate extensive tephra-fall and pyroclastic density currents.

A brief note on the structure of this paper: the format of the paper suits the Nature Communications style, where the methods are presented after the discussion and conclusions.

2.1.1 Author contributions

This work is the combined effort of multiple researchers. Here I lay out the contributions each co-author made to the work: I authored the manuscript, carried out all analyses and led the research under the supervision of Eliza Calder. Field work was undertaken by Eliza Calder, Firawalin Desalegn, Karen Fontijn and myself. Joaquin Cortés provided training and consultation on electron microprobe analysis undertaken by myself. Ian Butler provided equipment and training in the processing and analysis of XCT data. Development, characterisation of the thermal behaviour, parameterisation and coding of the thermal model was conducted by myself. The application of the method of lines to solve the problem in spherical coordinates within the thermal model was developed by Mark Naylor. Conversations with Eliza Calder, Joaquin Cortés, Karen Fontijn, Will Hutchison, Mike Branney, Ulrich Keuppers, Donald Dingwell, Kai-Uwe Hess and Hans-Ulrich Schmincke all helped to develop the ideas presented in this work.

2.2 Paper: Fluidal pyroclasts reveal the eruption dynamics of pumice cone-forming eruptions

2.2.1 Introduction

Peralkaline rhyolites (molar $NaO_2 + K_2O$ / $Al_2O_3 > 1$) are medium to low viscosity volatile rich magmas and are found in rift zones worldwide (Mahood, 1984). Despite this, relatively little is known about the style and eruption dynamics of volcanism characterised by them. Eruption dynamics are typically controlled by the interplay between the geochemical and rheological factors influencing the effectiveness of degassing. Peralkaline rhyolite melts exhibit low viscosities compared to other rhyolites of equivalent silica enrichment, a property attributed to the depolymerising effects of excess alkalis and high halogen concentrations (Baasner et al., 2013; Di Genova et al., 2013; Dingwell et al., 1998; Hess et al., 1995). Peralkaline rhyolite eruptions are commonly associated with an enigmatic suite of eruption products including, but not limited to, obsidian lava flows, welded ignimbrites and pumice cones. Overall, the absence of direct observations of peralkaline eruptions, the unusual geochemistry of the melts, and the fact that deposits from peralkaline rhyolite eruptions do not fall neatly into established eruption classifications means that the eruption styles of peralkaline rhyolites are largely unknown. The evaluation of hazard and risk at a given volcano is contingent on having a robust conceptual model of how the volcanic system operates and the nature of its associated eruptive activity. For peralkaline volcanoes worldwide, the paucity of this knowledge is a significant limitation.

The East African Rift (EAR) is characterised by the greatest density of silicic peralkaline volcanoes on Earth, and furthermore, Ethiopia is regarded as the fifth most volcanically threatened country (Loughlin et al., 2015); with 10 million people living within 30 km of a volcano (Aspinall et al., 2011). Here we present a study of unusual, yet uniquely well preserved, fluidal-shaped pyroclasts found in peralkaline rhyolite pumice cone deposits at Aluto volcano in the Main Ethiopian Rift (MER) (a northerly segment of the EAR).

Somewhat similar pyroclasts, termed globules, have been observed in peralkaline rhyolite deposits on Gran Canaria, Pantelleria and in the Kenyan rift (Sumner and Branney, 2002; Johnson, 1968; Schmincke, 1972), and are characterised as fluidly-shaped glassy pyroclasts with a thin skin and highly vesicular interior. There is currently no consensus on how they form or what style of eruptive activity they are indicative of. Here, for the first time, these pyroclasts are investigated in detail using scanning electron microscopy (SEM) and XCT providing unique insights into their 3D structure. We present field and clast observations, undertake thermal modelling and develop the first comprehensive conceptual model for the formation of these peralkaline fluidal-shaped clasts, henceforth referred to as pumiceous achneliths. This new understanding of pumiceous achneliths forms the basis of a conceptual model of pumice cone forming peralkaline rhyolite eruptions and provides some important constraints on this hitherto ambiguous style of activity. This allows for a better understanding of the likely hazards associated with future eruptions of peralkaline rhyolite volcanoes, potentially worldwide.

2.2.2 Results

Aluto caldera

Aluto is a 12 km wide caldera complex in the central MER situated directly south of Lake Ziway (Figure 2.1) (Hutchison et al., 2016c). The complex underwent major explosive eruptions at around 310 ka, likely associated with caldera collapse, and since at least ∼60 ka it has erupted a series of smaller scale pyroclastic deposits and obsidian lava flows across the main edifice (Hutchison et al., 2016c; Fontijn et al., 2018). This recent volcanism (< 60 ka) is dominated by peralkaline rhyolite magmas, thought to be the product of protracted (> 80 %) fractional crystallisation of a basaltic parental melt (Gleeson et al., 2017). At Aluto, these eruptions typically entail the formation of a pumice cone with, in most cases, pyroclastic density current (PDC) deposits followed by the emplacement of obsidian lava flows. Pumice cones are a volcanic landform commonly produced during peralkaline rhyolite eruptions, and due to their resemblance to basaltic scoria cones, have generally been considered to develop during relatively low-intensity strombolian-style

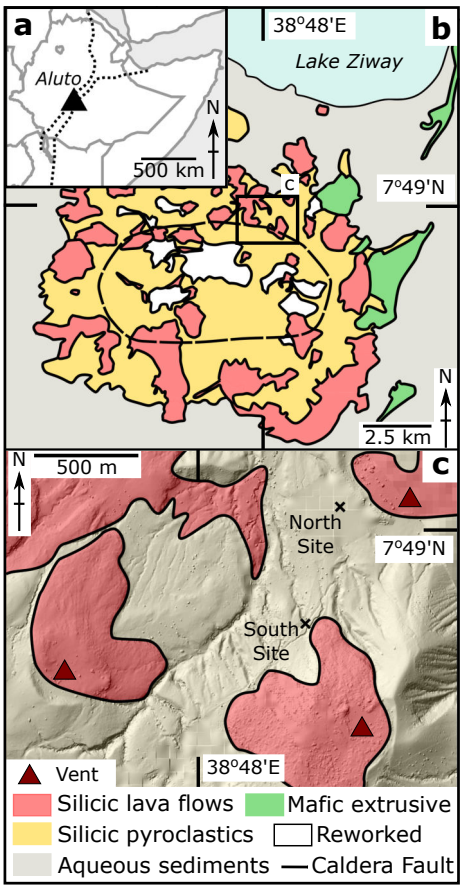

Figure 2.1: *Contextual and simplified geological map of Aluto caldera and the sampling sites (**a**) Map showing location of Aluto in Ethiopia; (**b**) Simplified geological map of Aluto after Hutchison, 2015.; (**c**) DEM hillshade overlain by geology showing north and south study sites. DEM produced using Aluto LiDAR data from Hutchison et al. (2016c)*

eruptions (Orsi et al., 1989; Houghton et al., 1985). The presence of PDC deposits from pumice cones at Aluto and elsewhere (ie. Monte Pilato, Lipari (Davì et al., 2011)) suggests this assumption may not be universally correct.

Deposit Description

The pumiceous achneliths on which this study is based are sourced from two separate sites (termed here north and south site respectively) within pumice cone deposits adjacent to, and stratigraphically below, obsidian lava flows in the NE section of the caldera (Figure 2.1). The north and south sites are 600 m apart (Figure 2.1), but are proximal to, and

stratigraphically below different obsidian lava flows. They are also stratigraphically discontinuous and so represent separate deposits. However, they are otherwise nearly identical in their lithological, sedimentological and chemical characteristics. The deposits are each 2-3 m thick and comprise unconsolidated, poorly sorted massive breccias. They are massive, clast supported, and ash and matrix poor.

The North and South deposits represent the proximal deposits of pumice cones (estimated 300 m and 600 m from the likely source vents respectively, Figure 2.1) produced prior to the emplacement of their associated obsidian lava flows. To account for their very poor sorting yet high angularity, these deposits either represent proximal fall deposits produced during a prolonged but highly unsteady eruption, as seen in violent strombolian eruptions (Pioli et al., 2008), or fall deposits which have been very-locally remobilized (avalanched), from their parent cone.

Clast Descriptions

The deposits contain clasts of tube pumice, microvesicular pumice (total pumice: 80 wt %), dense obsidian bread crust bombs (5 wt %), assorted siliciclastic and ignimbrite lithics (5 wt %), and pumiceous achneliths (10 wt %). All clasts other than the pumiceous achneliths are angular. The achneliths are a very distinctive clast type; they are well- to sub-rounded in form, have a thin (10-100 μm) smooth gray-to-black glassy skin and a highly vesicular interior (Figure 2.2). In-situ, pumiceous achneliths have highly irregular polygonal shapes, fill their void space in the deposit, and press-up and deform against adjacent clasts (Figure 2.3). They also span a range of sizes, from mm to cm (to decimeters at other localities). There is no systematic spatial distribution of clast types throughout the deposit.

In thin section, some pumices contain small (<20 μm) microlites but the pumiceous achneliths are aphyric. EPMA glass analyses (see Appendix C.1) show that all juvenile clasts are peralkaline rhyolites (pantellerites) with a mean glass SiO_2 concentration of 73 wt %, a peralkalinity index (molar Na_2O + K_2O / Al_2O_3) of 1.6, $FeO_{(t)}$ of 5.4 wt %,

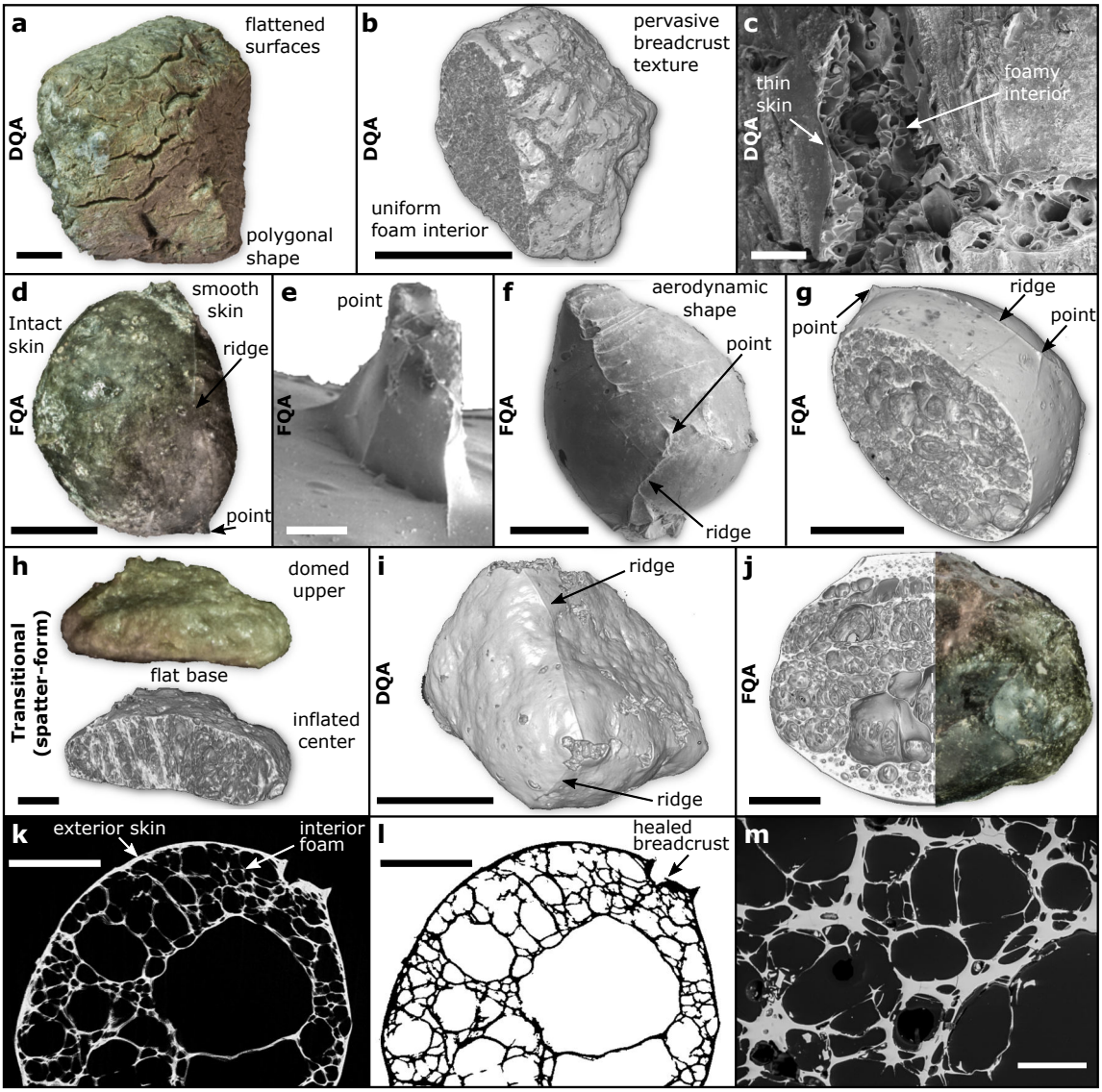

Figure 2.2: *Images displaying the primary features of pumiceous achneliths (**a**) Photograph of a deposit quenched achnelith (DQA); (**b**) Seconday electron scanning electron microscope (SE SEM) image of a DQA; (**c**) 3D rendering of an x-ray microtomographic (XCT) scan showing a DQA; (**d**) Photograph of a flight quenched achnelith (FQA), (**e**) SE SEM image of a point structure on an FQA; (**f**) SE SEM image of an FQA; (**g**) 3D rendering of XCT of an FQA; (**h**) Photograph and 3D rendering of spatter-form lapillus, displaying aspects of FQA and DQA origins (ie. deformed droplet); (**i**) 3D rendering of DQA showing remnant ridge structures identical to those seen on flight quenched achneliths; (**j**) Photograph and 3D rendering of a spherical FQA showing bands of variable vesicle size, shape and number density; (**k**) Reconstructed XCT slice showing a cross-section through an FQA, displaying the basic structure of internal foam with a thin exterior skin; (**l**) Binarized XCT slice (same as k) showing a healed breadcrust crack. This also exemplifies the data used for bulk clast volume calculation; (**m**) Electron backscatter image showing the glass foam network within a DQA. Larger vesicles have retracted internal bubble walls indicative of bubble coalescence.*

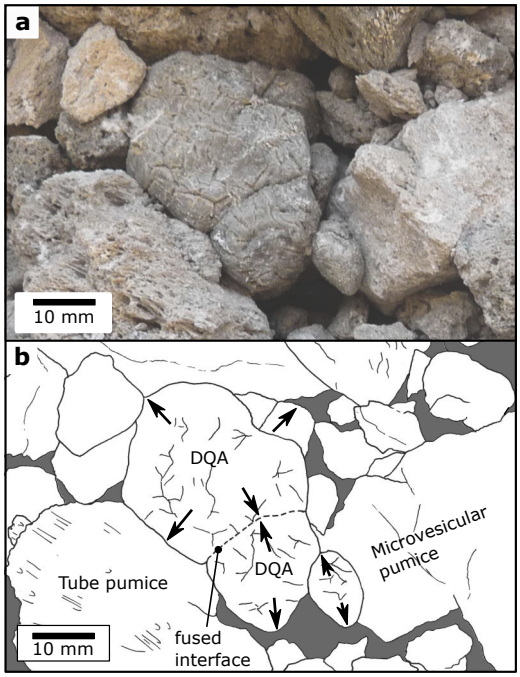

Figure 2.3: *Images showing the in-situ inflation of deposit quenched achneliths* ***(a)*** *Image of deposit quenched achneliths, showing evidence of in-situ inflation into void spaces between and against adjacent pumices. Note the polygonal form of the achneltih as a result of compression against adjacent clasts. (**b**) Annotated and line drawing of the same image. Arrows indicate the inflation of the DQAs. The central DQA is formed by the fusion of two adjacent DQAs, forming a single pyroclast.*

and average F and Cl concentrations of 3700 ppm and 1900 ppm respectively. Different clast types are indistinguishable based on their major element geochemistry and Cl concentrations. Fluorine provides some distinction between clast types, with tube pumice having the highest concentration, microvesicular pumice and dense obsidian bombs having the least, and deposit quenched achneliths with a concentration spanning much of the range of the other clast types (see Appendix C.1).

The pumiceous achneliths at Aluto comprise a glassy foam body surrounded by a thin (10 —100 μm) skin of smooth, black obsidian (Figure 2.2). In thin section, the glasses are isotropic with no apparent alteration, suggesting they are relatively fresh and similar to their original form. Their high vesicularity (67 to 93 vol %) imparts a low bulk density of 0.2-0.8 g cm^{-3}. Due to resolution constraints of the XCT scans, vesicle shape can only be described qualitatively, and varies from near spherical to highly tortuous within the same

clast. Many vesicles are coalesced.

The pumiceous achneliths can be subdivided into two morphologically distinct groups: flight-quenched achneliths (FQAs), distinguished because they possess aerodynamic, spherical to teardrop shapes (Figure 2.2 d, e, f, g, j) and deposit-quenched achneliths (DQAs), distinguished because of their highly irregular, polygonal shapes formed through in-situ inflation (Figure 2.2 a, b, i and Figure 2.3). In both groups, the delicate outer obsidian skin is still intact (Figure 2.2 d, f, g, i, k, l) and confirms clast roundness is not imparted by abrasion during transport. FQAs tend to be smaller than DQAs, and in these deposits have mean diameters (of their equivalent sphere) of 4 mm and 15.5 mm respectively (Figure 2.5). However, DQAs up to 30 cm in length have been found elsewhere at Aluto. There is no clear difference in vesicularity, nor vesicle shape between FQAs and DQAs. It is important to note that breadcrust textures are present in both FQAs and DQAs. However, DQAs display wider cracks, which are better connected, and are present more frequently than in FQAs. In some examples, breadcrust cracks have apparently healed; where ductile melt from the interior has reformed a skin in the place of the crack (Figure 2.2 k, l and Figure 2.4). FQAs often display a surficial point-and-ridge structure, with points in a roughly tetrahedral coordination around the teardrop-shaped to sub-spherical clast joined on the surface by small ridges (Figure 2.2 d, e, f ,g). A remnant version of this structure can often be seen on DQAs (Figure 2.2 i).

There are two end member textures of pumice in the deposits: tube pumice, with very high vesicle aspect ratios and microvesicular pumice, which has highly tortuous microvesicles that lack any preferred orientation and have a small aspect ratio. Pumice is sometimes heterogenous on a centimeter scale, containing zones of both pumice texture end members. Dense, angular obsidian bread crust bombs are also present. They possess macrovesicular cores and are significantly denser than both the pumiceous achneliths and the pumice. It is not clear whether these clasts are juvenile or accessory. Conduit-derived, accessory lithic components represent pre-Aluto as well as Aluto stratigraphy: with small (2.5 mm mean diameter), oxidised, angular fragments of siliciclastic sediments, and green welded ignimbrite (the ‘Qgei’ ignimbrite of Hutchison et al. (2016c)).

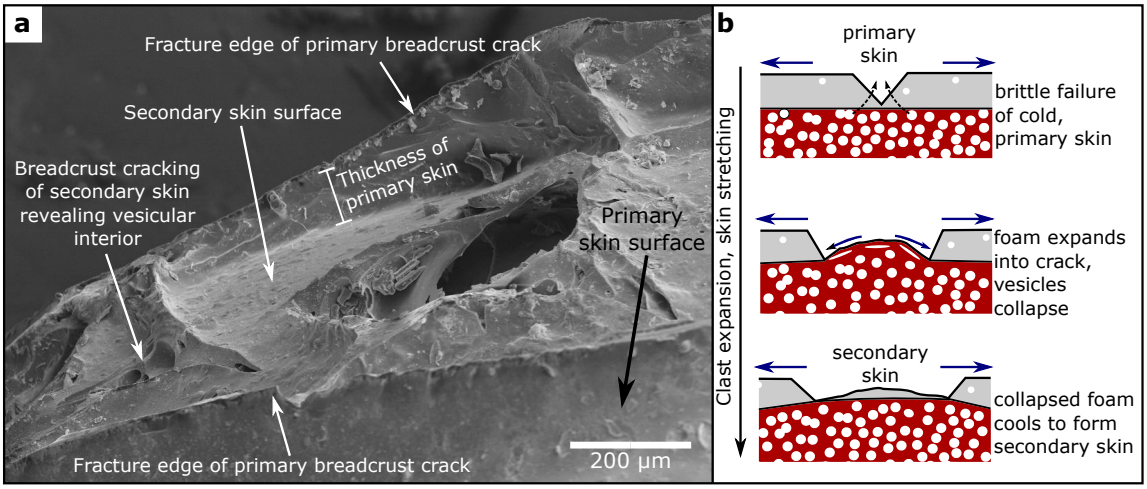

Figure 2.4: *The healing process of breadcrust textures in pumiceous achneltihs (**a**) Annotated oblique SEM image of a breadcrust scar on an FQA. (**b**) Conceptual model showing the formation of breadcrust scars, a feature developed during the transition between brittle and ductile skin regimes in the growth of pumiceous achneliths. This process enhances cooling of the internal foam, and keeps the surface temperature higher allowing extended ductile behaviour by advection.*

Thermal Modelling

The pumiceous achneliths, i.e. fluidal-shaped clasts, are unique because they represent ductile processes in a deposit of otherwise brittlely fragmented pyroclasts. To investigate whether peralkaline rhyolite magmas could remain ductile during flight, a numerical, forced-convection and conduction-based thermal model was developed (see Appendix D.2). The time taken for different sized pyroclasts to cool to the point where 10 % and 100 % of the pyroclast's radius was below the estimated glass transition temperature (T_g) was determined. It is important to note that here we define T_g to be the temperature at which the melt with 1 wt % H_2O reached 10^{12} Pa s: 400 °C according to the model of Di Genova et al. (2013). The results of the thermal model are presented in Figure 2.5. Taking the mean clast diameter for DQA clasts from the clast-size histogram we show that the whole clast (ie. 100 % diameter) will have cooled to below T_g after 15 to 50 seconds. In contrast, a FQA of mean diameter will have reached the same point by only 2 seconds. For comparison, cooling of the outermost 10 % (by diameter) is in the order of a few seconds for both clast types. We repeated the model runs using a range of possible T_gs, the results

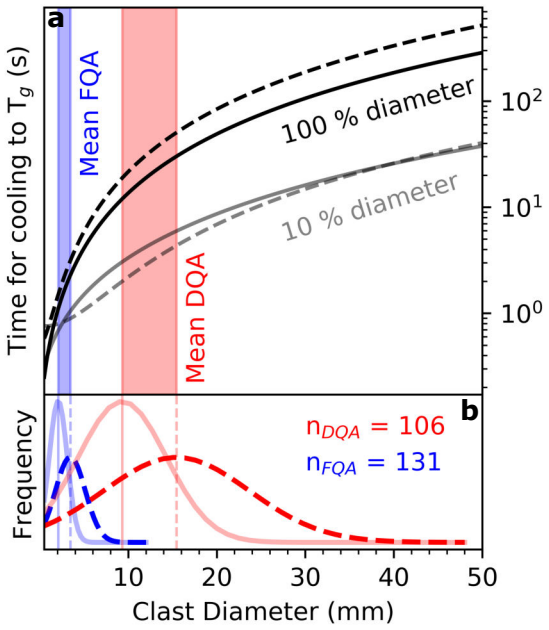

Figure 2.5: *The cooling rates of pumiceous achneliths during flight by clast diameter (**a**) The results of the thermal modelling with the black and grey lines representing the time taken for 100 % and 10 % of the diameters respectively to cool below T_g. The dashed lines show the results assuming a vesicularity of 0.9, whilst the solid lines represent a vesicularity of 0, thus bracketing the true vesicularity for any given pyroclast. (**b**) Best-fit gaussian size distributions of FQAs (blue) and DQAs (red). The dashed lines indicate the diameters of the achneliths as measured (ie. vesicular), and the solid lines indicate the recalculated diameters once the vesicularity (assumed to be 0.9) has been removed. In both panels, the mean diameters of the original FQAs and DQAs (ie. zero vesicularity) and the final inflated FQAs and DQAs (ie. porosity = 0.9) are shown by vertical lines and provide the range of diameters over which the mean FQA and DQA evolved from fragmentation to quenching.*

suggest that cooling times are relatively insensitive to this parameter within a realistic range of input values. For example, where $T_g = 520°C$, the point at which a peralkaline rhyolite with 0.1 wt % H_2O should have a viscosity of 10^{12} Pa s (Di Genova et al., 2013), the resulting difference in the cooling time for exteriors of the mean FQA and DQA are within model precision, and for the interior of the mean DQA (where the difference should be greatest) is of the order of 5 seconds.

2.2.3 Discussion

Although not common, clasts similar to our pumiceous achneliths, previously referred to as globules, have been observed within welded ignimbrites elsewhere. Globules have not been formally defined but are described as comprising either a foam or single central vesicle surrounded by a thin skin. These globules have been found within welded ignimbrites at Mt Suswa (Kenya) (Schmincke, 1972, 1975a), Pantelleria, and Gran Canaria (Sumner and Branney, 2002). In each of these cases, the ignimbrites are peralkaline trachyte in composition. The Monte Pilato pumice cone on Lipari contains some clasts that closely resemble DQAs, but are simply considered pumice by the authors (Fig. 5e in Davì et al. (2011)). Those clasts are found in unconsolidated fall and flow deposits and are high-K rhyolites. As seen at Aluto, and in all the above cases there is evidence for post-deposition expansion of the pyroclasts. There is currently no consensus on the origin of globules; some authors suggest they represent reheated, brittlely-fragmented shards reshaped during flight (Schmincke, 1975a), whilst others invoke ambiguous, non-brittle fragmentation in eruptions that are dynamically similar to basaltic fire fountaining, yet still produce pyroclastic density currents (Hay et al., 1979). A common feature of the globules described previously, and their proposed origins, is the shaping of the clasts by surface tension, defining them as achneliths; a form of pyroclast first described in basaltic systems(Walker and Croasdale, 1971). To form an achnelith, the structural relaxation timescale (τ) of the melt (ie. the time required for stress to be relaxed by ductile, structural reorganization of the melt) must be less than the timescale for cooling to the glass transition (t_{tg}) during flight. This (ie. $\tau < t_{tg}$) allows for ductile, surface tension driven deformation (Porritt et al., 2012).

The structural relaxation time of a given melt is a function of its viscosity and the bulk shear modulus ($\tau = \eta/G$) (Dingwell and Webb, 1989). The viscosity (η) of the melts that form pumiceous achneliths at Aluto has been estimated using the VFT equation (Giordano et al., 2008) with modified fit parameters for peralkaline rhyolites (Di Genova et al., 2013) (Figure 2.6). It should be noted that F has a network modifying influence on the viscosity of silicate melts (Dingwell et al., 1985) of the same magnitude as water on a wt % basis (Giordano et al., 2004), and the peralkaline rhyolite viscosity model (Di Genova et al.,

2013) does not explicitly take F into account in model coefficients. However, F concentrations in the samples used to calibrate the model (pumice from the same eruption: mean 3900 ppm F (Gioncada and Landi, 2010)) are very similar to those measured in glasses at Aluto (mean 3700 ppm F). The model is therefore considered to implicitly take the influence of F into account for the Aluto samples.

The aphyric nature of the pumiceous achneliths at Aluto precludes any standard geothermometry. Instead, we assume eruption temperatures around 750 °C, the storage temperature of other pantellerites from Aluto, based on the alkali-feldspar —melt geothermometer (Gleeson et al., 2017). At these temperatures, we estimate the viscosity of the melts when dry to be around $10^{7.7}$ Pa s. However, pantellerites typically contain between 2.5 and 5 wt % H_2O prior to eruptive degassing (Field et al., 2012; Neave et al., 2012), and at their eruption temperature have melt viscosities similar to a basalt (Di Genova et al., 2013; Giordano et al., 2008; Korotev, 1996) (Figure 2.6). The presence of just 1 wt % H_2O, for example, reduces the viscosity at 750 °C to just $10^{4.9}$ Pa s. At this viscosity, $\tau = 7.9 \times 10^{-6}$ s. Cooling times (t_{tg}) are significantly longer than this (0.7 to 50 seconds) for pumiceous achneliths (Figure 2.5), confirming $\tau < t_{tg}$, and that reshaping by surface tension is possible. The existence of achneliths in pyroclastic peralkaline rhyolite deposits therefore provides an important real-world validation of the inferred low viscosity and glass transition temperatures of these magmas previously determined experimentally (Di Genova et al., 2013; Dingwell et al., 1998; Hess et al., 1995).

The sequence of mechanisms by which pumiceous achneliths are formed can, to an extent, be deciphered from their texture and surface features. Typical spheroidal achneliths, such as those formed in Hawaiian fire-fountain eruptions (eg. Pele's tears) are thought to be produced during non-brittle fragmentation of a low viscosity basalt magma (Namiki and Manga, 2008; Porritt et al., 2012; Walker and Croasdale, 1971). However, we infer primary fragmentation for the pumiceous achneliths to have been brittle. This is evidenced by the point-and-ridge structures on the surface of many achneliths (both DQAs and FQAs) (Figure 2.2e, f, g, i) which we propose are retracted bubble walls between fragments of bubbly conduit magma (Figure 2.7). The smaller achneliths originate as cuspate shards whilst

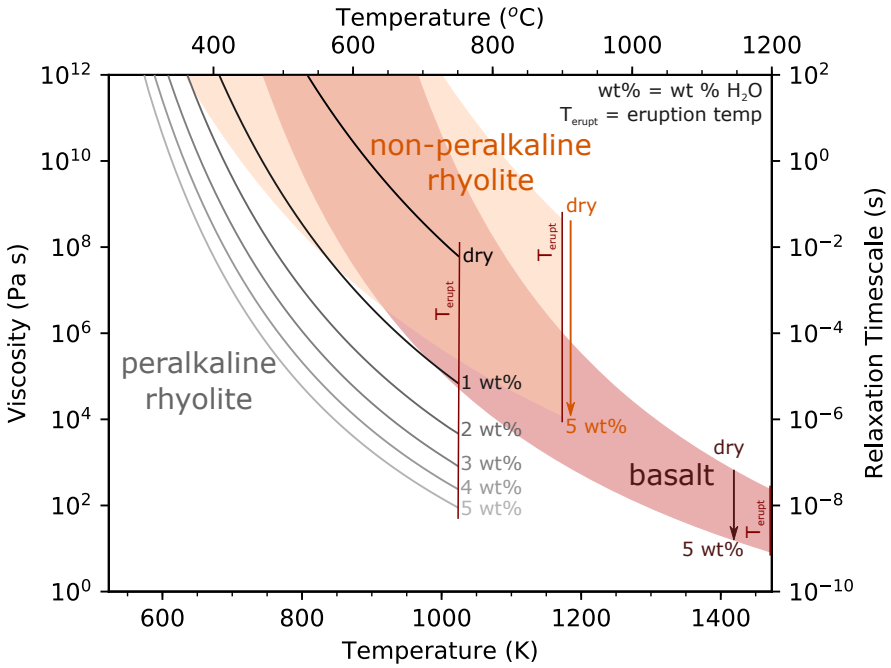

Figure 2.6: *Viscosity-temperature relationship for peralkaline rhyolite melt with varying water concentration based on the model of Di Genova et al. (2013). Pantellerites typically contain between 2.5 and 5 wt % H_2O prior to eruptive degassing (Field et al., 2012; Neave et al., 2012). For comparison, the viscosity-temperature relationship calculated by the VFT equation (Giordano et al., 2008) is shown for a typical, non-peralkaline (in this case peraluminous), rhyolitic melt (Rhyolite Glass Mountain - 1 standard) and basaltic melt (Basalt Hawaii Volcanic Observatory - 1 standard). Note that at eruption temperature, hydrous Aluto peralkaline rhyolites have a similar viscosity to basalts, and possess exceptionally low glass transition temperatures (temperature at which viscosity = 10^{12} Pa s).*

the larger achneliths may originate as clots of bubbly magma. Post-fragmentation cooling and degassing at the clast surface develops a coherent skin of higher viscosity melt, and the associated reduction in volatile diffusion rates prevents significant gas flux from the fragments. The fragments thus form partially closed systems and inflate during progressive degassing and flight. It is possible that basaltic achneliths form in a similar manner, only their prolonged fluidal behaviour and lower viscosities mean that such surface features might have been lost.

The aerodynamic morphologies of the pumiceous achneliths at Aluto show that they were still capable of ductile deformation after apparently brittle fragmentation. For such low viscosity melts to fragment requires rapid decompressive stresses, such that strain cannot be structurally relaxed. Hughes et al. (2017) investigated the fragmentation styles of pantelleritic pumices from the Cuddia di Mida pumice cone eruption, and found that the required conduit-averaged decompressive strain rates implied unrealistically high mass fluxes ($>10^8$ kg.s^{-1}). A potential solution is to invoke strain localisation, where spatial variability in water content, microlite content, bubble number density and size can generate high-strain-rate shear zones, where the strain rate is sufficiently magnified to elicit brittle fragmentation (Wright and Weinberg, 2009). At Aluto, there is clear cross-conduit variability in the rheological behaviour of magma; where some fragments produce aphyric fluidal achneliths, while the remainder form microlite-bearing brittlely fragmented, angular pumice. The pumices also display variability in bubble elongation and bubble number density (coevally-produced tube pumice and microvesicular pumice), which shows that strain conditions vary across the conduit (Polacci, 2005), and further supports the notion that strain localisation might have played a role in the brittle fragmentation of low viscosity magma at Aluto (Wright and Weinberg, 2009; Dingwell et al., 2016).

The process of inflation is elucidated by textural variations and the presence of both breadcrusted and non-breadcrusted pumiceous achneliths (Figure 2.2). This shows that inflation occurs in two end-member regimes: This first being ductile skin behaviour, where the rate of strain experienced by the skin due to wholesale clast expansion (aka. rate of skin stretching) does not exceed the rate at which it can be structurally relaxed ($\frac{1}{\tau}$) and so

expansion is accommodated ductilely. The second regime results in brittle skin behaviour, where strain accumulates at a rate greater than it can be structurally relaxed, resulting in brittle cracking (bread-crusting). The transition from the ductile to brittle skin regime occurs where the strain rate exceeds the structural relaxation rate of the outer portion of the pyroclast. The rate of stretching of the outer portion of the pyroclast is a function of the internal bubble growth rate. The rate of internal bubble growth is liable to be greater at lower viscosities (Sparks, 1978), and so reduces with continued degassing and cooling. When in the brittle skin regime, the interior must be sufficiently low viscosity to allow bubble growth to induce strain in the outer portions of the pyroclast, but the outer portion of the clast must be sufficiently viscous for the strain rate to induce a brittle response. There is a delicate balance between cooling, degassing and bubble growth rates, but the balance is tipped towards brittle skin behaviour in larger pyroclasts, where the interior remains thermally insulated and low viscosity, whilst the outer is cold and brittle. In smaller pyroclasts, the interior is less insulated, and so cools at a similar rate to the skin; undergoing wholesale quenching before entering the brittle skin regime. This explains why larger bread crust textures develop more often in the larger DQAs than in the smaller FQAs. This also suggests that for small FQAs, expansion must occur rapidly and early-on in the ductile skin regime, before the skin has quenched (in under 2 seconds (FQA curves in Figure 2.5)).

The skin of the pumiceous achneliths is particularly thin (10-100 μm) compared to typical millimeter scale of breadcrust bomb rinds (Benage et al., 2014; Wright et al., 2007). This likely results from expansion during regime 1, where the ductile skin is stretched to cover the larger surface area and is necessarily thinned. In some breadcrusted FQAs there is evidence of transitional behaviour between the end-member ductile and brittle skin regimes: where breadcrust cracks have healed (Figure 2.2k, l, 2.4). Here we propose that the skin has become sufficiently viscous to crack brittlely, exposing the bubble rich interior through continued expansion. The hotter interior behaves in a ductile fashion, so vesicles collapse by diffusive degassing, bubble burst, and stretching. This process forms a new coherent skin, regenerating the surface, and replacing the crack with a scar (Figure 2.4). This translation of hot material under the skin to the surface advects heat, acting both

to maintain ductility at the surface of the clast, allowing reshaping, while also cooling the interior. During the ductile skin regime, surface tension and drag reshapes the clasts to attain their spherical to droplet shape. As the free surface energy is directly proportional to the surface area, and the surface area is proportionally smaller at larger volumes, shaping by surface tension is liable to be more pronounced in smaller clast diameters, which is shown by the relative shapes of DQAs and FQAs, and also recognized in basaltic achneliths (Porritt et al., 2012). Though surface tension should act to remove irregularities such as the surficial point-and-ridge structures, the high surface area of the points and ridges will promote rapid cooling, increasing their viscosity and preserving their shape whilst the main body of the clast continues to inflate and reshape.

The existence of FQAs and DQAs indicates there is significant variability in the rheology of different pumiceous achneliths throughout deposition. The aerodynamic shapes and relative paucity of bread crust textures in FQAs (Figure 2.2) implies that they cooled below their glass transition temperature in-flight, quenched before entering the brittle skin regime, and were not deformable upon impact. The DQAs however, remain above, or exceed their glass transition temperature until after deposition to allow for inflation and plastic deformation against adjacent clasts in the deposit (Figure 2.7). We propose that although these clasts represent the same eruptive material, their respective sizes result in distinct temperature-time paths after fragmentation. The small size and higher surface area to volume ratio of FQAs resulted in a faster cooling rate, allowing them to embrittle before impact. The larger DQAs retained heat longer, remaining plastic post-deposition, allowing vesiculation and expansion to continue. This is confirmed by the results of the thermal model, that demonstrate in most cases, the disparity of behaviour between FQAs and DQAs can be explained by their relative sizes: the mean FQA has completely cooled by around 3 seconds, whereas this takes between 15 and 50 seconds for the mean DQA (Figure 2.5). FQAs are therefore frozen during transit before deposition, whereas the interior of the DQAs remain above T_g and continue to degas and expand after emplacement. However in reality there is some overlap in the diameters of FQAs and DQAs (Figure 2.5), as well as transitional spatter-form clasts (Figure 2.2h) which were clearly small and droplet shaped during flight but deformed on impact. This can be explained by natural

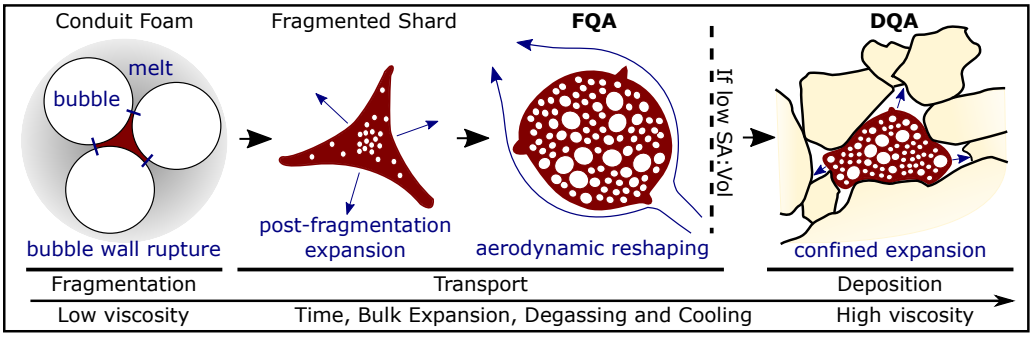

Figure 2.7: *Conceptual model showing the generation of flight quenched achneliths (FQAs) and deposit quenched achneliths (DQAs). A foam is first fragmented generating shards, due to their low viscosity, they continue to degas. As the skin forms through cooling, they become a closed system and inflate. Inflation continues through transport and the clasts are shaped aerodynamically and to minimise free surface energy. If the surface area to volume ratio (SA:Vol) is high, they harden before impact forming FQAs. If the SA:Vol is low, they remain plastic post-deposition and expand into place forming DQAs.*

variability in parameters such as initial temperature, volatile content, flight path, and the thermal influence of surrounding pyroclasts during transport. Further, the surface temperature of pyroclasts may increase after deposition; the reduced surface heat flux due to the absence of forced convection, and the persistence of conductive heat flux from the centre can allow the surface temperature to rise (Capaccioni and Cuccoli, 2005). It may be the case therefore, that the outer portions of some pumiceous achneliths cool through their glass transition before impact but rise above it again after deposition, allowing for prolonged plastic behaviour. The post-deposition inflation of pumiceous achneliths, and partial fusion with adjacent clasts provides a degree of cohesion to these deposits to the extent where they can be considered incipiently welded. Had the deposits contained a greater proportion of pumiceous achneliths or had inflation progressed further, it is feasible that the deposit would have welded. We also note that most globules that have been found elsewhere occur within welded deposits. We therefore propose that inflation of these pyroclasts after deposition may be a significant factor contributing to the very commonly welded nature of peralkaline rhyolite pyroclastic deposits.

The time-scale of the formation of these achneliths provides important constraints on the eruption styles that generate pumice cones. Significantly, the output of the thermal model provides an estimate for the time interval between fragmentation and deposition

for DQAs. As we have established, DQAs must at least in part exceed their glass transition temperature after deposition in order to deform plastically, whilst the presence of a bread-crusted skin shows that at least the outer-most portion of the DQA cooled below T_g. For a DQA of any given size therefore, the time-of-flight should be somewhere between the 10 % (cooled crust) and 100 % (cooled interior) curves presented in Figure 2.5. Here we see that for a mean DQA from Aluto, the time between ejection from the vent and deposition was between 4 and 15 to 50 seconds. This provides an important insight on the depositional mechanism of pumice cone deposits. The cooling rates of DQAs show either that deposition occurred over a short time scale (between 4 and 50 seconds), or that clasts were entrained in a hot fluid prior to deposition thus minimizing the cooling rate. Three reasonable scenarios that satisfy these conditions are deposition from ballistic trajectories, deposition from the turbulent edge of the lower portions of an ascending column, or entrainment in, and deposition from, a hot pyroclastic density current. For these deposits, considering the high angularity of pumice clasts, and the lack of matrix, ballistic or column-edge deposition are considered most likely. In the case of the north and south deposits, DQAs have been found at distances of 300 and 600 m from their source vents. Taking the average DQA at 15.4 mm with a density of 600 kg m^{-3}, and even assuming extreme conditions of ballistic transport (ejection velocity 300 m/s, 45 ° ejection angle and a tailwind of 20 m/s), the maximum distance such a pyroclast should reach is 185 m (Mastin, 2001). In addition, DQAs at Aluto are typically smaller than 10 cm in diameter, considered to be the lower limit for pyroclasts to follow ballistic trajectories (Sparks, 1997). For these reasons, the DQAs at Aluto are thought to be sourced from the edge of an ascending column, the flaring or inclination of which allows for the deposition of particles beyond their ballistic limit (Riedel et al., 2003), whilst minimising the duration between primary fragmentation and deposition. It should be noted however, that scenarios 1, 2 and 3 are all plausible mechanisms for the production of DQAs elsewhere.

We conclude that these unusual pyroclasts - pumiceous achneliths - found in pumice cone deposits (potentially globally) provide important insights on the nature of these hitherto enigmatic eruptions: Despite their fluidal appearance and apparent low viscosity, pumiceous achneliths are initially fragmented brittlely alongside more typical pumice.

Their prolonged relaxation times and degassing allow them to form their final, conspicuous morphology. We also find pumiceous achneliths are in this case not ballistically emplaced, but fall from the edge of ascending eruption columns. There is also significant conduit-wide variation in strain-rate and magma rheology to explain the presence of pumice and pumiceous achneliths within the same deposit and the brittle fragmentation of low viscosity melts. Taken together, these conclusions show that pumice cones can generate intense eruption columns. This is in contrast with prior strombolian interpretations of pumice cone eruptions, established in response to the resemblance of pumice cone structures to basaltic scoria cones (Orsi et al., 1989; Houghton et al., 1985). This has important implications for the hazards posed by such eruptions: in particular, in formulating more accurate conceptual models for the associated activity. It is now clear that pumice cone eruptions may be associated with wide-spread tephra fallout, column-collapse-type pyroclastic density currents, occasional cone-avalanches, and in later eruption stages, the emplacement of obsidian lava flows. The evidence for cross-conduit variations in viscosity and strain-rate during the explosive phase of these eruptions suggests a highly unsteady and non-uniform setting. This implies that the eruptions themselves may be complex, with the potential for multiple stages of eruption column generation and collapse. Notable and somewhat similar eruptions have occurred at Chaitén (2008) (Alfano et al., 2011) and Cordón Caulle (2011) (Castro et al., 2013); both rhyolitic with tephra fallout, pyroclastic density currents and obsidian flows, but where pumice cones themselves haven't been well documented. This provides a clear rationale for considering small to moderate pyroclastic density currents as potential proximal to medial hazards around the edifices, and that moderate tephra-fall hazards (equivalent to eruptions of VEI 3 to 4) should be considered. In summary, pumice cone eruptions remain little studied, but are liable to be associated with more hazardous eruptions than previously assumed.

2.2.4 Methods

Bulk Deposit Analysis

The samples were collected during a 2-week trip to Aluto volcano, Ethiopia. The two deposits under investigation (north site and south site) were logged, photographed and a bulk sample, free of surface wash, was collected at each. Bulk samples were dried at 100 °C for at least 24 hours, and sieved by hand into 1 ϕ size fractions and weighed. Each sieved fraction, depending on the number of clasts present, was then representatively split for manual analysis of the components. The results of the granulometry can be found in Appendix C.2 under sample numbers MER62-16 (north site) and MER65-23 (south site).

Deposit Componentry

Clasts within each sub-sample were then assigned to 1 of 6 component types, using a binocular microscope where necessary: tube pumice, microvesicular pumice, flight-quenched achneliths (FQA), deposit-quenched achneliths (DQA), dense obsidian or lithic. These classes were then weighed and the number of clasts in each category counted. All 189 FQAs and DQAs were individually measured on three axes using a digital caliper to a precision of $\pm$ 0.02 mm. As $>$ 95 % of clasts were equant according to the Zingg classification (Zingg, 1935), the mean of the three axial measurements was considered the diameter of the pyroclast.

Geochemistry

The glass composition of a sub-sample of tube pumice, microvesicular pumice, DQAs and dense obsidian was analysed using the Cameca SX100 Electron Microprobe at the University of Edinburgh School of Geosciences. DQAs were found to be entirely crystal free, but care was taken to avoid any crystal present in the other pyroclasts. Major elements plus Chlorine and Fluorine were measured against a Lipari obsidian secondary standard. Accelerating voltages and beam sizes were set at 15 KeV and 14 μm respectively, and the beam current was tailored on a per-element basis to minimise diffusive loss (1 nA: Na, Mg,

Al, K, Ca and Si; 80 nA: F, Cl, P, S, Ti, Fe and Mn). Analyses with totals < 96 wt % were discarded leaving 79 sets of analyses from the range of pyroclasts analysed. The remaining values were normalized to 100 % to account for variable secondary hydration. The glass compositions were then compared and the glass densities calculated using the partial densities method (Bottinga and Weill, 1970).

X-ray microtomography

A sub-sample of each component class in addition to 3 grades of bulk fine ash was taken and prepared for secondary electron backscatter analysis using the Carl Zeiss SIGMA HD VP Field Emission SEM at the University of Edinburgh School of Geosciences. This provided images for qualitative descriptions of smaller clasts and micron scale surface features. An additional subsample of 4 FQAs and 3 DQAs was selected for x-ray microtomography (XCT) using the in-house constructed XCT scanner at the University of Edinburgh School of Geosciences. Clasts were measured and the x-ray source-sample distance was adapted for each clast to ensure a whole-clast analysis whilst attaining an optimum resolution. Each sample was rotated around 180° and a series of exposures taken. These images were reconstructed and corrected for beam hardening using Octopus v8.7 ready for analysis.

For quantitative analysis, the image set for each pyroclast was segmented and binarized using the computer-learning based 'Trainable WEKA Segmentation' plugin in ImageJ (FIJI) (Arganda-Carreras et al., 2017) whereby the user manually trains a classifier to recognise the different phases present (glass vs. vesicle), the classifier then automatically places each pixel into the defined classes. Due to resolution constraints, vesicularities were not directly calculated from the results of the segmentation, instead bulk volumetric measurements of each pyroclast were extracted from the segmented images using the particle analysis function in ImageJ. As these clasts are simple two-phase systems (glass and void space), the bulk density and vesicularity could then be calculated using a mass balance approach by measuring the mass of each clast, and assuming a glass density of 2.47 g cm^{-3} (calculated from the EPMA glass composition data).

Thermal Model

The thermal evolution of FQAs and DQAs during flight through the air was modelled assuming spherically symmetric projectiles with radiative and convective cooling at their outer boundary. For simplicity, and in order to present a maximum cooling rate, conditions were modelled to simulate a ballistic flight path, rather than entrainment in a hot plume or pyroclastic density current. This provides a temperature profile through the clasts as a function of time. The diffusion of heat through pyroclasts is a function of the thermal conductivity, temperature gradient and the length of the diffusion path. The vesicularity and diameter of these achneliths are coupled and increase through time, thereby reducing thermal conductivity and increasing the length of the diffusion path. However, as we have no independent constraints on the vesiculation and expansion rate, capturing this is beyond the model. Maximum and minimum cooling rate scenarios were modelled instead with a constant diameter and vesicularity throughout flight, thus bracketing the true temperature-time path. A series of pyroclast diameters were modelled with a minimum (not inflated $\phi = 0$) and maximum (greatest observed inflation $\phi = 0.9$) vesicularity and the time taken for 10 % and 100 % of the diameter of each sized pyroclast to cool below T_g was recorded. As the temporal resolution of the model is a 1 second time-step producing a somewhat stepped relationship, the curves presented in Figure 2.5 are best-fit 2nd order polynomials to the model results.

For simplicity, the vesicular achneliths were modelled as an isotropic foam without a skin, and without advective heat loss through gas escape or melt migration to the surface. The thermal properties of this foam were calculated as follows. The thermal conductivity appropriate for this particular peralkaline rhyolite melt (K_{melt}) was calculated by the method of Geotti-Bianchini and Loherngel (1993) and the thermal conductivity of the gas inside vesicles was neglected allowing the bulk thermal conductivity of the foam (K_{foam}) to be calculated by the Rayleigh-Maxwell equation:

$$K_{foam} = \frac{K_{melt}\ (1 - \phi)}{(1 + \phi)} \tag{2.1}$$

The heat capacity of the achneliths (Cp_{foam}) was then calculated as the weighted sum

of the heat capacity of pantellerite (Cp_{melt}) from Di Genova et al. (2014), and the heat capacity of the vesicle gas (Cp_{gas}) (taken as that of steam at 950 K (Wagner and Pruss, 2002)):

$$Cp_{foam} = \frac{\phi\ Cp_{gas}\ \rho_{gas} + (1-\phi)\ Cp_{melt}\ \rho_{melt}}{\rho_{foam}} \tag{2.2}$$

where the melt density (ρ_{melt}) is calculated by the partial densities method of Bottinga and Weill (1970). The foam density (ρ_{foam}) is calculated by mass balance considering ρ_{melt}, the porosity (ϕ), and assuming the pores (vesicles) are filled with H_2O behaving as an ideal gas. The thermal diffusivity of the achnelith (k_{foam}) can then be calculated as (Bagdassarov and Dingwell, 1994):

$$k_{foam} = \frac{K_{foam}}{\rho_{foam}\ Cp_{foam}} \tag{2.3}$$

Radiative (F_r) and convective (F_c) surface heat flux at the clast surface is calculated as a function of the heat transfer coefficient (h_c), black body emissivity (γ) and the temperature at the clast surface (T_s) and the temperature of the surrounding fluid (T_∞) by the following equations:

$$F_c = h_c\ (T_s - T_\infty) \tag{2.4}$$

$$F_r = \gamma\ (T_s^4 - T_\infty^4) \tag{2.5}$$

The initial T_s is 750 °C, the pre-eruptive temperature calculated for peralkaline rhyolites at Aluto using the alkali-feldspar - melt geothermometer (Gleeson et al., 2017). The temperature of the surrounding fluid is 25 °C: standard conditions and a realistic for air temperature at this altitude in Ethiopia. The heat transfer coefficient is a function of the Reynolds (Re) and Nusselt (Nu) numbers:

$$Re = \frac{(u\ d\ \rho_{air})}{\mu_{air}} \tag{2.6}$$

$$\frac{h_c\ d}{K_{air}} = Nu = 2 + \sqrt{0.25 + 3 \times 10^{-4} Re^{1.6}} \tag{2.7}$$

where u is the average velocity of the achnelith during cooling, d is the diameter of the achnelith, μ_{air} is the air viscosity and K_{air} is the thermal conductivity of air from Thomas and Sparks (1992). The 'Eject!' model of Mastin (2001) was used to calculate u, assuming spherical particles with the average diameters and density of pumiceous achneliths, exit velocities of 100 m s^{-1} (realistic for ballistic ejection (Riedel et al., 2003)) and with no zone of reduced drag around the vent.

In the thermal model, the time dependent heat flow equation was discretised as a matrix in spherical coordinates following Buttsworth (1997) and the temporal component was solved using the method of lines (Schiesser, 1991). Table 2.1 shows input parameters used for the thermal model.

Parameter	**Value**	**Unit**	**Ref**
Altitude	1790	m.a.s.l	-
Density (melt)	2.47	g cm^{-3}	1
Average velocity	30	m s^{-1}	2
Ambient temperature	298.15	K	-
Initial temperature (melt)	1022.15	K	3
Density (air)	1.027	kg m^{-3}	4
Viscosity (air)	1.851 $\times 10^{-5}$	Pa s	4
Thermal conductivity (melt)	1.224	W m^{-1} K^{-1}	5
Heat capacity (melt)	1.42	J K^{-1} g^{-1}	6
Density (vesicle gas)	205	g m^{-3}	7
Heat capacity (vesicle gas)	2.343	J K^{-1} g^{-1}	8
Black body emissivity	5.669 $\times 10^{-8}$	W m^{-2} K^{-4}	9
Glass transition temperature	673.15	K	10

Table 2.1: *Table showing the input parameters for the thermal model and their sources. 1: (Bottinga and Weill, 1970), 2: (Mastin, 2001), 3: (Gleeson et al., 2017), 4: (International Civil Aviation Organization and Langley Aeronautical Laboratory, 1955), 5: (Geotti-Bianchini and Loherngel, 1993), 6: (Di Genova et al., 2014), 7: (Schaschke, 2014), 8: (Wagner and Pruss, 2002), 9: (Thomas and Sparks, 1992), 10: (Di Genova et al., 2013).*

2.3 Post-Script

We show in this paper that pumice cones (at least at Aluto) aren't simply built through the accumulation of ballistic material as is often invoked for basaltic scoria cones, but

instead, most-probably accumulate through the ultra-proximal column-edge deposition of pyroclastic material. The fact that such eruptions generate columns shows that they are capable of widely dispersing tephra, and may produce pyroclastic density currents through column collapse. This has important implications for the hazards associated with future eruptions not only at Aluto, but volcanoes elsewhere that produce pumice cones. However, the paper indicates that there is much yet to learn about these eruptions. Important question surround the broad context of these eruptions, and more detailed insights into eruption styles and processes that may lead to hazardous phenomena. Such questions include:

- Is there a typical eruption sequence for pumice cone-forming eruptions?
- What sort of magnitude and intensity are these eruptions?
- Given that they produce eruption columns, do they generate PDCs, and if so, how mobile are they?

To answer these questions, detailed and extensive field investigations are required, which are the subject of the following chapter. Ultimately this broad understanding of eruption processes at Aluto will inform a final PDC hazard analysis of Aluto in chapter 4.

Chapter 3

Post-Caldera Eruptions at Aluto Volcano

What has been will be again,
what has been done will be done again

Ecclesiastes 1:9 (NIV)

3.1 Introduction

Since Aluto's one or two caldera forming eruptions between 300 and 320 Ka (Hutchison et al., 2016c), eruptive activity has been widely distributed around the edifice in the form of spatially distinct eruptions. Though relatively low volume in comparison to the caldera forming phase at Aluto, these eruptions have been numerous and have cumulatively built much of the irregularly shaped edifice we see today. From the DEM, one can identify a multitude of craters, most of which are associated with pumice cones, and from many of which emanate silicic lava flows. These craters (82 visible at the surface), are geographically distinct but are spatially clustered, with the greatest number densities around the caldera ring fault (itself part inferred from the location of the craters) and along cross cutting regional Wonji faults (Hutchison et al., 2015). More vents exist on the southern prominence than the north, which combined with the greater volume and height of the southern prominence suggests that this region of the volcano has erupted a greater proportion of magma in Aluto's post-caldera history than any other. These eruptions have been the subject of relatively little study, but are thought to be the source of many of the Holocene tephras in the lake cores of nearby lakes Lanagno and Abijata (McNamara et al.,

2018). These tephras indicate post-caldera eruptions in the Holocene have taken place in a series of eruption pulses at 3, 6.5 and 11 Ka, at a time averaged return period of around 250 years (McNamara et al., 2018). However, medial to distal lake tephras present a biased record, as small eruptions produce tephra that may not reach medial to distal lakes, or reach lakes in such small volumes that their deposits are quickly reworked, or eroded and lost (Lowe, 2011). This would imply that in reality, return periods may be shorter than this, and that we may have no or little record of smaller eruptions. Very little is understood about the nature of these eruptions, but McNamara et al. (2018) tentatively suggest they may range in magnitude and style from vulcanian to sub-plinian, based on comparisons with distance-thickness relationships from better constrained eruptions elsewhere. Fontijn et al. (2018) provide a similar estimate and suggest these eruptions are highly unsteady in nature. Though this corroborates the findings in the previous chapter (Clarke et al., 2019), much of this work is based on only a few distal tephras, and is contrary to studies of pumice cone forming eruptions on Pantelleria (Orsi et al., 1989) and Mayor Island (Houghton et al., 1985). Many questions remain which require detailed field studies from proximal to distal locales around these post-caldera pumice cone forming eruptions. Questions such as:

- Are pumice cone forming eruptions similar in style and magnitude?
- What are typical pumice cone forming eruption scenarios?
- Do pumice cone forming eruptions produce eruption column? How tall are they? Are they steady or unsteady?
- If eruption columns are produced, do they collapse to generate pyroclastic density currents?
- What volcanic hazards should be of concern during a future pumice cone forming eruption in the Main Ethiopian Rift?
- How do the proximal and distal deposits of pumice cone forming eruptions relate to one-another?
- What insights can we glean from deposits at Aluto to inform quantitative, probabilistic PDC hazard assessments

In order to answer some of these questions, the following chapter presents and discusses the results of two targeted field campaigns investigating the proximal deposits of around 9 pumice cone forming eruptions around Aluto caldera, as well as medial deposits associated with an unknown number of pumice cone eruptions on the southern flank.

3.2 Methods

3.2.1 Fieldwork in the Main Ethiopian Rift

Fieldwork in the Main Ethiopian Rift was divided into two main field seasons. One for 3 weeks in November 2015, and a second for 1 month from November 2017. Unfortunately, political tensions in Ethiopia eventually lead to the instigation of a state of emergency in 2016, which means I spent less time in the field than originally intended. However, sufficient field work was conducted to develop an understanding of the nature of pumice cone forming eruptions at Aluto capable of informing a hazard assessment. These field expeditions focused on two volcanoes, Aluto and Corbetti, with minor additional excursions to investigate Bora-Bericha volcano and Butajira volcanic field. For Aluto, key sites were selected to investigate ignimbrites and pumice cones, using the maps, digital elevation model (DEM) and advice of William Hutchison. The sites were selected to ensure coverage of Aluto geology at a range of altitudes, to include pumice cones with a range of morphologies, to find the most complete exposure and to cover multiple flanks of the volcano (Figure 3.1). With around 95 localities at Aluto, the sites are all grouped thematically and by region, and are described, interpreted and discussed in the following sections: *Aluto's southern flank*, *Aluto's NW sector*, *Aluto's northern flank*, and *Aluto's central region*. A final discussion based upon the findings in each of these regions is presented at the end of the chapter. Due to constraints on time, accessibility and exposure, Aluto's western and eastern flanks were not investigated. Preliminary work from Corbetti is presented in Appendix A.

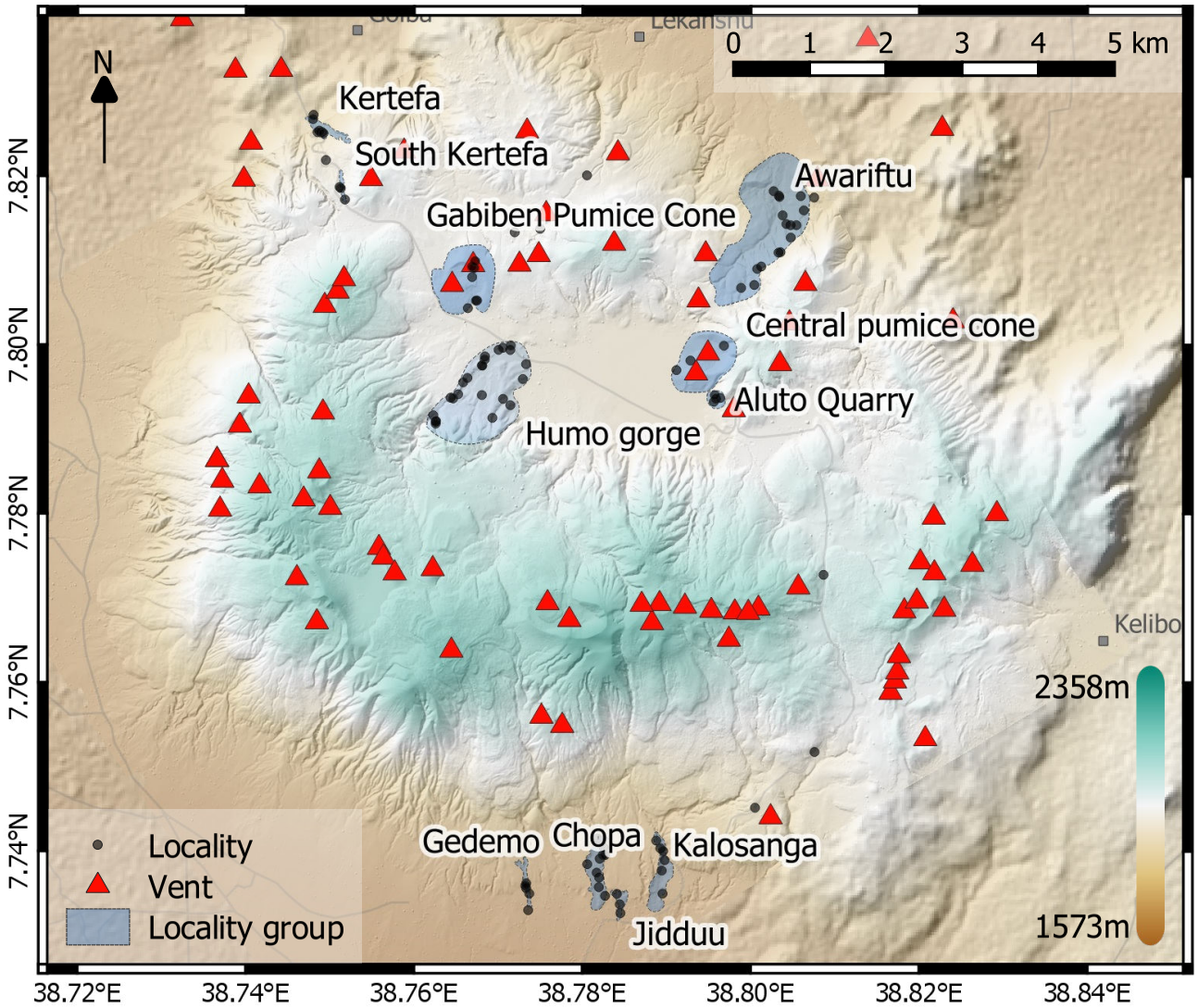

Figure 3.1: *Map showing the 95 localities investigated around Aluto volcano, the sub-regions to which they belong and the location of volcanic vents at Aluto. DEM from Hutchison et al. (2014).*

3.2.2 Stratigraphic framework and definitions

The Main Ethiopian Rift presents a number of challenges in developing a robust stratigraphic framework. Firstly, due to a persistently arid climate, there is very little charcoal for dating Holocene volcanic activity using ^{14}C (Fontijn et al., 2018). There has been some success in generating a dated volcanic record from lake tephra sections in the MER (McNamara et al., 2018), and from Ar-Ar dating of occasional crystal-bearing pumices and lavas (Hutchison et al., 2016b). However, geochemical correlation of distinct eruptions, particularly from the same volcanic centre, is challenging, as the geochemistry of the pantellerite glasses from different eruptions is remarkably homogeneous and often impossible to distinguish (McNamara et al., 2018; Fontijn et al., 2018). In addition to this, the medial tephra record (which links the proximal on-edifice deposits and the distal lake tephras) is largely reworked and removed as a result of a very mobile lake shore line over the course of the Holocene (Benvenuti et al., 2002a). This means that many of the on-edifice Holocene deposits (on which this work focuses) are stratigraphically isolated, largely un-tied to the lake tephra record, and with local dated marker horizons few and far between. Broadly speaking, all of the eruption units encountered in the following chapter post-date the latest caldera collapse at 306 ± 12 Ka (Hutchison et al., 2016c). The oldest post-caldera date is from an obsidian lava flow which emanates from the most prominent vent on the southern caldera rim. This flow is Ar-Ar dated at 61 ± 8 Ka (Hutchison et al., 2016b), but rests on top of a thick pile of older deposits that also post-date caldera collapse. The lava flow also has a relatively fresh-looking topographic surface compared to many other obsidian lavas at Aluto. The youngest date is sourced from a rare piece of charcoal underneath 'pumiceous pyroclastic deposits' near the eastern caldera rim, dated at 0.4 ± 0.05 Ka (Hutchison et al., 2016b). There are no known historical records of eruptions from Aluto, and there have been no eruptions within living memory. It can be said, therefore, that the deposits encountered in this chapter are all sourced from eruptions between around 306 Ka and the last few hundred years. Where more precise age constraints for particular deposits or sequences are available, they are provided.

Previous work has suggested a hiatus in eruptions between caldera collapse and post-

caldera volcanic activity (Hutchison et al., 2016b,c). However, this is based on the gap between the caldera collapse date, and the oldest post-caldera date (61 ± 8 Ka). Considering there is extensive post-caldera primary volcanic stratigraphy between this dated lava and the caldera ignimbrites (detailed in the 'Humo Gorge' section of this chapter), the existence or magnitude of this hiatus is not clear, and more dated material is required to verify the claim.

Attempts have also been made to correlate events across Aluto's edifice: the 'Qup' fall deposit for example, is an eruption unit originally identified by Hutchison et al. (2016c). Originally, Qup was thought to be laterally extensive across the whole edifice; forming a useful marker horizon to develop a broader stratigraphic framework (Hutchison et al., 2016c). However, the Qup deposit was later found to be the product of multiple distinct eruptions (Fontijn et al., 2018). Instead, the 'true' Qup fall deposit (defined in Fontijn et al. (2018)), seen high in the stratigraphy in the NW of the edifice, has been dated to around 7.3 Ka (McNamara et al., 2018), and is thought to be sourced from a pumice cone eruption somewhere in the NW of the edifice. Previously, distinct obsidian lava flows have been correlated and grouped into 'Qpo' (oldest) and 'Qpoy' (youngest) (Hutchison et al., 2016c) (see Figure 1.4). Though these may indeed represent relatively older and younger flows, correlations based on these groupings are misleading, as they are in reality sourced from distinct eruptions, potentially quite separated in time. As I shall present in this chapter, the history of post-caldera volcanism at Aluto is one of a multitude of eruption centres, the deposits of which often have a limited dispersal and may or may not overlap. If or where they do overlap, Aluto pumice cone deposits are often nearly identical in character and geochemistry. The distinction of deposits from individual eruptions is therefore generally limited to the lateral traceability of individual deposits, and what can be gleaned from the geomorphology and topographic relations from the 2 m resolution LiDAR data set of Hutchison et al. (2014). In localised areas (100s of m to km), where there is sufficient exposure, these relationships can be established with relative certainty. However, obtaining the relationship between deposits from distinct sectors of the volcano (kms to 10s of kms) is very challenging without far more extensive field work. Therefore, in this chapter, I investigate disparate eruptive centres that I mostly consider in isolation. Though this is

not ideal, it fulfils the aims of the investigation; to better understand the styles and processes during individual eruptions at Aluto. Within individual centres, I develop localised relative stratigraphies based on the concept of 'eruption units' from Fisher and Schmincke (1984), and leave their relationship to the regional stratigraphy ambiguous wherever they cannot be well-linked. An eruption unit is defined as *'a thickness of volcanic material deposited from an eruption pulse, an eruption phase or an eruption'* (Fisher and Schmincke, 1984). An eruption unit is neither an eruption event, nor a particular lithological unit, but instead links the two. Some eruption units comprise multiple facies; for example, a gradational lapilli fall to ignimbrite deposit may be considered an individual eruption unit because together they are lithological units that record an eruptive event (column collapse). However, if these units were not gradiational, they would be considered distinct eruption units as they aren't necessarily co-genetic. One complication of this system is when primary pyroclastic units are interbedded with secondary or reworked sedimentary units, that aren't related to any particular eruptive event, even though the constituent material may be the product of a volcanic eruption(s). When this occurs at Aluto, sedimentary units are simply labelled as lithological units following the same sequential numbering system as the over- and underlying primary pyroclastic eruption units. Here, units at each general location are given the same initial letter, and then a sequential number relating to the relative position of the eruption unit in the local stratigraphy; for example 'A5', relates to 'Awariftu valley, eruption unit 5', and 'H2' relates to 'Humo gorge, eruption unit 2'.

Another important point to mention is the use of the term *'ignimbrite'* throughout this work, which often carries many connotations and assumptions. In line with the scheme of Branney and Kokelaar (2002), I use *ignimbrite* to refer to the primary flow deposits of any pyroclastic density current (PDC), regardless of lithology, volume, footprint or specific generation mechanism. An ignimbrite may comprise one or more volcaniclastic lithofacies. By the scheme of Branney and Kokelaar (2002), ignimbrite lithofacies are purely descriptive, and are based on the grainsize and fabric of the deposit. They aren't necessarily the product of any particular process, but inform the process of deposit interpretation. Here I provide a definition of the lithofacies definitions that appear in this work.

- *Massive Lapilli Tuff (mLT).* A tuff in which the clasts are lapilli sized (2 mm to 64 mm), and the overall deposit structure is massive.

- *Diffusely Bedded Lapilli Tuff (dbLT).* A lapilli grade tuff possessing a poorly defined, but present, horizontally bedded fabric (relative to the deposit margins).

- *Cross Stratified Tuff (xsT).* An ash grade (<2 mm) tuff possessing a well defined cross stratified fabric. These may be cross beds (>1 cm) or cross laminations (<1 cm).

- *Diffusely Cross Stratified Tuff (dxsT).* An ash grade tuff possessing a poorly defined cross stratified fabric.

- *Diffusely Cross Stratified Lapilli Tuff (dxsLT).* A lapilli grade tuff with a diffuse cross stratified fabric.

Additionally, the grain size refers to the typical clasts, rather than the matrix, of any volcaniclastic deposit. Rare, atypcially large clasts (with respect to the rest of the deposit), or accretionary pyroclasts are excluded from the overall lithofacies terminology, but are mentioned in the specific eruption unit description. Clasts larger than 64 mm are referred to as blocks which are angular, or bombs which are rounded. These lithofacies terms are combined with standard sedimentological descriptions to encapsulate the nuances of particular eruption units. In this thesis, I present stratigraphy in the form of graphical logs, or series of graphical logs side-by-side in what I term a fence diagram. The symbology used in these in these logs is consistent with general practices and recommendations of Branney and Kokelaar (2002), and is purely descriptive; in other words, symbols refer to lithofacies, features and relationships that can be seen in the field, rather than particular interpretations of rock type such as ignimbrite, or lapilli fall deposit. These symbols are summarised in Figure 3.2.

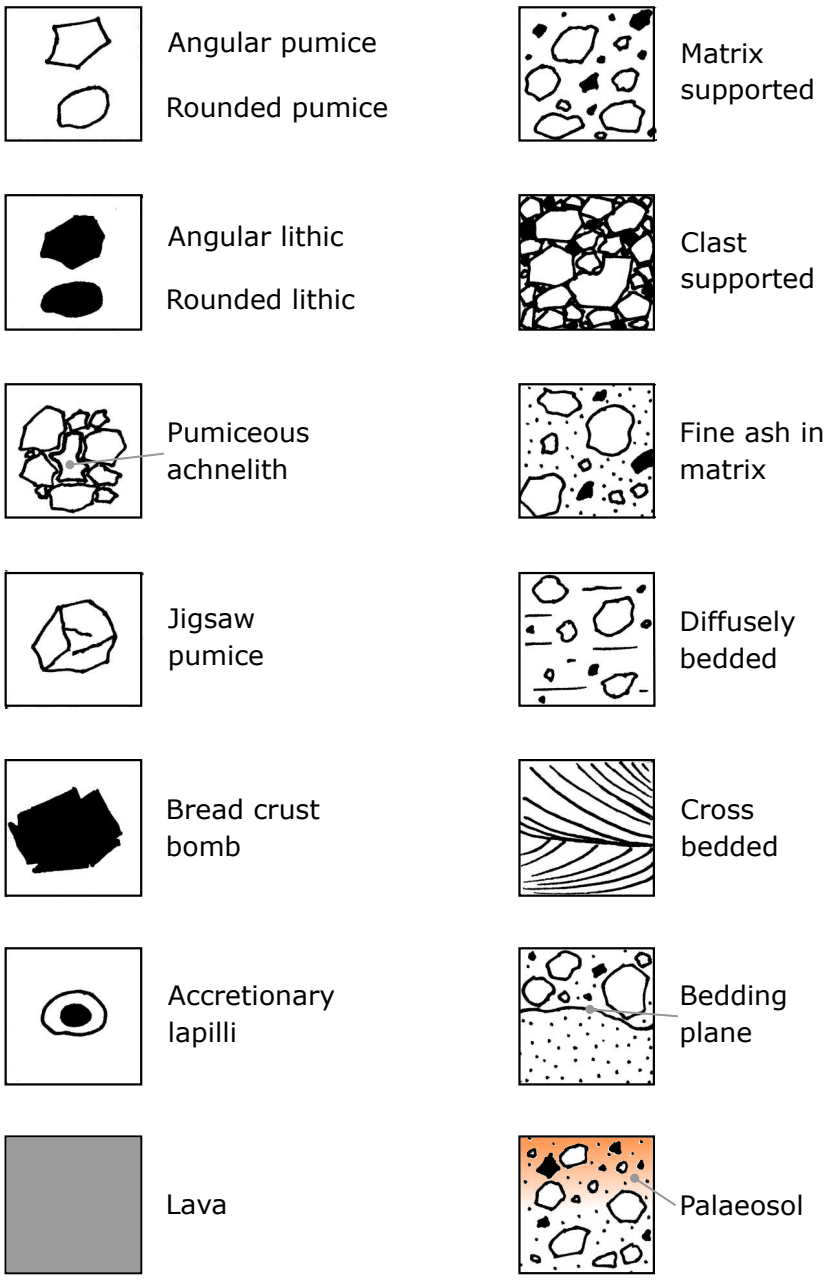

Figure 3.2: *Key to the symbology used in the graphical logs and fence diagrams throughout this chapter. On the left are pyroclast and rock types, on the right are deposit-scale characteristics.*

3.3 Aluto's Southern Flank

3.3.1 Introduction

The southern flank of Aluto caldera is incised by a series of gorges. During the autumn 2017 research expedition, we investigated four of these gorges, named in order from east to west: Kalosanga, Jidduu, Chopa and Gemedo (Figure 3.3). Due to fluctuating lake levels since the Pleistocene, the lower slopes of Aluto's southern flank has been submerged by the lakes within the Ziway-Shala lakes basin on multiple occasions (Benvenuti et al., 2002a). Lake Langano to the south of the edifice is currently at a particularly low stand, revealing the sedimentary and pyroclastic sequences within the gorges we have investigated. Units within each gorge dip to the south, overall at a shallower angle than the topography. Therefore, stratigraphically lower units are exposed from north to south. The objectives of these investigations were to develop a stratigraphy of these sequences in order to answer the following questions:

1. What is the geological history of the SE sector of the volcano?
2. Were PDCs generated from this sector of volcano?
3. What were these PDCs like? Was their base concentrated or dilute? Were they channel-confined or sheet-like?
4. Are these deposits sourced from one or many eruptions, and how are they spaced in time?
5. Does the intercalation of primary pyroclastic deposits and lake sediments provide any time constraints on eruptive activity in this sector of Aluto?

In the following sections, each gorge is described on a eruption unit-by-unit basis and local stratigraphies are developed. In the discussion, the local stratigraphies are combined to develop a broader-scale stratigraphy of Aluto's southern flank and a broader geological history is developed.

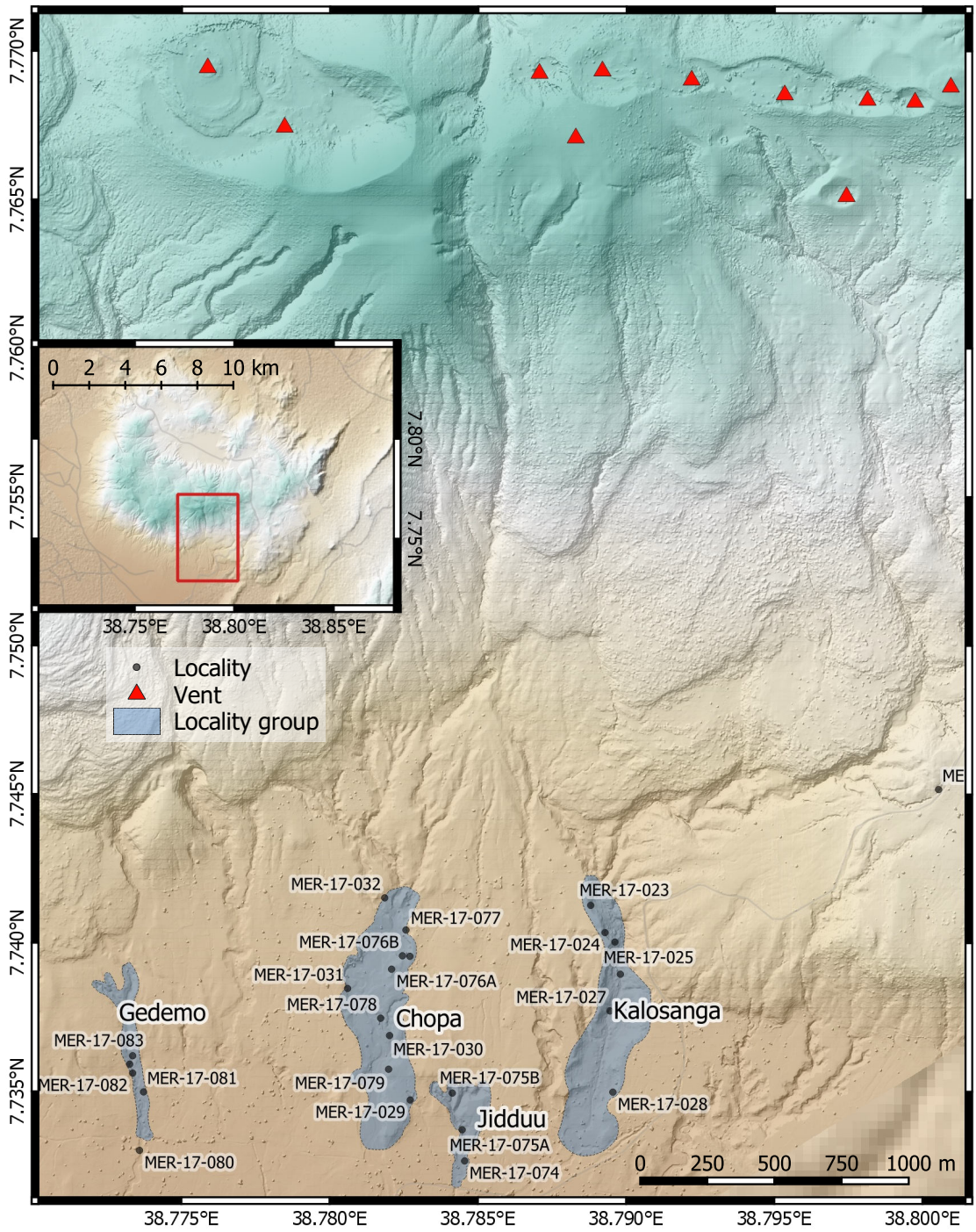

Figure 3.3: *Overview of the Southern flank of Aluto including the four wadis investigated in the following section: Kalosanga, Jidduu, Chopa and Gemedo. The line of vents to the north are the most proximal up-slope vents to the pyroclastic deposits in the wadis, and so are considered their most probable source.*

3.3.2 South-Flank Wadi Sections

Kalosanga

Kalosanga gorge comprises eight units: K1 to K8 from stratigraphically highest to lowest (Figure 3.14). Due to the lack of foot access to certain exposures, only K1 to K4 have been observed close-up. Units K5 to K8 have been described from a distance, and so the interpretations of these units are tentative. There is an obsidian lava flow to the east of Kalosanga, and the pyroclastic deposits exposed in Kalosanga onlap the edge of the flow. The flow is K/Ar dated to 78 ± 20 Ka (Woldegabriel et al., 1990), indicating the pyroclastic deposits in the gorge are younger than this.

Locality MER-17-26 is a cliff section, providing a near complete stratigraphy of Kalosanga gorge, displaying units K2 to K8 (Figure 3.4). Unit K8 is the hardest to interpret from a distance, but appears to comprise matrix supported, rounded pumices and occasional lithics. Interpretations of either primary ignimbrite or reworked pyroclastic material are equally appropriate.

K7 is a diffusely bedded, very poorly sorted, matrix supported and pumice-poor conglomerate. The long axes of its cobble-sized clasts lie sub-parallel with bedding and are imbricated. K6 is a massive, well sorted, pale white-coloured fine grained deposit that maintains its thickness along the entire exposure. This is most probably an ash fall deposit from Aluto. Above K6 is a deposit that is very similar in character to K7, but with coarser boulder-sized lithic clasts. K5 and K7 represent similar depositional regimes but have an intermediate period of quiescence to allow ash to settle. This, the large clast size and the matrix supported nature, suggest that K7 and K5 represent individual debris flow events; such as lahars or flash floods. Sediment concentration must have been high, but not so high as to entirely suppress turbulence, allowing for the development of diffuse bedding and the alignment of clasts. This suggests they represent sediment rich flows that straddle the debris flow/hyperconcentrated flow boundary.

Unit K4 is a brown palaeosol with moderately to well rounded pumices supported in

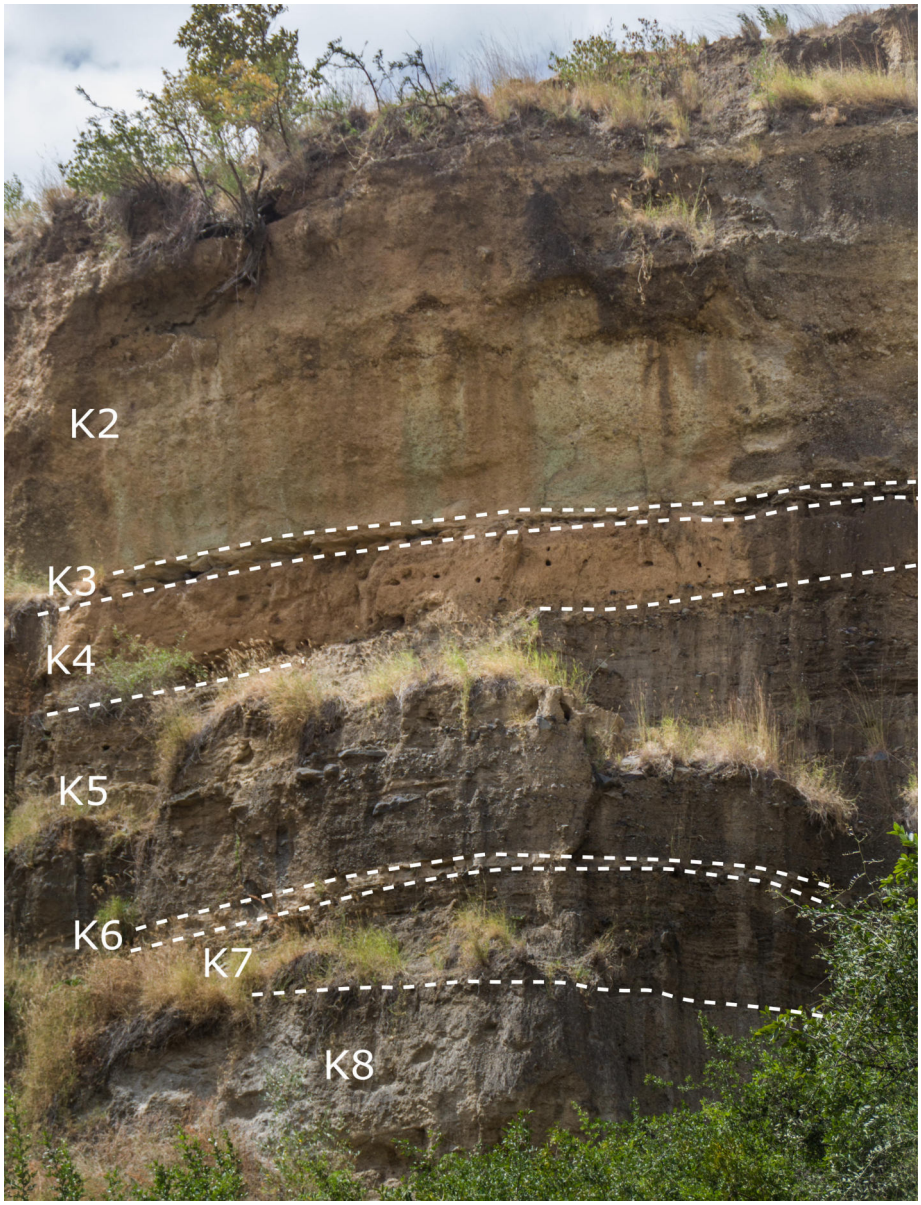

Figure 3.4: *Annotated photo of section MER-17-26 displaying much of the stratigraphy of Kalosanga gorge (units K8 to K2). Height of cliff is around 11 meters.*

a matrix of fine ash and small angular chips of obsidian, suggesting it was originally an ignimbrite. In places, such as MER-17-25 (Figure 3.5), there is some localised variation in the lithofacies near the top which may either be primary, or associated with soilification.

K3 is a thin, coarse-ash fall deposit. The deposit is planar bedded, with 2 beds, each 1 cm thick. As there is no evidence of a time gap between K3 and the overlying unit K2, this fall deposit may be sourced from the same eruption column that later collapsed to produce the overlying ignimbrite (K2). K2 is a 4-5 m thick, strongly-indurated, matrix supported mLT ignimbrite that shows significant variation in its components with height. The lower 30cm of the deposit is clast supported (Figure 3.5), relatively lithic poor and contains small, moderately rounded pumices. Towards the middle of the ignimbrite, it becomes more matrix supported. In the middle, meter-long lenses of lithic rich material are surrounded by more pumice rich ignimbrite. Towards the top, the deposit becomes more clast supported, but maintaining the lithic concentration and size seen within the middle of the deposit. The increasing lithic concentration with height suggests the deposit represents a waxing flow, with the coarse, dense lithics reaching further from source with time. For the deposition of material from a flow, there must be a net substantive deceleration (Branney and Kokelaar, 2002); considering the waxing nature of the flow that deposited this ignimbrite (ie. acceleration in a Eulerian reference frame), deposition can only be accommodated by depletion (ie. deceleration in a Lagrangian reference frame). A scenario that satisfies these conditions is a concentrated, waxing PDC travelling down a concave slope.

K1 is the uppermost unit exposed in Kalosanga gorge and consists of a 3m (minimum) thick, pale white, matrix supported, pumice-rich mLT ignimbrite. The deposit contains small angular lithics of obsidian and various red oxidised volcanics. The deposit was sieved, the results of which can be found in Appendix C.2 under sample MER-17-23A. It has a median grain size of -0.37, and is very poorly sorted at 3.44 ϕ, with a pumice to lithic ratio of around 2:1 by weight.

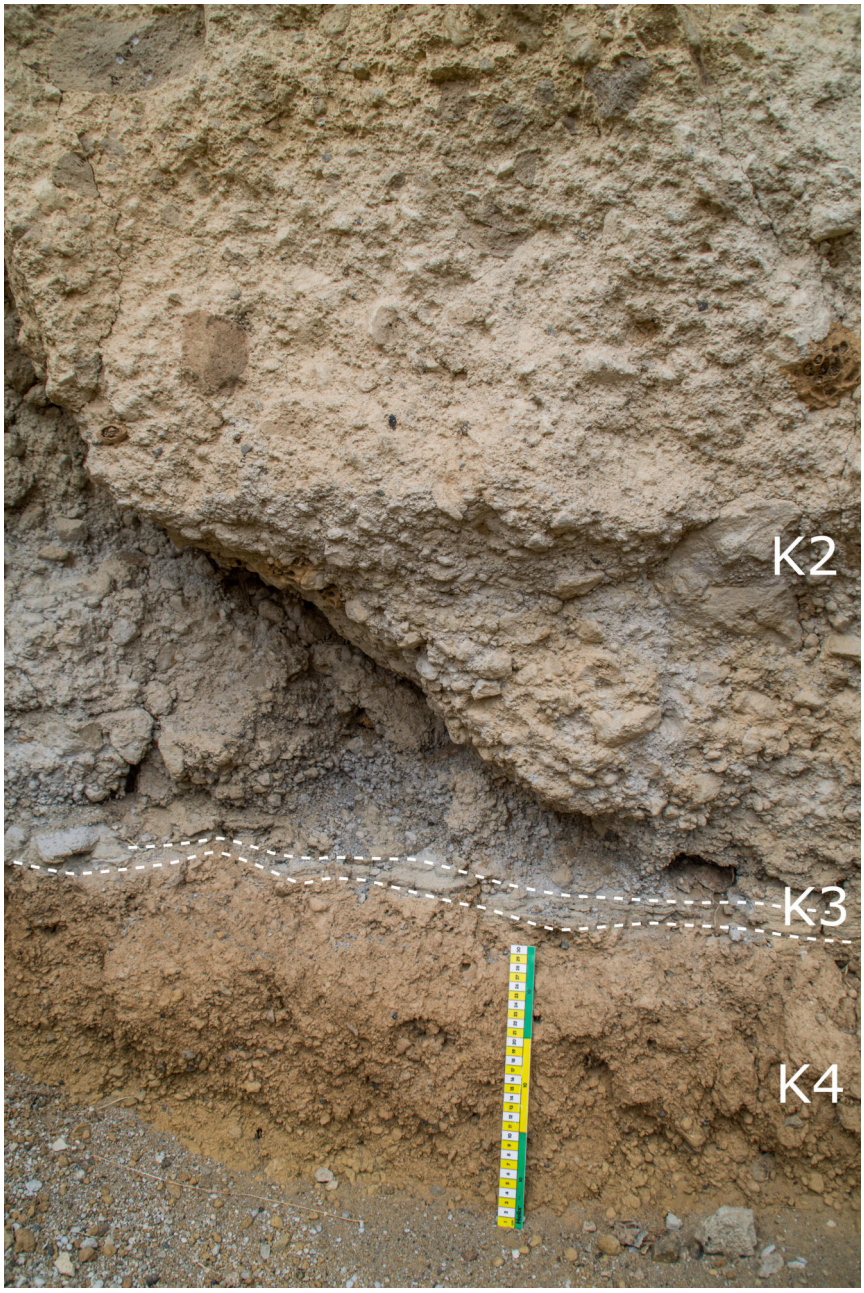

Figure 3.5: *Annotated photo showing units K4 to K2 at MER-17-25. Here, the top of K4 is clast supported, but in the majority of exposures, the unit is matrix supported. The scale length is 30cm.*

Figure 3.6: *Photo of the middle of ignimbrite unit K2, showing matrix support, induration and pumice/lithic textures. Units of scale are cm.*

Jidduu

Jidduu, a gorge around 0.5 km SW of Kalosanga, and is much shorter by comparison. As Jidduu is further south and stratigraphically lower than the other gorges, most of its 10 units are reworked by palaeo-lake Langano, but some units (J3, J5 and J9) are primary deposits from Aluto.

The bottom of the succession (Figure 3.7) consists of a thick pumice rich conglomerate (J10). In Figure 3.15, only the top 5 m are shown, but J10 extends stratigraphically lower as you continue further north along the valley from MER-17-75 to MER-17-75B. The deposit comprises moderately to well rounded pumices in a clast supported network with some granule sized material in the matrix. The deposit is well to moderately sorted, and contains a large number of graded packages, cross beds, reactivation surfaces and planar beds. Beds are steeply dipping, near their repose angle, away from Aluto's edifice. Beds show greater or lesser degrees of pumice angularity. Compositionally, the deposit seems very similar throughout with no obvious increase in the proportion of lithics to pumice. The sedimentary structures, sorting, and rounding of pumices in the deposit imply that there was significant interaction with water during deposition. However, once deposited, it is unlikely that clasts were left to roll over the surface for long in order to develop the much greater degrees of rounding typically seen in, for example, beach deposits. Instead, it is likely that new pyroclastic material was deposited on top relatively rapidly, or was deposited below the fair-weather wave base. The thickness of the deposit suggests the material was filling a basin. The steeply dipping, thick beds of conglomerate are typical of the foreset portion of a Gilbert-type prograding delta, often found in lacustrine (and particularly rift) settings (Postma, 1990). This suggests J10 represents the slope facies of a delta into palaeolake Langano. The more angular beds may represent the occasional input of primary volcanic flows (ie. lahars and PDCs, in the form of turbidity currents) down the delta front.

Above this lies a 1 m thick, inversely graded, pumice lapilli fall deposit (J9). It consists of very well sorted angular pumice lapilli in a clast supported network with very few

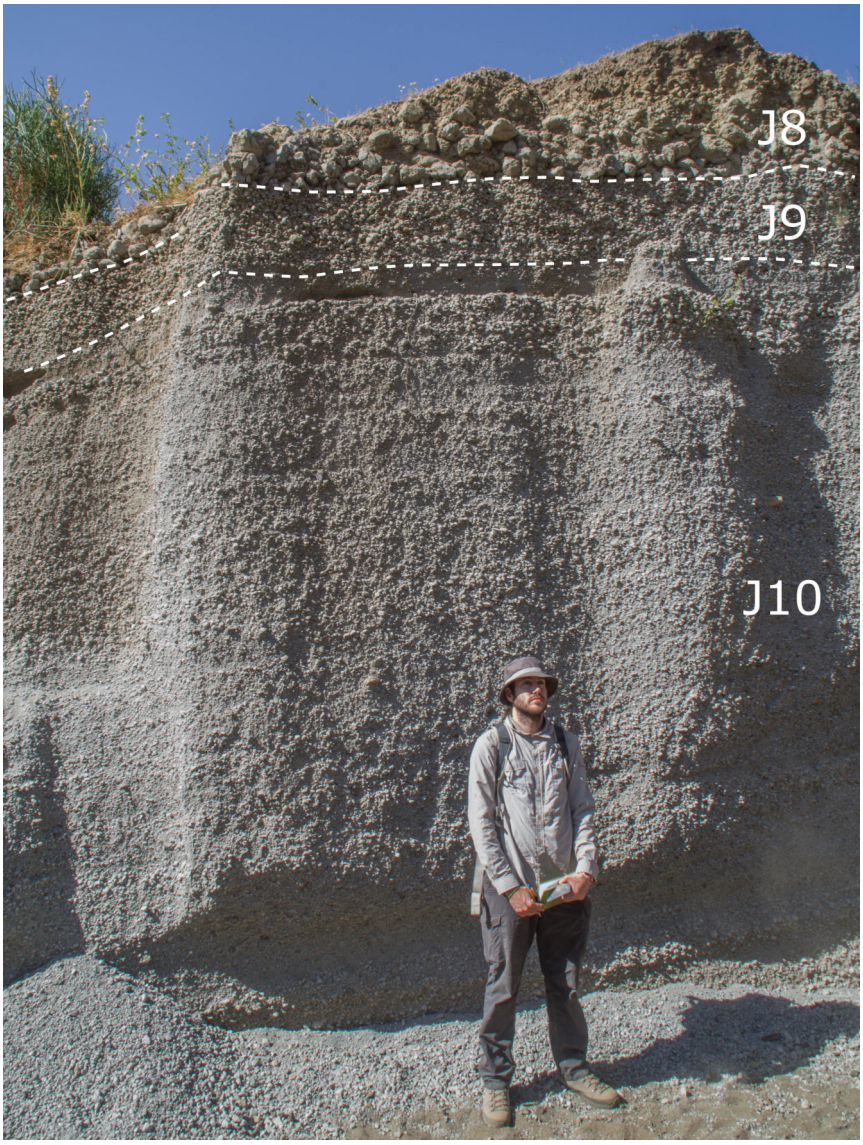

Figure 3.7: *Annotated photo of section MER-17-75 showing the lower three units of Jidduu gorge. 180cm Pablo Tierz for scale.*

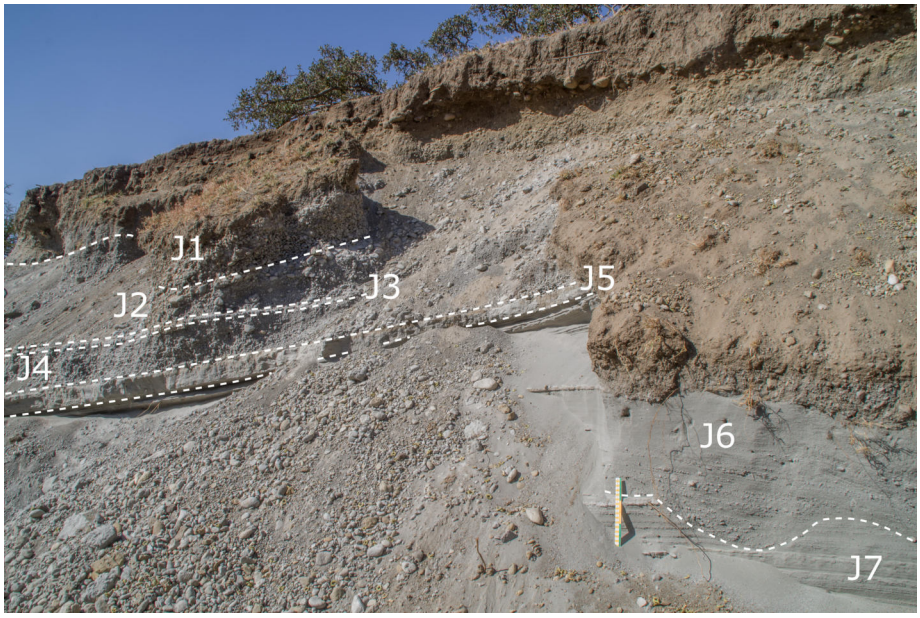

Figure 3.8: *Annotated photo of section MER-17-74. J7 to J5 show the transition from very shallow lacustrine to sub-aerial conditions whilst J4 to J1 show a return to lacustrine deposition. 30 cm scale.*

lithics. Deposit J8 is a coarse lapilli/bomb grade monolithologic pumice deposit with well to moderately rounded, clast supported, reworked pumice and no matrix. It is massive. Above J8 is a 50 cm thick fine grained, planar laminated deposit of fine to course ash in normally graded packages (Figure 3.8). This likely represents ash settling through a still, perhaps very shallow, body of water without wave action. This unit is cut by small channels around 30 cm deep which are filled by unit J6: a cross bedded, poorly sorted flow deposit with 30 cm long stringers of coarser pumice clasts. It is matrix supported with a coarser grain size distribution within the channels. Pumices are well rounded and there are few lithic components. J6 may be small-scale fluvial deposits filling channels cut into the fine ash of unit J7, which would suggest the palaeolake level is relatively lower compared to the delta slope deposits of J10. J5 is a massive, very well sorted fine ash fall deposit with a thin, brown palaeosol at the top, suggesting sub-aerial, oxidising conditions.

Units J4, J2 and J1 are very similar in all but grain size. They comprise very well rounded matrix supported pumices without any matrix material, and imply significant water reworking. Unit J4 has a minor lithic component consisting of small obsidian chips,

whilst J2 and J1 are monolitholigic pumice. The rounding of the pumices suggests that they have been extensively rolled in a current or by waves. This suggests that palaeolake levels might have risen slightly (eustatic) or that the land level fell (isostatic). In such a tectonically active, and climactically variable region, either isostatic or eustatic changes are plausible. Unit J3 is a thin (2 cm) medium ash fall deposit with planar laminations within this sequence and probably represents ash fall from Aluto into the shallow lake.

The frequent change between sub-aqueous and sub-aerial settings in this section implies they were deposited near a fluctuating shore line resulting in repeated facies changes. The very well rounded nature of the pumices in J4, J2 and J1 suggests they have been rolled around extensively, quite possibly through wave action. These features are often found in the topset facies of Gilbert-type deltas (Postma, 1990), and represents the further progradation of the delta and/or a drop in palaeolake level.

Le Turdu et al. (1999) describe a strikingly similar succession on the piedmont of Aluto's southern flank, which they refer to as the O'itu-Woshe section. They also interpret this as a Gilbert type delta, quite possibly the same delta described here. An AMS radiocarbon date from charcoal in a sandy-gravelly bed near the base of this delta succession has been reported as 5700 ± 110 ^{14}C yr BP (Le Turdu et al., 1999) (sample H1362).

Chopa

Chopa gorge lies around 200m to the NW of Jidduu and contains excellent lateral exposure of 9 units (C1 - C9) (Figure 3.16). Near the southern end of the gorge, at MER-17-78, there is a 4.5 m thick exposure displaying units C9 to C6 (Figure 3.9).

Unit C9 is a lithic rich conglomerate which is matrix supported at the base and becomes clast supported near the top. In the bottom portion of the unit, pumices are rare, and where present are very well rounded and small. They, along with granule sized lithics, form the matrix which is diffusely cross bedded and supports moderately rounded large lithics. The lithics are inversely graded towards the centre of the deposit. Above this is a

Figure 3.9: *Section MER-17-78 in Chopa gorge, exposing units C9, C8 and C6. 170 cm Firawalin Dessalegn for scale.*

clast supported section with a granule grade matrix. It has a greater proportion of pumice to the lower part of the unit and is overall finer-grained than the middle of the deposit. The very top of C9 is only exposed at MER-17-78, and consists of a finer grained unit with cross bedding, altered to a palaeosol. C9 clearly comprises reworked material with an unusually high concentration of lithics relative to pumices for Aluto, suggesting they are concentrated relative to the source deposit. This is most easily achieved through density segregation of particles through water. The extreme rounding of the small pumices and rounding of the lithics suggest there has been extended transport before final deposition. The cross bedding at the base and top of the deposit suggests the particle concentration of the flow was not high enough to suppress turbulence. This could represent one, or a series of, flood or lahar events depositing coarse, lithic-rich material. The fine material at the top has formed a brownish-red palaeosol, and so must have been exposed sub-aerially. However, it is cross bedded and too coarse to represent wind blown sediment, so is interpreted as a stream-flow fluival deposit exposed sub-aerially for a significant period.

The units stratigraphically above C9 are best exposed at MER-17-76/77, and show excellent lateral exposure clearly revealing their complex field relations (Figure 3.11). Here, units C7 and C8 can be seen to drape the underlying topography (Figure 3.10). C8 is

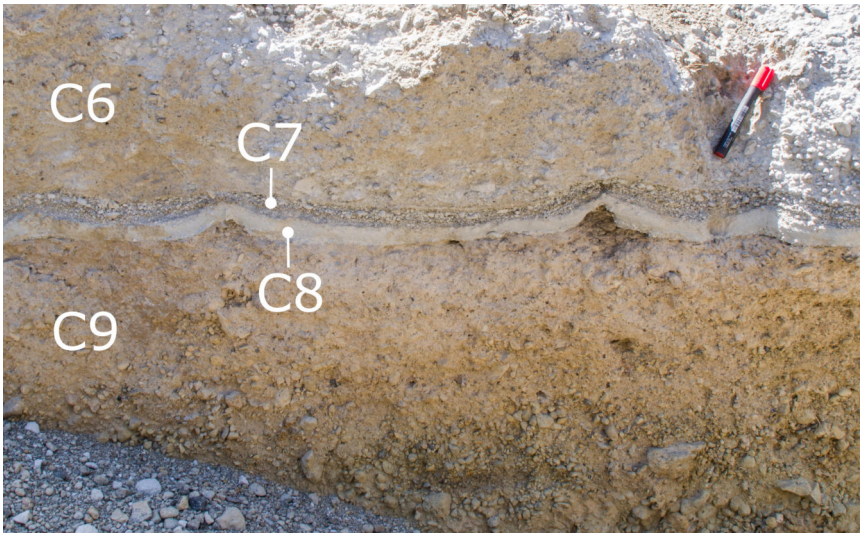

Figure 3.10: *Exposure of fall deposits C7 and C8 in Chopa gorge at MER-17-76/77. 14 cm pen for scale.*

a medium ash grade, 3 cm thick fall deposit. Unit C7 is a 3 cm, inversely graded, clast supported lapilli pumice fall deposit. Considering the palaeosol beneath, both probably represent tephra fall from Aluto onto dry land at the beginning of an eruption.

Unit C6 is a 3 m thick mLT ignimbrite with an inverse and then normal lithic grading pattern. The ignimbrite is matrix supported and has moderately rounded pumices, angular obsidian lithics, and a fine ashy matrix. The inverse then normal grading of the lithics may be explained by a sustained waxing then waning current. The top of the ignimbrite has formed a thin palaeosol. Above this palaeosol is another 2 m thick ignimbrite: C5. C5 is a massive matrix supported mLT with a fine ashy matrix and lithics comprising dense obsidian chips and red oxidised volcanics. The lithics are normally graded, and the pumices inversely graded throughout the deposit, suggesting the deposit represents the waning stages of a PDC (Branney and Kokelaar, 2002).

The lower part of the succession (C9 to C5) is cut by deep channels that are now occupied by unit C4, a hyperconcentrated flow deposit. C4 is pumice rich, very poorly sorted and matrix supported. The pumices are moderately to well rounded and lie within a cross bedded matrix that lacks fine ash and preserves small bubbles. There are some lithics

within the deposit which tend to be smaller than the pumices. The unit becomes finer and the cross bedding is better developed towards the top. The deposit exists in both channel filling and sheet-like overbank facies (Figure 3.11). The overbank facies of the deposit are finer grained, posses well-developed low angle cross bedding and occasional pebble sized pumices and lithics. Where the lahar deposit fills channels, its terraces are buried and preserved by the overlying ignimbrite C3 (Figure 3.11).

C3 is a relatively thin (1 m) mLT ignimbrite that mostly consists of moderately-rounded coarse pumice clasts in a fine ash matrix. The ignimbrite is massive and matrix rich. The lithics are rare and are typically dense obsidian chips far smaller than the pumice clasts. C3 is cut out entirely further North along Chopa valley, where it truncated by an indurated ignimbrite forming a palaeosol (C2). C2 is a near-clast supported mLT ignimbrite with a very poorly sorted assortment of moderately rounded pumices and angular lithics of similar size. It is massive and generally around 0.5 m thick. The deposit is indurated and yellow to rust-coloured indicating it is a palaeosol.

Stratigraphically highest in Chopa gorge is a pale white, matrix rich mLT ignimbrite (C1) with a fine ashy matrix and lithics comprising dense obsidian chips, green ignimbrite and red oxidised volcanics. The lithics are normally graded and the pumices inversely graded, suggesting this deposit represents the waning stage of a PDC. This ignimbrite forms many of the small hummocks on the flanks of the gorge and the surroudning plane.

Figure 3.11: *Exposure MER-17-76/77 at Chopa gorge showing all of the Chopa units and their field relations. C4 can be seen on the right as a channel-filling lahar and on the left as a thin, sheet like deposit. Terraces within C4 can be seen in the channel-filling regions. C3 blankets the C4 lahar deposit, burying lahar terraces on the right. C1 exists as small hills on the shoulders of the gorges. 180 cm Pablo Tierz for scale.*

Gemedo

Gemedo gorge is the westernmost gorge investigated on the south flank of Aluto. It comprises 4 separate units: G1 to G4. Unit G4 is best exposed at the north end of Gemedo gorge, and is the only sub-aqueously deposited unit in Gemedo. Much of the deposit is very similar in character to unit J10 in Jidduu gorge, and is considered a lateral continuation of the same deposits. The lower portion of G4 is dominated by a matrix supported, diffusely cross-bedded, granule grade deposit with larger clasts of very well rounded pumice. In the middle, the unit is clast supported, with graded packages of very well rounded pumice and rare, rounded lithics with a granule grade matrix. The top of the unit is very similar to the base. Much of the deposit is structured as foresets that dip steeply to the south. There is a 0.5 m thick palaeosol at the top of the unit, showing that the lake level dropped, exposing these volcano-deltaic sediments to the atmosphere, and marking a lithological transition from sub-aqueous to sub-aerial facies.

G4 and its palaeosol is deeply incised by channels, showing these channels were cut well after the lake level dropped. The channels are filled with, and over-topped by, the upper 3 units G3, G2 and G1. Unit G3 is a pale white, massive, matrix supported mLT ignimbrite with a very high clast concentration. Clasts comprise moderately rounded pumices and small angular lithics. It is in character very similar to G1, but can be distinguished by its generally higher clast concentration.

Unit G2 is ephemerally exposed, and is only visible in a few sections along the valley. It lies between ignimbrite units G3 and G1 and is a cross bedded, matrix supported reworked unit. It contains some small, well rounded pumices and small angular lithics but is mostly matrix. The matrix is granule sized and has no fine ash component. This unit was most likely deposited from small streams or a sheet-flood.

Unit G1 is a pale white, matrix supported mLT ignimbrite with moderately rounded pumices. In places (such as MER-17-81, Figure 3.17), the base of the unit contains very coarse, meter-scale lithic clasts with rare, smaller pumices in the matrix (Figure 3.13).

However, more typically, the unit is massive, and comprises moderately rounded pumices, and rare small angular lithics suspended in an ash rich matrix. It is typically very matrix rich.

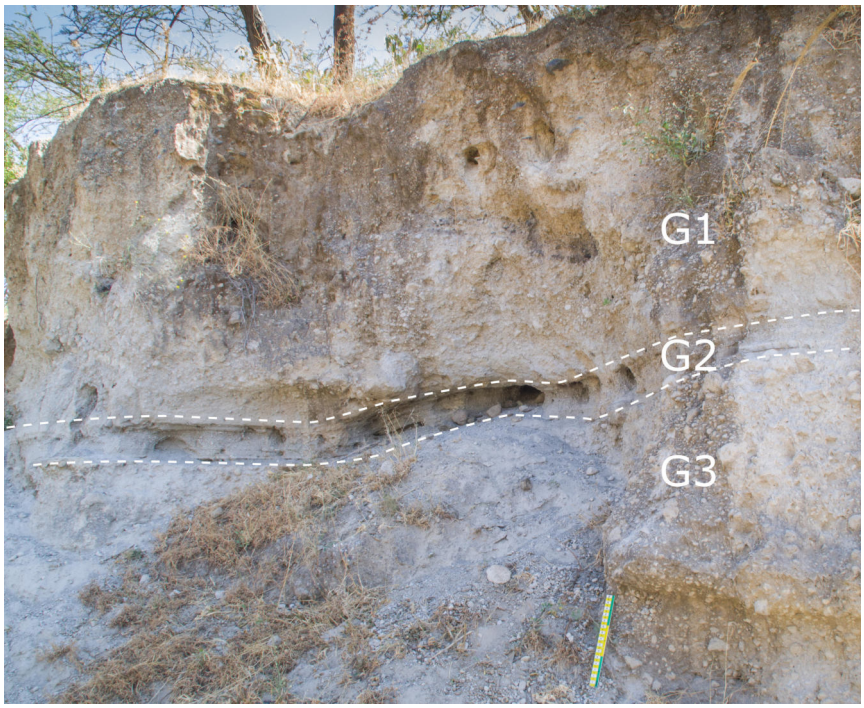

Figure 3.12: *Top of section MER-17-82 showing the upper 3 units of Gemedo gorge: G3, G2 and G1. The scale is 30 cm long*

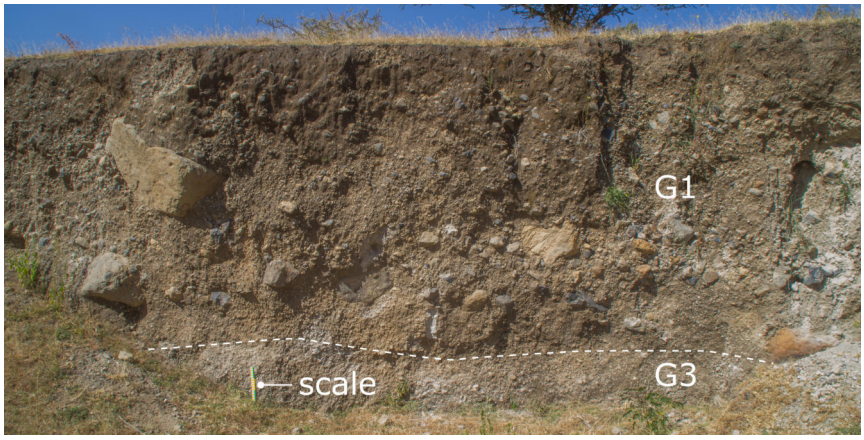

Figure 3.13: *Annotated photo of section MER-17-81, showing a very coarse, lithic rich exposure of G1 overlying unit G3. The scale is 30 cm long*

3.3.3 Fence Diagrams

Fence diagrams for each gorge are presented on the following pages. Each diagram is collated from a series of logs. Some logs are themselves collations of geographically-proximal logs. Brief unit descriptions are also provided.

Kalosanga Gorge

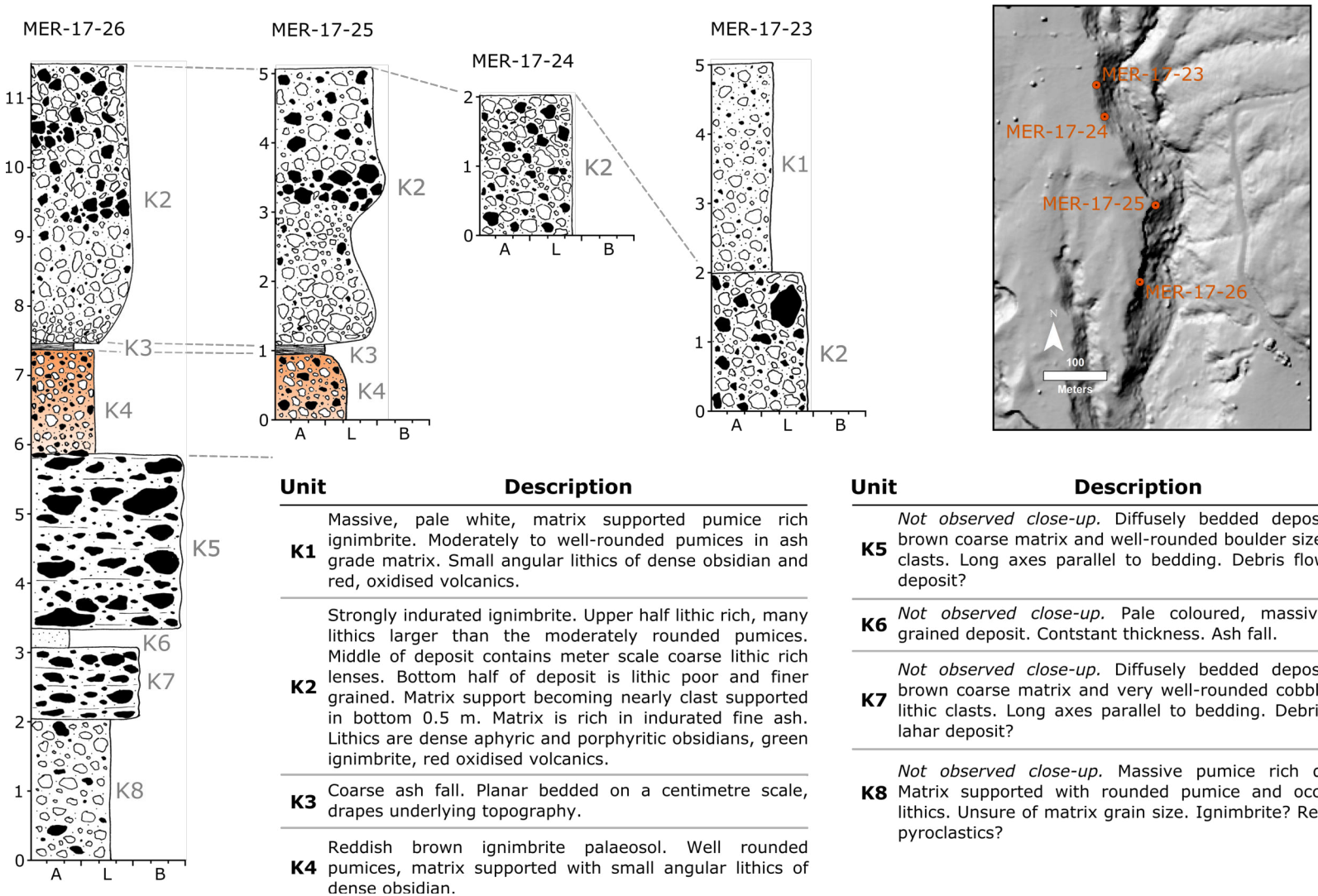

Unit	Description
K1	Massive, pale white, matrix supported pumice rich ignimbrite. Moderately to well-rounded pumices in ash grade matrix. Small angular lithics of dense obsidian and red, oxidised volcanics.
K2	Strongly indurated ignimbrite. Upper half lithic rich, many lithics larger than the moderately rounded pumices. Middle of deposit contains meter scale coarse lithic rich lenses. Bottom half of deposit is lithic poor and finer grained. Matrix support becoming nearly clast supported in bottom 0.5 m. Matrix is rich in indurated fine ash. Lithics are dense aphyric and porphyritic obsidians, green ignimbrite, red oxidised volcanics.
K3	Coarse ash fall. Planar bedded on a centimetre scale, drapes underlying topography.
K4	Reddish brown ignimbrite palaeosol. Well rounded pumices, matrix supported with small angular lithics of dense obsidian.

Unit	Description
K5	*Not observed close-up.* Diffusely bedded deposit with brown coarse matrix and well-rounded boulder sized lithic clasts. Long axes parallel to bedding. Debris flow lahar deposit?
K6	*Not observed close-up.* Pale coloured, massive, fine grained deposit. Contstant thickness. Ash fall.
K7	*Not observed close-up.* Diffusely bedded deposit with brown coarse matrix and very well-rounded cobble sized lithic clasts. Long axes parallel to bedding. Debris flow lahar deposit?
K8	*Not observed close-up.* Massive pumice rich deposit. Matrix supported with rounded pumice and occasional lithics. Unsure of matrix grain size. Ignimbrite? Reworked pyroclastics?

Figure 3.14: *Fence diagram of Kalosanga gorge including descriptions of stratigraphic units. Heights are provided in meters and are relative to the base of the exposure.*

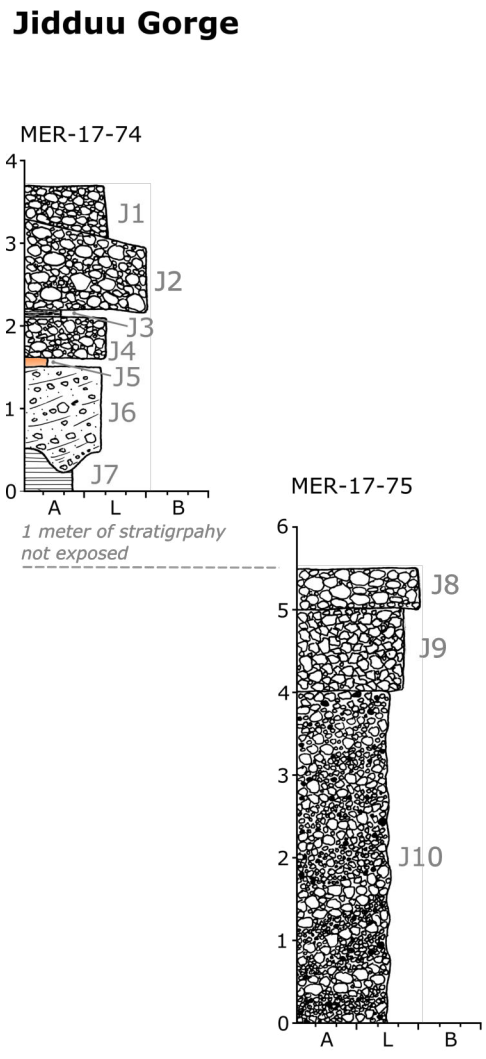

Unit	Description
J1	Massive, clast supported reworked small lapilli grade deposit with very well rounded pumices and no matrix. All clasts are pumice.
J2	Massive, clast supported reworked coarse lapilli grade deposit with very well rounded pumices and no matrix. All clasts are pumice.
J3	Thin (2 cm) medium ash, very well sorted fall deposit. Planar laminations that drape topography.
J4	Massive, clast supported reworked small lapilli grade deposit with very well rounded pumices and no matrix. Minor lithic component consisting of small angular chips of obsidian.
J5	Massive, very well sorted fine ash deposit (18 cm thick) with brown palaeosol at top.
J6	Poorly sorted, cross bedded flow deposit with well rounded pumices supported in an ashy matrix. Coarser clasts occur in short (~ 30 cm) stringers forming foresets. No visible lithics component. Fills in channels in underlying topography. Coarser in channels, cross bedding less apparent outside of channels. Fluvial stream flow or hyperconcentrated flow deposit?
J7	Planar bedded fine to coarse ash in small normally graded packages.
J8	Coarse lapilli to bomb grade, clast supported reworked pumice deposit. Clasts are moderately to well rounded with no matrix. All clasts are pumice.

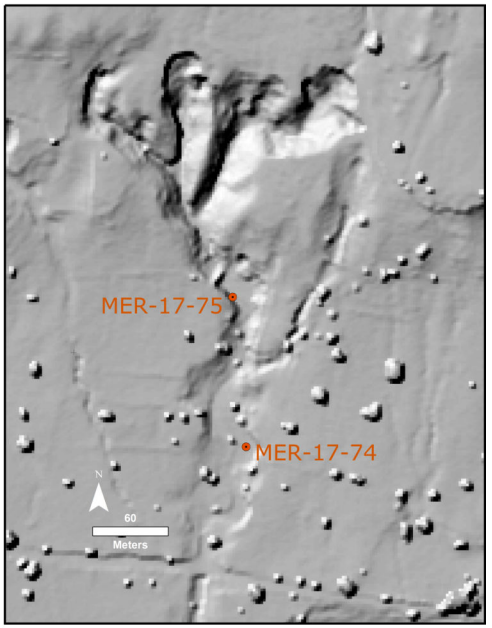

Unit	Description
J9	1 m thick, angular pumice lapilli fall deposit. Massive and inversely graded. Very rare lithic components.
J10	Steeply bedded reworked pumice deposit. Moderately to well rounded, clast supported pumices in coarser and finer lapilli grade beds. Very few lithics and granule sized matrix. Prograding Gilbert-type delta slope foreset facies with some beds of primary pyroclastic marterial.

Figure 3.15: *Fence diagram of Jidduu gorge including descriptions of stratigraphic units. Heights are provided in meters and are relative to the base of the exposure.*

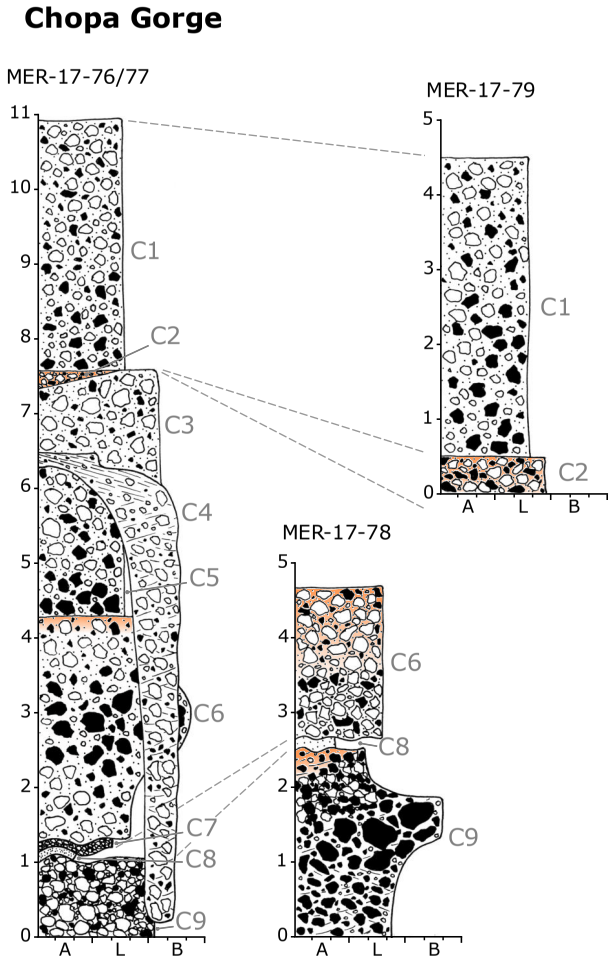

Unit	Description
C1	Matrix supported, massive, pale white coloured ignimbrite with a very fine ash matrix. Pumices are well rounded and are inversely graded. Lithics, comprising angular chips of dense obsidian, green ignimbrite and red oxidised volcanics, are normally graded.
C2	An indurated, reddish ignimbrite palaeosol which is cut out in many exposures. Nearly clast supported with ashy matrix. Moderately rounded pumices and dense obsidian lithics that are generally finer grained than the pumice.
C3	Matrix supported, massive ignimbrite with moderately rounded pumices. Relatively lithic poor with only a few dense obsidian chips in an ashy matrix. Underlying surface is undulating.
C4	In some exposures, present as thin 'sheet-like' hyperconcentrated flow deposit that laterally transforms into a chanel filling lahar deposit. In valleys, forms a coarse, matrix supported conglomerate with moderately to well rounded pumices and a large assortment of lithics. The matrix lacks fine ash but gas bubbles are preserved. The overbank facies are finer grained with small pumice and lithic clasts in a low angle cross bedded matrix.
C5	Matrix supported, massive, lithic rich ignimbrite with particularly lithic rich base. Lithics comprise dense obsidian chips and red oxidised volcanics which are normally graded. Pumices are moderately to well rounded and are inversely graded. The matrix is ashy.
C6	Matrix supported, massive, pumice rich ignimbrite with lithic rich centre. Pumices are moderately rounded in an ashy matrix. At top and bottom ashy matrix contains small abundances of obsidian chips. In the centre of the flow lithics become larger and more abundant, and pumice become smaller and less abundant.

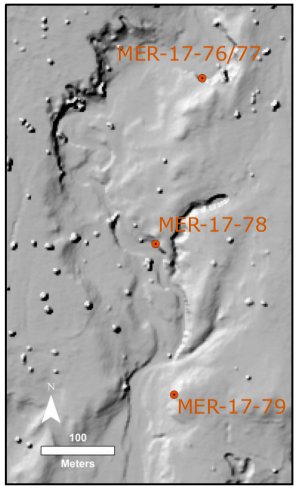

Unit	Description
	At the top of the deposit there is a thin indurated layer with a brown hue.
C7	Thin (3 cm), clast supported, inversely graded lapilli pumice fall deposit. Drapes underlying topography.
C8	3 cm thick, massive, medium to coarse ash fall deposit. Drapes underlying topography.
C9	Top is cross bedded fine palaeosol with small well rounded pumices and lithics, then transforms into massive pumice and lithic clast supported deposit. Base is diffusely cross bedded matrix supported lithic breccia with inversely graded lihtics towards center. Lahar deposit?

Figure 3.16: *Fence diagram of Chopa gorge including descriptions of stratigraphic units. Heights are provided in meters and are relative to the base of the exposure.*

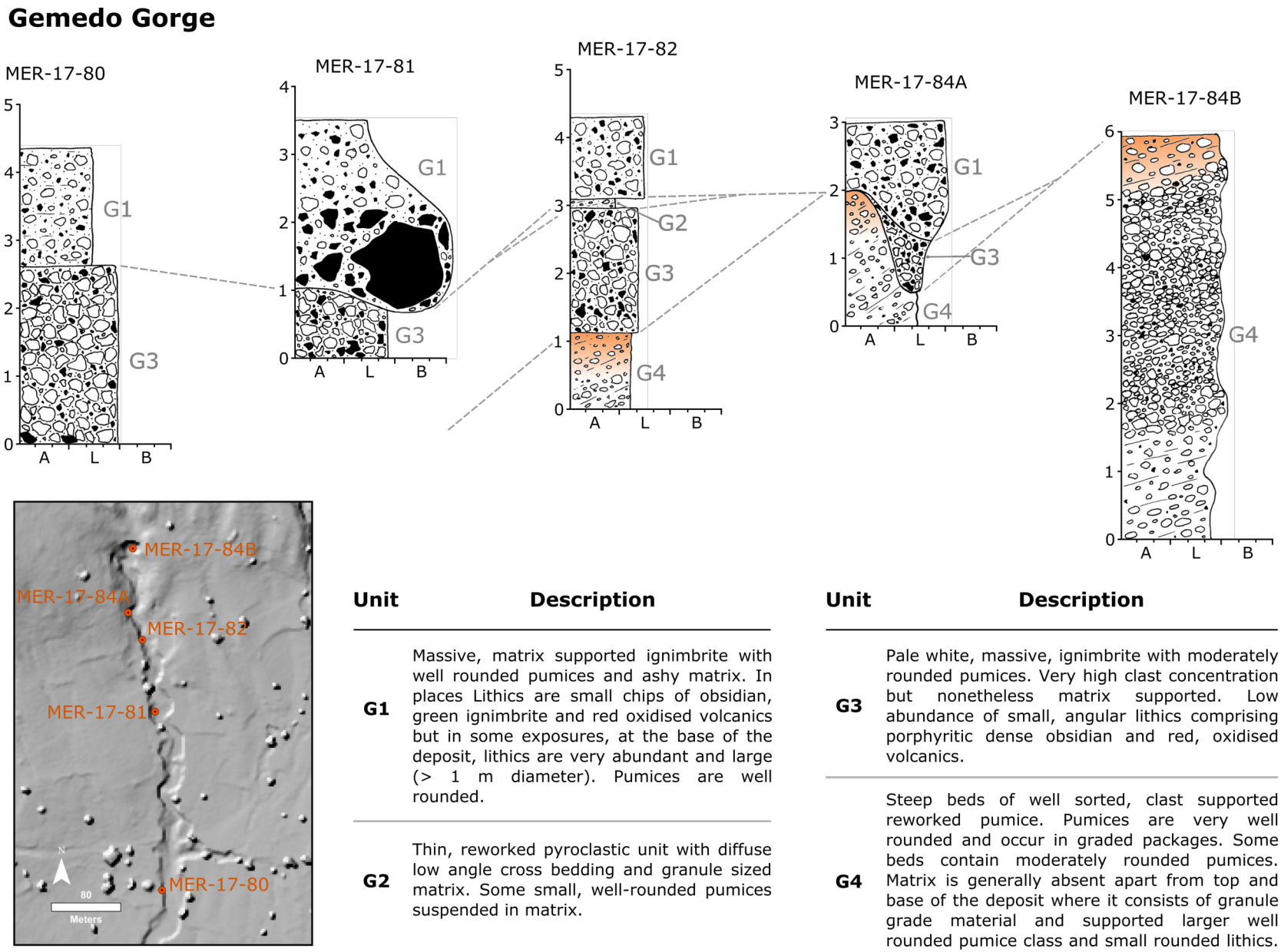

Unit	Description
G1	Massive, matrix supported ignimbrite with well rounded pumices and ashy matrix. In places Lithics are small chips of obsidian, green ignimbrite and red oxidised volcanics but in some exposures, at the base of the deposit, lithics are very abundant and large (> 1 m diameter). Pumices are well rounded.
G2	Thin, reworked pyroclastic unit with diffuse low angle cross bedding and granule sized matrix. Some small, well-rounded pumices suspended in matrix.

Unit	Description
G3	Pale white, massive, ignimbrite with moderately rounded pumices. Very high clast concentration but nonetheless matrix supported. Low abundance of small, angular lithics comprising porphyritic dense obsidian and red, oxidised volcanics.
G4	Steep beds of well sorted, clast supported reworked pumice. Pumices are very well rounded and occur in graded packages. Some beds contain moderately rounded pumices. Matrix is generally absent apart from top and base of the deposit where it consists of granule grade material and supported larger well rounded pumice class and small rounded lithics. Gilbert-type foresets.

Figure 3.17: *Fence diagram of Gemedo gorge including descriptions of stratigraphic units. Heights are provided in meters and are relative to the base of the exposure.*

3.3.4 Discussion

The stratigraphy of Aluto's southern flank

The stratigraphy and geological history of the southern flank of Aluto has been established by combining the field data from Kalosanga, Jidduu, Chopa and Gemedo in reference to the LiDAR elevation data set of Hutchison et al. (2014). The ignimbrites present at the top of Kalosanga, Chopa and Gemedo gorges (K1, C1, and G1 respectively) are strikingly similar. They are ash-rich, with well rounded pumices and small lithics. They are all a distinctive pale white colour in exposure and are not indurated. In cross section (A' to A" in Figure 3.18), the base of these units (which are placed at the correct height in each gorge) can be traced across the south flank as a single planar surface. This surface exactly coincides with breaks in slope across the section; where the non-indurated nature of the deposits has made them easier to erode than the underlying units. This therefore appears to be a single, traceable mLT, henceforth referred to as the O'itu Woshe ignimbrite. When observing the topographic data in plan view (also in Figure 3.18), exposures of this unit can be seen as small hummocks or 'islands' on an erosional terrace allowing the exposure and lateral extent to be mapped by topography.

The lateral traceability of the O'itu Woshe ignimbrite makes it distinct on the south flank of Aluto, as the lower units occur in discrete sequences of lahars, ignimbrites, fall deposits and palaeosols for which there is no obvious correlation from gorge to gorge. This would suggest that the lower units are not laterally continuous on a hundred-meter scale. There are two possible scenarios that satisfy this observation: (1) the lower pyroclastic units filled older drainages and [the flow deposits] were valley-confined thus limited in lateral extent. The upper ignimbrite rests on a flat surface, and so might have been emplaced once these palaeo-drainages were filled by the lower units. (2) That all of the pyroclastic units were deposited on a relatively flat surface but with a limited lateral extent, forming a complex of overlapping 'tongues'. In this circumstance, the overriding O'Itu Woshe ignimbrite would also represent a larger, more sheet-like flow.

The relationship between Jidduu and Chopa gorges (shown in section B' to B" of Fig-

ure 3.18), and the deposits of Gemedo shed light on the issue. The base of the O'itu Woshe ignimbrite outcrops at the same altitude in either gorge. In Jidduu gorge, the unit below is J10: a series of southward dipping, Gilbert-type delta foresets. Whilst unit C9, a reworked but very compositionally and structurally different unit, lies below the same surface in Chopa gorge. The juxtaposition of the two different units: C9 and J10 at the same altitude only 150 meters apart shows that there is either a fault or unconformable surface laterally separating the two, rather than a gradual syn-depositional lateral facies change. The high resolution LiDAR DEM shows no linear surface expression in the correct orientation that could be considered a fault, nor are there any streams or breaks in slope. These lower units are therefore more likely to be laterally separated by an unconformity. The unconformity must be steeply dipping so as not to be exposed in either gorge, suggesting it may be a palaeo-valley side. However, the lack of exposure means we must look elsewhere to be certain. In Gemedo, we see the same facies change directly exposed: from delta slope sediments, to fluvial and sub-aerial facies. Here, the sub-aerial and fluvial sediments fill drainages cut into the deltaic sediments and a palaeosol. This supports the notion that the sub-aerial pyroclastics of the SE flank fill drainages cut into lower sub-aqueous delta sediments, rather than having being emplaced on a flat surface as a series of tongues with limited lateral extents.

A geological history of Aluto's southern flank

From the stratigraphy of Aluto's southern flank we can reconstruct a geological history. This history is also graphically summarised in Figure 3.19:

1. Lake levels were higher than present day, allowing the formation of a prograding, Gilbert-type delta at an altitude of at least 1650m, depositing units J10 and G4. During this time, debris flows (perhaps PDCs or lahars) carrying pyroclastic material from Aluto were swept down the delta front as turbidity currents forming occasional beds of more angular pumice. The age of this delta is provided by charcoal found near its base, carbon dated to 5700 ± 110 yr BP (Le Turdu et al., 1999).

2. Lake levels began to drop and/or the delta continued to prograde, with alternating

sub-aerial and sub-aqueous facies deposits forming on top of the delta. This includes some ash and lapilli pumice fall layers, presumably from Aluto volcano.

3. Lake levels continue to drop, allowing the surface of the delta to develop a palaeosol.

4. Fluvial/wadi/lahar channels are cut into the delta succession.

5. These channels are filled by pyroclastic deposits from a series of eruptions from Aluto. There is a hiatus between eruptions long enough to develop palaeosols in the channel filling deposits. The lack of fluvial sediments in these channels suggests the climate was typically arid, although the presence of some lahar deposits suggests there might have been some intense rainfall capable of mobilising recently-erupted material. PDCs in this succession tend to be channel-restricted, evidenced by the lack of correlatable units between gorges at the same stratigraphic height.

6. Over multiple successive eruptions, these channels were filled providing a relatively flat surface over which the O'itu Woshe ignimbrite was deposited.

7. A drainage system from the Aluto catchment develops, cutting the modern gorges: Kalosanga, Chopa, Jidduu, Gemedo (and more) through the whole succession.

The nature of ignimbrites and ignimbrite-forming eruptions on Aluto's southern flank

The nature and architecture of the ignimbrites preserved on the southern flank of Aluto provide insights into eruptions that produced them, and the flows that deposited them. All of the ignimbrites found in the gorges can be classified as massive lapilli tuffs, this implies the lower depositing portion of the PDC had a high particle concentration able to suppress turbulence and the generation of sedimentary structures. The main features that differentiate deposits on the south flank are the ratio of clasts to matrix and grading patterns. The clast to matrix ratio in the deposit is the net result of a complex combination of features including total grain size distribution of the flow, distance from source, elutriation and responses of the flow to topography. Without exposure of the full flows, is impossible to determine the source of this variation in these particular deposits. The grading patterns

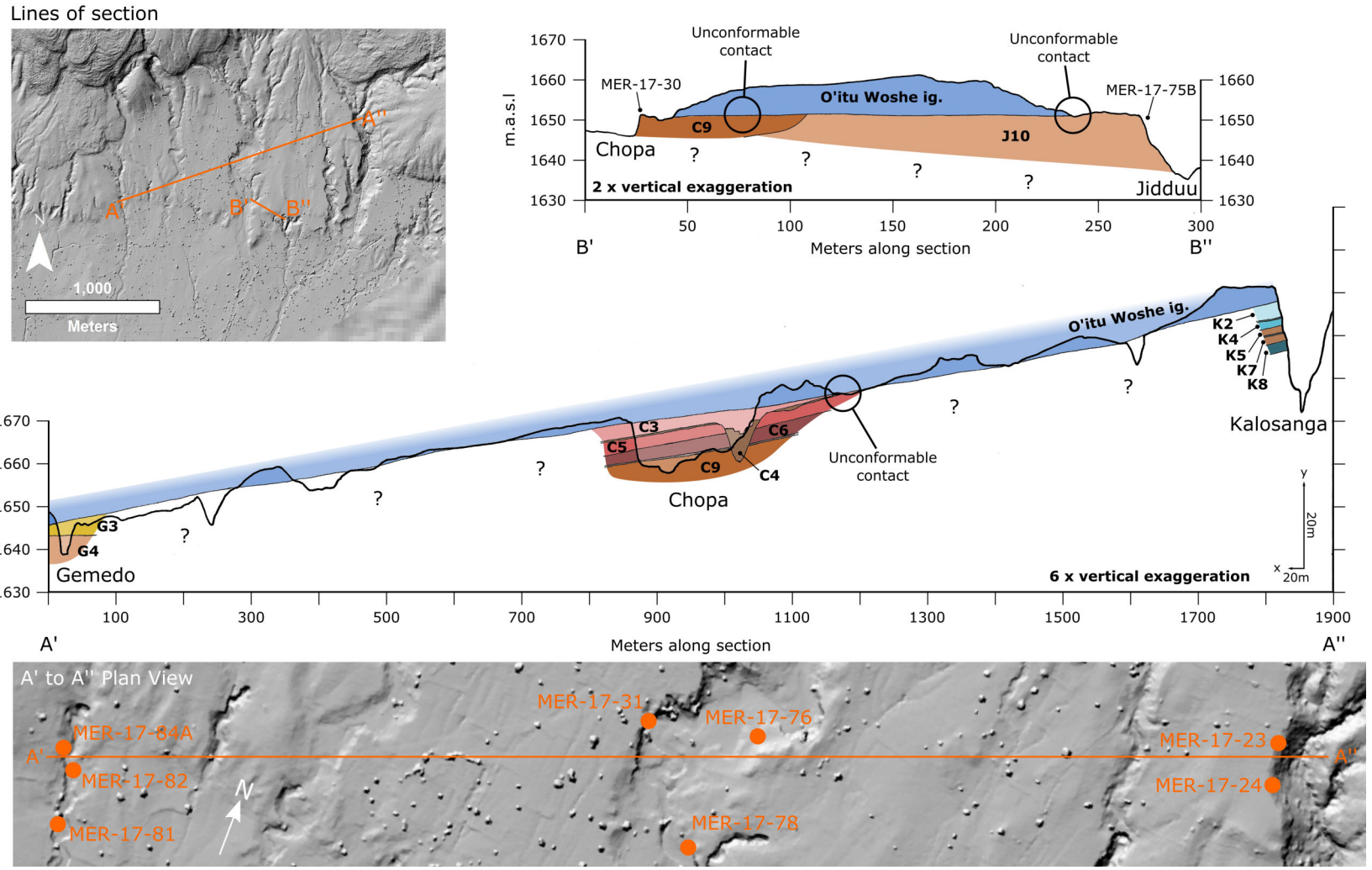

Figure 3.18: *Cross sections: A' to A", of the south flank of Aluto through the Kalosanga, Chopa and Gemedo gorges. and B' to B", through Chopa and Jidduu gorges. The bottom of the figure shows a plan view of section A' to A" including the localities and sections it is based upon.*

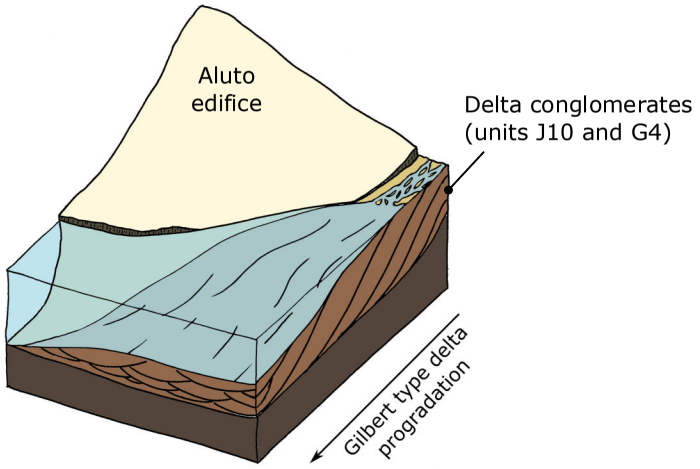

1. Lake levels were higher than present day, allowing the formation of a prograding, Gilbert-tpye delta at an altitude of at least 1650 m.a.s.l., depositing units J10 and G4. Age of deposit is around 5700 y BP.

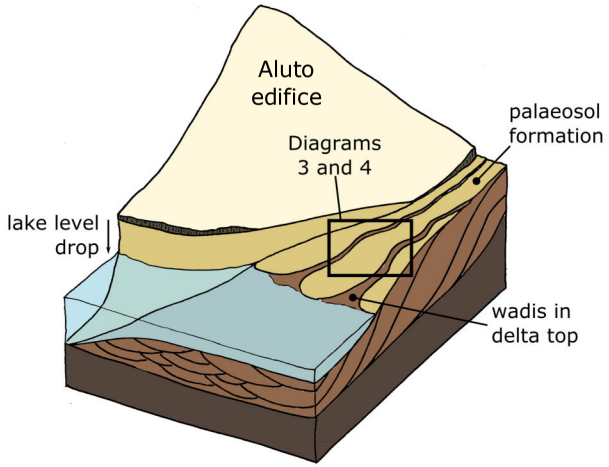

2. Lake levels drop and/or the delta progrades. Topset sequences of Gilbert type delta deposited. Top of delta exposed to atmosphere and development of palaeosol. Wadis are incised into delta top.

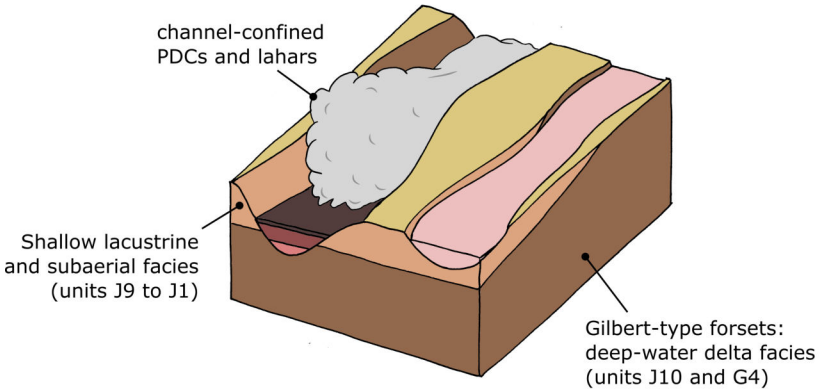

3. Wadis begin to fill with subaerial pyroclastic units and lahars. Each palaeo-wadi contains distinct sequences of channel constricted volcanoclastics.

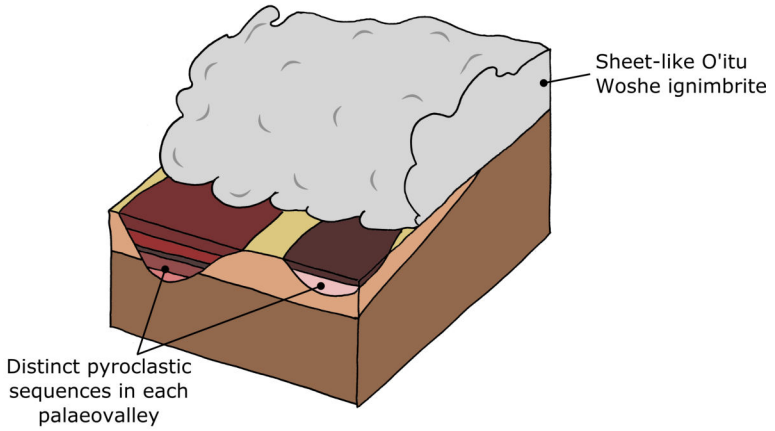

4. Once palaeo-wadis are full, a flat surface is produced. This surface is blanketed by the O'itu Woshe ignimbrite.

Figure 3.19: *Block diagrams showing the development of the south flank of Aluto. Not to scale.*

present in some of these ignimbrites (such as K2, C6, C5 and C1) may be explained by the waxing or waning, and accumulative or depletive nature of the flows (Branney and Kokelaar, 2002). Most flows with grading patterns in this succession indicate deposition during the waning phase of the current, apart from C6 which represents deposition during a waxing and then waning current. These gradual changes in component sizes throughout these deposits suggests they were progressively aggregated from a relatively sustained flow, though their thinness (all less than 4 m), shows that although sustained, they could have been deposited relatively rapidly. Albeit crude estimates of accumulation rates of massive lapilli tuff portions of the Bishop Tuff (Wilson and Hildreth, 1997) ($\geq$12.5 mm s^{-1}), would suggest a 4 m thick ignimbrite could accumulate in around 5 minutes. However, comparisons of accumulation rate between large ignimbrites associated with caldera collapse events and smaller, channel constricted PDCs such as those at Aluto are questionable.

PDCs with a high concentration of particles at the base are typically less mobile than those that are dilute (e.g Ogburn, 2012; Branney and Kokelaar, 2002). Though strict volumes for the ignimbrites exposed in the gorges cannot be ascertained due to lack of lateral exposure, unknown source vent location and lack of distal deposit preservation (likely to be due to flow into the palaeolake), these ignimbrites (with the possible exception of the O'itu Woshe ignimbrite) are clearly relatively small in terms of total volume. They are restricted to individual palaeo-channels and the thickest deposits are around 4 m. Assuming the palaeo-gorges were similar to present day Chopa, one of the widest gorges in the area at 200 m, and the flows reached 4 km from source (the distance between the most distal ignimbrite outcrop and the line of most probable source-vents), a 4 m thick deposit is on the order of 0.003 km^3; similar to many Montserrat block and ash flows (Ogburn, 2012; Barclay et al., 2006). The relatively small volume and probable lower mobility of these PDCs may explain why they are typically valley-confined. However, there is no record of the dilute, typically more mobile upper portion of the flows; they are likely to have deposited 'downstream' and possibly over the sides of the gorges. If they deposited further downstream, they may form small ash rich beds in the lake, if they deposited over the sides of the palaeo-channels, they have a very low preservation potential. The more mobile, dilute upper portions of the flow may present a significant hazard, but the lack of

deposit makes this hard to quantify in any way other than by comparison with similar, better constrained flows elsewhere.

Owing to the similarity of the PDC deposits in terms of their architecture, location, composition and appearance, it is reasonable to assume the eruptions that produced them may have been similar in character. The heterolithologic lithic components, lack of large blocks of lava, and the ash and pumice rich nature of the ignimbrites suggests they are pumice-flows, rather than block and ash flows. This, and the presence of underlying fall deposits, indicates that these ignimbrites are sourced from column-collapse, rather than the collapse of unstable lava domes or flow fronts.

If eruption columns were produced, these eruptions must have been more intense than typical Hawaiian or strombolian eruptions which do not generate such features. The intensity of an eruption (mass eruption rate) as defined by Pyle (2015) is best established from the column height, which can be used to calculate the mass eruption rate (Sparks, 1997). If the eruption was not observed, the column height is typically deduced from isopach and isopleth maps of the tephra fall deposits (Pyle, 1989). Ignimbrites K2 and C6 both have thin (cm scale) underlying ash to small lapilli fall deposits, without an intermediate palaeosol, suggesting the fall deposits represent buoyant column phases of the same, ignimbrite-forming eruptions. Unfortunately there is insufficient exposure to generate isopach and isopleth maps of these deposits, preventing rigorous assessment of the column-height. However, they can be compared to those from better constrained deposits to crudely bracket a likely column height and eruption intensity. The source vents for the eruptions that produce the PDCs and related fall deposits on the south flank of Aluto are most probably located on the ridge leading to the summit, between 3 and 4 km uphill from the gorges on the south flank. The thickness of the K3 coarse ash fall deposit preserved under ignimbrite K2 is 3 cm, and fall deposits C8 and C7, under ignimbrite C6, are each 2cm thick. Therefore, assuming there was an isotropic wind field (where $'distance\ from\ vent' = \sqrt{A}$), the 3 cm isopach for this eruption is at a $\sqrt{A}$ of around 3 to 4 km. We can compare this to the same parameter in a range of better constrained eruptions. For the 1959 eruption of Kilauea Iki, a tall hawaiian lava-fountaining eruption,

the 3 cm isopach was at a $\sqrt{A}$ of 0.9km (Klawonn et al., 2014), suggesting the eruption intensity, and thus column height, was greater at Aluto. On the other hand, Aluto's eruption intensities were clearly lower than the wind-still plinian Rungwe pumice eruption, where the 3 cm isopach lies at a $\sqrt{A}$ of >100 km (Fontijn et al., 2011), and smaller still than the sub-plinian phases of the 2011 eruption of Puyehue-Cordón Caulle (where the 3 cm isopachs are at a $\sqrt{A}$ of 27 km and 40 km respectively) (Pistolesi et al., 2015). The isopachs bear most resemblance to those describing the fall deposits from the 26^{th} September 1997 vulcanian explosion of Soufriere Hills volcano, Montserrat. Here plumes reached around 3 km above sea level and the 3 cm isopach could be found at a distance of around $\sqrt{A}$ 3 km (Bonadonna et al., 2002). There is significant uncertainty in comparing fall deposits from these distinct eruptions, especially considering there is no knowledge of the wind field during the eruptions at Aluto, but they do provide an initial loose calibration for the likely eruption intensities.

Lahars on Aluto's southern flank

Ignimbrites are not the only form of volcanic mass-flow found in the palaeo-gorge successions on Aluto's southern flank. Water deposited flows of volcanic material are also present. The most significant of these is represented by Chopa gorge's C4, where lahar deposits fill and over-top palaeo-channels. Thin low-angle cross stratified hyperconcentrated flow deposits form the overbank facies which transform to coarse, diffusely cross stratified deposits in the channels. The presence of cross bedding suggests they represent relatively water-rich lahars ($>$ 40 vol % and $<$ 80 % water (Vallance and Iverson, 2015)) rather than debris flows. The matrix supported nature and presence of bubbles within the matrix implies they are not normal stream flows.

As previously discussed, the lack of normal fluvial sediments in these palaeo-channels suggest they were typically dry with occasional high-energy flow events, and so can be considered wadis. This is supported by the general trend of aridification since the mid-holocene ($\sim$ 5500 yr BP) inferred from stable isotopes and pollen in lake sediments (Lamb et al., 2004), and the lowering and separation of lakes in the Ziway-Shala lake basin recorded by

lake deposit architectures (Benvenuti et al., 2002a). This incidentally, matches the time-frame for the change from deltaic to sub-aerial facies on Aluto's southern flank (base of delta dated to $\sim$ 5700 yr BP). The lack of snow or ice capping the volcano and low lake levels suggests that intense rainfall is the most likely trigger of these lahars, as there are no sources of water for ingestion by a dry mass-flow, or by melting near the vent. In the present day climate of the Ethiopian rift valley, rain triggered lahars are conceivable, and likely to be seasonally controlled: 87 % of rain in Ziway precipitated during the spring and summer rainy seasons, and during these periods (known locally as *Belg* and *Kiremt* respectively), rainfall intensities regularly reach and sometimes exceed 40 - 50 mm h^{-1} (Fazzini et al., 2015). On Montserrat, by comparison, lahar activity was found to be strongly associated with 24 hr periods experiencing >40 mm of rain (Barclay et al., 2006). Lahars therefore, may present a hazard during the rainy seasons following a future eruption at Aluto.

3.3.5 Summary

Aluto's southern flank has, over the last 5700 years, recorded a period of delta advance into a palaeolake with a relatively higher water level than present-day lake Langano, followed by its transition to shallow-lacustrine and then sub-aerial facies. The delta was fed sediment by eruptions of Aluto volcano, sometimes this sediment has been significantly reworked, but primary flow deposits are also represented in this succession. Eruptions from Aluto continued throughout shallowing and surfacing of the delta, recorded primarily as ash and lapilli fall deposits.

Once exposed to the surface, the delta top was incised by channels which began to collect primary pyroclastic deposits and lahars from Aluto. Eruptions in this sector of the volcano probably produced short eruption columns, with coarse tephra dispersed over a limited area around the vent. These columns were unstable and often collapsed to produce pyroclastic density currents. These PDCs were low volume (producing deposits on the order of 0.003 km^3) and had a high clast concentration at the base. The flows were confined

to the channels incised into the exhumed delta, though the behaviour of the upper ash-rich (typically more mobile) portion of the flows is not recorded. Rain triggered lahars were often generated following these eruptions. The eruptions occurred in intervals, with periods between eruptions long-enough to develop palaeosols. After the drainages had been filled, a relatively flat surface was formed and the more voluminous, sheet-like O'Itu Woshe ignimbrite blanketed the succession.

3.4 The Kertefa Pumice Cone Complex (KPCC)

3.4.1 Introduction

Aluto's NW flank faces a large flat plain. Across the plain, around 7 km away from the vents on the NW flank, lies the town of Adami Tulu with (in 2007) a population of around 21,000 people (Central Statistics Agency -Government of Ethiopia and Minnesota Population Center - University of Minnesota, 2007). Many more people live in rural settlements closer to the volcano. This is in addition to the world's largest rose farm, which provides many jobs in the area (AfriFlora and Sher Ethiopia, 2017), and the main road, forming the main transport route along the rift valley. A cursory analysis of the LiDAR DEM of Aluto (Hutchison et al., 2014) reveals many volcanic craters and cones in the area, indicating this sector of the volcano has produced many eruptions in the past. The plain itself comprises fall deposits from Aluto (Fontijn et al., 2018), in addition to early to mid-holocene reworked pyroclastic lake sediments (Benvenuti and Martini, 2002). Past eruptions of Aluto have clearly affected this area, and so eruptions from this part of the volcano are of obvious interest when assessing the present-day volcanic hazards. Two large sections on the NW flank: Kertefa gorge and South Kertefa Wadi (Figure 3.20), record a series of eruptions sourced from this sector of the volcano. The following section aims to describe and interpret these eruptions, and discuss the implications this has for modern volcanic hazards at Aluto.

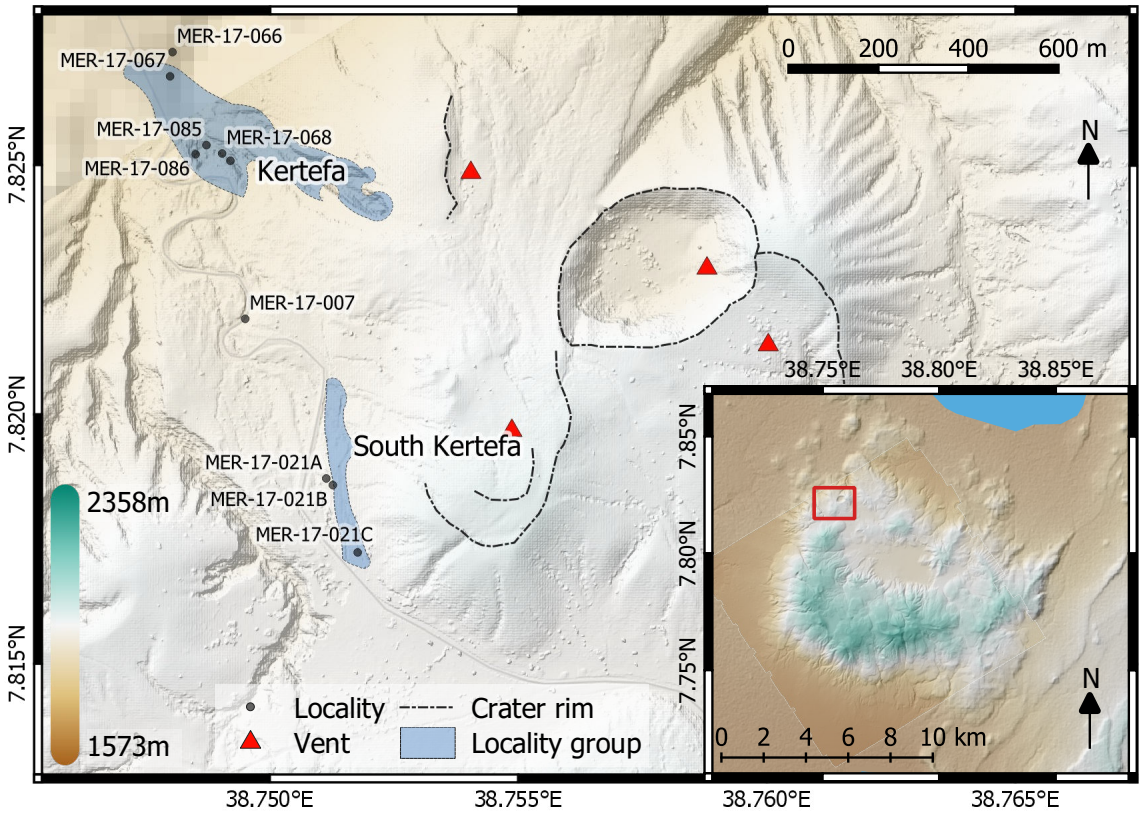

Figure 3.20: *Map showing the NW flank of Aluto including Kertefa Gorge and the South Kertefa Wadi. DEM source: (Hutchison et al., 2014).*

3.4.2 Stratigraphy of the KPCC

Kertefa Gorge

Kertefa gorge cuts into the outer NW flank of Aluto, a few meters to the north of the main road into the caldera (Figure 3.20). The gorge is orientated NW/SE at 140° and cuts deeply into the flank of the volcano revealing a series of pyroclastic units sourced from multiple eruptions in the area. The gorge contains the best-exposed section through a pumice cone sequence observed yet at Aluto with increasingly distal deposits from the pumice cone exposed from SE to NW along the gorge. The term pumice *cone* here is not entirely appropriate as the sequence comprises multiple source vents with fissure and cone like morphologies, as such, this NW pumice 'cone' sequence shall be henceforth referred to as the Kertefa Pumice Cone Complex (KPCC). The gorge also records a series of ignimbrite forming eruptions prior to the development of the KPCC and a fall deposit from the later 'Qup' eruption of Fontijn et al. (2018). The overall stratigraphy of Kertefa gorge is presented in Figure 3.24. The eruption units are described in detail in the following section.

The stratigraphically lowest units exposed in Kertefa are a series of very similar massive lapilli tuffs (K14 to K7). They vary in thickness from a few tens of centimeters (K12 and K13), to around 1.5 m (K11). All units have thin, red, indurated tops. The deposits are matrix supported and ash rich, generally lithic poor but occasionally contain decimetre scale lenses with higher lithic concentrations. Most lithics are small and lithologically varied, with chips of dense obsidian, oxidised volcanics and siliciclastics. Some units are massive but most show grading patterns, units K11 and K12 both grade inversely from bottom to middle and then normally from middle to top. Other units display normal or inverse grading. This feature tends to vary from exposure to exposure.

The base of unit K18 at MER-17-85A has a region at its base rich in white ashy material which might represent ash-fall reworked into a PDC. Thin, discontinuous rust-red bands are present throughout the unit, and often, but don't always, mark changes in componentry of the deposit. Unfortunately they weren't accessible and it isn't clear to what depth they penetrate the exposure, which may indicate whether or not they are palaeosols. They

aren't present in other localities and so are instead thought to be produced by localised, recent water flow. It's conceivable they represent high-stand water flow during times when the gorge floor was higher than its present day level. The correlation with changes in componentry may be due to the variability in permeability the components elicit.

Above this is unit K5 (Figure 3.21); a unit that transforms from a lapilli to block sized fall deposit at the base to a massive lapilli tuff flow deposit at the top. The base consists of large, angular pumices forming a clast supported framework with very few small lithics. The fall deposit is normally graded and at around 1 m from the base, the pumices separate from one another and become supported by a fine ashy matrix. Progressing further up the unit, the size of the pumice lapilli continues to decrease. Around the boundary between the fall and flow units pumices are mixed in respect to their angularity, suggesting either mixing of the substrate material into the deposit or continued deposition of fall into the flow. Within the upper flow portion of unit K5, pumices are all moderately to well rounded. There are very few lithics but they are typically small chips of obsidian.

Unit K4 is the first, unequivocal pumice cone deposit within the succession. The unit comprises block-sized, clast supported, pumices and some smaller lithics. The lithic concentration is higher than most of the deposits in the gorge (estimated 5 modal %). Many of the pumices are fractured but whole, forming 'jigsaw' clasts, which show that there hasn't been significant movement of the deposit after initial deposition. The deposit is massive and thins quickly from one end of the gorge to the other. At the eastern end it is around 8 meters thick, 200 meters away at the western end, it has thinned to around 0.5 m. This would indicate a 3.75 % (or 2°) slope. The true dip of the slope is calculated assuming the dip direction is perpendicular to the alignment of vent 1 (at 175°), the section's azimuth is 140°, and the apparent slope angle (thinning rate of K4 in section) is 2°. This provides a true dip of only around 3.5°. This should certainly be considered a minimum as (1) the eastern end of the deposit is truncated by more pyroclastics and an obsidian lava flow and (2) the thicker eastern end of the section is 0.5 km from the vent, and so only represents the distal (often shallower (McGetchin et al., 1974)) portion of the cone-slope. In fact, when slope is calculated between each log within the gorge, the gradient can be seen to increase

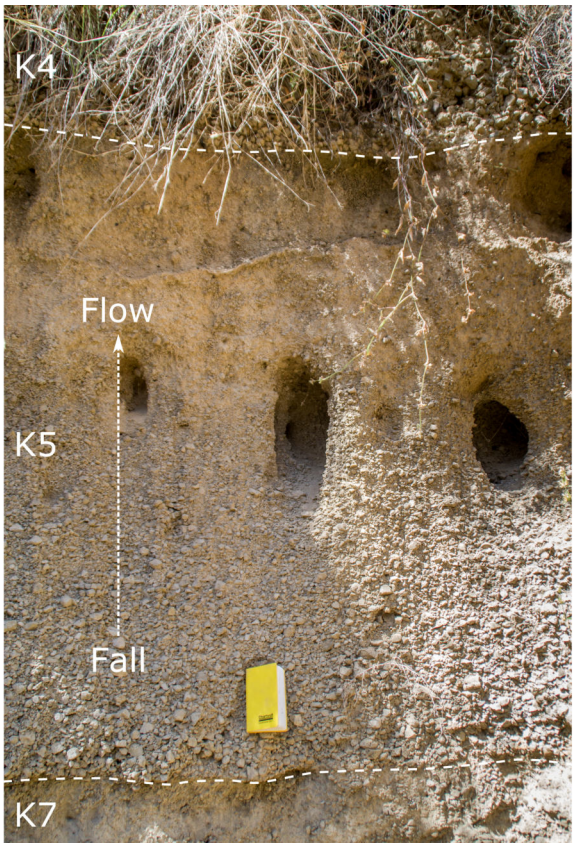

Figure 3.21: *Photo of unit K5 at MER-17-66, showing gradation from clast supported, coarse, angular fall deposit to matrix supported, rounded, ash rich flow. Notebook is 19 cm long.*

towards the vent, typical of fall deposits. The massive nature of the deposit and the lack of flow evidenced by the jigsaw pumices shows that the slope of the cone was less than the critical repose angle of the pumice breccia (typically 30° to 38° for scoria (McGetchin et al., 1974)); providing a maximum slope angle. This shows that the slope of the pumice rampart was shallower than repose, somewhere between 3.5° and 30°.

The colouration of the pumices in this deposit is particularly noticeable. Colour varies within the deposit both laterally and vertically (Figure 3.22). Vertically, at the eastern end of the gorge, it is grey at the base, then yellow, pink, then yellow returning to grey at the top. Laterally, this three-colour variation reduces to grey and yellow and then to just grey moving from east to west along the valley away from the vent. The grain size follows this sympathetically, with the smallest pumices being grey, the largest being pink and the medium sized pumices being yellow. The bulk colour of the deposit reflects the abundance of each grain size. The colouration of the deposit is sourced from the colour of individual pumices, rather than colour variations crossing individual clasts. The pumice colour is not superficial; when broken-open it permeates the entire clast. This suggests the colouration is not due to percolation of fluids into the deposit and precipitation of minerals onto clast-surfaces after deposition.

Above the pumice cone fall deposit is unit K3. The lower portion of K3 is a diffusely bedded lapilli tuff with a moderately high concentration of moderately to well rounded pumice lapilli in a fine ashy matrix. Further up this unit, the concentration and size of pumice lapilli reduces significantly until the deposit is almost completely ash (Figure 3.23). The deposit appears very lithic poor and the diffuse bedding in K3 suggests that the base of the PDC was dilute enough not to entirely suppress turbulence. There is no palaeosol between K3 and K4, and where the lapilli rich facies of K3 is in contact with K4, the contact appears gradational, suggesting they were erupted sequentially during the same eruption in a transition between convecting and collapsing column phases. In other places only the upper, finer grained dxsT to xsT facies is present (Figure 3.23A and B), here the contact between the pumice cone fall (K4) and ignimbrite (K3) is sharp. This would suggest that (1) the lower, mLT facies of K3 was not deposited everywhere, perhaps

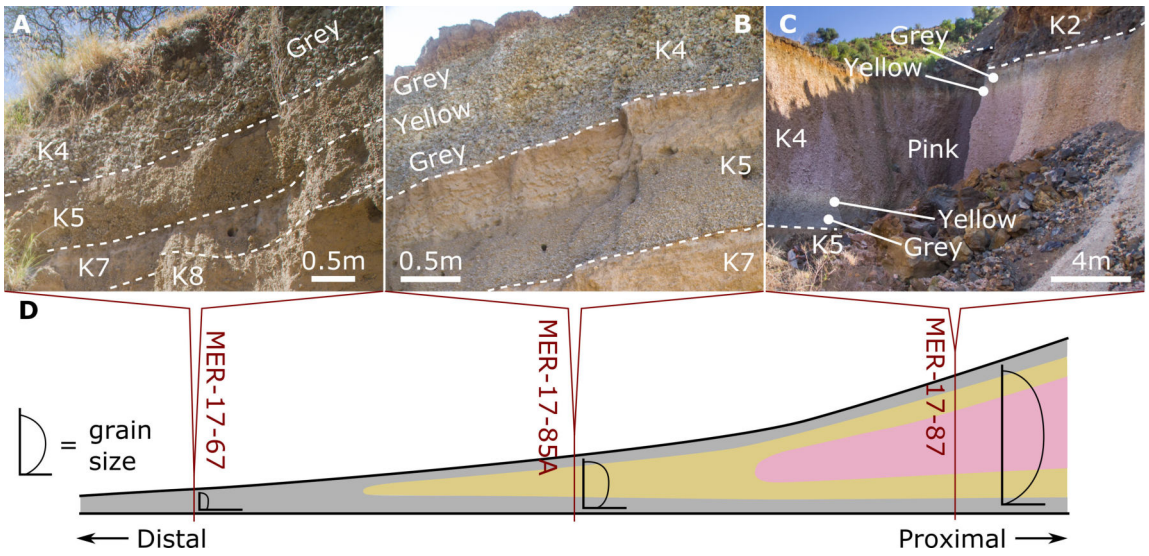

Figure 3.22: *(A) Photo of K4 at MER-17-67, showing the thickness of the deposit is grey. (B) Photo of K4 at MER-17-85A, showing grey pumices at the top and bottom, with yellow pumices in the centre. (C) Photo of K4 at MER-17-87, showing the full three colour variation of the pumices in the deposit. (D) Schematic representation of colour and grainsize variation within unit K4 and the relative position of photos A, B and C (not to scale).*

only in topographic lows and (2) that there was a period of erosive (non-depositional) flow between the deposition of the mLT and xsT of K3. The evidence of this erosive period is further supported by the deposition of the finer grained facies directly onto *pink* pumice. As discussed previously, the top of unit K4 consists of yellow then grey pumice, both of which must have been removed to allow contact between the pink pumice of K4 and unit K3. The ignimbrites between unit K1 and K4 at the western end of the gorge (MER-17-66) are tentatively correlated with K3 as they fit stratigraphically, follow the same normal grading pattern and reducing clast concentration, in addition to the lack of palaeosol separating them from K4. The contact between K4 and K3 is high up the south western wall of the gorge but much lower on the north eastern wall, implying that the palaeosurface here was dipping steeply to the north. The K3 ignimbrites are therefore most likely to have been sourced from a vent south of the present day gorge (palaeo-uphill).

The dbLT and xsT facies of K3 are truncated by obsidian lava flow K2. From the 2 m LiDAR DEM of Hutchison et al. (2014), satellite imagery and field photos, the extent of K2 can be mapped (Figure 3.29). Kertefa gorge is the most distal outcrop of K2 and so only

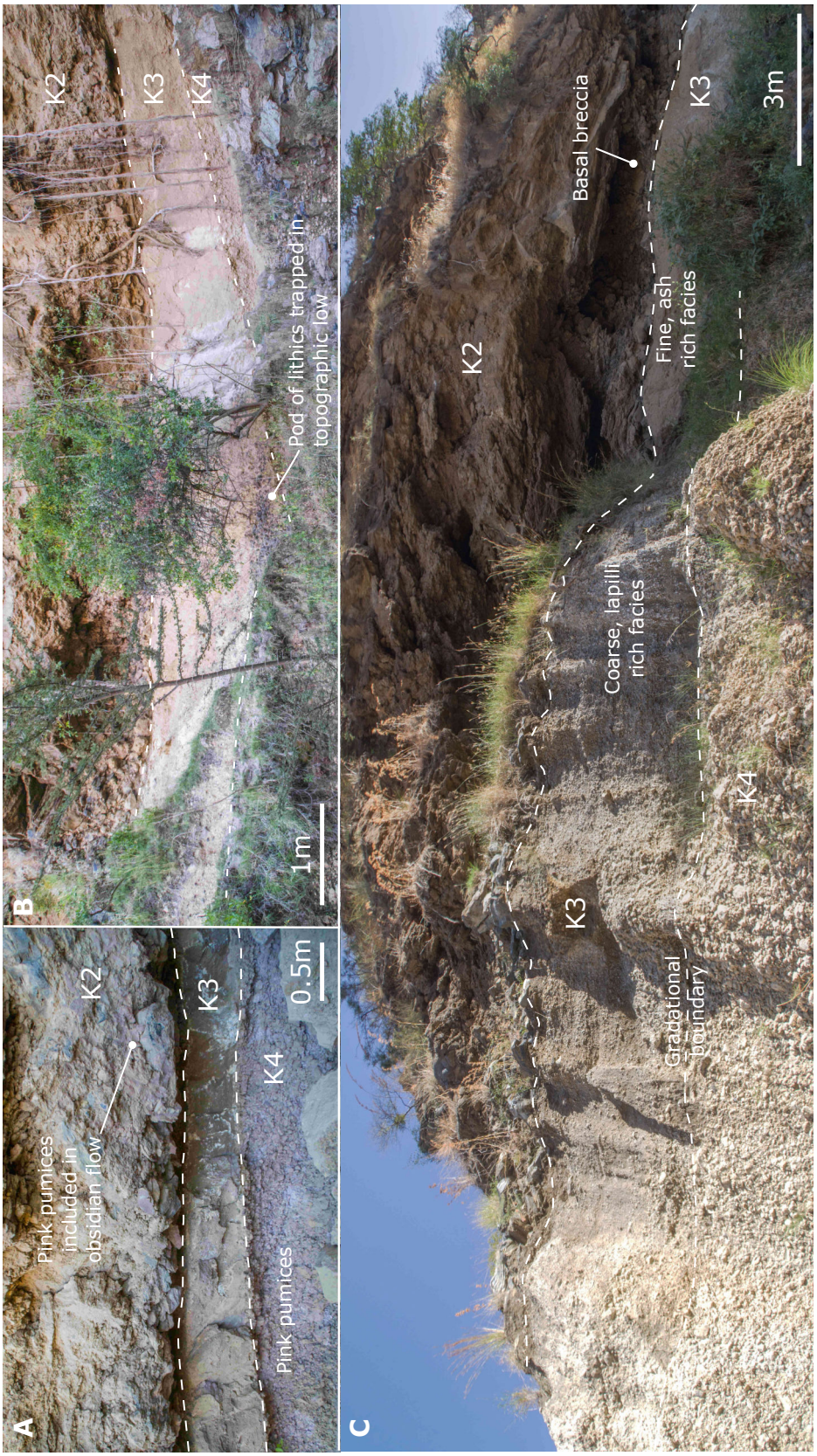

Figure 3.23: *(A) Photo at MER-17-85B showing the fine grained facies of K3 lying on top of the pink pumice of K4, implying erosion through the yellow and grey portions before deposition of K3. Pink pumices included in base of obsidian flow K4 show that coulee has flowed over bare exposures of K4. (B) Fine grained facies of K3 lying on pink pumice of K4 at MER-17-85B, here a pod of lithics from the K3 PDC has been trapped in a topographic low. (C) Panorama of MER-17-86, showing the field relationships of units K4 to K2. Note the gradational boundary between K4 and K3. K3 can be seen to become finer grained with height.*

the very tip of the flow is present at the top of the gorge. The maximum thickness of the flow at this point is around 10 m. The flow is blocky and microvesicular, with rare glassy enclaves and deformed layers. Within the bottom meter or so, clasts of pink pumice are embedded, enveloped and sometimes plastically deformed into the flow, forming a coarse basal breccia presumably comprising 'upstream', loose pyroclastic material picked up by the advancing lava flow (Figure 3.23B). There is no evidence of any hiatus between the emplacement of the K2 lava flow and the underlying pumice cone deposits. Obsidian lavas often occur after the cone building phase of pumice cone eruptions (Hutchison, 2015), suggesting K2 was emplaced during the final stages of the same eruption that produced the underlying pumice cone.

The upper-most unit exposed in the gorge is K1, a 0.5 m thick, lithic-poor pumice fall deposit. It is only exposed at MER-17-66 meaning the thinning direction or rate can't be assessed. It is therefore unclear from which vent it is sourced, though its position in stratigraphy suggests it is relatively recent. The top 10 cm has been soilified, but it is thought to be the 'Qup' pumice lapilli fall unit described in Fontijn et al. (2018), dated at 7.3 Ka (McNamara et al., 2018).

South Kertefa Wadi

To the SE of Kertefa gorge, further up Aluto's edifice is a narrow wadi that cuts into the side of the South Kertefa pumice cone (Figure 3.20). The wadi curves around the base of the pumice cone, roughly parallel with its contours. The wadi exposes a series of pyroclastic units (SK10 to SK1), most of which form the bottom slopes of the adjacent, south Kertefa pumice cone. Stratigraphic logs of South Kertefa Wadi are presented in Figure 3.27, and descriptions of the eruption units are provided below.

The bottom of the wadi in the NW exposes SK10, a nearly clast supported, massive, lithic rich mLT ignimbrite with moderately rounded pumices. The matrix contains fine ash and the lithics are very heterolithologic. The upper surface of the deposit undulates and there is no clear palaeosol. Above this is SK9 to SK8, a graded, massive ash rich

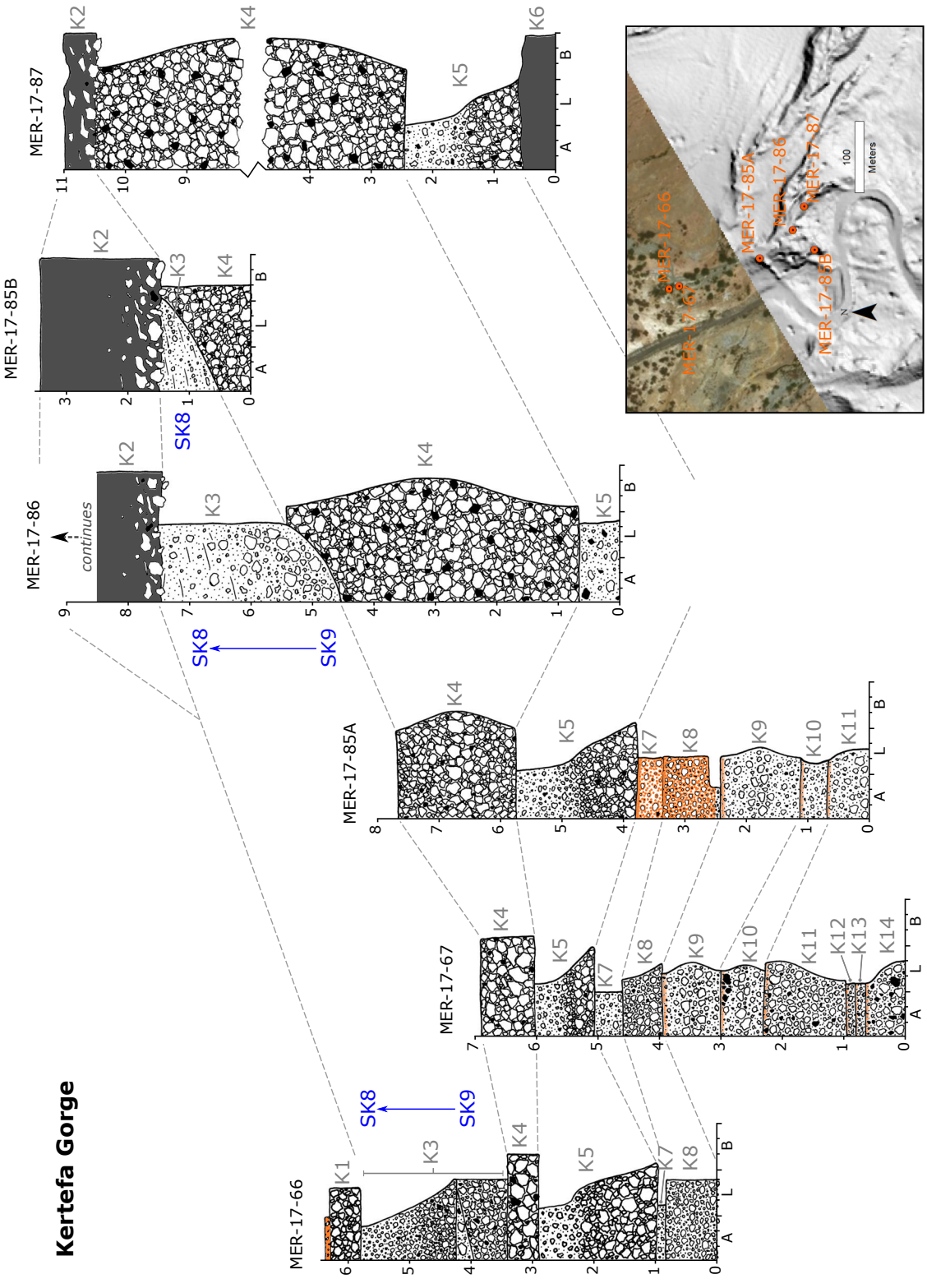

Figure 3.24: *Fence diagram showing the stratigraphy of Kertefa gorge. Heights are provided in meters and are relative to the base of the exposure. Blue text refers to correlated units in the south Kertefa wadi sections.*

ignimbrite sequence. mLT facies dominate near the base of SK9, with lapilli sized clasts of rounded pumice and smaller, angular lithics are present and supported in the matrix. SK8 is characterised by the absence of larger lapilli with very few, well rounded small pumices and no visible lithics in a primarily ashy ignimbrite. The boundary between the two is unclear, most probably a result of the small, similar grain size. A boundary may be marked by a zone with pockets of whiter ash suspended in the browner ash which which forms the majority of this deposit. These white pockets are interpreted as sods of co-ignimbrite ash associated with SK9 worked into the SK8 ignimbrite. The brown colouration of the deposit is more intense towards the top of the unit, and is interpreted as soilification. The colouration of the white ash, and lack of soilification, may be due to a finer co-ignimbrite ash grain size, though this is speculative. These field relationships are best observed at MER-17-21A, shown in Figure 3.25.

Units SK7 to SK4 lie above this palaeosol at MER-17-21A (Figure 3.25B and C). SK7 is an ephemerally preserved, thin ignimbrite with a fine ashy matrix and lapilli sized rounded pumices. This is overlain by two very similar, normally graded pumice units. The pumices are moderately rounded and have a small amount of ashy matrix. They are clast supported and there are small bubbles in the matrix, suggesting they represent lahars. Unit SK4 is an angular, well sorted, clast supported fall deposit. In places, it is massive, with slight inverse grading (Figure 3.25A), and in others the bottom half is diffusely bedded and is less well sorted (Figure 3.25B and C). This unit is thought to be the 'Qup' fall deposit (Fontijn, pers. comm), described by Fontijn et al. (2018), which often displays rhythmic bedding, and is relatively lithic poor. Qup was considered to have been erupted from the nearby vent 0 in the NW of the caldera (Fontijn et al., 2018) (Figure 3.29). However, this seems unlikely, as the Qup deposits at south Kertefa wadi lie higher in the stratigraphy that the rest of the KPCC deposits, which themselves onlap the pumice cone produced by vent 0. The KPCC deposits therefore post-date vent 0, precluding it from being the source of Qup. The thickness of SK4 is highly variable along the Wadi. The deposit here is reported as 280 cm thick by Fontijn et al. (2018), but at MER-17-21A it is thinned by erosion and soilification. At MER-17-21B, Qup is thinned by erosion prior to the deposition of the following flow units.

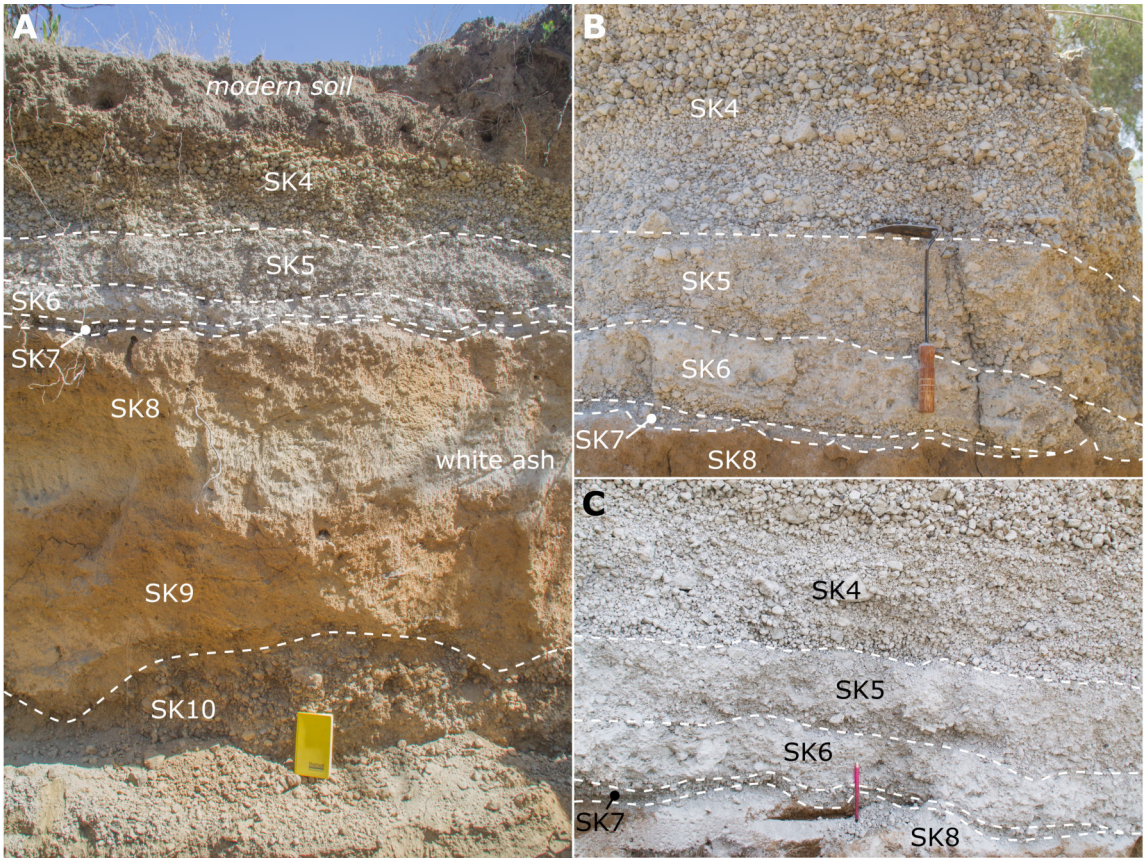

Figure 3.25: *(A) Photograph of MER-17-21A showing units SK10 to SK4. The notebook is 19 cm in length. (B) Photo of units SK8 to SK4, showing pinching out of SK7. Tool is 30 cm in length. (C) Photo of units SK8 to SK4. Pencil is 12 cm in length.*

The units above SK4 comprise reworked pyroclastic material in the form of lahars and modern soil, the relationships of which can be seen in 3.26. SK3 is a bedded hyperconcentrated flow deposit with a granule to ash grade matrix. It is matrix supported and the pumices are moderately rounded. There are very few lithics. This probably represents re-mobilised loose material from the Qup eruption. SK3, and the units below down to SK8, are cut by channels that are preserved along the length of the wadi wall. They are filled with hyperconcentrated flow deposits comprising granule grade, cm scale cross beds of rounded pumice and rare lithics. Nearer the tops of the channels beds become planar, and there are thin, massive, ashy beds preserved which may be primary fall deposits or finer material depositing through still water. The top of SK2 is buried by SK1, a highly soilified, ash rich, massive ignimbrite. The lack of palaeosol and the topographic immatu-

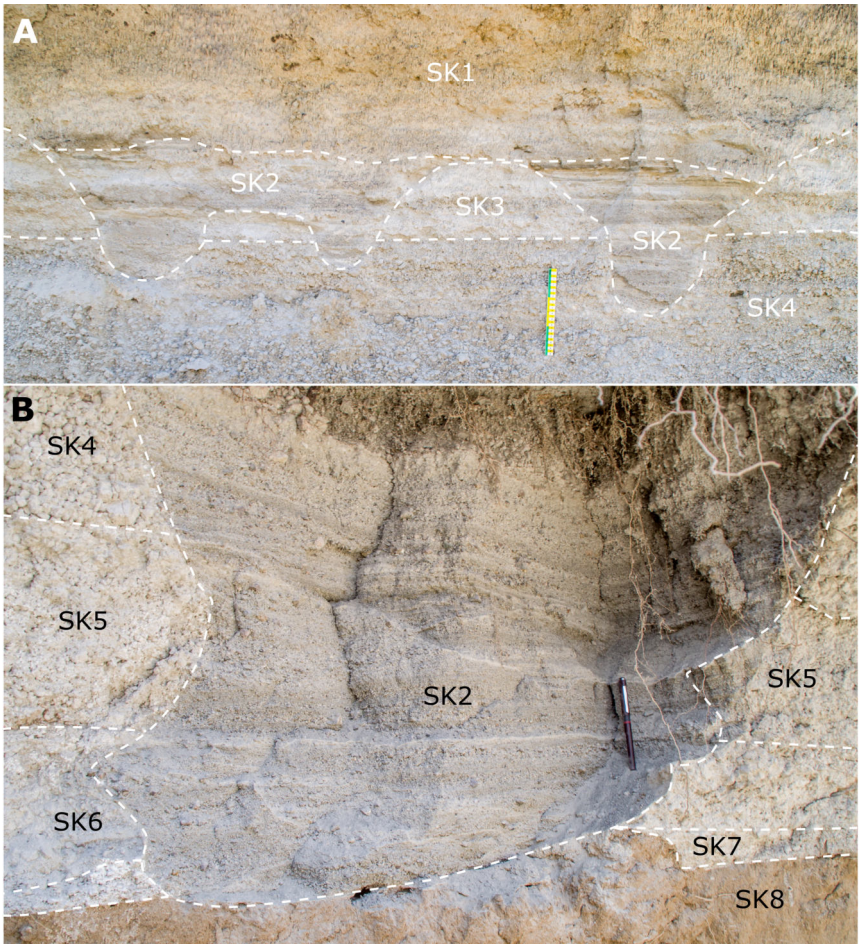

Figure 3.26: *(A) Photograph of MER-17-21B showing units SK4 to SK1. The scale is 30 cm. (B) Photo of units SK8 to SK2. Pen is 15 cm in length. Both show the field relationships of these units, with SK2 existing as a channel filling lahar that cuts into the loose pyroclastics of the Qup eruption.*

rity of the palaeo-surface (ie. presence of sharp edges of channels etc.) between SK2 and SK1, suggests that there wasn't a significant time gap between the deposition of SK2 and the emplacement of SK1.

3.4.3 Discussion

The NW flank of Aluto has recorded a series of eruptions which cumulatively form the KPCC. The best exposed eruption in this sequence is that which produced units K5 to K2 and SK9 to SK8, which I name the *Diima* eruption; the word *Diima* meaning pink/red in

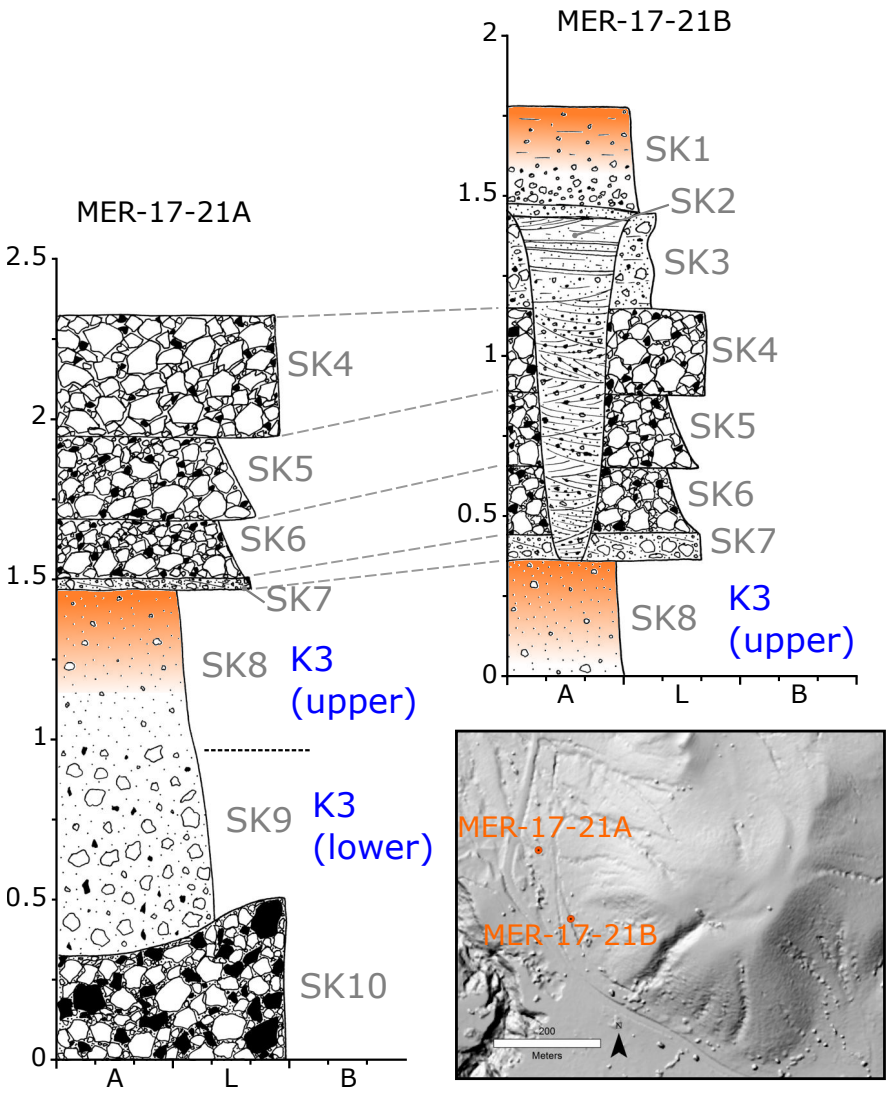

Figure 3.27: *Fence diagram showing the stratigraphic relationships in the South Kertefa Wadi. Heights are in meters relative to the base of the deposit. Blue text refers to correlated units in the Kertefa gorge sections.*

Oromo, referring to the distinctive colour of the larger proximal pumices. There are three main eruptive phases which constitute the KPCC: Firstly are the Pre-Diima eruptions represented by the ignimbrites K14 to K6. Following this is the Diima eruption itself, represented by units K5 to K2 and SK10 to SK8. This is followed by the Qup eruption, which deposited units K1 and SK7 to SK1. The following section provides a detailed account of each of these phases.

The Pre-Diima Eruptions

The pre-Diima deposits are challenging to interpret, as it is unclear which of the indurated, orange-stained layers are true palaeosols and which are simply the result of more recent fluid flow. All of the deposits are very similar: occasionally graded massive lapilli tuffs around 0.5 m to 1.5 m thick. Their similarity in form implies that they might be generated by similar mechanisms, and in many ways resemble the ignimbrites seen on the southern flank of Aluto. Their massive nature shows they were deposited from concentrated flows, and the variable lithologies of the lithic components and lack of abundant lava blocks suggests they are sourced from a collapsing eruption column rather than a collapsing lava flow or dome front. Their source is unclear, but is presumably relatively local. It is quite possible their source were vents -1 and/or 0 (Figure 3.29), now partially buried by the later eruptions at the KPCC. The K6 obsidian flow, only exposed at the eastern end of the valley might have been sourced from the same vent, and it is possible ignimbrites K14 to K7 represent an explosive phase of this eruption in a similar fashion to the K3 ignimbrite during the Diima eruption. However, the lack of exposure makes this challenging to determine conclusively.

The Diima Eruption

To properly discuss the eruptive sequence of the Diima Eruption, I first need to establish the relative age of each geomorphological feature produced at each stage of the KPCC's development. Analysis of the DEM around the Kertefa field sites reveals multiple vents

(Figure 3.29). Do they represent multiple stages of the same eruptive episode, or were they formed during distinct eruptions? The deposits exposed in Kertefa gorge, when taken in the context of the DEM, provide some clues.

As discussed earlier, the extent of the K2 obsidian flow can be mapped from the LiDAR DEM in combination with satellite imagery and field photos. As these flows are gravity-driven, they can be traced uphill to their source. This reveals that K2 originates from a southerly vent, adjacent to and above the South Kertefa Wadi section (vent 3 in Figure 3.29). Further downstream to the north, the flow diverges into two major tongues around a relict crater rampart (vent 1 in Figure 3.29). This shows that the crater rampart developed before the lava flow was emplaced. The crater rampart itself is made of the pink pumice (unit K4) (Figure 3.28), showing that K4 is sourced from that vent. As discussed in section 3.4.2, the eruption of the pumice cone units K4 to K3 is relatively continuous and there is no evidence of a significant time gap between K3 and the emplacement of obsidian flow K2. This suggests they are produced during the same eruptive episode. Therefore, vents 1 and 3 from Figure 3.29 were active during the same eruption.

Vent 3 is defined by a small cone that sits atop vent 2 (Figure 3.29) and together form the South Kertefa pumice cone. However, it's uncertain whether they developed during the same eruptive episode. The portion of the cone associated with vent 2, is deeper incised by gullies than the small cone associated with vent 3. This could be interpreted as a significantly younger, less incised cone sitting atop a lower, eroded and gullied cone. However, the slope of the vent 3 cone is much shallower than the vent 2 cone; steeper slopes increase the flow velocity of water runoff and enhance gully incision (Valentin et al., 2005) meaning that the gullying may be a poor proxy for relative age in this instance where slope is inconsistent. Unfortunately, the South Kertefa Wadi section doesn't penetrate deep into the cone to provide a simple answer, but it does reveal the deposits of at least 2 eruptions defined by palaeosols. The most recent of these two eruptions represented by units SK7 to SK1 (Qup) was sourced from the NW of the caldera, indicated by isopach mapping of Fontijn et al. (2018). However, it is uncertain from which vent it was sourced. The lower units of the South Kertefa Wadi (SK10 to SK8) are all ignimbrites and are likely to be

sourced more locally, perhaps from the South Kertefa pumice cone. Do they pertain to the eruption of vent 2, 3 or both?

According to their position in the stratigraphy (just below the Qup deposits) units SK8 and 9 are most likely to be sourced from vent 2 or 3. These units are also very similar in character to K3 in Kertefa gorge (both lapilli-rich mLT grading into ash rich ignimbrites, and both beneath the K2 obsidian). This is commensurate with the probable southern source of ignimbrite K3 in Kertefa gorge, and so they are considered the same eruption units. This would imply that the locus of eruption moved from vent 1 (producing K4) southwards to vent 3 (producing SK8/9 and K3) during the course of a single eruption.

Considering the vent-opening sequence, the Diima eruption is interpreted to have occurred as follows, and is summarised graphically in Figure 3.30. The Diima eruption initiated in the north of the complex with the opening of the vent 1 fissure. The eruption produced a column of tephra, producing the lower fall-deposit K5, which then collapsed to generate a pyroclastic density current, depositing the upper K5 ignimbrite. This was followed by the ultraproximal deposition of the pink pumice rampart (K4) by pumice fall. Deposit K4 records a waxing and waning of the eruption column, with larger clasts reaching further from the vent during the medial stage of rampart development. As the eruption progressed, the locus of activity moved to the southern end of the fissure, developing the South Kertefa pumice cone from vent 2. As the eruption column waned and collapsed, K4 diffusely transformed with stratigraphic height into ignimbrites K3, SK8 and SK9. The Diima eruption was therefore sufficiently intense to generate an eruption column. This indicates that intensities greater than those typically seen during Hawaiian or strombolian eruptions, and the rampart might have been the product of column-edge deposition, the style invoked for other pumice cone deposits at Aluto (Clarke et al., 2019). The ignimbrites fill wide gullies cut into the K4 rampart and cone deposits, and it is likely that the gullies were formed by earlier more erosive phases of the same PDCs. The eruption ends after the extrusion of obsidian lava flow K2, which filled a continuous depression along the fissure to the north, as well as flowing through two breaches in the western wall of the pumice cone and rampart. The explosivity of the eruption that produced the obsidian lava flow

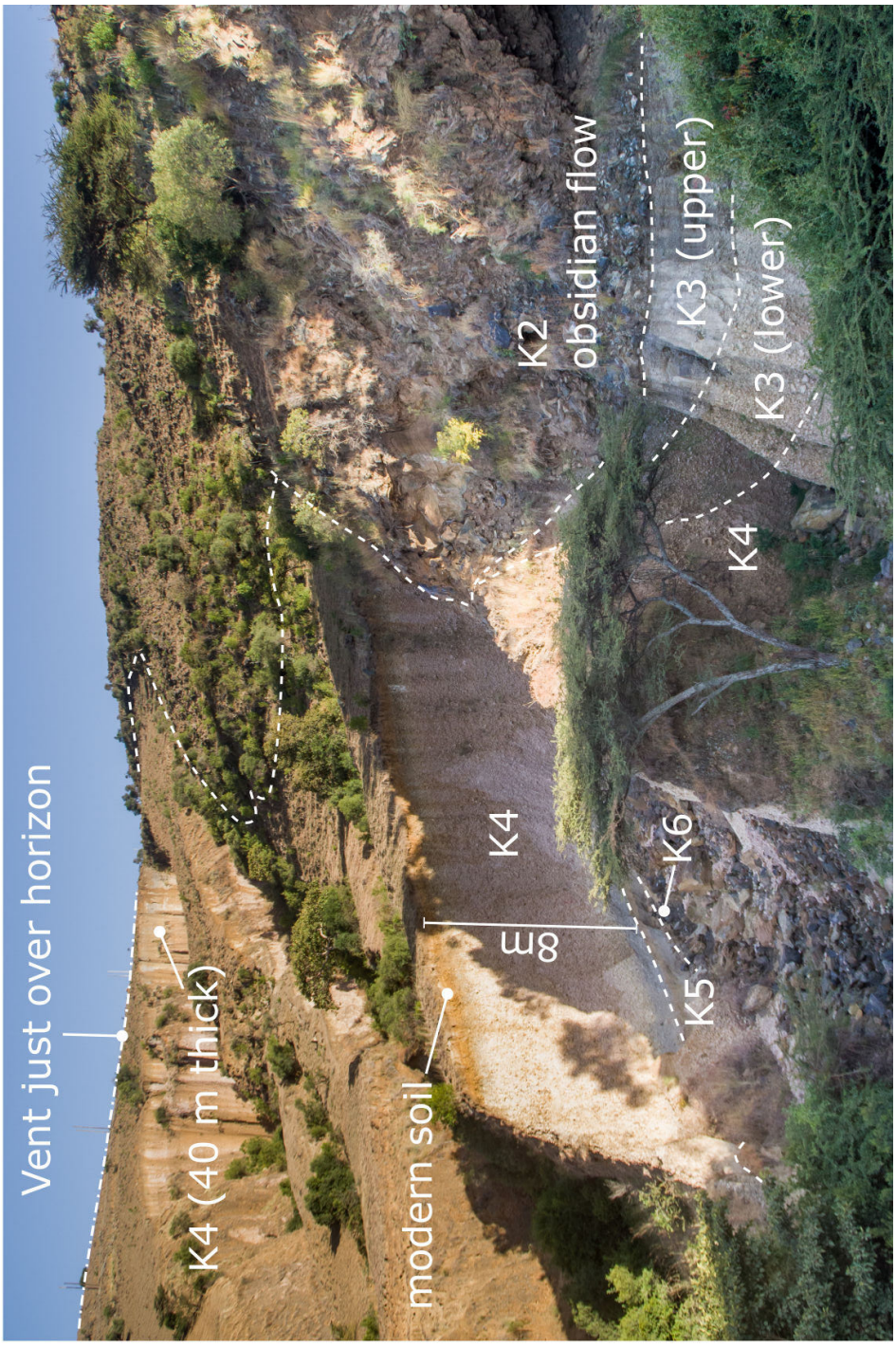

Figure 3.28: *Photo taken from southern shoulder of Kertefa gorge facing east. Showing field relationships of units. Note in particular pink colouration of material forming the rampart of vent 1 (top left), showing that this vent is the source of the pink K4 pumice cone unit.*

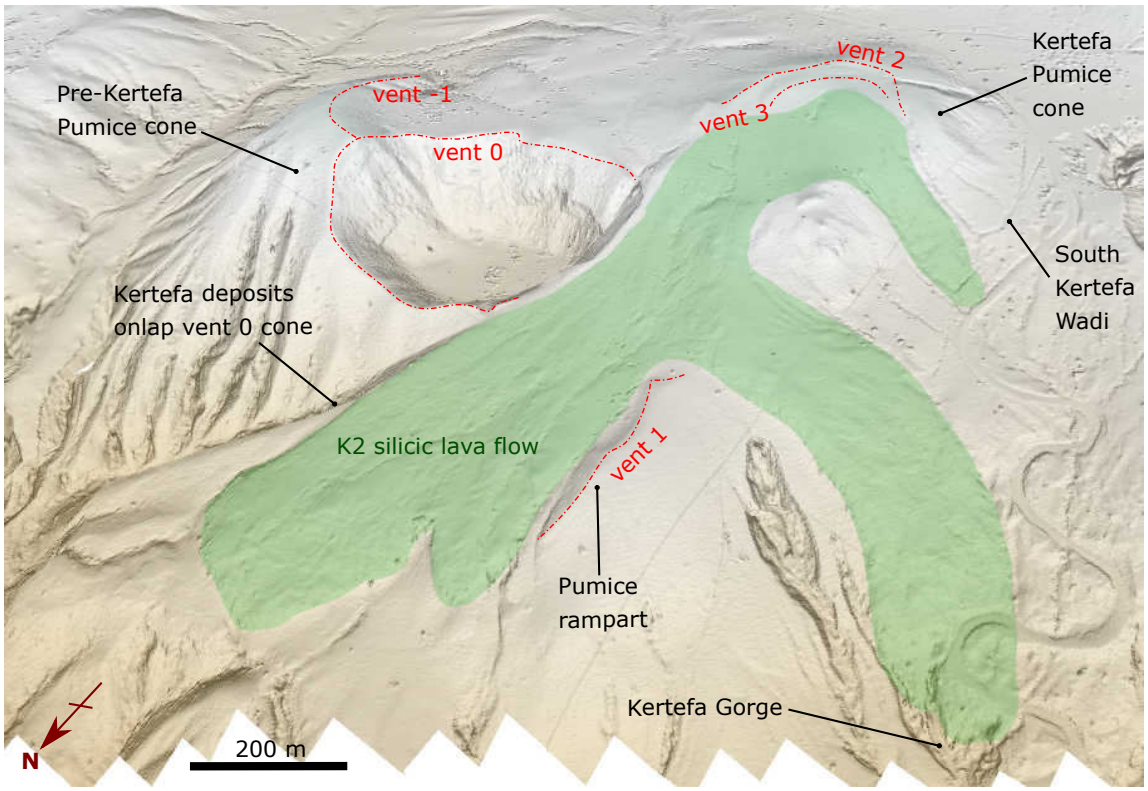

Figure 3.29: *1.5 × vertically exaggerated 3D view of the Kertefa pumice cone complex. Dotted and dashed lines show crater rims from different eruption phases at the complex, beginning at -1 and ending at 3. Vent 3 is the source of the silicic lava flow 'K2' marked in green. Using the 2m LiDAR DEM from Hutchison et al. (2014)*

is unknown. However, considering the syn-effusive/explosive eruptions that generated the Chaitén and Cordón Caulle rhyolite lava flows (Castro et al., 2014), it should certainly be considered plausible that similar explosive processes occurred at Aluto.

The structure of the KPCC is roughly linear, a feature common for vents at Aluto (Figure 3.31). The orientation of these lineaments varies across Aluto and can be broadly divided into two categories: those that mark the outline of an ellipse on a volcano scale, interpreted as the caldera rim (C and D in Figure 3.31) and those that follow a path roughly N/S to NNE/SSW, interpreted as faults controlled by the regional extensional stress field (A and B in Figure 3.31) (Hutchison, 2015). Vents along these fissures appear to develop a range of deposit morphologies, from ramparts to discrete cones. Such morphologies are common in basaltic fissure systems (eg. Laki (Thordarson and Self, 1993), La Réunion (Bonali et al., 2011), Etna (Corazzato and Tibaldi, 2006), Eldfell (Thorarinsson et al., 1973)). Fissure eruptions represent transport of magma to the surface via dykes with changes in the degree of flow localisation during their eruption. The evolution in the locus and degree of localisation during eruptions from basaltic fissures is thought to be primarily controlled by viscous instabilities generated from cooling of the conduit magma against the colder country-rock (Wylie et al., 1999).

The 'Qup' Eruption

The products of the Qup eruption (as defined by Fontijn et al. (2018)) were deposited after 7.3 Ka and are exposed in the upper stratigraphy of the NW quadrant of Aluto (Fig.5 in Fontijn et al. (2018)). On the NW flank, the Qup fall deposit can be seen in Kertefa Gorge as K1, and in South Kertefa Wadi as SK4. In South Kertefa Wadi, units SK7 to SK5 and SK3 to SK1 are exposed above and below the fall deposit, representing the proximal flow deposits of the same Qup eruption. The thin, dxsLT ignimbrite SK7 was deposited by a dilute PDC towards the beginning of the eruption. Material generated in the early stages of the eruption was then remobilised by heavy rainfall to produce lahars represented by units SK6 and SK5. Following this, fall unit SK4 was deposited from an unsteady eruption column, evidenced by decimeter scale rhythmic graded beds. This column eventually col-

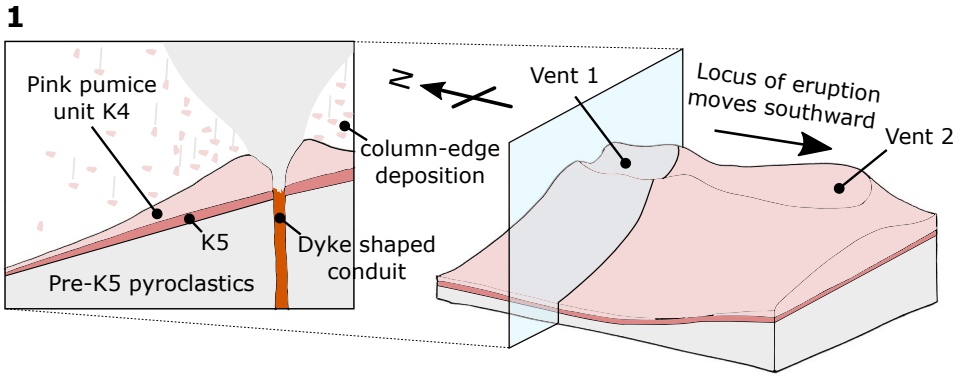

Violent strombolian to subplinian eruption produces pumice fall deposit K5. A perhaps slightly less intense phase then produces fall deposit K4 from column-edge deposition, forming a shallow-sloped pumice rampart. The eruption intensity waxes and then wanes, resulting in the inverse then normal grading of the K4 fall deposit. The origin of this unit can be traced from the N/S fissure, beggining at vent 1 in the north.

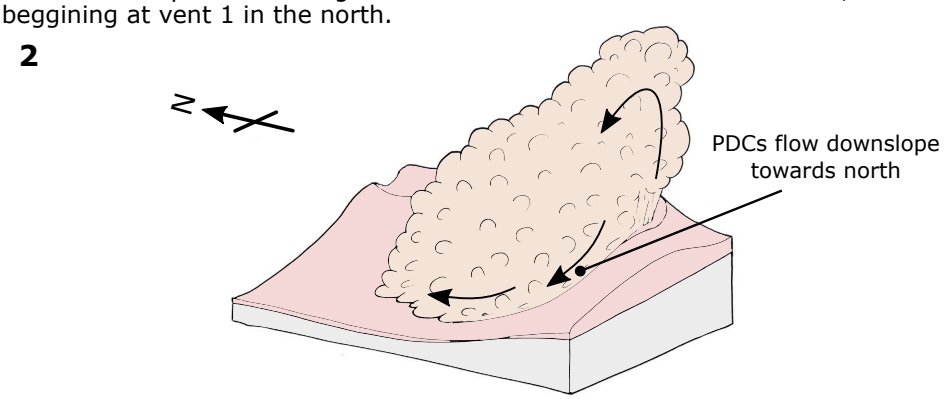

The eruption column wanes, eventually collapsing to produce PDCs. The architecture of the resulting K3 ignimbrite indicates they originate from the southern end of the N/S fissure at vent 2.

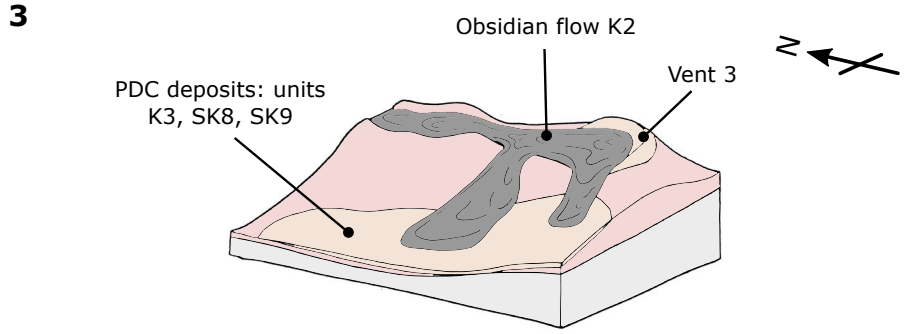

The eruption enters a more effusive phase, marked by the emplacement of obsidian lava flow K2 from vent 3. This may or may not be accompanied by explosive activity.

Figure 3.30: *Graphical summary of the development of the Kertefa pumice cone complex.*

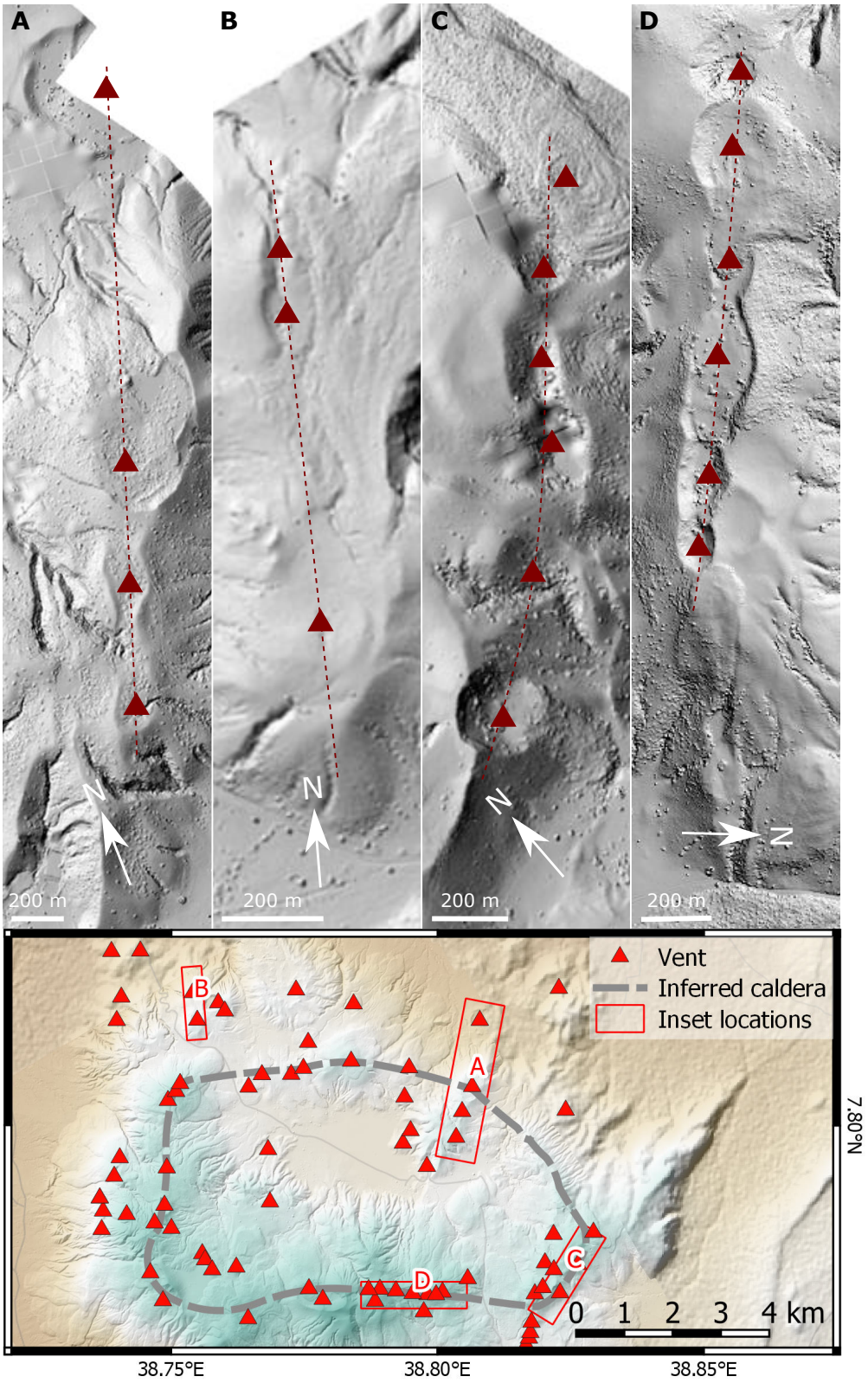

Figure 3.31: *LiDAR hillshade showing the vent alignment and pumice cone morphologies at Aluto. Note the combination of rampart-type and cone-type deposit morphologies, as well as the alignment along the inferred caldera margin (C and D), and other cross cutting linear structures (A and B). Red dashed lines mark the vent alignment, red triangles are placed in centre of craters. (A) NE of Aluto, (B) Kertefa Pumice cone complex, (C) SE caldera rim of Aluto, (D) Southern caldera rim of Aluto. Lower map indicates inset localities and the inferred caldera margin.*

lapsed, generating the ash rich, but high-basal concentration ignimbrite SK3. Shortly after this, but prior to the development of a soil, further lahars were triggered from the loose deposits of the Qup eruption. Channels were incised into the earlier Qup units and filled with hyperconcentrated flow deposits SK2. Thin, planar bedded ashy deposits at the top of these channels either represents further primary fall deposits or the deposition of finer grained refactory material through still water. After this, but prior to the development of a soil and the maturing of deposit topographies, a final PDC (SK1) was emplaced. The Qup eruption appears to have occurred during rainy conditions, initially producing unsteady, rhythmically bedded fall deposits with some occasional PDCs, but punctuated by periods of lahar generation, supplied by material from the ongoing eruption. The eruption ceased with the generation of a column-collapse PDC. An obsidian lava flow may or may not have been produced at the end of the eruption, to verify this, we would need to identify the Qup source vent.

3.4.4 Summary

Aluto's NW flank records a series of eruptions and provides one of the best exposures of a pumice cone forming eruption on Aluto. The eruptive history of the flank is dominated by the formation of the Kertefa Pumice cone complex; a fissure-fed pumice cone forming eruption that began with an intense teprha column and PDC forming phase which generated the pumice cone and rampart. Further PDCs breached the pumice cone and rampart in two places, which were later occupied by a silicic lava flow during the final stage of the eruption. This final stage of the eruption may or may not have been explosive. The sequence of this pumice cone forming eruption matches that of many others across Aluto's edifice, where a pumice cone formed from an intense but unstable eruption column, then breached by PDCs, then finally a silicic lava flow is generated filling the breach. The pre-Diima eruption deposits are poorly exposed and as a result, very little can be ascertained about the eruptions that formed them, other than they produced relatively small, concentrated PDCs generated by column collapse events, perhaps from one or more of the pre-Diima eruption vents shown in Figure 3.29. The flow deposits above

the Diima deposits exposed in South Kertefa Wadi are the only flow deposits associated with the Qup eruption described by Fontijn et al. (2018) to have been found, and indicate a proximal source in the NW of the caldera. The eruption began with the generation of column-collapse PDCs, followed by lahars. The eruption then re-established an unstable column, which generated the fall deposits seen in the upper stratigraphy across much of Aluto's north western sector. This column eventually collapsed, generating another PDC. The loose pyroclastics generated by this eruption were then re-mobilised by heavy rainfall generating lahars. Not long after this, a PDC, probably from yet another phase of the same eruption, blanketed the local area. This eruption is characterised by the repeated generation, collapse and re-establishment of eruption columns, indicating temporally unstable eruptions with multiple PDC-forming events.

3.5 Aluto's Northern Flank: Awariftu valley

3.5.1 Introduction

One of the primary routes into Aluto caldera by foot or donkey is Awariftu valley, situated on the Northern flank of the caldera. The valley hosts extensive exposures of primary pyroclastic deposits and volcaniclastic sediments. The main path cuts into the side of the 'Awariftu pumice cone' on the eastern side of the valley. Many of the sections presented here are found along this path, which runs on a tangent to the cone north-south. Further sections have been found to the north in wadis at the base of the valley. The vast majority of the deposits found in the valley are thought to be sourced from the Awariftu pumice cone, without any intermediate palaeosols. However, there is a palaeosol exposed in the lower stratigraphy marking the pre-Awariftu pumice cone surface, deposits below this are rarely exposed, challenging to correlate and may be associated with disparate sources. Due to the proximity of other vents to these deposits, it is hard to categorically assign all of the eruption units to the Awariftu pumice cone, however, correlations based on sequence stratigraphy and lithostratigraphy imply they are sourced from the same vent. A map of the valley and localities is presented in Figure 3.32. Considering the deposits of Awariftu pumice cone lie at the top of the stratigraphy in Awariftu valley, they must post-date the

pumice cone forming the western side of the valley (centered on 7.8102°N, 38.7944°E). The obsidian lava flow from this westerly pumice cone is Ar-Ar dated to 18 ± 8 Ka (Hutchison et al., 2016b), and is thought to pre-date the Awariftu pumice cone.

3.5.2 Stratigraphy of the Awariftu Valley

The stratigraphy of the 20 identified Awariftu valley deposits can be divided into three main groups: (1) The pre-Awariftu pumice cone deposits, (2) the Awariftu puimce cone fall deposits and (3) a series of interbedded PDC and fall deposits from the Awariftu cone. The entire succession is then overlain by an obsidian lava flow sourced from the same vent. The stratigraphy of the Awariftu valley is graphically summarised in a fence diagram (Figure 3.32). The eruption units within these logs are described in the following section.

The Pre-Awariftu Pumice Cone deposits

The most basal eruption units in the Awariftu valley are exposed in two locations around 1.3 km from each other, one (MER-17-33) in the wall at the head of the valley and the other (MER-17-73) at the base and foot of the valley. The lack of continuous exposure between these two disparate localities makes accurate correlations challenging. Their relative stratigraphic positions are also hard to ascertain. The units at both sites are shown in Figure 3.34. Generally speaking, the deposits at the base and foot of the valley are reworked, and as such are assumed to be younger than the primary deposits found nearer the head. Unit A20 is a moderately to poorly sorted, clast supported, lapilli grade, angular fall deposit with very little matrix (Figure 3.33). The clasts are primarily fractured pumice, but with some smaller lithics. The appearance of the deposit is very similar to the massive pumice cone fall deposits found elsewhere at Aluto (eg. deposit K4 in Kertefa gorge, central and quarry pumice cones, and Humo gorge). Above this, separated by an undulating surface, is A19, a coarse massive tuff with decimetre-scale pumices and lithics. The deposit is matrix supported and the pumices are moderately rounded. There is a greater proportion of lithic clasts when compared to the subordinate fall deposit. These

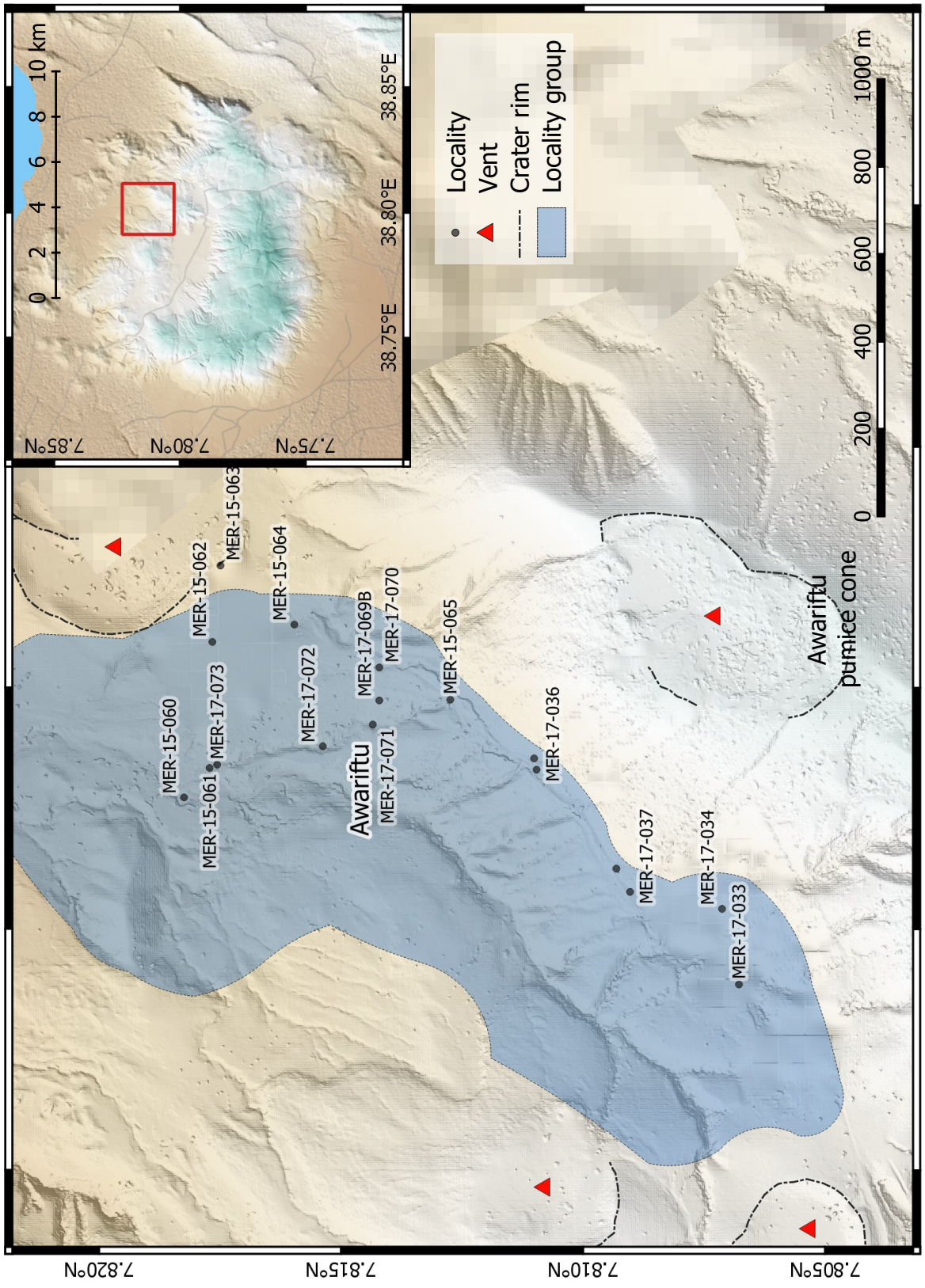

Figure 3.32: *Overview map of the Awariftu valley and localities. Blue polygon indicates Awariftu valley. Red triangles represent the locations of previously active vents identified from the Aluto LiDAR DEM (Hutchison et al., 2014) and field investigation.*

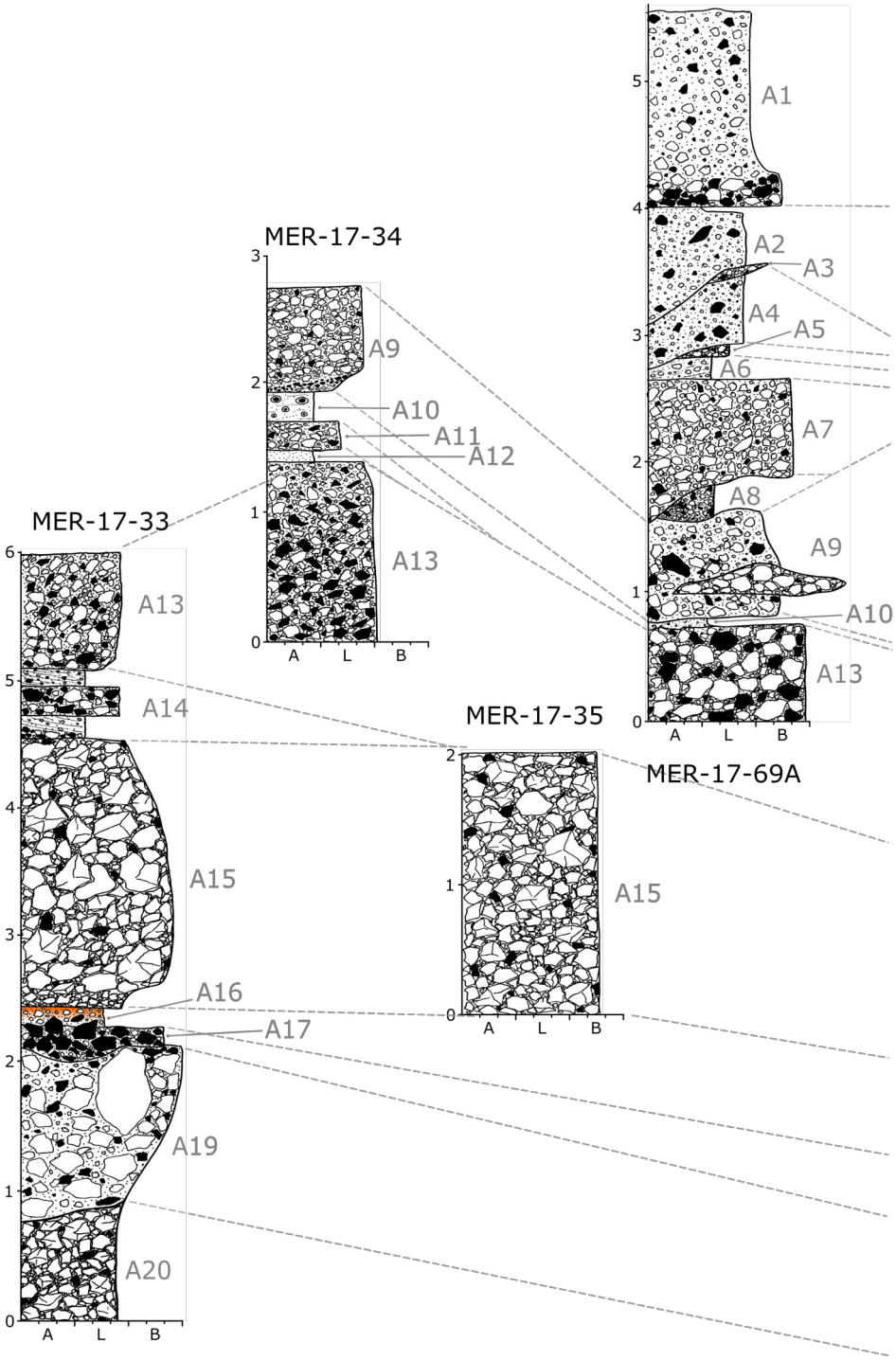
MER-17-33
MER-17-34
MER-17-35
MER-17-69A
A1
A2
A3
A4
A5
A6
A7
A8
A9
A10
A11
A12
A13
A14
A15
A16
A17
A19
A20
A
L
B

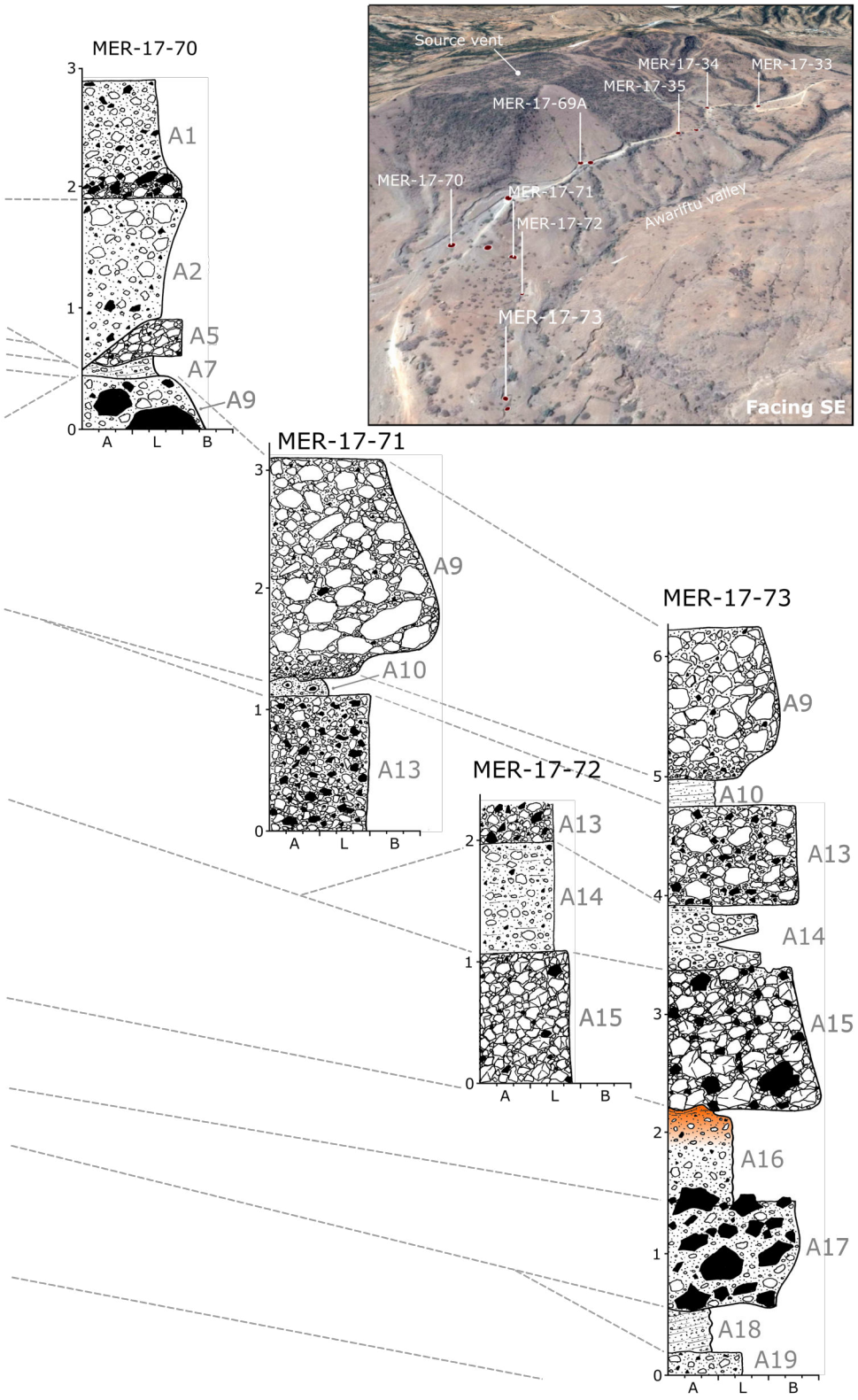

Figure 3.32a: *Fence diagram showing the stratigraphy of Awariftu valley*

two units are most probably sourced from the south-western vent shown in Figure 3.32, and represent a transition from a relatively stable column-edge deposition to column collapse and the development of PDCs.

The majority of the remaining pre-Awariftu pumice cone units (A19 to A16) represent reworking of these deposits. A18 is a cross bedded matrix supported breccia with small angular lithics and rarely small rounded pumices. The matrix comprises coarse ash grade material. The lack of fine ash in this deposit, in addition to the lack of pumices, might be explained by deposition by water. Above this is unit A17, a coarse, lithic-rich nearly clast-supported breccia (Figure 3.34). It is unclear whether this was deposited by a primary volcanic flow (ie. a PDC) or represents reworked material. The clear abundance of lithic components and relative paucity of pumice clasts shows there is a strong density segregation of particles in the flow. In clast supported exposures of this unit there is very little fine matrix, and so deposition by water is the favoured interpretation. The massive and coarse nature of the deposit suggests this was deposited from a high velocity, non-turbulent current and so a debris flow type lahar is most the appropriate interpretation.

The final pre-Awariftu unit is A16, a mLT with a soilified top (Figure 3.34). The unit varies in thickness considerably, at the head of the valley it is only around 20 cm thick, but reaches around 0.75 m more distally at the bottom of the valley. There aren't any bubbles in the fine ashy matrix of this deposit, suggesting it was not deposited by water. This represents a final explosive phase of the pre-Awariftu pumice cone eruption recorded in the Awariftu valley.

The Awariftu Pumice Cone deposits

The Awariftu pumice cone deposits are exposed at many localities along Awariftu valley. Many units can be traced and correlated laterally, though others are laterally discontinuous and are only exposed in one or two sections. The lowermost unit of the Awariftu pumice cone is A15, a massive, clast supported, poorly sorted pumice-rich (93 wt % pumice) deposit (Figure 3.35). Pumices, particularly larger ones, are fractured but whole, suggesting they

Figure 3.33: *Unit A20 exposed at MER-17-33. Shows the typical texture of pumice cone massive fall deposits. Numerous fractured pumices indicate the deposit did not flow during or after deposition.*

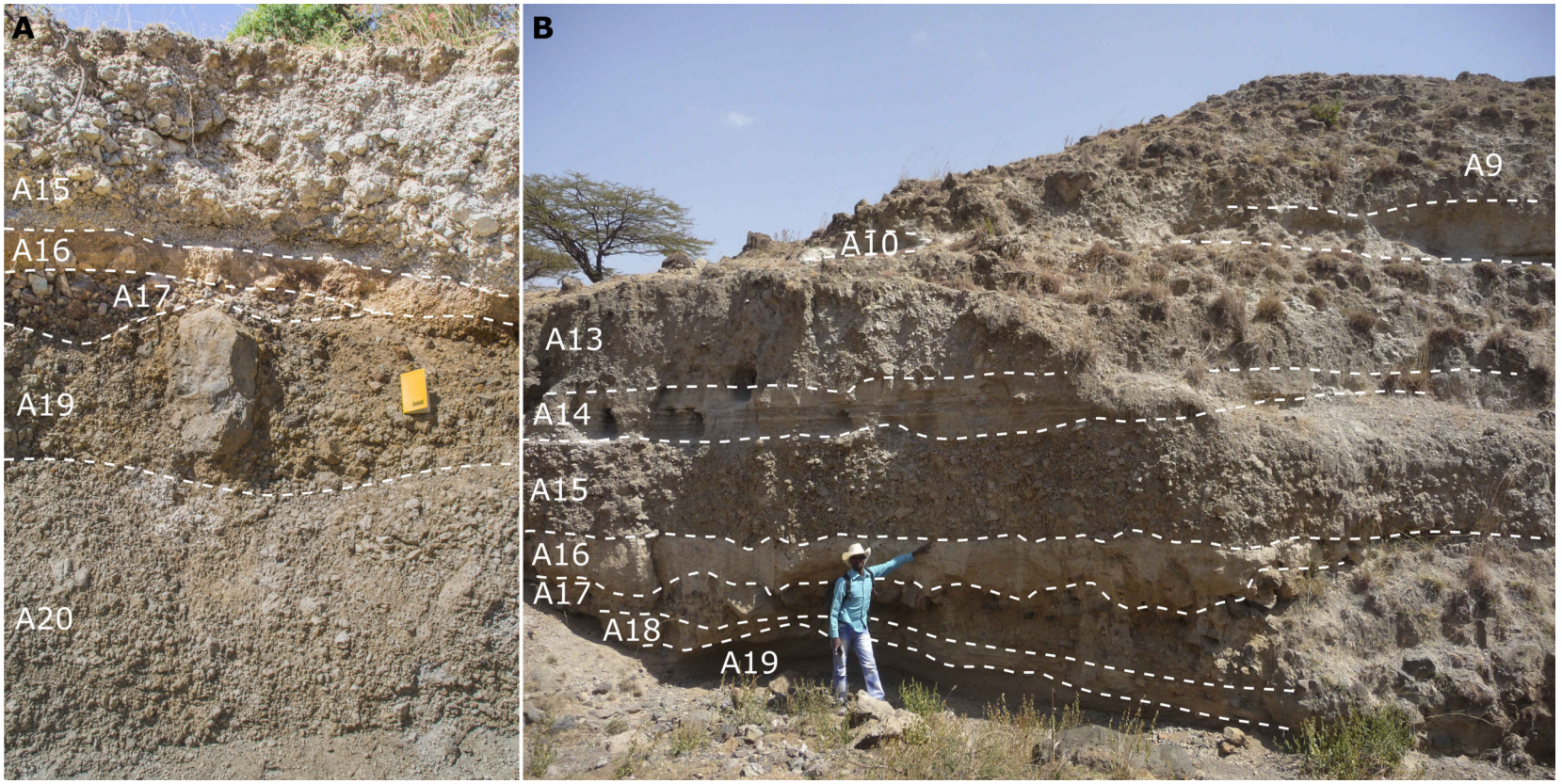

Figure 3.34: *Annotated photos showing the lower-most units (A20 to A9) exposed in Awariftu valley at (A) MER-17-33 and (B) MER-17-73. The upper units (A15 onwards) are thought to be sourced from the Awariftu pumice cone, but the lower units (A20 to A16) are most probably sourced from a different, earlier pumice cone found to the south-west of the valley head.*

experienced minimal flow after impact with the ground; making this a fall deposit. A15 contains a sizeable proportion of pumiceous achneliths, all of which appear to be deposit-quenched type (DQA), showing they were still plastic and inflated after deposition. In some parts of the deposit, most of the clasts are of this type, forming an incipiently welded pumice breccia. The presence of such pyroclasts of this size in a fall deposit indicates the time of flight from fragmentation to deposition must be short, and probably less than 30 seconds, implying they did not fall from great height (Clarke et al., 2019). The presence of many pyroclasts <10 cm indicates they are not ballistically emplaced (Sparks, 1997). The lower 20 cm of the deposit are coarse lapilli grade but the grain size rapidly increases to block size. At MER-17-33, this unit can be seen to reach peak grain size around half way (1 m) through, and then fine again towards the top. This suggests a waxing and then waning of eruption intensity, allowing larger pyroclasts to reach further during peak eruption intensity. This unit can be traced from south to north along the valley wherever the lower stratigraphy is exposed. At MER-17-73, the unit is only tentatively correlated with the others, this is because despite being in the correct stratigraphic position, the grain size is larger than the more proximal exposure at MER-17-72. The A15 deposit from MER-17-35A was sieved, the results of which can be found in Appendix C.2 under sample number MER-17-35A. It has a median grain size of -1.77 and is very poorly sorted at 2.26 ϕ.

Unit A14 is defined by a small package of deposits that are mostly reworked. Further to the north, at MER-17-72 and -73, A14 appears to be a single reworked deposit. In the south at MER-17-33, there are instead two thin reworked units with an intermediate mLT. The reworked deposits comprise matrix supported, well-rounded pumices and smaller angular lithics forming diffusely to well bedded structures. Many of the pumices have been largely altered to clay. There are some clast-supported lenses with a complete lack of matrix material, but otherwise the matrix consists of coarse ash which at MER-17-72 is muddy. These are interpreted as the deposits of hyperconcentrated flows. The presence of the intermediate primary PDC deposit at MER-17-33 (characterised by moderately rounded, larger pumices supported in a fine ashy matrix) suggests that this period of reworking and lahar generation occurred simultaneously with volcanism.

Figure 3.35: *Unit A15 exposed at MER-17-33. Shows the texture of a massive pumice cone fall deposit in (A) deposit scale and (B) pyroclast scale. In B, deposit quenched pumiceous achneliths can be seen to fuse together, forming an incipiently welded pumice breccia.*

Unit A13 (Figure 3.36) is easily distinguishable and traceable along the valley. It is a barely-matrix supported, lithic rich (83 wt % lithic), very poorly sorted, mLT. The pumices are rounded, the lithics are angular and are supported in a fine ashy matrix. The upper 30 cm of the unit (exposed at MER-17-34) is finer grained and more pumice-rich than the lower portions. The lithics in this unit are quite varied in type, mostly consisting of obsidian and a variety of altered volcanic and sedimentary basement. This unit was sieved, the results of which can be found in Appendix C.2 under sample number MER-17-34A. It has a median grain size of -3.2 ϕ, and is very poorly sorted at -2.59 ϕ. At MER-17-34, unit A12, a massive fine ash, drapes the top of A13, and is interpreted as a co-ignimbrite ash fall (Figure 3.36B). Unit A11 is only observed at MER-17-34, and comprises a thin mLT.

Above this is unit A10, which is thin but distinctive, and traceable along much of the length of the valley. It comprises mostly fine ash with some lapilli sized angular obsidian lithics. The unit is cross bedded in places (Figure 3.36) and contains some (but not a great number of) accretionary lapilli (Figure 3.37). The accretionary lapilli have an ash

pellet core and multiple concentric rims. The presence of multiple concentric rims on accretionary lapilli is attributed to the baking and then rotation of a coated pellet in a PDC (Brown et al., 2010). The low angle cross bedding in this deposit suggests deposition from a high velocity, turbulent (thus dilute), pyroclastic density current. The abundant fine ash and presence of accretionary lapilli suggests this may be phreatomagmatic in origin.

The units above A10 comprise a series of mLTs with two intercalated, well sorted pumice lapilli fall deposits (A5 and A3) (Figure 3.38). Unit A9 is best observed at MER-17-71 (Figure 3.37), and can be identified by its fine base grading into very coarse, block sized pumices. The deposit is pumice rich and lithic poor. There is a high concentration of larger clasts that are barely supported by a fine ashy matrix. Above this units A8 and A7 are very similar, barely matrix supported mLTs. The primary difference being A8 is finer grained than A7. Unit A7 was sieved from two locations, the results of which can be found in Appendix C.2, under sample numbers MER-17-69B and MER-17-36A. A7 at both site is very poorly sorted, but is more fines rich at MER-17-36A.

From unit A6 to the top of the succession, the massive lapilli tuffs (A6, A4, A2 and A1) are all similar. They have a much higher proportion of ashy matrix than the underlying mLTs. Unit A1 is distinguished by a coarse, particularly lithic-rich base around 30 cm thick. Within this succession, better sorted pumice fall deposits (A5 and A3) are sporadically preserved, and have been in the most part eroded by the overriding PDCs. A small sample of unit A3 was sieved, the results of which can be found in Appendix C.2 under sample number MER-17-69C. It is coarse, with a median grain size of -4.56 ϕ, and moderately sorted at 1.47 ϕ. Unit A2 is a distinctive mLT containing occasional pumiceous achneliths, presumably kept hot and ductile by during entrainment in a PDC. This unit was sieved, the results of which can be found in Appendix C.2 under sample number MER-17-69D. It is relatively fines rich, with a median grain size of -0.75 ϕ, and is very poorly sorted at 2.76 ϕ.

Capping this pyroclastic succession is an obsidian lava flow which halted up-slope, and so is set back from most of the exposures along the valley. It extends a maximum distance of around 600m from the vent. The obsidian is rich in phenocrysts (around 40 vol %). The

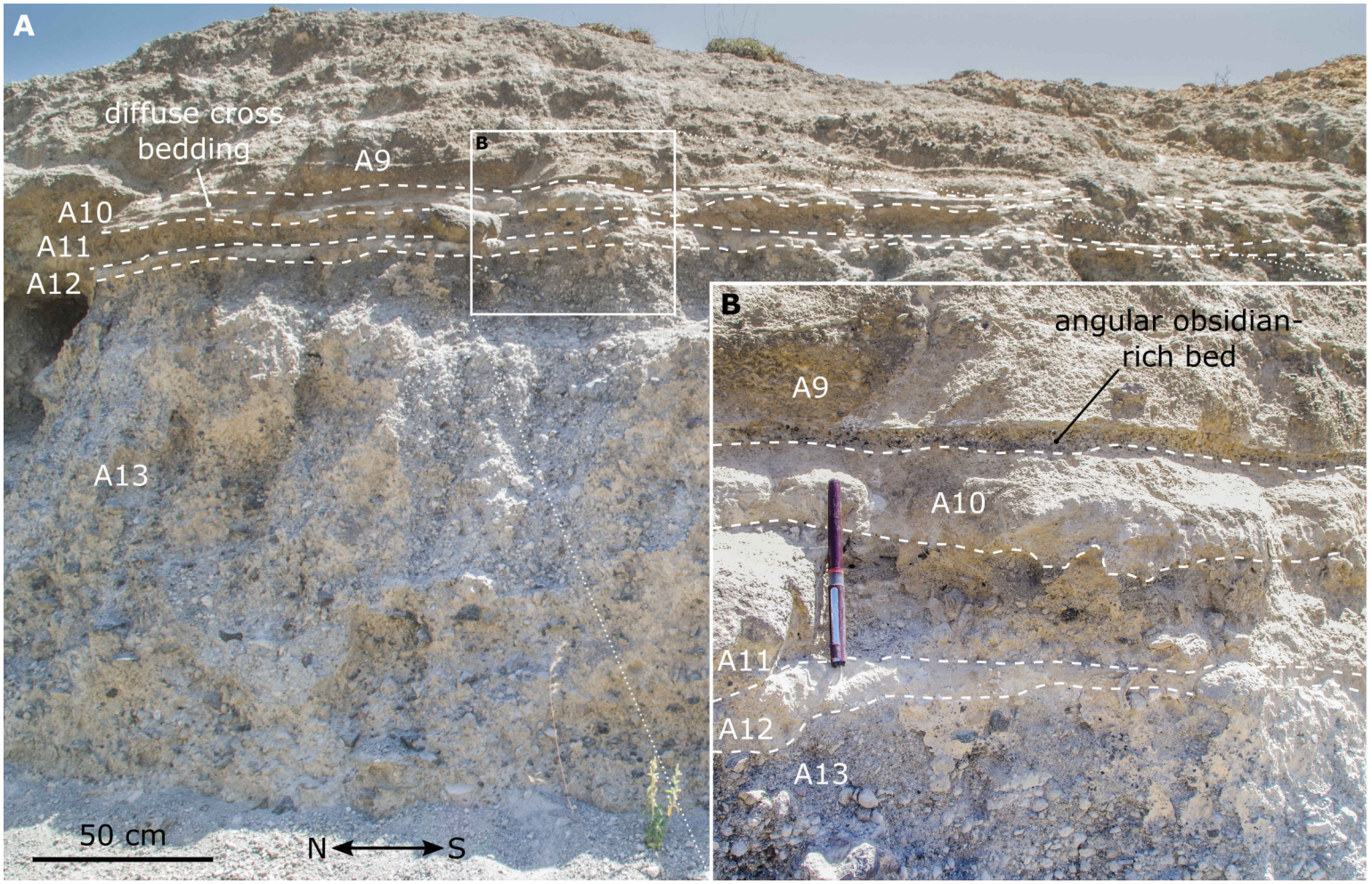

Figure 3.36: *Annotated photos showing the middle units (A13 to A9) exposed in Awariftu valley at MER-17-34. (A) deposit scale photo and (B) a more detailed inset showing the relationship and quality of the units exposed at this locality. Diffuse cross bedding in unit A10 is best seen in the broad scale image (A).*

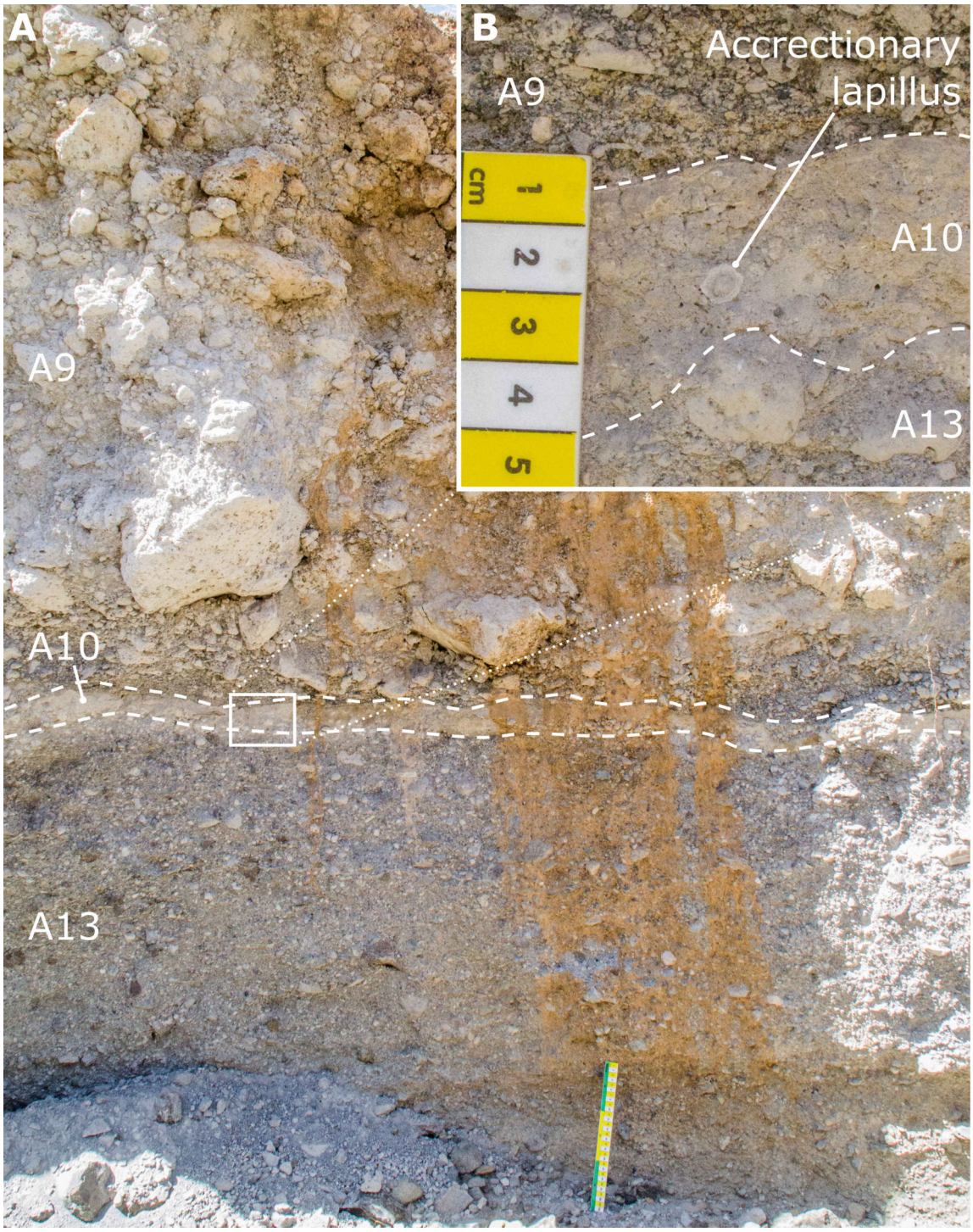

Figure 3.37: *Annotated image of units A13, A10 and A9 at MER-17-71. (A) Deposit scale overview and (B) Inset showing accretionary lapilli within fine ash bearing unit A10.*

phenocrysts comprise quenched, 1 mm scale quartz-k-feldspar granophyres. The flow can be seen in Figure 3.32 and the inset of Figure 3.32.

3.5.3 Eruptive history of the Awariftu Valley

Pre-Awariftu Pumice Cone activity

Assuming the tentative correlations of the pre-Awariftu deposits are correct, they represent the progress of a single eruption. The earliest recorded deposits of this eruption are the fall deposits of unit A20, producing a shallow cone (less than repose) of fractured pumice and occasional lithics. There is little fine ash in this deposit, indicating either a relatively low violence and fragmentation efficiency, or that fine ash was produced but was separated into a bouyant ashy plume. The following ash-rich ignimbrite deposit (A19) sourced from a collapsing column suggests that the pumice cone might have been generated during the bouyant phase of the same column. This is also supported by the short time of flight of DQA pyroclasts in the fall deposits, and the presence of small pyroclasts, incapable of being emplaced ballistically. This is evidence of ultraproximal deposition form the edge of the eruption column. As the eruption intensity waxed then waned, the eruption column became unstable, and collapsed to produce a PDC. The presence of fine ash in the ignimbrite so close to source (where ash is the product of primary fragmentation rather than milling in the PDC) suggests that the original column which produced the pumice cone was also rich in ash. This suggests that during the pumice cone building stage, fine ashy material was bouyantly entrained by the plume whilst the larger pumice lapilli and blocks rained-down from the column edge to produce the ash-depleted pumice cone deposit.

This was followed by a lahar, producing deposits A18 and A17. The source of this lahar is likely to be loose volcanic material produced during the previous eruption. Considering the probable southerly location of the eruption and the dip of the slope towards the north, the deposits at MER-17-73 may represent the downstream facies of the same lahar event. This may explain the presence of hyperconcentrated flow deposits (A18) downstream in the south but not upstream in the north; hyperconcentrated flows such as A18 are often

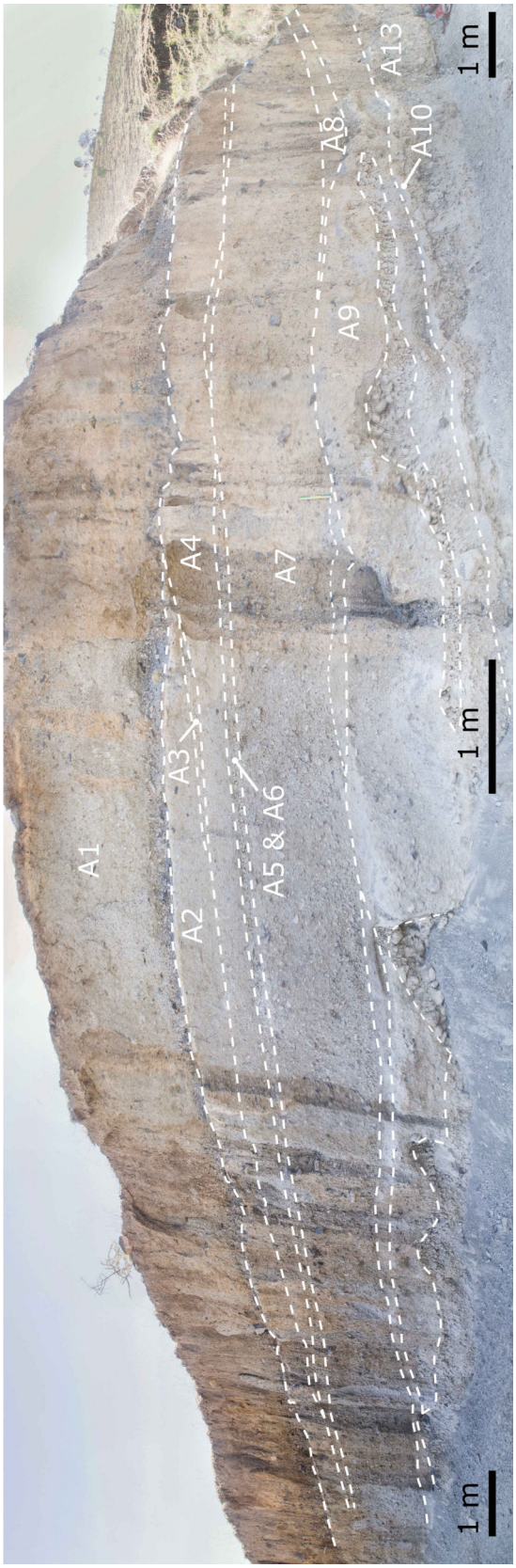

Figure 3.38: *Annotated photos showing the upper-most units (A10 to A1) exposed in Awariftu valley at MER-17-69. There is considerable image distortion reflected in the change in scale from the centre to edges of the image.*

produced by the downstream dilution of the current through de-watering of the debris flow portion (A17) further up-stream (Pierson and Scott, 1985; Vallance and Iverson, 2015). The onlap of deposit A17 downstream onto A18, suggests that these deposits represent the waxing phase of the lahar, with the progressive aggregation of more proximal (debris flow) facies over more distal (hyperconcentrated flow) facies. The source of water in this instance is unclear, there is little evidence for phreatomagmatism in these eruptions, perhaps showing that lahars weren't the result of a breached body of standing water. A more likely source is rainfall or a perturbed hydrothermal system.

The presence of a final PDC deposit (A16) capping this sequence (assuming it came from the same source), implies that lahars were produced before the eruption ended; either syn-eruptively, or in a pause in primary eruptive activity. The palaeosol at the top of the succession shows that there was a cessation of eruptive activity in the area, eventually broken by the eruption of Awariftu pumice cone.

The Awariftu Pumice Cone forming eruption

The most basal observed unit of the Awariftu pumice cone is fall deposit A15, strongly resembling other pumice cone massive pumice breccia fall deposits observed at the base of pumice cones elsewhere at Aluto. A15 is only ever observed distally, or at the base of exposures where the road cuts through the upper stratigraphy on the cone's flanks. Here, exposure of A15 reaches a maximum thickness of 2.5 m. As the prominence of the cone reaches around 200 m above the surrounding landscape, it is clear that a significant thickness of the cone remains unobserved. However, as A15 directly overlies a palaeosol, and appears continuous from distal to more proximal sections, it would be reasonable to assume this does indeed represent the first deposit of the eruption and that it might thicken proximally to form much of the cone's volume as deposit K4 does at Kertefa. The most distal exposure of A15 can be found around 900 m from the vent. Taking a prominence of 200 m, this implies an average slope of around 12°. This is consistent with the massive nature of deposit A15, which evidently does not exceed the repose angle of the constituent material. Like other pumice cones investigated at Aluto, this shallow cone was not em-

placed ballistically; lapilli-sized pumices forming the cone at a distance of 900 m from the vent precludes this. Again, ultraproximal deposition from the edge of eruption column best accounts for granulometry of Awarfitu pumice cone. Deposition from an eruption column is further supported by the later stratigraphy of this eruption, dominated by ignimbrites sourced from column-collapse events.

Following the main cone-building phase of the eruption there was a period of reworking and lahar generation producing hyperconcentrated flows (unit A14). It is unclear how long this period lasted, but the presence of a PDC deposit within the lahar sequence at MER-17-33 shows that it was contemporaneous with primary volcanic activity. Unit A13 is a particularly lithic rich ignimbrite with little matrix, followed by a co-ignimbrite ash fall deposit. From this point, the eruption is richer in fine ash, and the presence of accretionary lapilli in a dilute PDC deposit (A10) implies there might have been a phreatomagmatic component to the activity. PDC deposit A9 is almost devoid of lithics and contains very large pumices. Without full exposure from source to foot, it is impossible to ascertain whether these PDCs were more pumice-rich than the previous deposits or whether they simply didn't reach as far, exposing their pumice-rich terminal lobes. Beyond this point in the stratigraphy, there are a series of ignimbrites with a highly complex architecture; deposits regularly pinch-out, reappear and overlap. Within these ignimbrites there are thin, intercalated pumice lapilli fall layers which are very sporadically preserved. Together, this builds a picture of a highly unstable column, occasionally developing sufficient stability to convect pumice lapilli and produce fall deposits, but frequently collapsing to produce small scale PDCs that erode and partially remove the loose deposits below. These are the last recorded explosive deposits of the Awariftu pumice cone eruption, with the final eruption phase marked by the emplacement of a silicic lava flow.

3.5.4 Summary

Awariftu valley records at least two eruptive episodes. The first, less well exposed eruption consisted of the development of a shallow pumice cone by column-edge deposition. The

eruption column waned, becoming unstable and generating at least two pyroclastic density currents. Deposits were remobilised as lahars during this eruption. This process repeated itself during the eruption of the Awariftu pumice cone. This second eruption appears to be more voluminous, producing a greater thickness of deposits and the main topographic features of Awariftu valley. The eruption began with a pumice cone building phase through ultraproximal deposition from the edge of an eruption column. The eruption waned, with a highly unsteady eruption column producing a series of lapilli fall and pyroclastic density current deposits. Finally a silicic lava flow was emplaced. There also appears to have been a phreatomagmatic phase during this eruption, generating a dilute PDC. Both eruptions recorded in Awariftu valley produced lahars, showing that such an event may be common at Aluto during, and potentially after eruptions. This sequence of events (ultraproximal pumice cone building phase, PDC-forming phase, then obsidian flow emplacement) is similar to that of the pumice cone forming eruptions exposed at Kertefa and Humo gorge, and Central and Quarry pumice cones.

3.6 Volcanism at Aluto's Central vents

3.6.1 Introduction

Aluto's central region, a depression bounded on all sides by the deposits from eruptions that emanated from Aluto's caldera ring-fault, is dominated by a flat plain of primary and reworked pyroclastic material. This depression has acted as a basin for the eruptive products of the surrounding vents from every direction, and so provides an excellent record of Aluto's post-caldera eruptive activity. On this plain sit a multitude of sites of human, economic and commercial importance: multiple small settlements, in addition to a school and the Aluto-Langano geothermal power plant. Being a basin so proximal to many vents on all sides, these sites are likely to have the greatest probability of being impacted by volcanic mass flows during a future eruption at Aluto. Therefore, understanding the nature of the deposits at these locations is of critical importance in evaluating the possible impact of a future eruption. The main sites investigated in this region are *Humo Gorge*, in the south western wall of this central area, and the less comprehensively investigated

sites: *Quarry pumice cone*, *Gabiben pumice cone* and *Central pumice cone* (Figure 3.39). The main limitation in this region of the volcano is good cross-sectional exposure, which only Humo Gorge and Quarry have in abundance.

3.6.2 Humo Gorge

Humo Gorge cuts into the south western wall of the central region of Aluto volcano. The gorge hosts a number of pyroclastic deposits along its length, representing eruptions from multiple eruptions in the local area. Combined with the topographic data set of Hutchison et al. (2014), the architecture and deposits of Humo gorge indicate three distinct eruptions. The craters of two of these can be identified, and the third crater is proximal but unknown. The first and last eruptions are relatively well exposed, and reveal two pumice cone forming eruptions with partially over-lapping deposits. A 3D overview of the region with localities, broad stratigraphic attributions and a condensed geological history is presented in Figure 3.40.

Stratigraphy: Humo Gorge phase 1

The stratigraphically lowest units exposed around Humo gorge are associated with a single pumice cone eruption, which has developed a largely eroded and partially buried shallow pumice cone. The northern section of the gorge cuts through the rim of the pumice cone, providing cross sectional exposure from inside the crater, through the crater rim to the exterior from south to north.

The logs of this section of Humo are presented in Figure 3.41, and provide near continuous exposure from the base (unit H1), to the top capped by a palaeosol (unit H6). The most basal units are exposed in logs MER-17-44 and -46. Though they represent the same stage of the eruption, log -44 contains many additional reworked units. H1, the lowermost unit exposed, is a diffusely bedded, lapilli grade angular pumice deposit with a granule-sized matrix and little ash. It is also relatively well indurated, and is interpreted

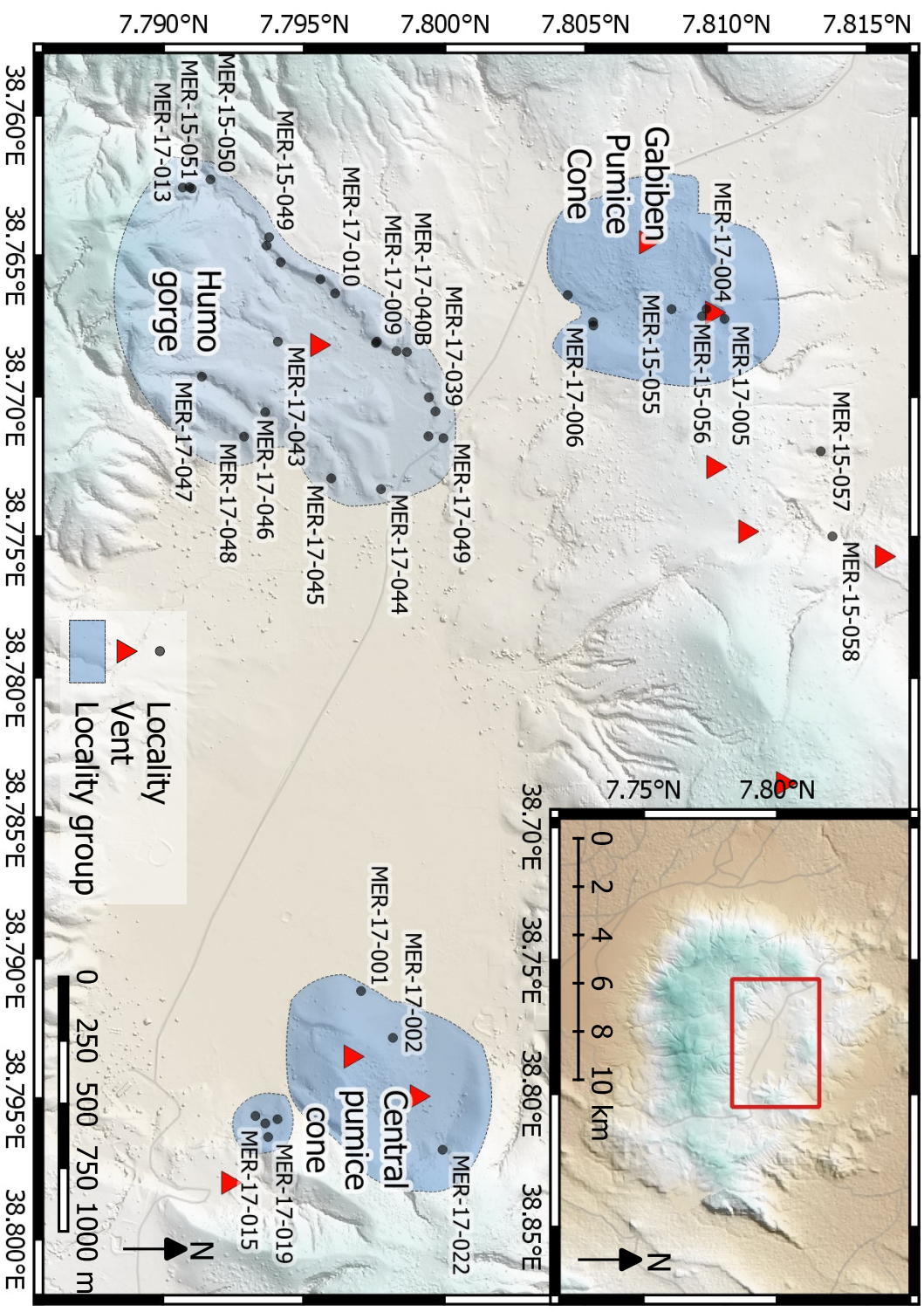

Figure 3.39: *The main field localities in Aluto's central region. Blue polygons indicate sub-regions which will be the subject of the following sections and red points indicate individual localities within these regions.*

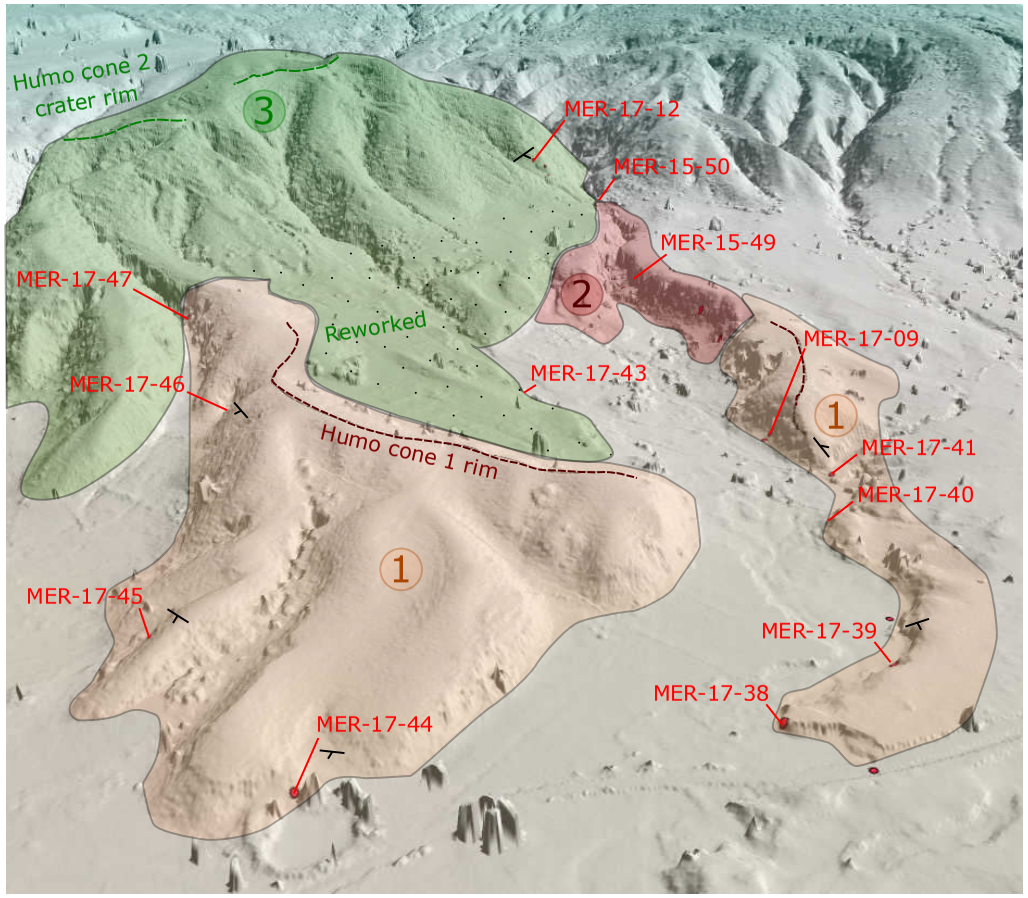

1

Development of Humo pumice cone 1. Pulsatory eruption column generating bedded ultraproximal fall deposits with granular flow down steep slopes. Followed by column collapse and the generation of PDCs

2

Proximal fall deposit from an unknown source overlying a palaeosol. Sustained pyroclastic fountaining generated gorge-filling ignimbrite. Followed by an an unsteady column producing multiple PDCs and co-ignimbrite ashes

3

Final Humo gorge pumice cone forming eruption. Initiates with fall deposit followed by column collapse and PDC generation. Next stage of the eruption consits of eruption column generating pumice-cone building fall deposits. Column became unstable genrating multiple fall and PDC deposits. Eruption finished with obsidian lava flow effusion. Finally, a stage of water reworking of loose deposits partially fill the crater of pumice cone 1.

Figure 3.40: *3D view of Humpo gorge and the surrounding region showing 3 distinct stratigraphic groups associated with distinct eruptions. A condensed geological history is presented alongside. The following section will describe and interpret the region's geological history. Ticks represent strike and dip direction.*

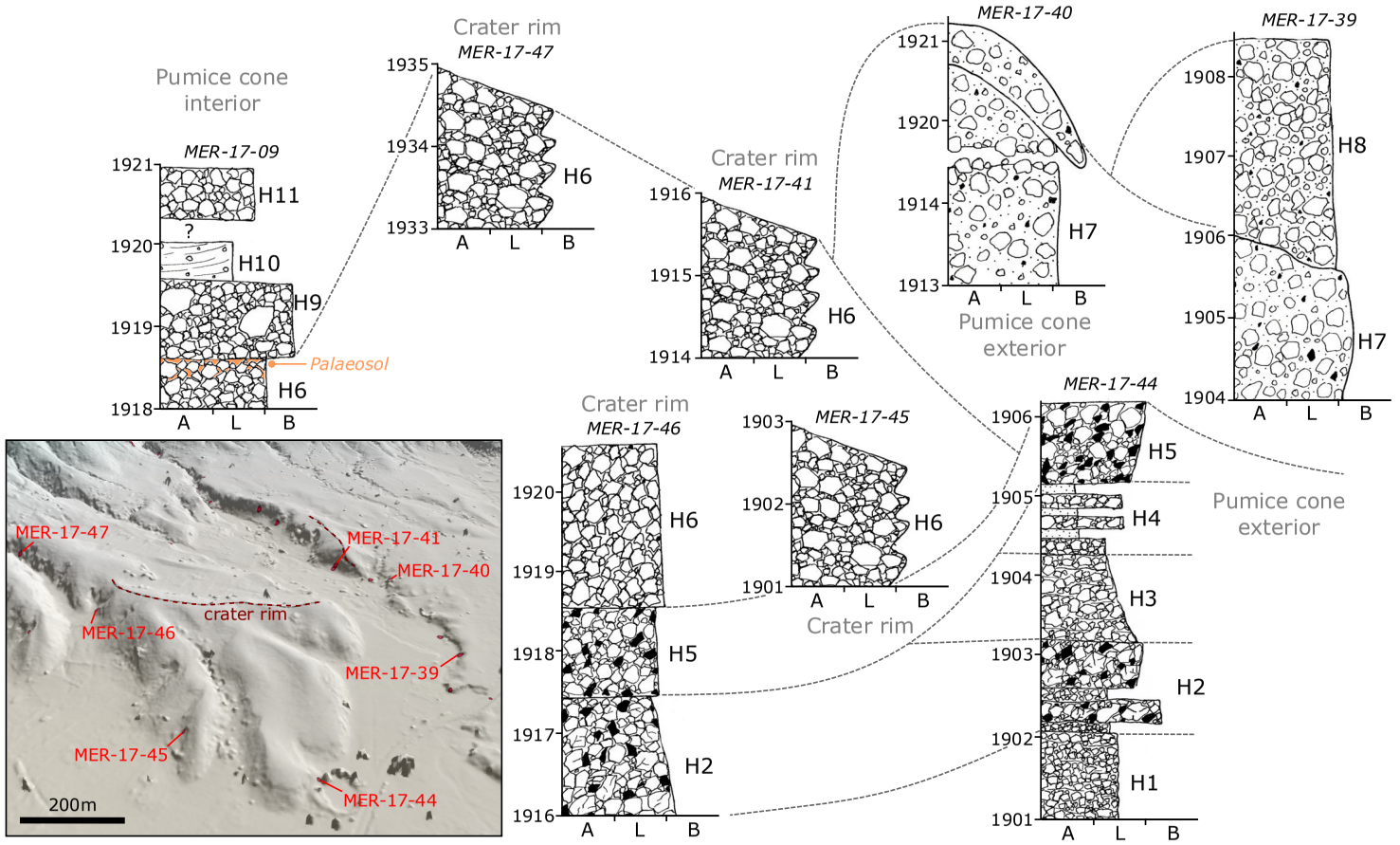

Figure 3.41: *Fence diagram of the Humo gorge logs pertaining to the first eruptive episode represented in Humo gorge. Heights are presented in meters above sea level.*

as a water-reworked lapilli pumice fall deposit. The next unit H2, is a lithic-rich, normally graded coarse lapilli pumice breccia. Many of the pumices are broken on impact but not separated, confirming this as a primary fall deposit. It appears identical to the massive pumice cone breccias which form shallow cones at other pumice cones around Aluto. In log MER-17-44, there are two thin lapilli pumice fall deposits, with a lower lithic concentration than the rest of H2. At log -44, unit H3, another reworked pumice fall deposit sits on top. Above this is a series of thin fall deposits which are grouped together as unit H4. The first is lapilli grade and around 10 cm thick, followed by a finer, massive ashy fall deposit that drapes the underlying lapilli; a sequence which repeats twice more. These units (H3 and H4) are absent at MER-17-46. The next unit, H5, is a lithic-rich mLT that is nearly clast supported. The pumices are woody (tubular vesicles) and rounded, and are set in a fine matrix.

Unit H6 can be found at numerous localities around Humo gorge. The lowest exposures occur at a range of altitudes, indicating it was deposited on an irregular surface. The thickness of the unit varies considerably, and is thickest around the apparent crater-rims that can be seen in the LiDAR DEM (Figure 3.40). The unit is nearly pure clast supported angular pumice, with very sparse, small obsidian lithics. In some places the deposit is massive, but in others it is diffusely bedded at a high angle forming small inversely-graded packages. The deposit is absent at more distal exposures on the outer slopes of the cone. At MER-17-09, the massive top of the unit has formed a palaeosol. Where H6 shows granular flow structures and bedding, they dip radially away from the center of Humo gorge (Figure 3.40). The unit is considered an ultraproximal fall deposit, forming the pumice cone itself. The presence of steeply bedded granular flow packages and absence of fractured but whole pumices typical of massive pumice cone facies at Aluto indicates this material was deposited on a steep slope at the angle of repose.

The final products of this eruption are found in the most distal exposures (MER-17-39 and -40) outside of the cone. H7 is a matrix-rich coarse mLT with rare lithic clasts, which is thickest (8 m) closest to the pumice cone rim (log -40). Here it forms an unusual double-hill structure (Figure 3.42). These structures are described by Hutchison et al.

(2015) as a ignimbrite 'blisters'; features seen in peralkaline rhyolite ignimbrites elsewhere, and thought to occur when an impermeable cap at the top of the ignimbrite is formed. As gases continue to be expelled from the deposit (from between clasts, and during volatile exsolution from the melt), they are trapped under the cap. If the cap is sufficiently ductile, it domes upwards forming a hollow blister before cooling in-place (Schmincke, 1975a). The structures present at Humo gorge, through resembling blisters in their domed and intensely indurated top, must have been formed through a different process. The driving force behind doming in blisters is the accumulation of gas, forming a hollow. At Aluto there are no hollows; the domed regions are simply filled with ignimbrite. Instead, I favour the interpretation of an explosion pit. Explosion pits and rootless cones often develop when lava flows inundate small bodies of water or septic tanks, causing rapid confined boiling, gas expansion and explosions (Thorarinsson, 1953). Here, instead of a lava flow, a PDC deposited ignimbrite H7 over a body of water. The water rapidly boiled, and without sufficient permeability in the overlying ignimbrite to allow rapid outgassing, nor sufficient strength or elasticity to contain the expanding gas, there was an explosion. This developed a central crater flanked by symmetrical mounds of ignimbrite, now cross-sectioned at MER-17-40. Towards the center of the crater, intensely indurated ignimbrite is plastered against the surface of these mounds at a very high angle (>50°), indicating it was cohesive when it was deposited there. As there are no fiamme or signs of intense welding or rheomorphism, this cohesiveness is likely to be due to water saturation rather than heat, further supporting the notion that this is a hydrovolcanic feature. There are multiple curviplanar surfaces of greater and lesser induration within the mounds either side of this pit, parallel with the upper indurated surface. This might have been the result of multiple explosions, cumulatively building ever large domes of ignimbrite explosion ejecta either side of the pit. This would require a re-supply of heat and water for each explosion. This might result from an ignimbrite emplaced in pulses over a flowing body of water. Each PDC pulse resulting in an explosion, plastering the crater walls with wet ejecta, and again exposing the pit allowing it to be refilled with water. This ignimbrite is followed by the final preserved product of this eruption: H8, an mLT which is very similar in all respects to H7, only it is less indurated and has a slightly lower proportion of ashy matrix.

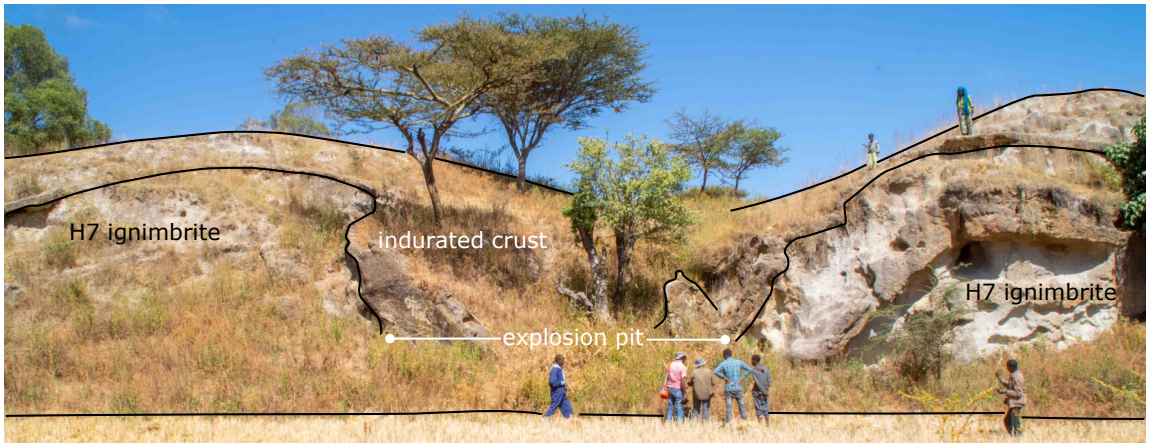

Figure 3.42: *Photo at MER-17-40, showing the explosion pit generated when ignimbrite H7 was deposited over water. The symmetrical domes are interpreted as cross sections through crater-rims. A crust of intensely indurated ignimbrite is plastered across the surface of the crater, the very high angle at which the crust is able to lie implies it was cohesive when it was deposited. As there are no fiamme or rheomorphic textures, this cohesiveness is probably due to water saturation rather than heat.*

Stratigraphy: Humo Gorge phase 2

The next phase of eruptive activity recorded in Humo gorge is less completely exposed, but forms the steep walls of the gorge itself. The location of the vent that produced these deposits is not clear, though the presence of sporadic, anomalously large ballistic pumices in the basal fall deposit indicates it must be relatively close. The stratigraphy of this phase is presented in Figure 3.43.

The most basal unit of this sequence is H9, an angular lapilli pumice fall deposit sitting on top of the palaeosol which marks the end of the first eruptive phase at Humo. The deposit also contains occasional large (>10 cm) pumice clasts, which are interpreted as ballistics, indicating the source vent must be relatively close (probably within a few hundred meters (Mastin, 2001)). Above this is H10, an ash rich dxsLT with sparse well rounded pumice lapilli, and small obsidian lithics. This is interpreted as the deposit of a dilute PDC. The contact between this and the overlying unit H11 is not exposed. H11 is an angular massive lapilli fall deposit, though is relatively inaccessible and is obscured by undergrowth.

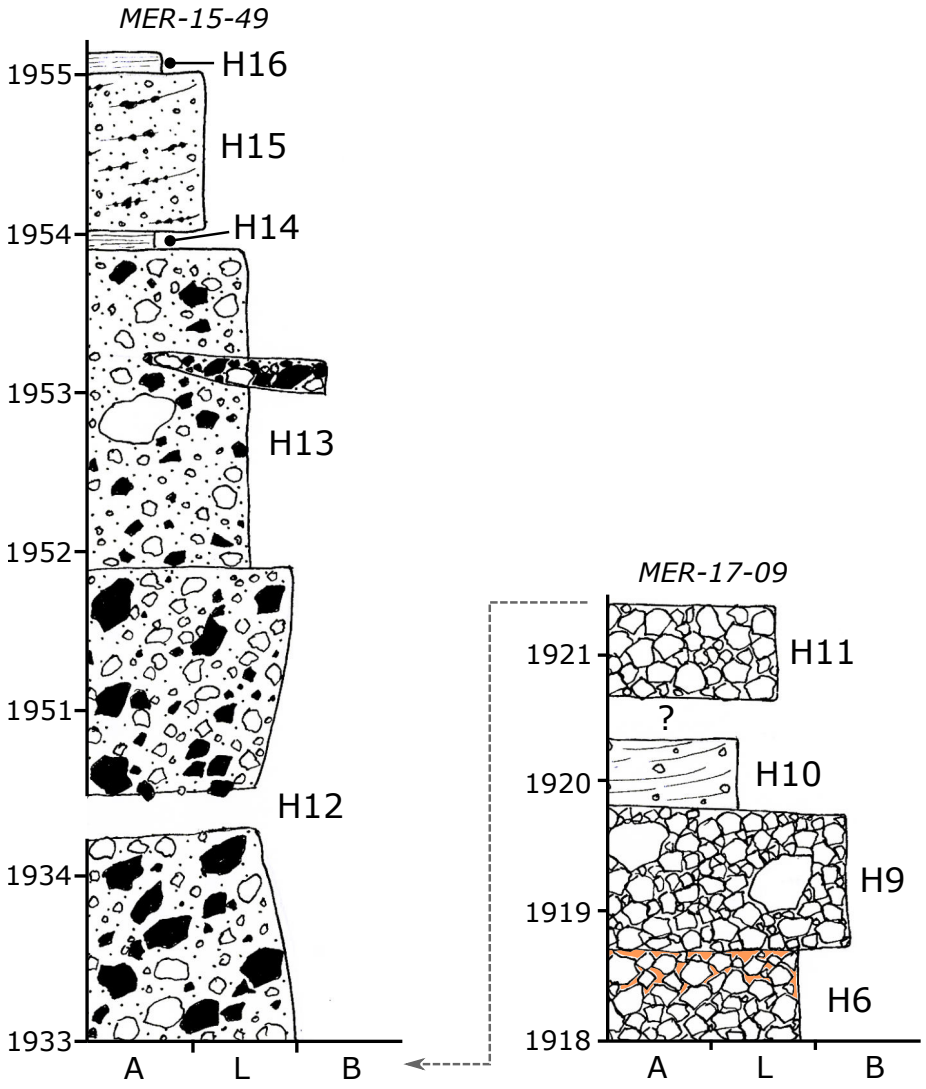

Figure 3.43: *Logs pertaining to the second phase of eruptive activity around Humo gorge. Heights are in meters above sea level.*

Above H11, there is a significant gap in the exposure, representing around 12 m of stratigraphy. H12 is the first unit observed at the base of the next exposure, and consists of a coarse-lapilli to block sized, lithic rich mLT, containing >10 cm blocks of bread-crusted obsidian. Occasional anonymous large blocks can also be seen within the break in exposure underneath this section, suggesting some of this gap may be occupied by ignimbrite H12. At 20 m, the unit is the thickest ignimbrite seen at Aluto. The ignimbrite is indurated and forms the vertical walls at the narrower southern portion of Humo gorge, rising to a terrace which itself is bounded by outer walls, indicating that it is filling a gorge. Towards the north, exiting the narrow portion of Humo gorge, this terrace can be traced and the deposit rapidly thins as it on-laps the deposits of the first phase of eruptive activity near Humo. The source of the ignimbrite is therefore upstream from the southern end of the gorge, flowing north, though a source cannot yet be definitively identified.

The upper section of this sequence is dominated by H13, another 2 m thick mLT, less indurated and less lithic-rich than H12. H13 contains coarse-lapilli sized, rounded pumices with smaller lithics and a greater proportion of matrix ash. There are occasional lenses of coarser lithic-rich material embedded in the deposit. The deposit is draped by a 10 cm thick laminated ash fall deposit, perhaps a co-ignimbrite ash from the H13 PDC. The penultimate unit in this section is H15, a 1 m thick, ash-rich dxsT with occasional thin lenses of coarser mLT. The cross stratification is antidunal, representing a high velocity dilute PDC flowing northwards. H16 is a thin, laminated ash unit that drapes this, most probably another co-ignimbrite ash.

Stratigraphy: Humo Gorge phase 3

The final phase of eruptive activity recorded at Humo gorge is the generation of the tall pumice cone that sits atop the southern portion of the underlying units described so far. At Humo gorge there is a distinct break in slope marking the beginning of the pumice cone as it rises around 160 m above the terrace formed by the underlying gorge-filling ignimbrites. A very steep road is cut into the side of the cone from the base to the crater rim, revealing the cone's stratigraphy. The final section of stratigraphy (MER-17-43) is

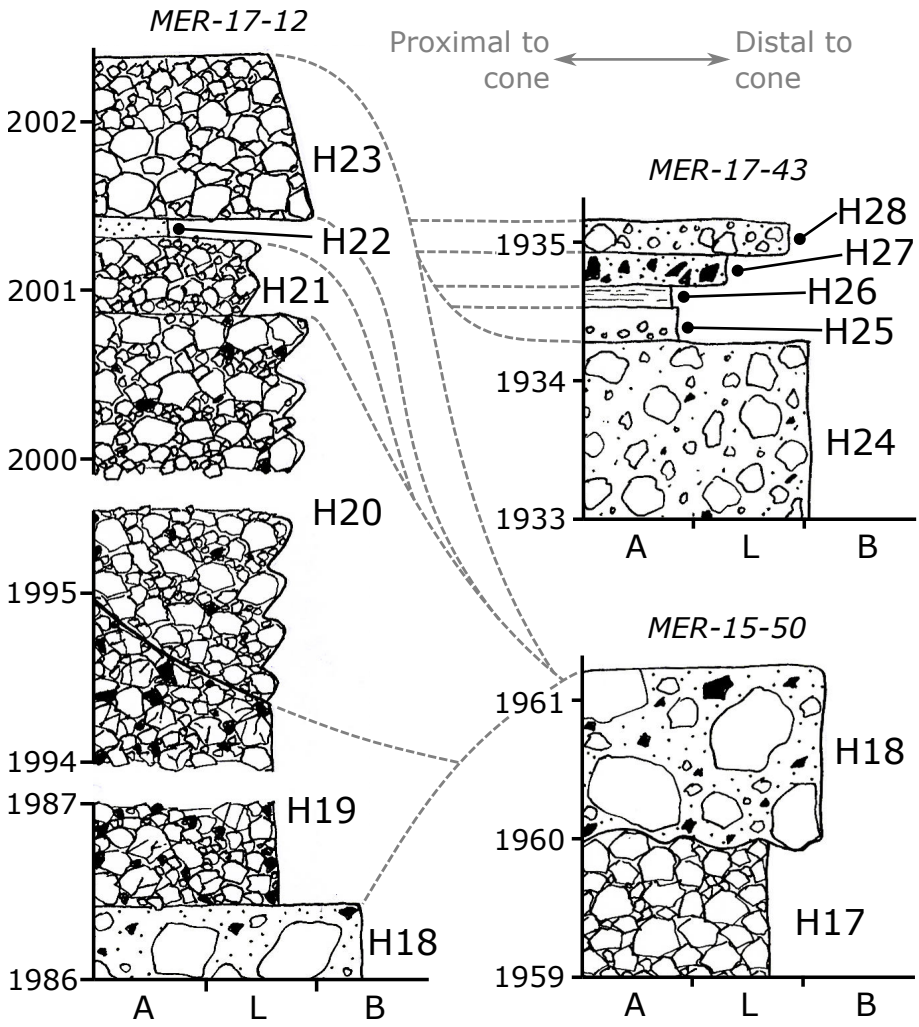

Figure 3.44: *Logs pertaining to the final phase of eruptive activity around Humo gorge. Heights are in meters above sea level.*

found off-lapping then on-lapping the base of the cone, partially filling the crater of the phase 1 pumice cone. The stratigraphy of Humo phase 3 is shown in Figure 3.44.

Just below the break in slope marking the base of the pumice cone, a small cliff section (MER-15-50) reveals the initial deposits of the phase 3 eruption. H17 is an angular lapilli pumice fall deposit with a strongly undulating, erosional upper surface. Above this (at 1960 masl) is a pumice and matrix-rich massive tuff with coarse lapilli to block-sized pumices (H18). This unit can be found in sporadic exposures on ascent of a the road that cut into the side of the pumice cone, with its upper surface rising to an altitude of around

1986 m. If this ignimbrite was horizontal, this would imply a thickness of around 26 m. However, it seems more likely that it is thinner, and was deposited on a slope. This is also supported by the sympathetic dip of H18's upper surface. The underlying hill that forms this slope may possibly be the unidentified source pumice cone formed during Humo phase 2.

The deposits above H18 represent the main cone-building phase of the eruption, and strongly resemble other cone-building fall and granular flow deposits of other pumice cone building deposits at Awariftu, Kertefa, Humo phase 1, Quarry and Central pumice cones. The initial deposits (H19) are relatively lithic-rich massive pumice breccias with fractured but intact pumices. The deposit is around 9 m thick at this locality (MER-17-12), but presumably thickens as you penetrate deeper into the cone. The deposit's upper surface is defined by multiple localised slumps, where the angle of the slope has reached the repose angle of the constituent material. From this point upwards, through unit H20 and H21, bedding is defined by lensoid, inversely graded granular flow packages that dip away from the crater rim at the top of the hill. This is one of the clearest examples of the transition between massive and granular flow bedded pumice cone facies at Aluto (Figure 3.45). The deposits in the upper granular flow facies are less lithic-rich than the underlying massive deposits, and the fractured but whole pumices are absent. Nearing the top of the cone, there is a thin ash fall unit (H22), followed by a normally-graded angular lapilli pumice fall deposit. There are more units exposed in the road-cutting closer to the top of this cone, but unfortunately local land-access issues involving a displeased man with a spear prevented further investigation. These deposits represent the top 5-10 m of the on-cone stratigraphy.

The off-cone Humo phase 3 deposits at MER-17-43 are exposed in a small cliff section cutting into material filling the Humo phase 1 crater (Figure 3.46). The first of these is H24, a pumice rich mLT containing very small obsidian lithics. This can be seen to continue south along the cliff section towards the cone. The final deposits, H25 to H28 are all water-deposited or reworked. H25 is an ash grade deposit in two distinct beds. The first contains large (<0.5 cm) bubbles, and so represents a lahar deposit. The second is

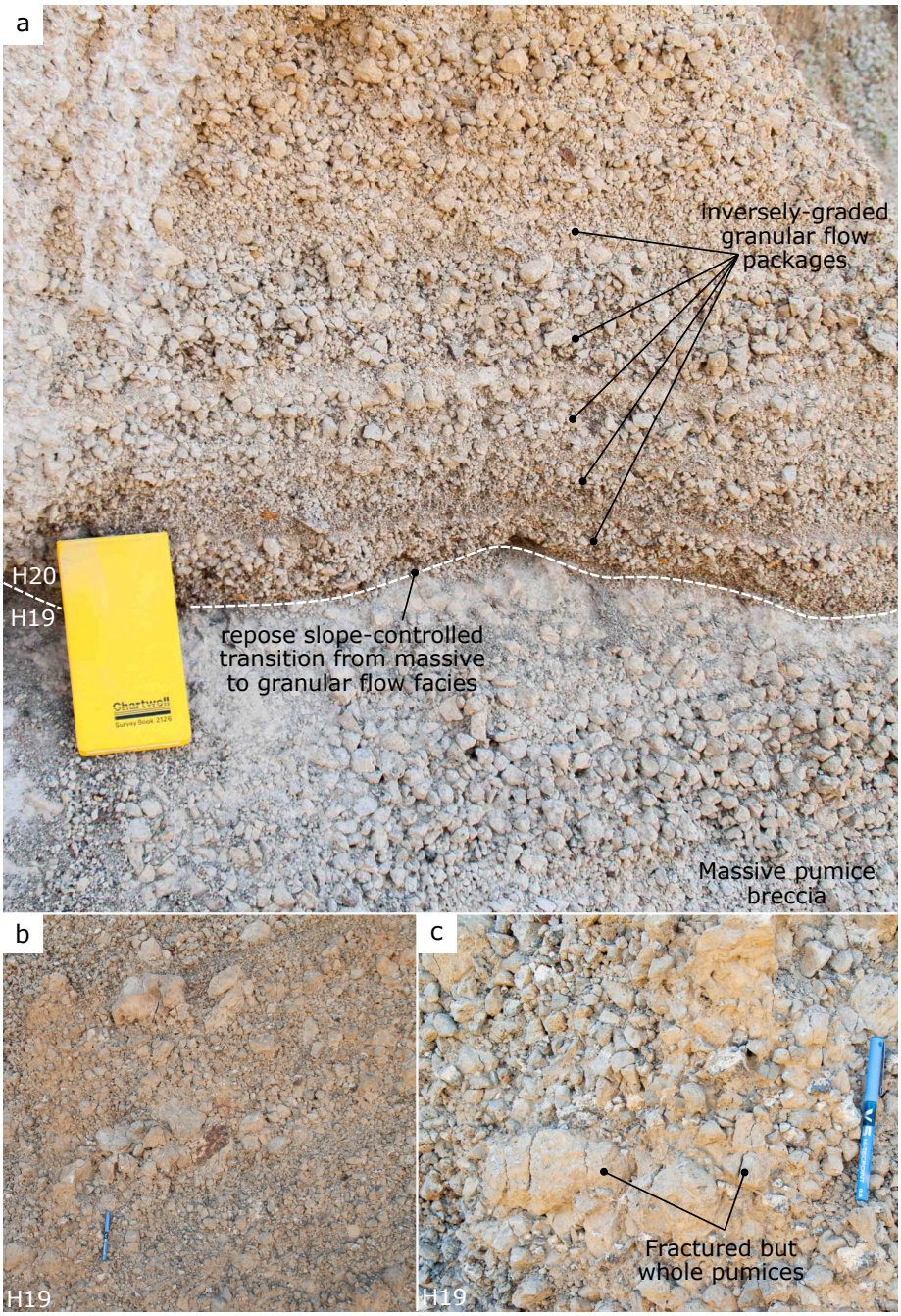

Figure 3.45: *Photographs of Humo phase 3 pumice cone showing the typical pumice cone building facies. (a) The two main cone-building pumice cone facies: the lower unit H19 is a massive pumice breccia, the upper unit H20 is a granular flow-bedded pumice breccia. The transition here is sharp, and occurs where the angle of the bedding reaches the repose angle of the constituent material. The notebook is 21cm long. (b) Overview of the structure of the massive pumice breccia, the pen is 15cm long. Very diffuse, discontinuous bedding can be identified by variation in average grain size. (c) Close-up of massive pumice breccia showing the fractured, yet whole pumices which indicate this deposit was not subject to flow after deposition.*

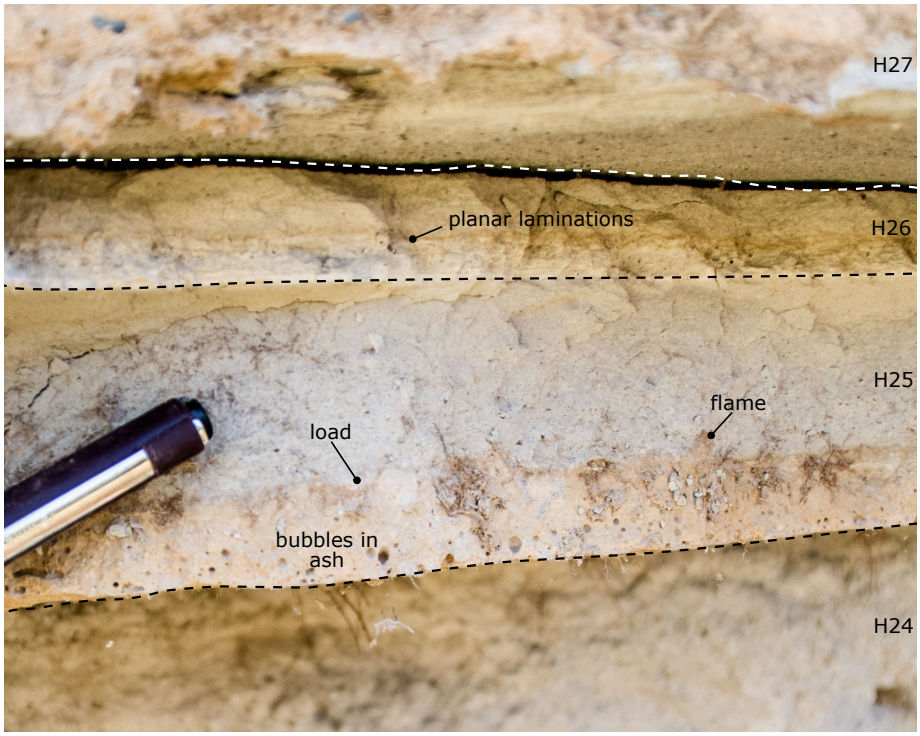

Figure 3.46: *Exposure of the final products of the Humo phase 3 eruption collected in the Humo phase 1 crater basin at locality MER-17-43. The final primary pyroclastic deposit of the eruption is ignimbrite H24 at the base. The remaining deposits are reworked and involve water depositional processes evidenced by bubbles in the ash, load and flame structures, and planar ash laminations from settling through water.*

a massive fine ash, deposited on top of the underlying bubble-rich deposit whilst it was still water-logged, forming load and flame structures. On top of this is a finely laminated ash deposit, possibly settled through water. The final two deposits are H27, a lithic rich reworked breccia, and H28, a diffusely bedded matrix-supported pumice conglomerate with no fine ash. This probably represents water-reworked debris from the eruption. This upper sequence represents the washing and reworking of loose volcanic material into the Humo phase 1 crater basin.

Discussion

The eruptive history of the Humo gorge region can be divided into three phases, each marked by a distinct eruption. These eruptions provide more examples to develop a picture of pumice cone forming eruptions at Aluto. The first eruption began with the de-

velopment of a ring-shaped pumice cone. The first of these deposits are massive pumice breccias, almost identical to others found during the initial shallow-cone building phases of pumice cone eruptions at Aluto. The northern part of the Humo region appears to have been wet, reworking these deposits at MER-17-44. Unit H4 represents a period of relative quiescence, with at least 3 discrete events generating fall deposits into water, separating them by size into pumice lapilli and ash beds. The return to massive pumice breccias after this point indicates that during Humo phase 1, the pumice cone was built incrementally during the same eruption. As the pumice cone developed, the sides steepened, resulting in the granular flow bedded pumice fall deposit H6. Locally, the slope was not sufficient to elicit flow, but the unit is still distinguishable from the underlying massive unit by the near absence of lithic clasts. The paucity of lithics may be a result of a better-established conduit, where loose conduit country-rock has already been reamed out in the initial phases of the eruption. There is an even greater paucity of lithics within the granular flow bedded pumice fall, which may be a result of density separation down slopes during granular flow; an effect recognised experimentally (Vallance and Savage, 2000). At the top of the Humo phase 1 crater rim, and within the crater itself, this is the upper-most unit that has been preserved, forming a palaeosol. The strong resemblance of this unit to others at Aluto pumice cones suggests similar depositional regimes and mechanisms, interpreted as ultraproximal column-edge deposition.

Though this remains a plausible mechanism for the phase 1 pumice cone, the morphology of the phase 1 cone is more ring-like than Kertefa or Awariftu, with shallower outer slopes, and a proportionally wider crater; very similar to widely recognised tuff cones (White, 1996). Given that other pumice cones that sit on the flat caldera-floor of Aluto possess this morphology (eg. Gabiben and Central Pumice Cone), and that there is evidence of water-reworking in the northern, lower altitude section of Humo, this might suggest there is a hydrovolcanic component to their formation associated with a shallow caldera lake. To this day a small ephemeral crater lake often forms during the rainy season at Aluto (Figure 3.47), and it is conceivable that in the past, when more humid conditions were prevalent in the rift valley (Benvenuti et al., 2002b), a more substantial crater-lake could have existed. Tuff cone eruptions are generally considered to begin with

an explosive phase generating a lithic rich breccia (Riedel et al., 2003), consistent with the lowermost deposits (H1 to H5). However, the other features typical of tuff cones: including xsT PDC deposits, and massive ash-grade fall and flow deposits are absent. The fine grained nature of phreatomagmatic deposits is attributed to the increased fragmentation efficiency achieved through molten fuel-coolant interactions (MFCIs) (White, 1996). MFCIs occur where there is very rapid transfer of heat between a fluid fuel and a vapourisable coolant, leading to self-propogating jetting, heat transfer and explosive vapourisation (Buchanan, 1974; Dullforce et al., 1976). This is promoted by a higher thermal gradient and a proportionally higher contact surface area between the fuel and the coolant. Most tuff cones described in the literature are basaltic, and magma MFCI experiments and models typically assume basaltic rheology and temperatures (White, 1996; Zimanowski et al., 1991). Where non-basaltic hydrovolcanism is studied, it generally concerns phreatoplinian eruptions (Branney, 1991; Wohletz, 1983), which are considerably higher magnitude, explosivity and intensity than eruptions at Aluto. Though the viscosity of Aluto peralkaline rhyolites are similar to basalts at eruption (Di Genova et al., 2014; Clarke et al., 2019), basaltic magmas are much hotter, meanining silicic magmas provide less heat to convert to mechanical energy, which may influence the ability for MFCIs to occur, and influence the production of fine ash. However, this still fails to explain the tuff-cone-like morphology of some pumice cones at Aluto, as the shape of the cone is a directly related to the MCFI fragmentation mechanism (White, 1996) which results in jetting (Riedel et al., 2003).

The final stage of the Humo phase 1 eruption involved the collapse of an eruption column producing at least 2 PDCs that deposited mLTs. mLTs are not typical of Surtseyan-type hydrovolcanic eruptions (Riedel et al., 2003), where pulsatory phreatomagmatic explosions inhibit stable column-forming processes. Instead PDCs are generally dilute, cold, and ash-rich; the product of wet fountain collapse (Sparks, 1997). The presence of mLTs, as opposed to xsTs, supports the notion that the cone-forming deposits of H6 were the product of an eruption column, and depositional processes may be similar to that inferred for other pumice cones at Aluto. It's not clear what controls the final morphology of these wide-cratered pumice cones, though a wider crater and shallower slope might be promoted by a wider conduit and more inclined column-edge. The processes that lead to the variabil-

Figure 3.47: *Photograph of Aluto caldera with a small ephemeral crater lake taken in May 2016 (Kiremt rainy season). During past more humid conditions, it is conceivable there might have been a more substantial crater lake. Photo credit: Friedemann Samrock*

ity in pumice cone morphology should be a priority for future work, in order to understand the range of eruption styles they represent. Such work may combine experimental and computer modelling methods to understand the processes that reproduce the natural variability seen in the field. Similar approaches have been taken to investigate the geometry of basaltic maars and diatremes (e.g Graettinger et al., 2014, 2015).

The second eruptive phase at Humo is less well constrained, and gaps in the stratigraphy make the eruptive history less clear. The eruption began with the development of an angular lapilli pumice fall deposit, almost devoid of lithic clasts, but containing large ballistic pumices. This would suggest this is relatively proximal pumice fall, probably within a few hundred meters of the vent. Though the exact source location is not known, it is potentially buried, forming the hill underneath the Humo phase 3 pumice cone. This fall deposit is followed by the column collapse, and the generation of a PDC. These PDCs were fine grained and dilute. Whilst dilute PDCs can be formed during column collapse events, this tends to occur when a PDC with a concentrated base experiences a hydraulic jump (e.g. Douillet et al. (2013)), or when the upper dilute portion of a more concentrated flow decouples due to topographic flow-stripping (Branney and Kokelaar, 2002; Williams, 2010). It is also important to note that ignimbrites only represent the portion of the current which is

depositing sediment, and so these dilute facies may represent a trailing dilute section of an otherwise accelerating concentrated current. Considering the lack of context and exposure, it is challenging to ascribe a particular origin. Regardless, the eruption returns to a relatively stable bouyant eruption column phase, depositing further lapilli pumice fall deposits.

The following gap in the stratigraphy makes the transition to the next phase of the eruption unclear, and it is possible that the remaining units are in fact produced by a separate eruption. However, in the absence of evidence to the contrary, I favour the simpler explanation that they are the product of the same eruption. The next phase of the eruption, sourced somewhere uphill and south of Humo gorge, was further column-collapse, generating a concentrated-based PDC that deposited unit H12, largely filling Humo gorge before spreading and thinning at its mouth to the north. The deposit is full of lithic clasts, which may provide a clue to why the column collapsed. The lithics are sourced from conduit erosion, and are denser than the pumices. The erosion and widening of the conduit can lead to an inability for the column to entrain enough air to heat and maintain buoyancy, compounded by the greater bulk density of the erupted material, leading to its collapse (Wilson et al., 1980b). This was followed by the production of another PDC, this time more pumice and ash rich. There was sufficient time after the deposition of this ignimbrite for co-ignimbrite ash to settle on top. The final stage of this eruption is marked by a final dilute PDC, and subsequent co-ignimbrite ash.

The final phase of eruptive activity in the Humo region is very similar to that at other pumice cones around Aluto. As at Kertefa, the eruption initiated with the development of a pumice lapilli fall deposit followed by column collapse and a pyroclastic density current. This is prior to the main cone-building phase of the eruption, and blanketed an underlying hill. The eruption column then re-established, with material dropping from its edge forming an ultraproximal cone comprising a thick poorly sorted pumice fall deposit (H19). To begin with, the slope was not sufficiently steep to elicit slumping, resulting in a massive deposit with fractured but whole pumices. As the cone grew, the sides steepened, eventually leading to small granular flows developing on its surface. This convecting eruption column phase continued, though the stratification of deposits further up the section indicates that

the column became unsteady. There is a reduction in grain size, perhaps indicating that the mass eruption rate was reducing, and the column waning. However, without rigorous isopach and isopleth maps, I cannot deconvolve whether variations in grain size are a result of mass eruption rate, total grain size distribution, or changing wind direction. The final deposits of the eruption can be found from the foot of the cone, partially filling the Humo phase 1 crater. These deposits indicate the waning eruption column finally collapsed, generating a PDC that deposited ignimbrite H24. Following the eruption, material was clearly re-mobilised by water, forming the bubble-rich ash deposit H25. There might have been shallow standing water, through which the finest grades of ash settled to form the finely laminated H26 ash. Further re-mobilisation events then deposited two reworked units on top. The lack of intercalated primary deposits indicates that this occurred after the eruption had finished. At the majority of pumice cones at Aluto, the eruption ends with the effusion of a silicic lava flow. From the DEM, it is clear that the crater of the Humo phase 3 cone is filled by such a flow. However, the topography is muted by overlying pyroclastic deposits, and it is challenging to identify whether the lava is sourced from Humo phase 3, vents up-hill and to the south of Humo phase 3, or both. It is likely that Humo phase 3 ended with the production of a silicic lava flow, but it is not conclusive. The silicic lava flows that overlie the phase 3 deposits are themselves overlain by another obsidian flow that has been Ar-Ar dated to 61 $\pm$ 8 Ka (Hutchison et al., 2016c), indicating that the entire Humo sequence pre-dates this, currently representing the oldest known pyroclastic stratigraphy in the caldera after caldera collapse.

3.6.3 Other Field Sites

There are numerous other field sites I investigated in the central region of Aluto. Many of them have limited exposure, or there was insufficient field-time to investigate them in great detail. However, they do provide further evidence to determine the nature and processes of pumice cone forming eruptions. In the following section, I describe and discuss three of these sites: *Gabiben Pumice Cone* in the NW corner of the caldera floor, *Quarry pumice cone*, and *Central pumice cone*, both on the eastern edge of the caldera floor near Aluto

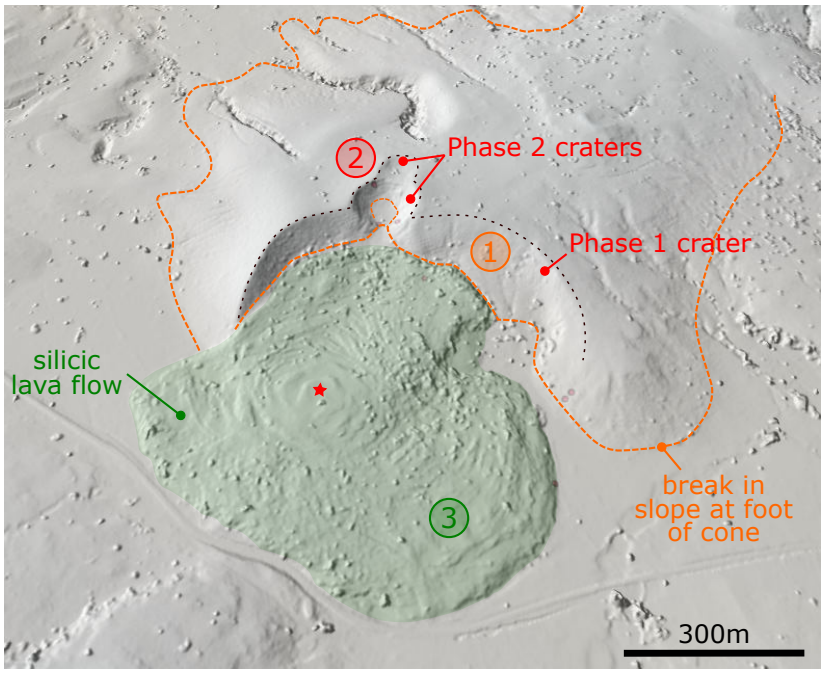

Figure 3.48: *3 dimensional view of Gabiben pumice cone and a brief summary of its eruptive history. A red star marks the source location of the silicic lava flow. Orange dashed lines mark the break in slope at the bottom of the cones and the red dashed lines mark the crater-rims. DEm from Hutchison et al. (2014).*

geothermal power station. The location of these sites is shown in Figure 3.39.

Gabiben Pumice Cone

Gabiben pumice cone, named by the local children who play on its flanks, is a shallow relief pumice cone, similar to Humo phase 1, with two or three overlapping craters. The main cone is crescent shaped, with its crater filled by a silicic lava flow. The pumice cone, with its 2/3 craters, lines up with a further two relatively small obsidian lava flows and shallow pumice cones to the NE, each about 1300 m apart. The vents are interpreted to lie along a regional Wonji fault that cuts this section of the volcano (Hutchison et al., 2015). An overview of Gabiben can be found in Figure 3.48.

The eruption can be divided into 3 main phases. The first phase involved the deposition of the main shallow pumice cone. Small superficial exposures indicate the upper portion

of the cone comprises a massive lapilli to block grade pumice breccia with fractured but whole pumices and a variety of lithics. The deposit is very similar to others seen in the earlier stages of pumice cone eruptions elsewhere at Aluto. The slope never reached a sufficient angle for the deposit to transition to a granular flow-bedded pumice lapilli deposit. The crescent shape of this cone suggests the wind was blowing to the NW at the time of the eruption, and the column was relatively weak, allowing it to be bent over to the NW. There is no evidence of PDCs being generated by this eruption, though there is very little exposure to base this on, and any ignimbrites are likely to form part of the flat, unexposed caldera floor.

The second phase of the eruption involved the creation of a second and possibly third crater. The eruption phase that produced the second crater also constructed a small ring of tephra. The steep walls of the second crater expose numerous sections of bedded pyroclastic material that dip away from its center. Where this second crater intersects the first, adjacent exposures show that beds dip inwards towards the centre of the phase 1 cone (Figure 3.49). The deposits at the intersection of these two cones is highly disorganised, and hydrothermal alteration and talus makes it very challenging to interpret. It is possible the second crater may have developed during the later stages of the first. There is significant hydrothermal alteration around the crater walls, with much of the pyroclastic material altered to clay. There are small visibly degassing fumeroles emanating from the northern and SW crater walls. The gas does not smell sulphurous, indicating that SO_2 is not a major component with a concentration of <4.7 ppm (Kleinbeck et al., 2011). Fumeroles, surface alteration and greater gas fluxes coincide with faults at Aluto (Hutchison et al., 2015; Braddock et al., 2017); the Gabiben eruption might have also taken advantage of the same permeable pathway. The alteration of the deposits exposed in the phase 2 crater make them difficult to interpret, but comprise lapilli to block sized pyroclastics with some obsidian lithics. It is hard to tell whether the matrix consists of primary ash, or altered material. There is a small third crater intersecting the NW of the main phase 2 crater. It is around 2 m deep, and 50 m in diameter. As it is entirely destructive, only excavating a hole rather than building any substantial cone, it may be the product of a phreatic explosion.

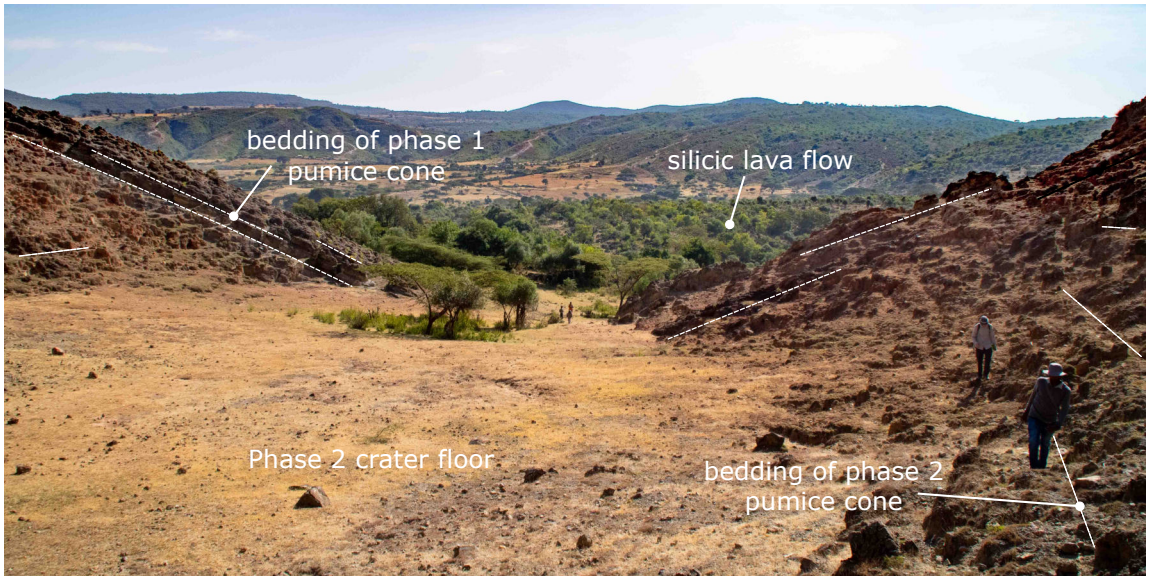

Figure 3.49: *Photograph showing the Gabiben phase 2 crater. The beds where the phase 2 pumice cone intersect the phase 1 pumice cone dip towards the centre of the phase 1 crater. Within phase 2, the beds dip away from the center of the crater. The interface between the two is complex, and implies they might have been erupted contemporaneously. The picture is taken facing SE through the intersection between the two pumice cones.*

The final phase of activity at Gabiben is marked by the emplacement of a silcic lava flow. This is one of the most accessible flows at Aluto, and appears relatively fresh and un-buried, making it one of the better sites to study the obsidian lavas that coat much of Aluto's topography. Unfortunately there is no absolute age constraint on this lava, but the fresh appearance of the obsidian, and the lack of burial suggests that it is relatively young. Petrographically, the obsidian is crystal rich; around 30% crystal by volume in sample MER-17-03A (Figure 3.50). The main crystallising phases are quartz + K-feldspar + aegirine + aenigmatite, set in a relatively unaltered glass. Many of the phenocrysts comprise a K-feldspar core with a granophyric quartz and K-feldspar rim. The rim often captures existing phenocrysts of aegirine and aenigmatite during its growth. Granophyric textures are thought to develop during rapid crystallisation near eutectic conditions often during volatile saturation (Lentz and Fowler, 1992), as a product of significant undercooling (Morgan and London, 2012). Late-stage rapid crystallisation promotes disequilibrium conditions; where the crystallising boundary region oscillates between Si over- and under-saturation due to repeated Al depletion and saturation from feldspar growth. During Si-undersaturation, alkali-feldspar grows, depleting the melt in Al; leading to Si over-saturation. When this

occurs, quartz growth is promoted, depleting the melt of Si, providing time for diffusion of Al back into the crystallisation boundary region. This process repeats itself, promoting the localised oscillatory growth of Quartz and feldspar on a microscopic and sometimes macroscopic scale (Lentz and Fowler, 1992; Morgan and London, 2012). Undercooling in lavas is generally thought to be a result of three non-mutually exclusive processes: (1) adiabatic cooling during the decompression of the gas phase, (2) the gas phase, which suppresses the liquidus, may be suddenly lost, upsetting equilibrium and (3) rapid cooling on contact with the atmosphere (Sparks and Pinkerton, 1978). The granophyres at Aluto are indicative of the third effect: granphyric textures usually permeate the entire ground mass, but at Aluto form discrete clusters with euhedral to subhedral edges (Figure 3.50b). This implies that granophyric crystallisation was halted before completion, with most of the melt quenching to glass. This is most probably due to thermal quenching on eruption. Though much of the crystal cargo in the porphyritic obsidian at Aluto is developed during storage, a significant proportion of it is therefore grown in situ, on emplacement. The crystal fraction of a magma or lava strongly influences the bulk viscosity (Einstein, 1906; Costa, 2005), and so the timing of the growth of crystals is of critical importance when identifying how the viscosity of these lavas evolves during eruption and emplacement. Any investigations into the bulk rheological behaviour of these flows should consider that a large proportion of the crystal fraction grows rapidly *after* extrusion (Pinkerton and Sparks, 1978).

Aluto Quarry

Aluto Quarry, on the eastern reaches of the caldera floor, is the source for much of the building material used to construct the roads on the edifice that service the geothermal power station. This has left a large hole in the side of a pumice cone, and an opportunity to access stratigraphy unusually deep into the cone. The Quarry was omitted from the first field expedition as it was occupied by a troop of baboons. Though they were no longer there during the second expedition, there was limited time resulting in a lack of detailed logs. This site presents a superb opportunity to study a pumice cone in detail during future investigations. An overview of the Quarry, and its relationship to the rest of the cone, can be seen in Figure 3.51. The pumice cone has an elongate fissure-like crater;

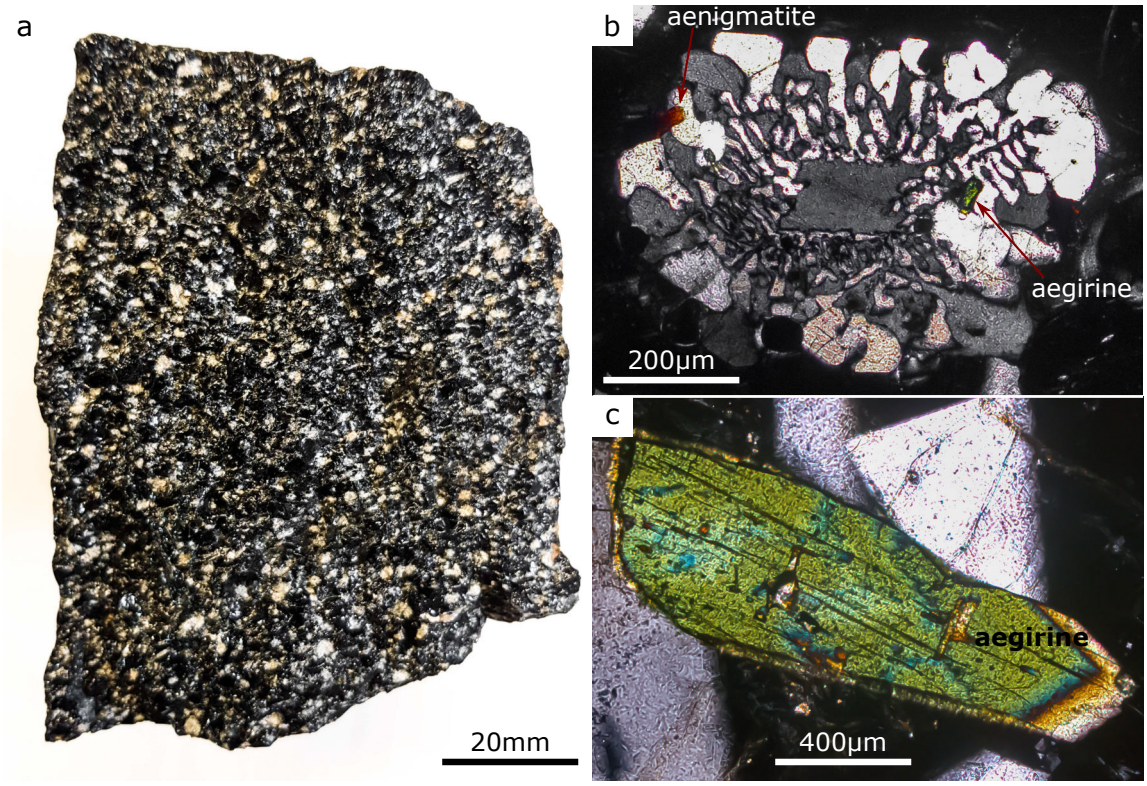

Figure 3.50: *Images of sample MER-17-03A, a porphyritic obsidian from the Gabiben phase 3 lava. This is a relatively fresh example of a porphyritic obsidian lava flow typical of those at Aluto. This example shows the typical assemblage of Quartz + K-feldspar + Aegirine + aenigmatite. (a) Hand sample image showing white anhedral to subhedral phenocrysts in a black glassy groundmass. (b) Thin section of a typical 'phenocryst' in Aluto obsidian lavas. The phenocrysts comprise a K-feldspar core with a granophyric rim where quartz and K-feldpsar are intergrown. There are often smaller aegirine and aenigmatite crystals trapped in the granophyric rims. (c) Aegirine is a major crystallising phase in these rocks.*

similar to that at Kertefa. The fissure follows a NNE trending normal fault zone, known as the 'Artu Jawe fault zone' (Hutchison et al., 2015), which forms a near-vertical 50 m tall scarp cutting the caldera floor. Numerous pumice cones, including Awariftu, follow the trend of this fault to the NNE and it is thought to have provided a permeable pathway for magma, and more recently gases, to reach the surface (Hutchison et al., 2015).

From the overview (Figure 3.51), the base of the cone can be clearly identified by a break in slope. At the southern end of the cone, the crater forms a crescent shape, with a lava flow emanating from the opening. The surface of this flow is buried, and its topography is muted, though small exposures at its front indicate that it is a silicic lava flow. The deposits covering this lava flow are modern, probably deposited during the rainy season during particularly heavy rain; indicated by the very large boulders strewn across the surface, and the well developed drainage system running from the top of the cone, roughly following the path of the fault towards the south. In a broad sense, the eruption followed a similar pattern to pumice cones elsewhere on Aluto: initially generating a pumice cone, and finishing with the emplacement of an obsidian lava flow. The resemblance continues close-up. The bottom of the quarry (the stratigraphically lower portion of the cone) comprises a very coarse, block-sized massive pumice breccia (Figure 3.52 a,c,d). The breccia comprises angular pumices, many of which contain distinct cm scale zones of either fibrous or isotropic vesicles. The deposits also contain a variety of lithics, including welded ignimbrite, non-obsidian lavas, dense obsidian and pre-Aluto sedimentary rocks. Amongst this assemblage are deposit quenched pumiceous achneliths (DQAs), identical to those described in Clarke et al. (2019). Though the massive deposit looks like it might have formed by modern slumping of the quarry side, these DQAs are ductiley-deformed against adjacent clasts, indicating the deposit last moved when the clasts largely exceeded their glass transition temperature. This shows that the deposit is primary. The center of the nearest crater is around 300 m away, further than the 185 m maximum distance pumiceous achneliths of this size should be able to travel via ballistic trajectories (Clarke et al., 2019). Considering these pyroclasts are still largely above their glass transition temperature at deposition, and thus took less than around 30 seconds to get there, they must have fallen from the edge of an eruption column, rather than from an umbrella cloud. The

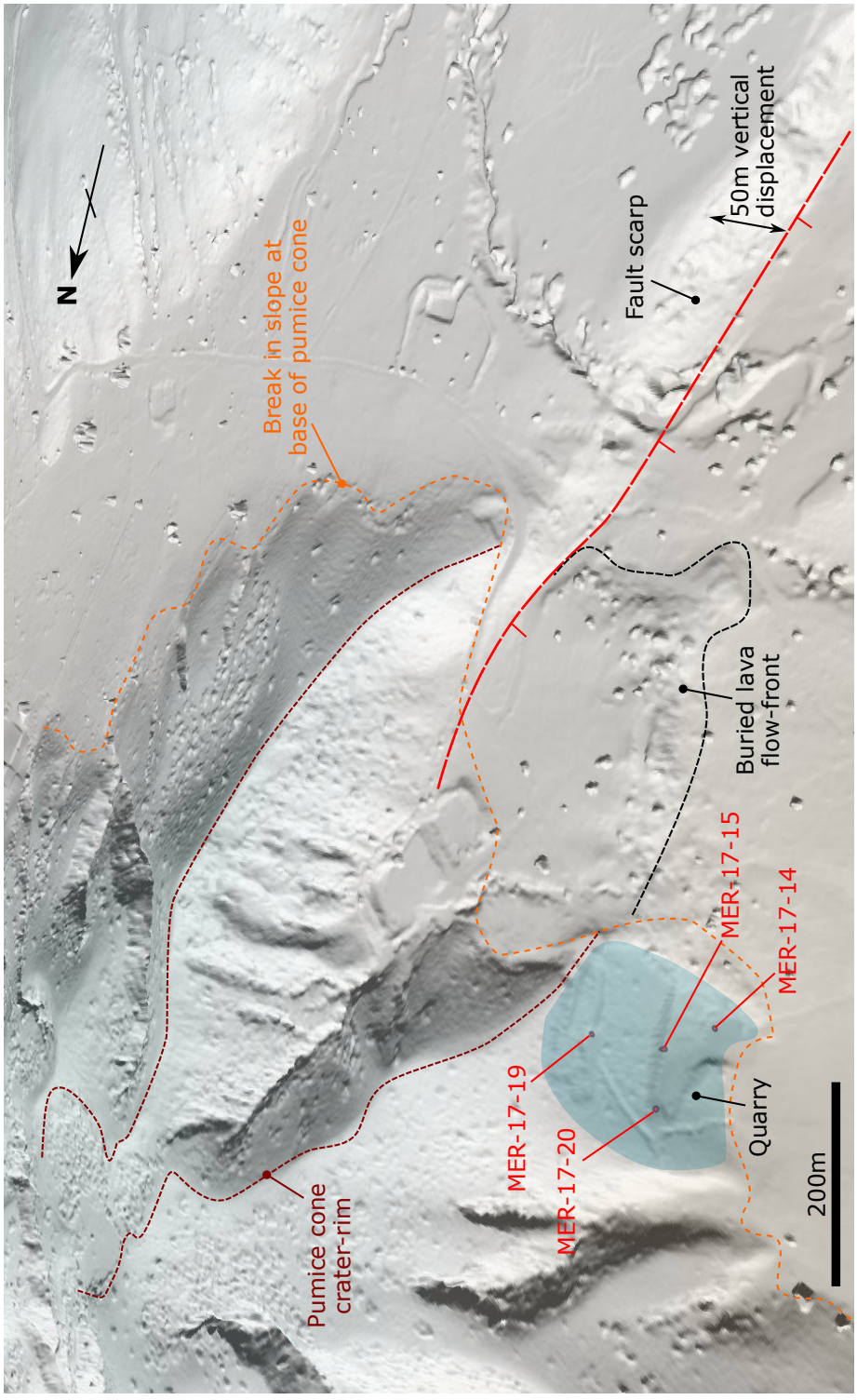

Figure 3.51: *A 3 dimensional overview of the Quarry pumice cone and its surroundings. The cone sits on a NNE trending normal Wonji fault, parallel with the long axis of its crater. Aluto quarry is cut into the south-western most portion of the cone. DEM source: Hutchison et al. (2014).*

deposit is clast supported, with a complete lack of matrix material and very poorly sorted. It is very similar to the massive pumice breccias seen time-and-time again at the base of pumice cones around Aluto. Further up the succession, the deposits become bedded, and by MER-17-19, at the top of the cone close to the crater rim, they look very similar to the granular flow bedded units seen at Humo and elsewhere (Figure 3.52b). The deposit here was sieved, the results of which can be found in Appendix C.2 under sample number MER-17-19A. It has a median grain size of -3.53 ϕ, and is moderately sorted at 0.68 ϕ. Apart from the absence of pumiceous achneliths, the componentry of this deposit is very similar to the base, though with a lesser proportion of lithic clasts and a finer lapilli grain size. The absence of pumiceous achneliths is notable, and investigation of the deposits half way between the top and bottom (at MER-17-20) confirm that the proportion of pumiceous achneliths decreases towards the top of the pumice cone deposits. The deposit here was sieved, the results of which can be found in Appendix C.2 under sample number MER-17-20A. It has a median grain size of -3.95 ϕ, and is moderately sorted at 0.53 ϕ. There are no PDC deposits found on the cone slope, though that is perhaps to be expected considering that PDCs are unlikely to be depositing material so proximally on a steep slope (Branney and Kokelaar, 2002). At Humo for example, PDC deposits are absent on the phase 1 cone, but are present at more distal localities, and at Humo phase 3, collect off the main cone without appearing on its flanks.

The eruption of the quarry pumice cone initiated with a column-forming phase, producing an ultraproximal massive pumice breccia that built the foundation of the cone through the accumulation of pyroclastic and lithic material falling from the edge of an eruption column. As this accumulated the sides steepened, eventually resulting in the localised slumping of fall material and the generation of small granular flows down the flanks of the pumice cone. As the column subsided, it may or may not have generated PDCs. The final stage of the eruption involved the generation of a silicic lava flow. More recently, the cone's morphology has been significantly modified through erosion, presumably during Ethiopia's rainy seasons.

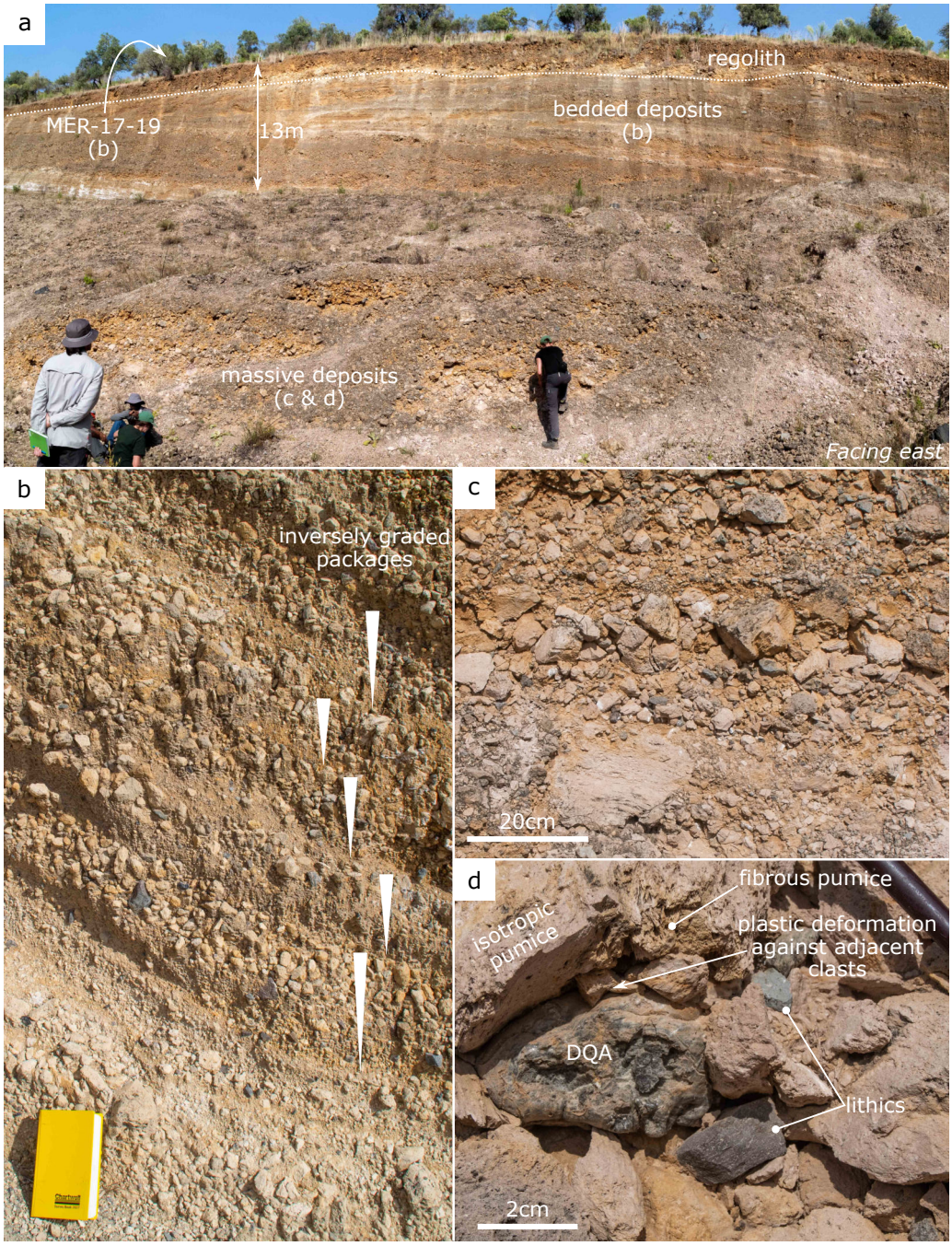

Figure 3.52: *Photographs displaying key features of the Quarry pumice cone. (a) An overview of the quarry, showing massive pumice breccias at the base, turning into bedded units towards the top. Letters underneath the annotations refer to the other plates in this figure. MER-17-20, the location of image 'b' is another smaller quarry located atop the ridge in this photo. (b) Small graded granular-flow packages of pumice lapilli. These beds are discontinuous on a 1 to 10m scale. Pumiceous achneliths are absent from this part of the deposit. Fine ash in this photo is superficial surface wash, and is nearly absent when fresh deposit is exposed. (c) Massive deposit close to where photo 'a' was taken at the base of the quarry. Very poorly sorted pumice breccia with a high proportion of lithics and pumiceous achneliths. (d) Close-up view of the massive pumice breccia. Pumiceous achneliths deform against adjacent clasts showing this is a primary deposit.*

Central Pumice Cone

Central pumice cone sits just NW of the quarry pumice cone. Exposure in the cone is limited, but a small road-cut along its western edge (MER-17-01), in addition to two small gorges incised into the rear (eastern wall) of the cone (MER-17-22), provide some insights. A 3D overview of the cone is presented in Figure 3.53.

The cone itself is built from a massive pumice breccia comprising angular pumice lapilli, a variety of lithics, pumiceous achneliths (some up to 30 cm in diameter), dense obsidian and breadcrust bombs. There is some matrix material, though the deposit has experienced significant alteration to clay. This is yet another example of an initial shallow pumice cone comprising a massive pumice breccia. The slopes did not become steep enough to develop granular flow structures. The crescent shape of the cone indicates that there was an eastward wind blowing during the eruption, and that the eruption column was relatively weak, bending over in response. There is a small silicic lava flow on the southern arm of the crescent-shaped pumice cone; this is unusual, as in most cases around Aluto, silicic lava flows emanate from the center of the main crater of their source pumice cone. It's not particularly clear why this has occurred in this instance. The eastern wall of the pumice cone hosts a steep fronted silicic lava flow. To either side of the flow are small gullies (Figure 3.53a), marking the unconformable, near vertical contact between the lava flow and the adjacent massive pumice breccias of the original pumice cone. The base of lava flow rests on the same material, perched around 1/3 of the way up the wall of the pumice cone. The lava flow thus occupies a box-shaped hanging-valley incised into the rear of the cone. The lava flow at this location is around 35 m thick, much thicker than many of the flows at Aluto, which are often only around 10 m (eg. Gabiben). This suggests the flow had cause to inflate, occupying vertical space rather than continuing to flow down hill; in other words, it reached a blockage. In front of the lava flow, sits a fan of material that partially fills the crater of central pumice cone, and onlaps the first silicic lava flow (Figure 3.53b). This material might have originally filled the hanging valley that silicic lava flow 2 now occupies, and shows that silicic lava flow 2 was emplaced after central pumice cone and silicic lava 1. The most probable source of silicic lava flow 2 is from another vent

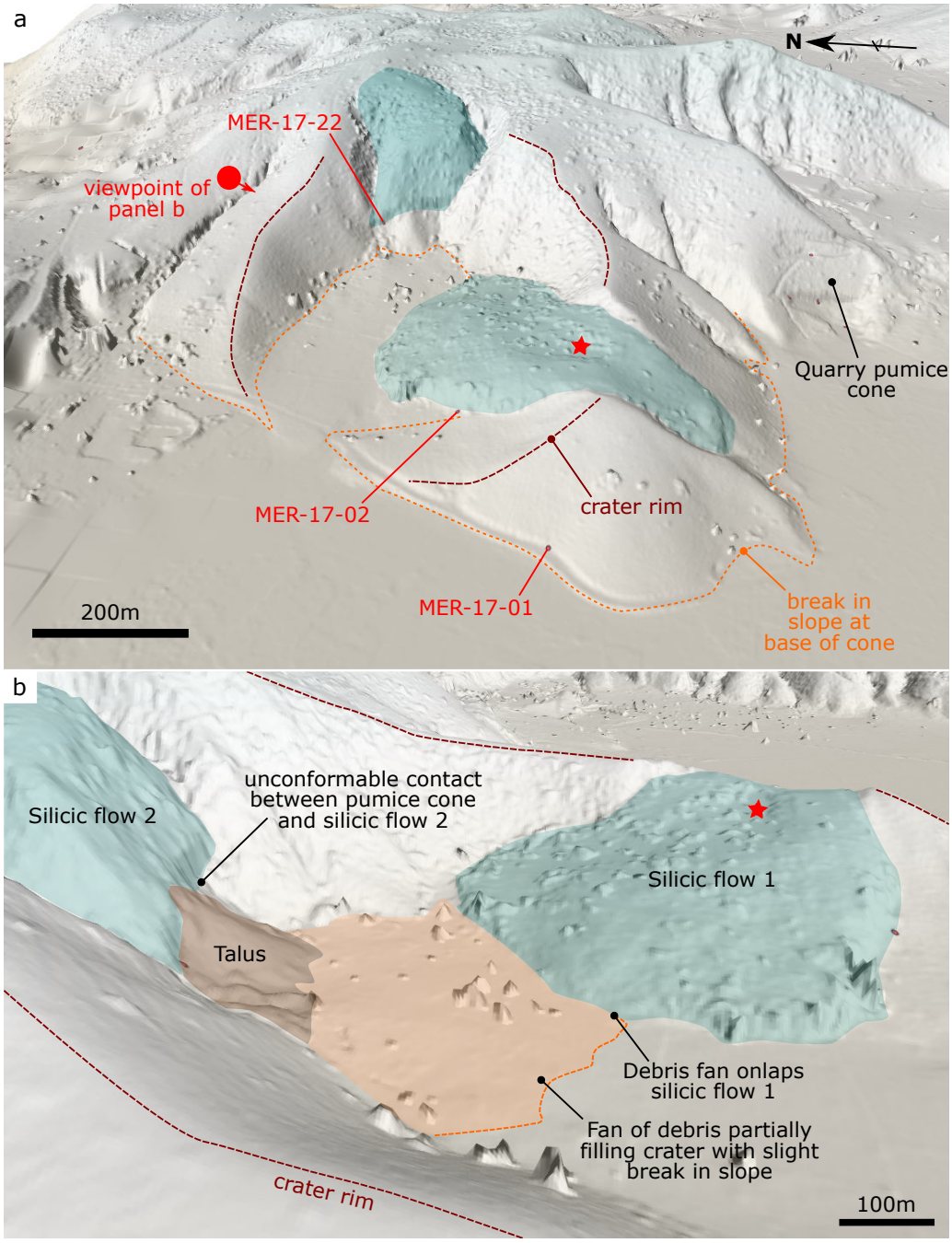

Figure 3.53: *3 dimensional overviews of Central pumice cone. (a) the whole pumice cone, with its crescent morphology. The cone is partially subsumed by the later Quarry pumice cone to the east. Orange dashed lines show the break in slope, and red dashed lines show the crater rim. The red star marks the source of silicic lava flow 1. (b) Oblique view of the central pumice cone, showing the main geomorphological features of the cone. Silicic flow 2 forms the rear wall of the cone and has a steep fan of talus at its base. This talus sit on top of a very low relief fan of material, perhaps the remnants of central cone's collapsed rear wall.*

of the Quarry pumice cone described in the previous section. A plausible scenario is that sometime after the production of central pumice cone and its obsidian lava flow, the quarry cone eruption began, partially burying the eastern flanks of central cone and subsuming it. The final stage of the quarry cone eruption involved the emplacement of silicic lava flow 2, which, whilst flowing down the side of its cone, encountered the outer eastern wall of central pumice cone. This blocked its path, at which point the flow began to inflate and grow thicker. Lava flow inflation is most commonly associated with basaltic volcanism (Walker, 1991), but has been recognised more recently in silicic lavas (Griffiths and Fink, 1997; Tuffen et al., 2013), and relies on the development of an insulating upper crust, allowing the interior of the lava to continue to flow and accumulate without freezing. Once the lava flow had gained sufficient mass to overcome the strength of the pumice cone wall, it broke through, bulldozing the eastern wall of central pumice cone producing a debris avalanche forming the fan that now partially fills the crater of central pumice cone. The flow had apparently cooled sufficiently whilst it stalled, so that it did not flow extensively through the gap it created. The steep talus at the front of the lava flow mainly comprises blocks of obsidian, and probably represents unstable or overhanging lava, no longer supported by the wall of central pumice cone. This processes is graphically depicted in Figure 3.54.

In non-rhyolitic systems, lava flows have commonly caused the collapse of their parent cone, typically through undercutting and rafting of the overlying cone (e.g Sumner, 1998; Sohn and Chough, 1993). Although in the case of central pumice cone, the lava flow collapsed an adjacent cone, it shows that it is entirely plausible that localised pumice cone collapses can occur during the final obsidian flow-forming phases of pumice cone eruptions. If a pumice cone were to collapse whilst perched on a tall, steep slope, it is possible that such debris avalanches may present a considerable hazard. This may have happened at two adjacent pumice cones on Aluto's steep SW flank (Figure 3.55). In each case, there are large obsidian lava flows emanating from the craters of these cones. Remnants of pumice cone flank and crater rim still exist on the eastern side of the flows, but on the steep western side, they are absent. It may be the case that the pumice cone only developed on the western side of the vent due to a strong wind during deposition. However, it is also possible that the absent eastern flanks of the pumice cones were pushed down the steep

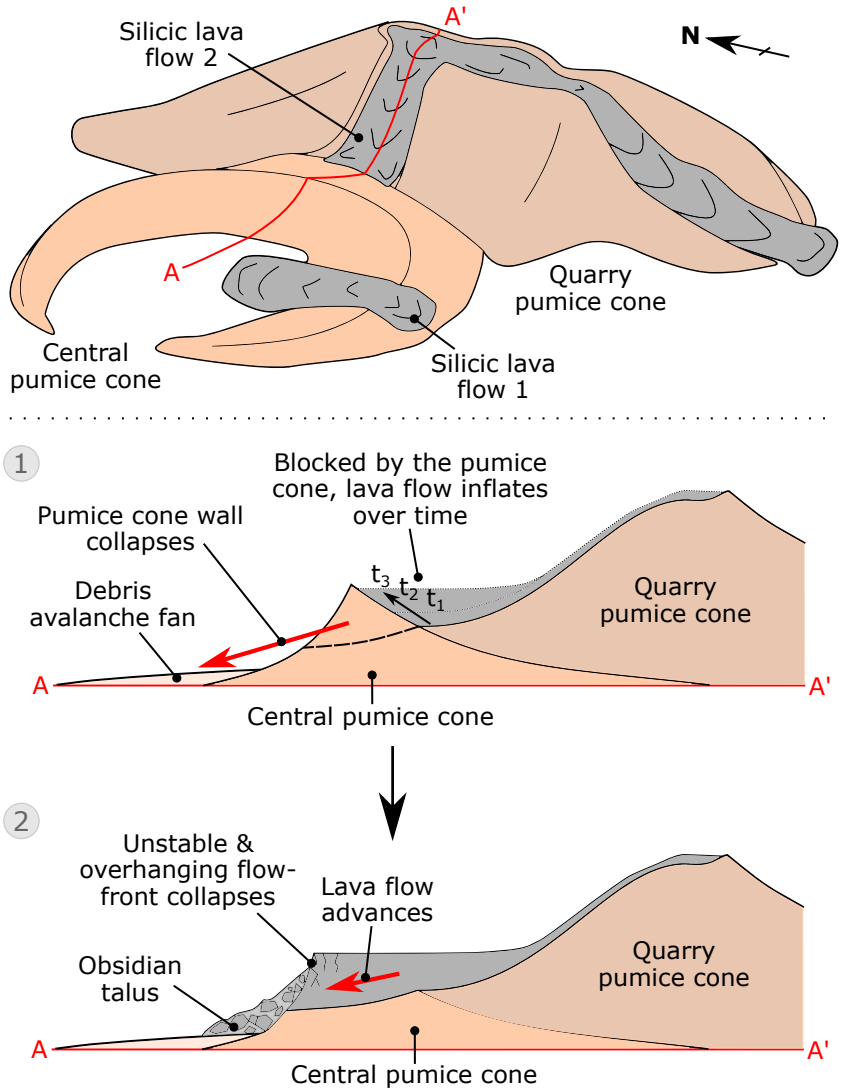

Figure 3.54: *Diagram showing the processes leading to the collapse of the easterly wall of Central pumice cone. Silicic lava produced during the Quarry pumice cone eruption piled up against the outer wall of central pumice cone. Eventually the wall gave-way, producing a debris avalanche fan partially filling the crater. The lava flow advanced, and unstable and overhanging lava flow collapsed at the flow front developing a talus slope. Not drawn to scale.*

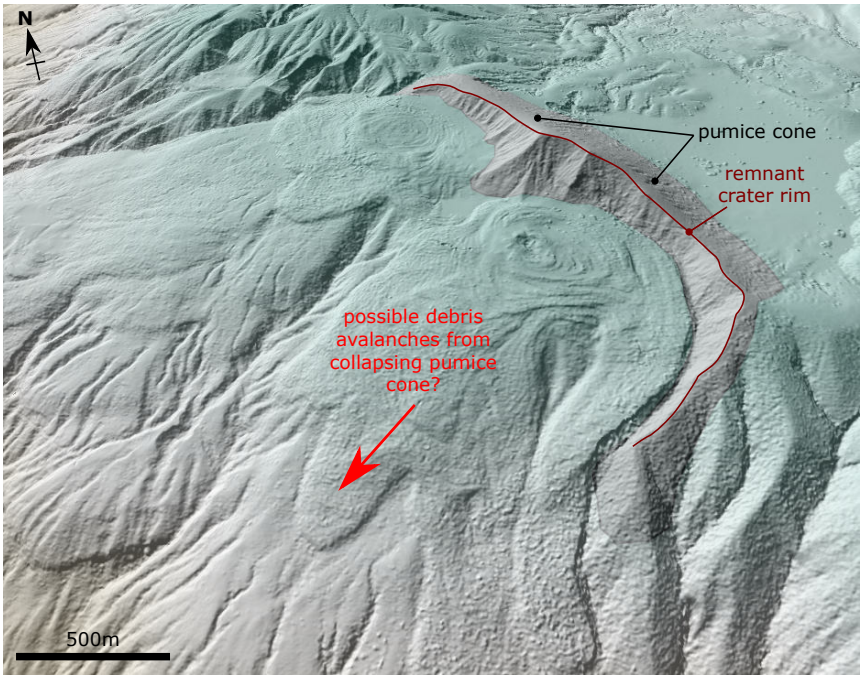

Figure 3.55: *Central pumice cone has shown that pumice cones can collapse under the weight of an advancing silicic lava flow. This figure shows two pumice cones with large obsidian lava flows on the SW rim of the caldera. Pumice cone structures only exist on the eastern side of the vents, and it is possible that the western portions of the cones, as they were deposited on the steep volcanic flank, collapsed under the weight of their lava flows. This might have produced debris avalanches, which if similar volume to the eastern portion of the cones, could be on the order of* $1.5 \times 10^6 m^3$ *in volume.*

slopes by their obsidian lava flows. Further investigation is needed to verify whether this did indeed happen, but it is plausible that large debris avalanches might have accompanied the final lava-flow forming stages of these pumice cone forming eruptions. If the volume of the missing flanks were similar to those remaining, these avalanches could have been on the order of 1.5×10^6 m^3 in volume.

3.6.4 Summary

Aluto's central region hosts a multitude of vents, each on a different scale, but undergoing very similar eruption processes. Two vents in the Humo region, one at Gabiben, one at central pumice cone and another at the quarry pumice cone all underwent the same sequence of pumice cone growth, followed by the effusion of a silicic lava flow. All of these examples began with the development of a shallower cone comprising massive pumice

breccias. The presence of deposit quenched pumiceous achneliths within these breccias >150 m from the vent at quarry and central pumice cones provide additional examples where such deposits are generated by the ultraproximal accumulation of tephra around the vent from column-edge deposition. Twice at Humo and once at quarry pumice cone, this shallow cone grew tall enough for the flanks to reach the repose angle of the constituent material, forming granular flow-bedded pumice lapilli fall deposits. On two occasions at Humo, PDCs were generated after the cone-building phase. It is possible PDCs were also generated at the other sites, and the absence of PDC deposits may result from a lack of proximal deposition on steep cone slopes, and a lack of medial exposure, though this cannot be confirmed without futher evidence. Finally, on one occasion at Humo, and at Gabiben, quarry and central pumice cones, silicic lava flows marked the end of the eruption.

In addition to providing more examples of pumice cone eruption sequences, the deposits in the central region provide some additional insights. Firstly, both Gabiben and Quarry pumice cones are situated above regional faults. This is commensurate with the findings of Hutchison et al. (2015) that such features provide structural pathways for magma to migrate to the surface at Aluto. Secondly, the obsidian lava flow at Gabiben indicates that though porphyritic on eruption, much of the crystal growth occurred during emplacement, which is likely to have a significant influence on the flow's viscosity over time. Thirdly, the presence of many reworked deposits and ignimbrite explosion pits at Humo suggests that the caldera has, in the past, hosted a shallow body of water. And finally, the breached western wall of central pumice cone by a silicic lava flow indicates that local pumice cone landslides may be a feature of the final silicic lava flow emplacement stage of pumice cone eruptions. If such a cone collapse were to occur in an unfortunate location, such as on the caldera rim, these mass flows might represent a significant hazard.

3.7 Discussion: Pumice cone forming eruptions at Aluto

The purpose of this fieldwork was to understand the range of eruptive activity that has taken place since caldera collapse at Aluto volcano, and whether there are typical styles or

patterns of eruption that might inform us of how future eruptions at Aluto may progress. From the digital elevation model, the dominant style of eruption at Aluto appears to be the generation of pumice cones, followed by the emplacement of silicic lava flows. Throughout this fieldwork I have investigated the proximal deposits from 9 of these pumice cone eruptions, in addition to the medial deposits from a number of eruptions on the southern flank, most probably, though not conclusively, associated with the pumice cones at the top of the slope. From these observations, a consistent picture of pumice cone forming eruptions has emerged. The variation in the size of different pumice cones and silicic lava flows indicates that eruptions occur across a range of scales. However, the style and sequence of eruption is very similar from event-to-event, regardless of the scale. Common stages include an initial explosive phase, generating a column and pumice lapilli fall deposits (*initial fall*), followed by the collapse of the column to generate a PDC and ignimbrite (*initial flow*). All pumice cones then generate a massive pumice breccia (mPbr), that develops a relatively shallow ring or fissure like structure that shows relatively rapid thickening towards the vent (*shallow mPbr cone*). Evidence from 4 separate cones (based on the presence, location and size of pumiceous achneliths) indicates they were developed from the ultraproximal fall deposits sourced from the edge of an eruption column. If this phase of the eruption persists, the cones grow taller, developing steeper flanks and generating granular flow bedded pumice lapilli fall deposits (*over-steepened cone*). Following this, the column becomes unsteady, generating PDCs, often this phase involves inter-bedded fall and PDC deposits, indicating that the column repeatedly re-establishes and collapses. The final stage of the eruption in all but one case is the emplacement of a silicic lava flow, creating an obsidian lava flow or couleé. Figure 3.56 provides a side-by-side comparison of how each eruption investigated in this chapter progressed through these steps.

From this evaluation, we can conclude that post-caldera eruptions at Aluto occur in a very similar fashion. We do not have enough examples to produce statistically significant results, but there are clear commonalities between these events that are useful in defining the probable styles and hazards that we might expect during a future eruption. From this evaluation of pumice cone eruption sequences at Aluto, I have developed an idealised pumice cone eruption sequence, which is presented graphically in Figure 3.57. Approaching

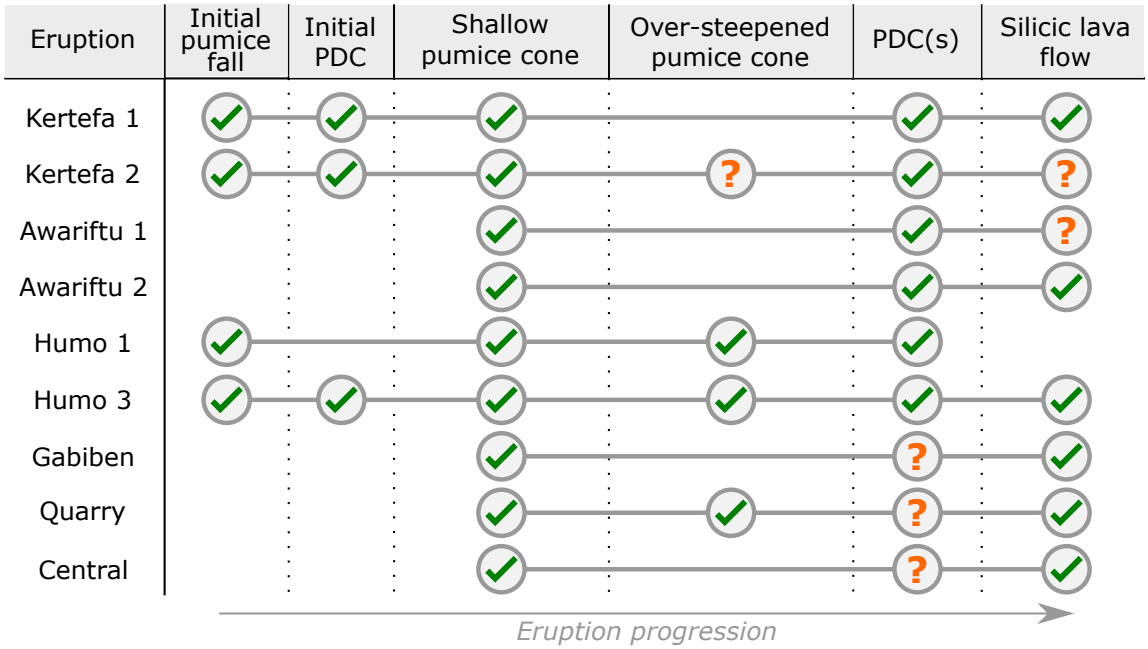

Figure 3.56: *Comparison between the pumice cone forming eruptions at Aluto. I have omitted the eruptions on the southern flank of the volcano as well as Humo phase 2, as only the medial (non-cone-forming) deposits were investigated. Each eruption progresses from left to right, with a tick indicating geological evidence for the relevant event having occurred, and a question mark indicating that an event might have occurred but there is not conclusive evidence either way. The absence of an event in the geological record is shown by an absence of a marker.*

half of the eruptions began with an initial pumice fall and PDC forming phase, associated with the production and then collapse of a convective eruption column. Every eruption generated a shallow pumice cone or rampart, comprising massive pumice breccias that in 3 of the 9 cases have evidence for having been built from the edge of an eruption column. In all but three cases, there is conclusive evidence that eruption columns then collapsed to produce PDCs. It is clear therefore, that unstable convective eruption columns, and crucially the PDCs which they produce, are a common feature of pumice cone forming eruptions at Aluto.

The facies sequence of pumice cone growth is very similar to that described in basaltic scoria cone systems: a shallow massive cone develops, grows and steepens, eventually leading to the granular flow of the constituent material when the repose slope is attained, allowing horizontal growth beyond the ballistic limit (McGetchin et al., 1974; Sohn and Chough, 1993). More recent work on basaltic scoria cones has attributed the bulk of their growth to the accumulation of material from the edge of an eruption column (Riedel et al., 2003; Martin and Németh, 2006), the same process invoked here. However, a key distinction between basaltic scoria cones and pumice cones at Aluto, is that basaltic scoria cones may be persistently active for months to years (Wood, 1980), and after their initial intense-phase, continue to grow slowly through accumulated ballistic deposition from low intensity strombolian venting (Taddeucci et al., 2015). During pumice cone forming eruptions at Aluto, there is no evidence of a significant time gap occupied by ballistic cone growth between the intense cone-growth and PDC forming phase, and the end of the eruption marked by a lava flow. Much greater similarity can be attributed to plinian cone-forming eruptions (Figure 3.58), such as the 1912 eruption of Novarupta (Fierstein et al., 1997), the 1932 eruption of Quizapu (Hildreth and Drake, 1992), and the 1886 eruption of Tawawera (Walker et al., 1984). In each of these cases, shallow cones of tephra accumulated around the respective plinian vents or fissures from column-edge deposition (Riedel et al., 2003). A similar cone structure also developed around the 2011 Cordón Caulle plinian vent, which produced PDCs and an obsidian lava flow (Pistolesi et al., 2015; Schipper et al., 2019). However, the cone at Cordón Caulle has not been the subject of thorough investigation, mostly due to the lack of cross-sectional exposure. In most cases, the deposits of plinian

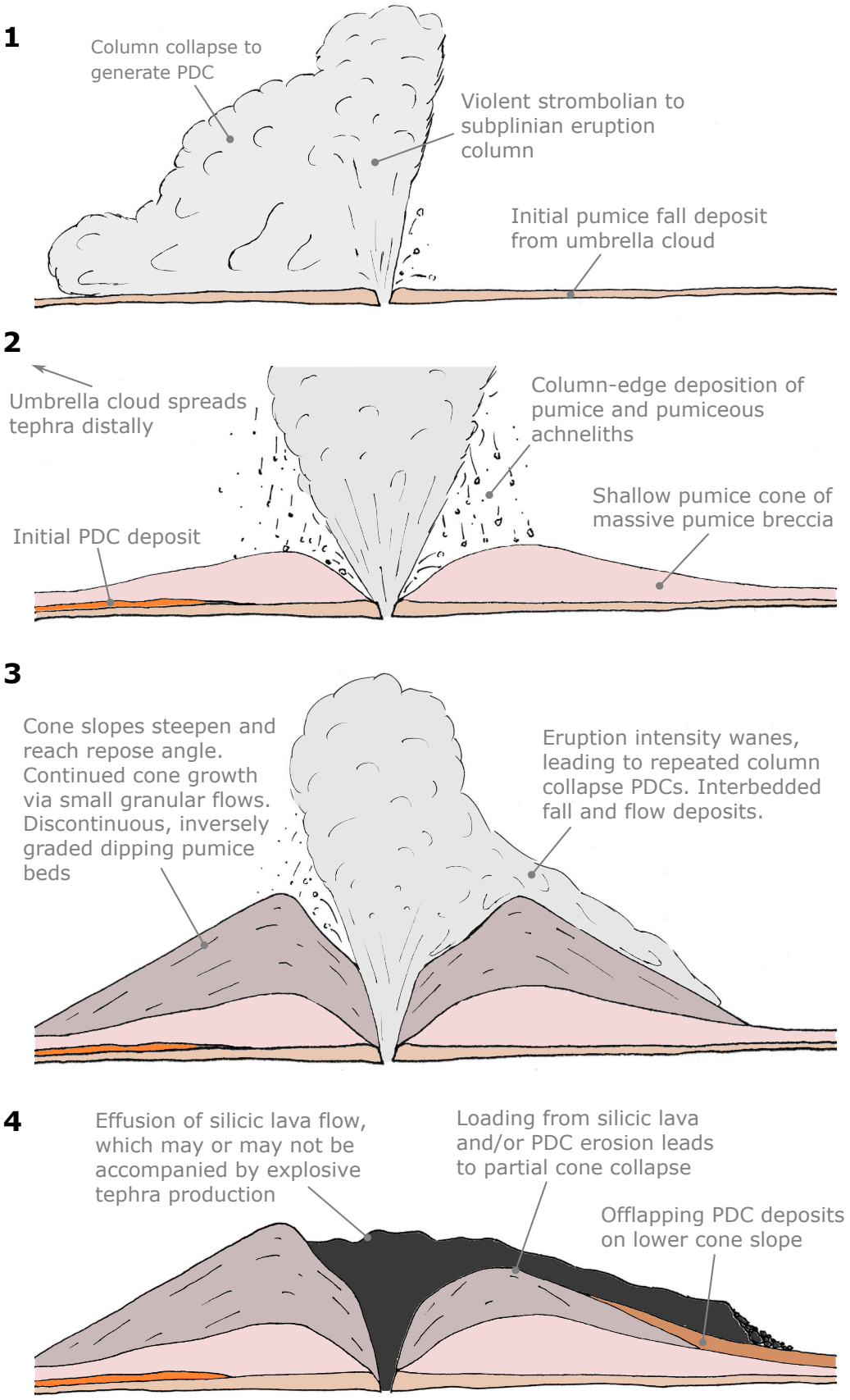

Figure 3.57: *A graphical summary of an idealised pumice cone eruption, displaying the typical pumice cone eruption sequence found to occur at Aluto.*

eruptions are rarely investigated within around 1 km of the vent, and such cones may be very common during eruptions where a convective column is generated, from which tephra can fall (Riedel et al., 2003). That is not to say that every pumice cone forming eruption at Aluto is plinian, this is not borne out in regional tephra stratigraphy (McNamara et al., 2018; Fontijn et al., 2018), and if it were the case thick plinian tephra fall deposits should blanket much of the edifice (which they don't). However, it does suggest that *convective eruption columns* are generated during pumice cone forming eruptions, and that such eruptions may be similar in style and processes to non-caldera forming rhyolite eruptions. Convective eruption columns are associated with relatively intense eruptions; where the mass eruption rate is sufficient to heat enough air drawn into the column fast-enough to maintain stability above and beyond the gas thrust region (Sparks, 1997). Such observations are consistent with those from the lake tephra record around Aluto (McNamara et al., 2018), which tentatively indicates that eruptions from Aluto span a range in magnitude and intensity from violent strombolian to sub-plinian (McNamara et al., 2018; Fontijn et al., 2018).

The steadiness of the pumice cone forming phase of the eruption is variable during and between distinct eruptions. It's notable that the shallow pumice cones always comprise massive fall deposits, and in some cases (eg. Kertefa, Humo 3), there are continuous grading trends. This suggets that the deposits are the product of a stable, continuous eruption column. However, this state does not persist, as later stages of pumice cone growth are characterised by unsteadiness as the eruption wanes. The presence of ignimbrites quickly following cone-forming fall deposits, and in some cases grading from one into the other, suggests that PDCs at Aluto are generated by column-collapse events. This is further supported by the diverse lithic components, and the frequent interbedding of fall and PDC deposits during this transition, indicating eruption conditions (mass eruption rate, vent radius, gas content) gravitate around those at the transition between a quasi-stable and collapsing eruption column. During this unsteady stage, multiple pumice fall events and PDCs should be expected. The PDCs generated during these collapse events almost always deposit massive lapilli tuffs, indicating that they generally posses a high particle concentration at their base (Branney and Kokelaar, 2002). On the southern flank of Aluto,

Figure 3.58: *A series of images showing 'ultraproximal cones' developed around rhyolitic vents at volcanoes worldwide. Their morphology is remarkably similar to pumice cones at Aluto. a, b and c are thought to be the product of column-edge deposition. The depositional mechanism of d is unknown. (a) Tawawera, NZ. Rampart structure (similar to Kertefa) deposited on the sides of a fissure vent. Source:Waitt and USGS (1986). (b) Quizapu, Chile. Shallow cone developed during the 1932 plinian eruption (Hildreth and Drake, 1992). Source: Google DigitalGlobe. (c) Novarupta, Canada. Shallow cone developed during the 1912 plinian eruption. Source: National Park Service (2018). (d) Cordón Caulle, Chile. 'Tephra cone' developed during the 2011 plinian eruption. Source: Figure 2b in Schipper et al. (2019).*

PDCs appear to be confined to drainages, though it is important to note that the more dilute upper-portion of these flows is generally not represented in the stratigraphy, with the exception of the ignimbrites of Humo 2. Due to their greater fluidisation and lower density, these dilute portions are liable to continue beyond the limit of the less mobile denser portion of the flow and detatch over topographic barriers (e.g Jenkins et al., 2013; Cole et al., 2015; Smith et al., 2018). Though the dynamic pressure of these dilute portions of the flow is typically lower than the dense basal layer (Sulpizio et al., 2014b), the impact on humans is the same due to very high temperatures (Baxter et al., 2017). Therefore, to fully evaluate PDC hazards at Aluto, we should not simply consider PDCs to be valley confined. The lack of vent-to-flow-lobe exposure, and the fact that many PDCs on the southern flank entered a palaeolake, means that their run out, and therefore mobility (dh/l) is unknown. The PDC deposits themselves are quite typical massive lapilli tuffs, and so better constrained PDCs elsewhere may provide justifiable analogues for mobility metrics.

This chapter has evaluated the nature of pumice cone forming eruptions using detailed field investigations and remote sensing data. These eruptions are hazardous, creating eruption columns which frequently collapse to generate pyroclastic density currents. The proximity of deposits from these eruptions to present-day communities and infrastructure around Aluto emphasises the need for a PDC hazard and risk analysis, which may inform any risk mitigation efforts or volcanic crisis plans. The research presented in this chapter provides a foundation for the PDC hazard and risk analyses presented in the next chapter.

Chapter 4

Pyroclastic Density Currents at Aluto Volcano: Hazard, Exposure and Risk

"Water and fire succeed
The town, the pasture and the weed.
Water and fire deride
The sacrifice that we denied.
Water and fire shall rot
The marred foundations we forgot,
Of sanctuary and choir.
This is the death of water and fire."

T.S Elliot, Little Gidding Part II

4.1 Introduction

An important step to understand the risk posed by PDCs at Aluto is to assess where they are likely to inundate during future eruptions. This is a complex question: the answer is a function of the PDC source-location, the volume and mobility of the PDC, the height from which the PDC collapses, the topography over which the PDC flows, and others. These features are not entirely independent of one another and themselves depend on many other variables which are unknown or poorly constrained prior to eruption. It is thus impossible to provide an entirely deterministic and precise evaluation of where a PDC will inundate. In the presence of large uncertainties, both epistemic and aleatory, providing a probabilistic answer is more accurate than a deterministic one. In order to asses which regions are at greatest risk of PDC inundation, the best that I can do is to quantify the uncertainty present

in the problem. Using knowledge of past events at Aluto, combined with other sources of information and targeted physical and statistical modelling, I can estimate the regions most likely to be inundated by PDCs in the future. This probabilistic assessment can form the basis of a PDC hazard map, and helps to determine the likelihood of population and infrastructure being adversely affected by PDCs during a future eruption at Aluto volcano.

There are various pyroclastic density current and mass flow models that could be applied to this problem, namely: Titan2D (Patra et al., 2005), VolcFlow (Kelfoun and Druitt, 2005), PyBox (Biagioli et al., 2019) (based on the 'box' or 'integral' model of Huppert and Simpson (1980)), or the Energy Cone model (Malin and Sheridan, 1982). Each model takes a distinct approach to provide a 'footprint' for a PDC given a variety of initial parameters of the PDC flowing over a particular topography. In the case of Titan2D and VolcFlow, this footprint is a deterministic inundation map displaying various aspects of the flow, such as flow depth and velocity of the flow front. In the case of PyBox and Energy cone models, the footprint represents an area at every degree of azimuth around the vent that could possibly be inundated by a given PDC flowing in that direction, the result being a binary map of at risk/not at risk of PDC inundation.

The Titan2D and VolcFlow models are the most sophisticated, as they consider the internal fluid dynamics of a PDC, how they respond to topography and ultimately estimate the behaviour and evolution of an individual PDC. An advantage of these models is their estimation of flow depth, sedimentation, and how the PDC responds to topography. This is useful, for example, to determine to what degree a flow will be channelised, and whether it may over-top a drainage. These models have been extensively used to develop hazard maps, typically employing a small number of simulations, each representing a different scenario (e.g Sulpizio et al., 2010; Sheridan et al., 2001; Saucedo et al., 2005). Both models are considered most appropriate for small volume or pulsatory PDCs, and are better at simulating dense particle suspensions than dilute PDCs (Ogburn and Calder, 2017). Based on the likely small volume, and the paucity of deposits from dilute PDCs at Aluto, either model would be appropriate for this system. However, these models present two main challenges: (1) individual models are computationally expensive, meaning only a few

initial parameters can be investigated. This means that the aleatory uncertainty is not fully explored, and so a fully probabilistic solution isn't generated. (2) They both require input parameters for which there are few or no constraints at less well studied volcanoes such as Aluto (ie. flow volume, internal friction angle, viscosity) and assumptions need to be made considering the choice of flow rheology and source type (ie. flux or pile). These epistemic uncertainties would propagate into any final results.

Individual PyBox and energy cone simulations are less computationally expensive, and so can be run in great volume to fully explore the aleatory uncertainty in the solution. Both models consider topography in a simple sense, in that they evaluate whether a flow may be able to surmount a topographic barrier along a 2D flow path, but as each simulation operates at an individual degree of azimuth, neither considers channelisation or over-topping of drainages. Of the two, PyBox is more sophisticated as it models the internal fluid dynamics of the PDC, can take into account total volume of the PDC, and sedimentation. However, this sophistication increases the computational expense, and requires a number of input parameters for which there are few or no constraints at less well studied volcanoes such as Aluto (ie. flow volume, temperature, granulometry and grain packing fraction).

The knowledge of past eruptions at Aluto volcano is sparse compared to knowledge at many other volcanic centres around the world, with much of this information presented in this thesis. There is thus considerable epistemic uncertainty, in addition to the aleatory uncertainties which are inherent to even well-known volcanic systems. The understanding of how future eruptions are likely to unfold is thus relatively poor. This should be reflected in the choice of the physical PDC model, both ensuring it is simple, requiring fewer assumptions to be made surrounding epistemic uncertainties, whilst also exploring the impact of aleatory uncertainty. Monte Carlo application of the 'energy cone' (EC) model of Malin and Sheridan (1982) fulfils these criteria. The EC model works by assuming a source location, a height from which the PDC collapses, and a single mobility parameter which in effect describes how rapidly the potential energy from column collapse is consumed during horizontal PDC propagation. In reality, the mobility of a PDC changes in space and time and is dependant on a large number of interacting phenomena. In the EC

model, all of these phenomena are integrated into a single number, the friction coefficient, represented by an angle. This angle can be conceptualised as that of a line connecting the PDC collapse source and the most distal reach of the PDC. A more mobile PDC (ie. one that reaches a greater horizontal distance proportional to its collapse height), will have a shallower angle; a lower friction coefficient. One can then imagine projecting this line from the PDC source at every degree of azimuth, forming a surface or 'energy cone'. If the topographic surface was flat, the map of where this cone intersected the ground would be circular in plan view, with the radius proportional to the flow mobility and collapse height. However, when the topography is irregular, this intercept footprint will intersect the topography at a longer or shorter horizontal distance from the source, producing an irregular footprint. By making reasonable assumptions of the PDC collapse height, the flow mobility, vent source location and with knowledge of the topography, I may determine the maximum area of PDC invasion from the column collapse event.

A single value of collapse height, mobility, [and at many volcanoes including Aluto] source location is clearly inadequate to describe all potential PDCs. However, if a range (or even better, a probability density function) of values for each parameter is known, I can employ a Monte Carlo approach, where a large number of representative events are simulated using the energy cone model to evaluate the full range of aleatory uncertainty. From this I can determine which locations around Aluto could be most frequently inundated. These areas are most 'prone' to PDC inundation, and should be considered to have a greater probability of inundation by a PDC during a future eruption.

This chapter aims to: (1) parameterise the input parameters for the energy cone model, producing a probability density function (PDF) for each parameter, (2) model a large number of PDC events sampling these PDFs for inputs to the energy cone model, (3) create a PDC inundation probability map for Aluto volcano from those simulations, (4) assess how this hazard map relates to the distribution of population and key infrastructure around Aluto and (5) produce examples of potential approaches to PDC hazard maps for Aluto volcano. An overview of the methodology used to achieve these goals is presented in Figure 4.1. Each of these steps is described and explored in the following sections.

4.2 Energy cone parameterisation

The first step in the process is to parameterise the energy cone model so that the parameters represent our best current understanding of PDCs at Aluto. The features that need to be parameterised are:

1. The height from which future PDCs are likely to collapse (H_c)
2. The PDC mobility, characterised by the effective coefficient of friction expressed as the angle of an energy line (ϕ)
3. The areas most probable to be future source vents of PDCs at Aluto

4.2.1 Collapse Height Parameterisation

The height from which the PDC collapses is a key parameter in the energy cone model. For a block and ash flow sourced from a collapsing lava-dome, the collapse height is simply the height of the lava dome itself, which may be taken directly from the DEM. However, in the case of column collapse or fountaining style PDCs, the collapse height is the maximum height that pyroclastic material is ejected above the vent before it begins its descent. The large proportion of juvenile pumice, lack of large blocks of lava-dome (in this case obsidian) and the frequent occurrence of fall deposits underneath ignimbrite deposits at Aluto suggests that PDCs are typically generated by column collapse. It is therefore essential to characterise the likely collapse height for PDCs produced during pumice cone forming eruptions at Aluto.

For column collapse or fountain collapse PDC energy cone models, the collapse height during any given eruption can be approximated as the top of the gas thrust region, as this is the point at which a plume either begins to convect upwards, or collapse depending on the precise eruption conditions (Sparks, 1997). Partial collapses can occur below this height, but for simplicity I only consider total column collapse from the top of the gas thrust region. As a rule of thumb, the gas thrust region is often considered to be around

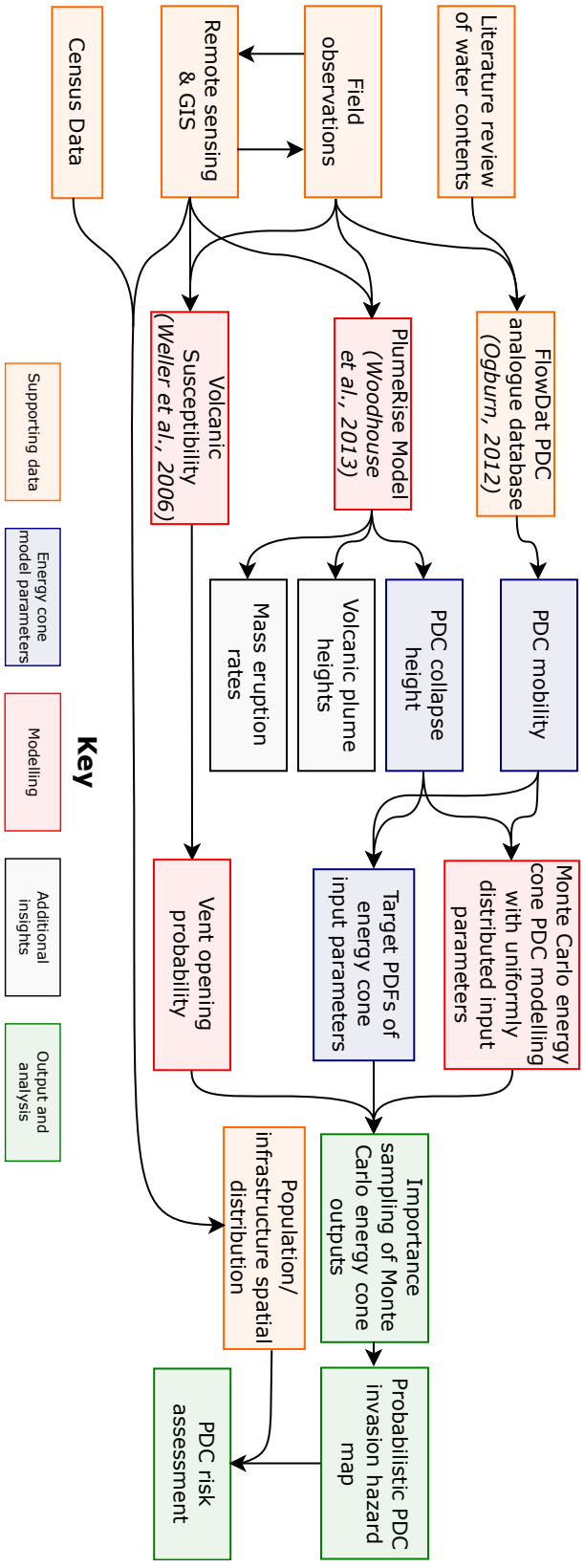

Figure 4.1: *Flow chart providing an overview of the methods employed to develop a probabilistic PDC invasion map. The following chapter will explore and describe each step in detail.*

10 % of the total plume height (Wilson et al., 1978; Tierz et al., 2016b,a). However, as no pumice cone forming eruptions have ever been observed, and there are very few isopach studies on their fall deposits, column heights are largely unknown. It is also challenging to robustly identify any analogues for such eruptions in the global geological record, as the deposits of pumice cones are dissimilar to those produced during the majority of studied eruptions. It is therefore necessary to derive this information from deposits at Aluto.

As I have already established from the investigation of pumiceous achneliths, and pumice cone deposits, pumice cones are most probably generated by ultraproximal fallout from convective eruption columns; showing that such eruptions must produce convective eruption columns. By modelling the conditions required to generate a convective eruption column, I am able to more precisely parameterise the eruption conditions. The interbedded fall and PDC deposits from various pumice cones at Aluto (Awariftu valley, Humo Gorge and South Kertefa), show that these convective columns were unsteady; frequently collapsing and re-establishing during the same eruption. This would suggest that conditions (vent radius, mass eruption rate, gas mass fraction, pyroclast-gas mixture density) gravitate around those near the boundary of a convecting and collapsing column. This further narrows down the conditions at the point of column collapse and PDC generation. The output of the model should also include the velocity profile of an eruption column with height, so that I can identify the top of the gas-thrust region (the collapse height), represented by the local minimum in particle velocity above the vent.

To do this, I have used the PlumeRise model of Woodhouse et al. (2013), as this allows simple exploration of the parameter space for convecting and collapsing eruption columns. The parameters required for the PlumeRise model, and the values chosen for Aluto, are summarised in Table 4.1. There are three remaining variables which are likely to vary considerably from eruption to eruption, and also during the course of each eruption. These are: vent radius, gas mass fraction (ie. wt % water in the magma for a non-phreatomagmatic eruption), and mass eruption rate. I will explore this parameter space in order to derive realistic parameterisations for (1) the height of the gas thrust region at the point of column collapse, (2) the probable mass eruption rate during these eruptions, and (3) the probable

Parameter	Unit	Value	Note
Vent elevation	m.a.s.l	2025	mean of previous vent-heights at Aluto
Vent radius	m	var.	radius of conduit mouth
Gas mass fraction	fraction	var.	mass fraction of gas (H_2O wt %)
Source temperature	K	1023.15	magma storage temperature
Pyroclast density	kg/m^3	1200	bulk mean density of pyroclast mix (1)
No-wind entrainment coefficient		0.09	recommended value (1)
Wind direction	deg	n/a	assuming wind-still eruption for simplicity
Wind velocity	m/s	0	assuming wind-still eruption for simplicity
Source mass flux	kg/s	var.	mass eruption rate

Table 4.1: *The input parameters for the PlumeRise model, where value = var., this is an independent variable to be altered when exploring parameter space. (1) refers to the source of these recommendations (Woodhouse et al., 2013)*

column heights reached during these eruptions.

PlumeRise Modelling

The PlumeRise modelling was conducted using the online application published by Woodhouse et al. (2013). The primary aim of this was to explore the parameter space in terms of mass eruption rate, vent radius and water content of the magma, and determine under what conditions a stable or collapsing column was generated; the ultimate aim was to extract the conditions at the boundary between a stable and collapsing column. The PlumeRise model is a thermodynamic and fluid dynamic-based model built on an established integral plume model originally developed by Morton (1956), and later adapted for volcanic plumes in a quiescent atmosphere by Woods (1988), combined with a model of smokestacks with a horizontal crosswind by Hewett et al. (1971). The PlumeRise model was developed to consider the influence of a complex wind field on the plume height, though in this circumstance, a quiescent wind field is assumed in order to remove a complex independent variable subject to aleatory uncertainty. The reported total column heights from this analysis are therefore maxima. I assume that each parameter is independent, and so the model was run using a range of vent radii (1 m, 5 m, 10 m, 20 m, 30 m, 40 m, 50 m, 80 m, 120 m) at a range of water weight percentages (2%, 3%, 5%, 7%), and for each combination exploring the range of mass eruption rates that produced a convecting and collapsing column. The boundary between the stable and collapsing regimes was defined

by the lowest mass eruption rate for each vent radius and water content that produced a stable column. This boundary was defined to a precision of 0.1 log units of mass eruption rate. Overall, I ran the model 280 times, the number of iterations minimised by estimating the location of the boundary based on previous model-runs. In summary, a stable column is favoured by a higher mass eruption rate, a smaller vent radius and a higher water content. For each run that produced a stable column, the results file was saved, which included data on, amongst other features, the vertical velocity of the plume with height. The results of this model are presented in Figure 4.2, and the raw outputs from PlumeRise can be found in the electronic appendices. From this I can determine that, according to the vent radii inferred at Aluto, the mass eruption rates associated with the collapsing phases of these eruptions are in the range of 2×10^4, to 6×10^6 kg/s. The mass eruption rate during the earlier, more stable column phase must be greater than or equal to this.

The model outputs from the stable columns also allow us to derive other attributes of these eruption columns. For example, the total height reached is an important parameter for tephra dispersion models. The modelled heights of the eruptions columns and the source mass eruption rate is shown in Figure 4.3. Assuming mass eruption rates modelled in Figure 4.2, column height just prior to collapse are expected to range from 3 to 12 km depending on the water content of the magma.

For energy cone parameterisation, it is necessary to know the height of the gas thrust region rather than the plume as a whole. The top of the gas thrust region is easily recognised in a plot of plume velocity against height. It is represented by a local minimum in the velocity in the lower part of the column. This was extracted from the model outputs from all of the stable columns using a minima-finding algorithm from Jones et al. (2001). The results of this are presented in Figure 4.4, and show that collapse heights are likely to be in the range of 50-500 m above the vent during pumice cone eruptions.

There appears to be considerable scatter in the relationship between the height of the gas thrust region and the mass eruption rate where mass eruption rates are above 10^6 kg/s. This is due to the strong influence of the gas mass fraction (i.e. water content

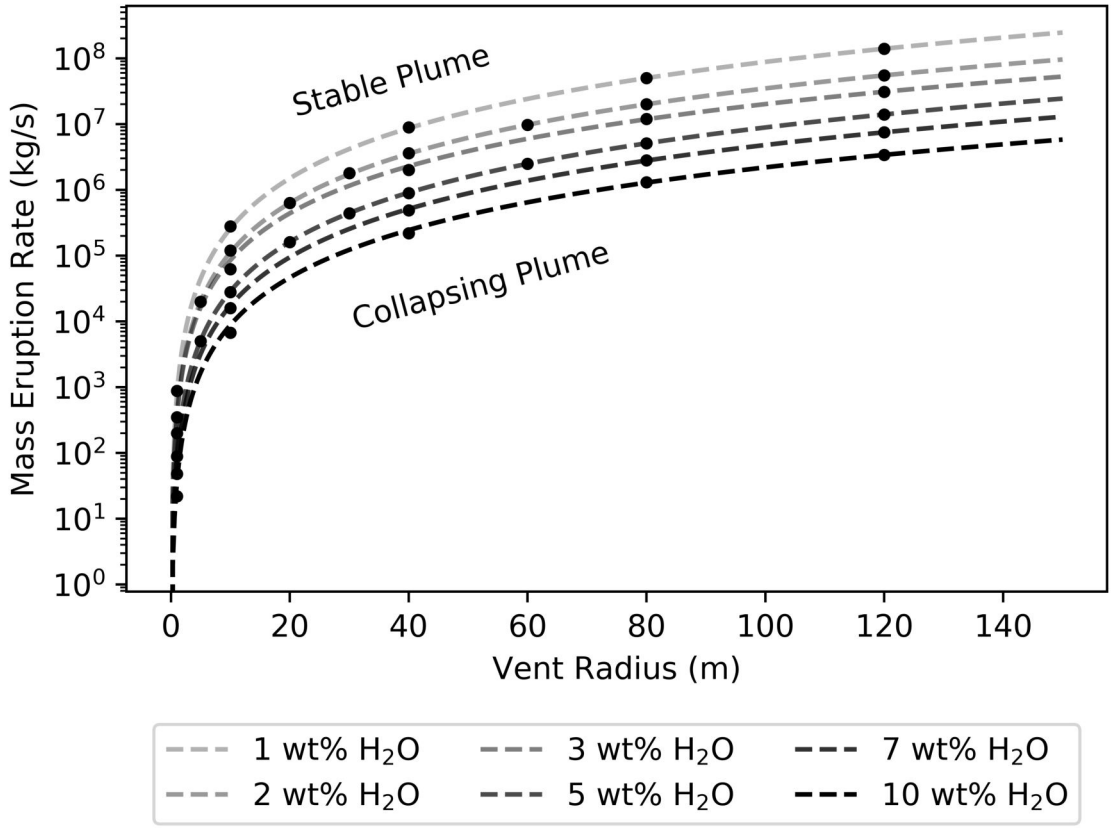

Figure 4.2: *The boundary between a stable and collapsing volcanic plume at Aluto depending on the mass eruption rate, vent radius and water content of the magma. The data in each water mass fraction series follow power law curves. For any given vent radius, these curves can be used to calculate the mass eruption rate at the point of column collapse assuming prior knowledge of the magma water content.*

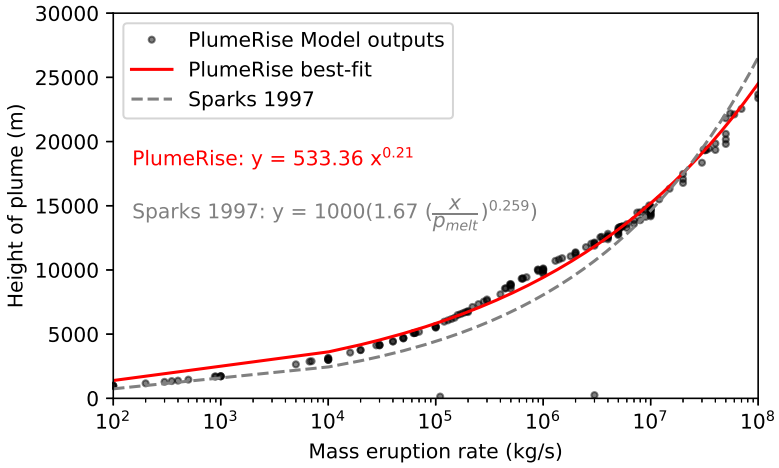

Figure 4.3: *The height of the eruption columns as a function of mass eruption rate as determined from the PlumeRise model. The output from this follows a power law, and is reassuringly similar to the generalised model of Sparks (1997) (assuming a melt density of 2300 kg/m^3 (Clarke et al., 2019)). Column heights of 3-12 km are predicted just prior to column collapse during pumice cone eruptions at Aluto (based on mass eruption rates from Figure 4.2), but may reach higher than this during a stable column phase.*

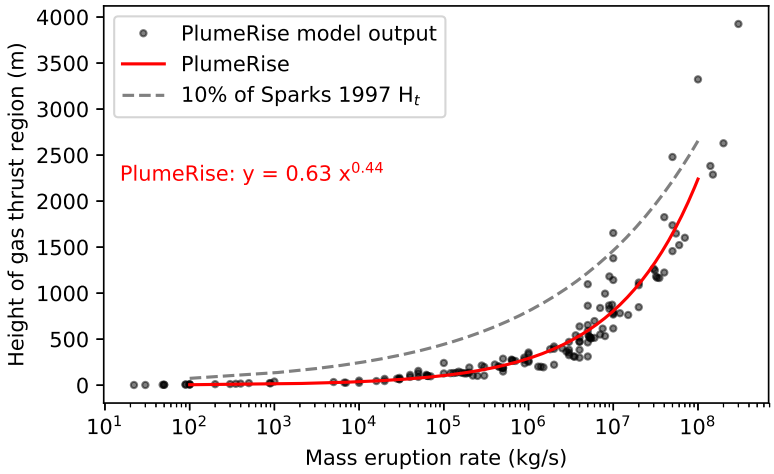

Figure 4.4: *The height of the gas thrust region as a function of mass eruption rate as determined from the PlumeRise model.The output from this follows a power law.This is presented alongside 10 % of the plume height calculated from the generalised model of Sparks (1997) (assuming a melt density of 2300 kg/m^3), representing what is often assumed to be a proportional height of the gas thrust region (Wilson et al., 1978; Tierz et al., 2016b,a). Gas thrust heights of 50-500 m are predicted just prior to column collapse during pumice cones at Aluto (based on mass eruption rates from Figure 4.2), but may reach higher than this during a stable column phase.*

of the magma). To quantify this influence, I have extracted the vent radii at the point of collapse and plotted them according to their water content against the height of the gas thrust region (Figure 4.5). This plot indicates that the higher the water content, the shorter the gas thrust region. Also the higher the vent radius (thus the higher the mass eruption rate at collapse), the taller the gas thrust region. The slope term of these best-fit power functions varies systematically with the water content, following a power-law relationship (Figure 4.5). The exponent of these power functions remains relatively stationary.

Parameterising collapse Heights at Aluto

From the outputs of the PlumeRise model calibrated for pumice cone eruptions at Aluto described so far in this chapter, I can derive three main equations that describe important parameters associated with these eruptions given a magmatic water content and vent radius. The mass eruption rate (MER, in kg/s)(Eq. 4.1), plume height (H_t, in m)(Eq. 4.2), and gas thrust/collapse height (H_c, in m)(Eq. 4.3):

$$MER = (809.11 \times H_2O^{-1.01} - 50.64) \times r^{(-0.01 \times H_2O + 2.54)} \tag{4.1}$$

$$H_t = 561.48 \times MER^{0.2} \tag{4.2}$$

$$H_c = 12.78 \times H_2O^{-0.61} \times r^{1.1} \tag{4.3}$$

Where H_2O is the water concentration in wt % and r is the vent radius in meters.

In order to parameterise the energy cone model, I require a PDF of the collapse heights at Aluto. This can be calculated through Monte Carlo sampling of PDFs for vent radii and water content, to systematically evaluate Eq. 4.3. In the following section I generate the PDFs.

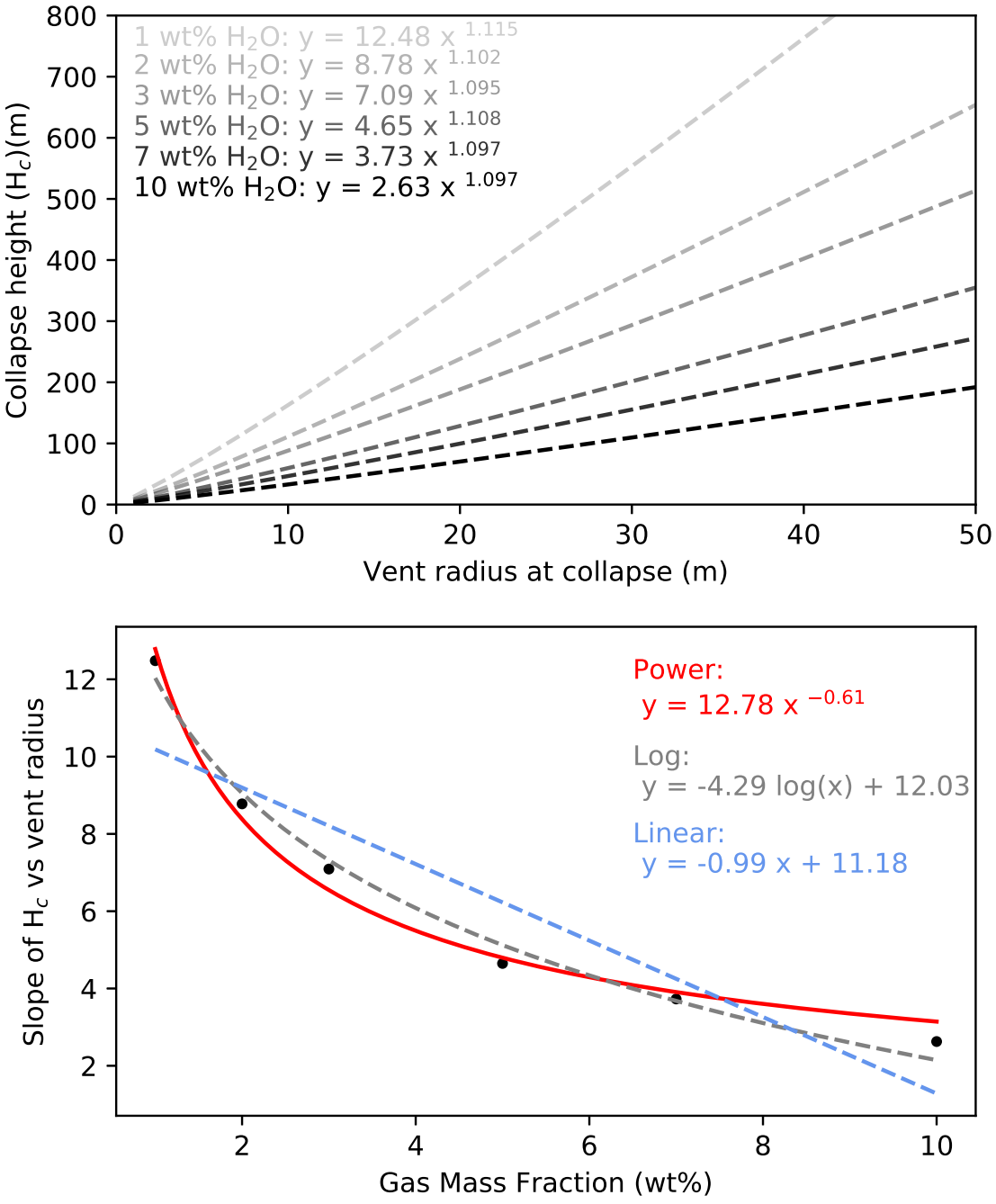

Figure 4.5: *(top) The height of the gas thrust region as a function of water content and the vent radius at the point of collapse. The higher the gas fraction, the shorter the gas thrust region. The power term in the power law is almost identical for the water content, but (bottom) the slope term varies systematically with the water content. A power function is chosen to best describe the relationship.*

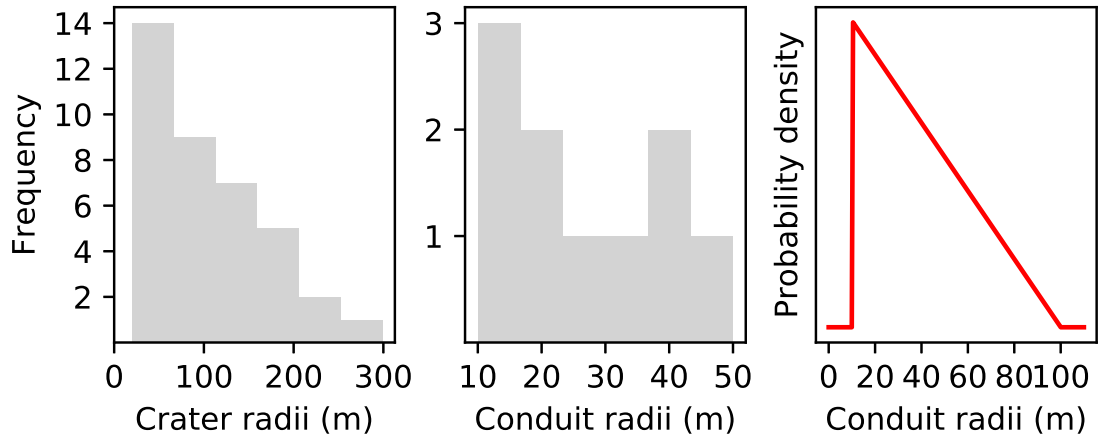

Figure 4.6: *Histograms of (left) the distribution of crater diameters obsevered at Aluto, (middle) the distribution of conduit diameters observed at Aluto and (right) the triangular probability density function assumed to represent the likely conduit opening diameters at the point of column collapse for eruptions at Aluto*

Parameterising Monte Carlo simulations of the PDC collapse height

An important parameter in predicting the behaviour of a volcanic plume is the radius of the conduit, as this controls the bulk density of material exiting the vent and the velocity at which material must exit assuming a particular mass eruption rate (Sparks, 1997). Despite being an immensely important parameter with a strong control on the plume behaviour, it is hard to accurately quantify in most eruptions. For open conduit volcanoes during low intensity eruptions one can measure this by direct observation, but for high intensity eruptions, the vent region is often visually obscured, and too hazardous to make the necessary observations. Even after the eruption has ceased, back-filling of pyroclastic material or lava completely buries the conduit-opening. In the case of Aluto, the conduit is obscured in almost every case by an obsidian lava flow. One approach to approximate the vent radius is to measure the total area of each crater floor and convert this to a radius assuming a cylindrical conduit. This provides a maximum [significantly overestimated] radius for each conduit. The results of this analysis at Aluto are presented in Figure 4.6.

The magnitude of overestimation using the crater-floor method is on the scale of 10s to 100s of meters. As the results from the PlumeRise modelling in the next section show, this

level of error is unacceptable if any degree of precision in the output is required. Instead, I developed a different, more direct, approach. This approach arose from the observation in the field that obsidian lava flows appeared to have a slight dip or bump at their source, on the scale of a few vertical meters, and usually a few 10s of horizontal meters across. The source of the flow can be identified easily in most cases as the point where surface folds, or 'ogives' converge to form a 'bulls-eye' shape. The source of the flow is the conduit opening, and any dip or bump in the elevation above the conduit opening is likely to be due to either drain-back or foam-collapse in the conduit (in the case of a dip), or the final viscous effusion of lava from the vent in the form of a small dome or spine (in the case of a bump). Although still an approximation of the true conduit diameter, this should more realistically reflect the diameter of the underlying conduit than is achieved by measuring the entire crater floor. This approach makes various assumptions: (1) that the conduit from which the obsidian lava flow is sourced is the same from which the explosive phase of the same eruption emanated and, (2) that the conduit radius has not changed significantly between the explosive phase and the end of the effusive phase.

For each obsidian lava flow at Aluto, I extracted a topographic and slope profile along the two horizontal major axes of the flow, ensuring the two profiles crossed where the ogives converged (ie. at the flow source). From these profiles I observed where there was a dip or bump in the profile either side of the flow source on the scale of multiple vertical meters. In many cases this topographic change was relatively obvious, but in others it was not present. In such cases, these flows were excluded from the analysis. For each flow which did exhibit measurable dips or bumps, I recorded the diameters of dips or bumps along the two intersecting profiles. The radius was calculated assuming a cylindrical conduit, and that the two profiles represented the long and short axes of an ellipse. This provided approximate vent radii for 10 of the pumice cones, the results of which are presented in Figure 4.6. Unfortunately, a sample size of 10 is not sufficient to build a robust probability density function. However, the histogram clearly shows there are more smaller conduits than larger ones, and provides a realistic range of conduit radii at Aluto. To ensure that I cover extreme events at Aluto, I set the maximum vent radii for Aluto at 100 m, twice that of the maximum measured vent radius. This was then used to generate a triangular prob-

ability density function representing the expected distribution of vent radii at the point of column collapse at Aluto. This triangular distribution, with the modal radius of 10 m, reaching a maximum of 100 m is consistent with the range of vent radii often modelled during investigations of plume dynamics (10s to 100s m) (Wilson et al., 1980a). However, as this is loosely constrained, this should be considered a potential source of epistemic uncertainty in the collapse height simulations.

The second parameter that needs to be established for the Monte Carlo simulations of the collapse height is the magmatic water content. Peralkaline rhyolites are typically water rich melts, generally considered to range in H_2O concentration from 4-5 wt% (Field et al., 2012). A review of water contents in melt inclusions in peralkaline rhyolites from the volcanic literature is presented in Figure 4.7. The distribution of published water contents in peralkaline rhyolites is bi-modal. However, as these values are sourced from a limited number of volcanoes (5), each with a different number of samples, this shape is subject to biases associated with the data set rather than any true 'global' distribution. Unpublished results from melt inclusion studies at Aluto indicate that its magmas lie on the upper end of the spectrum indicated in this data set (Iddon, pers. comm). As I do not know the distribution of water concentrations at Aluto, I assume a uniform PDF between 4 and 8 wt % H_2O; though this would benefit from better quantification once the data become available.

I ran 2×10^6 Monte Carlo simulations of eruption columns by evaluating equations 4.1 to 4.3, each time randomly sampling a water content from a uniform PDF and a vent radius from the triangular PDF. Histograms showing the results of these simulations are presented in Figure 4.8. I make the assumption that these parameters are independent of one another. However, in reality the water content, mass eruption rate and conduit diameter are linked (Sparks, 1997), and the nature of their interaction is likely modulated by diverse factors such as the magma viscosity, magma permeability, regional stress field and the strength of the conduit walls. By randomly sampling the PDFs of parameters independently from one another, I am likely to be evaluating the equations using unrealistic combinations of the input parameters. This will produce results that extend above and

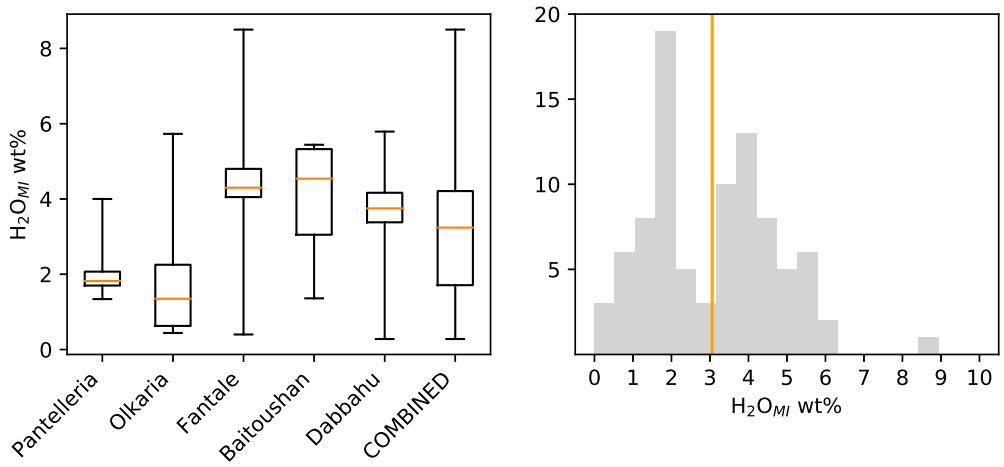

Figure 4.7: *Ranges of published melt-inclusion derived water concentrations in peralkaline rhyolites from volcanoes worldwide. Data are from from quartz and plagioclase -hosted melt inclusions. On the left: Whiskers show the range, the boxes span the upper and lower quartiles of the data. The orange centre-lines show the mean for each volcano. On the right: a histogram of all combined H_2O melt inclusion data, the vertical orange line marks the mean at 3.1 wt%. Overall, most pantellerites have water contents between 2 and 4.5 wt%, but span a range between 0.5 and 8 wt%. Data sources: Pantelleria (Lowenstern and Mahood, 1991; Lanzo et al., 2013), Olkaria (Wilding et al., 1993), Fantale (Webster et al., 1993), Baitoushan (Horn and Schmincke, 2000), Dabbahu (Field et al., 2012).*

below the range that should naturally occur, and present an unrealistic distribution within that range. However, the approach still has merit, in that it brackets the true distribution, provides a rough approximation of the shape, and allows us to do so without having to explore an enormous number of factors for which there are few constraints, and which are unlikely to be known before an eruption.

4.2.2 PDC Mobility Parameterisation

Once a pyroclastic density current has formed through column collapse, various factors dictate the final run-out. This includes the collapse height and the presence of any topographic barriers, but also various features intrinsic to the density current that broadly influence the 'mobility' of the flow by controlling the particle support mechanisms, such as fluidisation, componentry, granulometry, and the bulk and particle rheology (Smith et al., 2018; Breard et al., 2018; Calder et al., 1999; Branney and Kokelaar, 2002; Sulpizio et al., 2014a). The energy cone model does not attempt to deconvolve these physical properties,

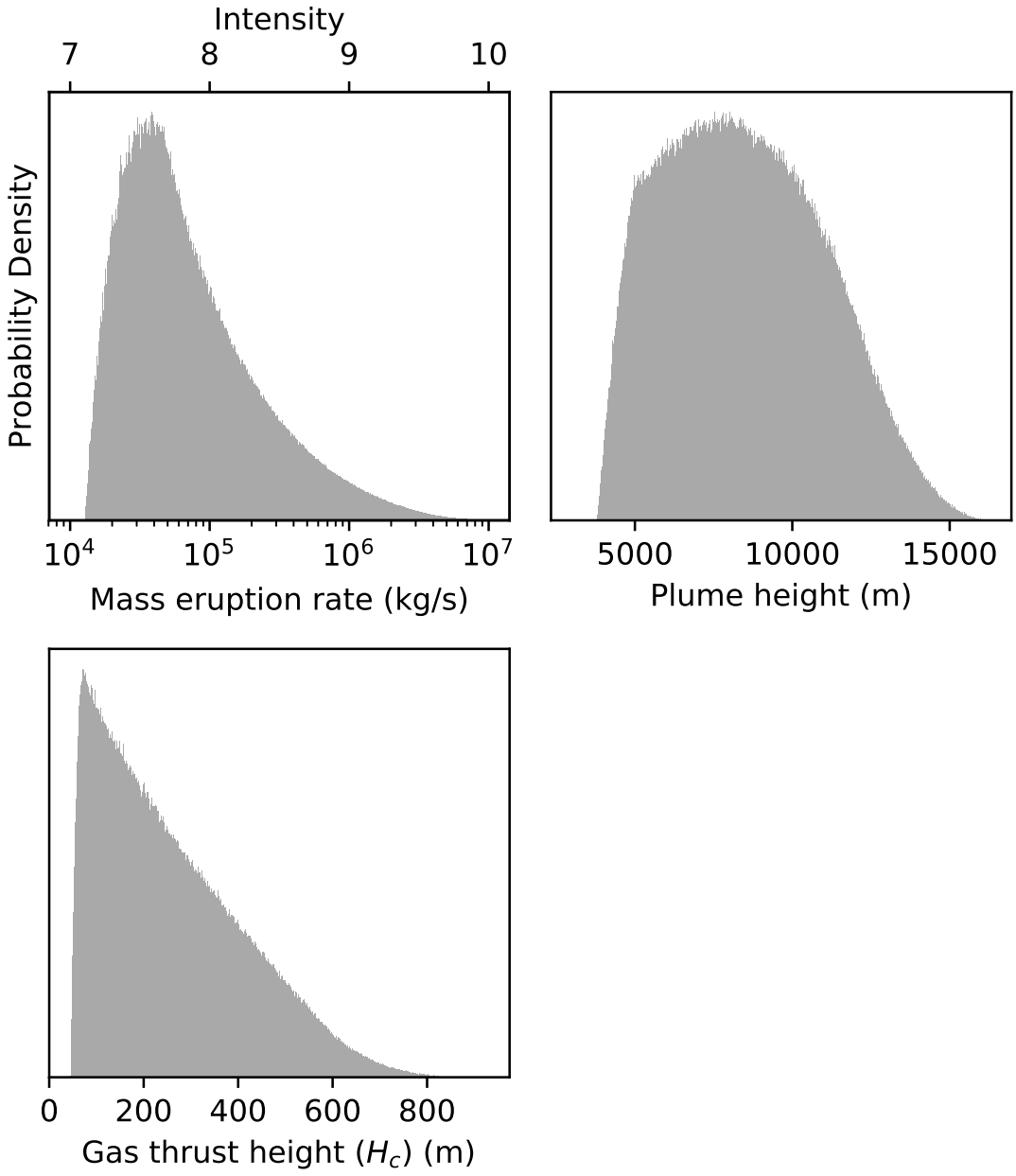

Figure 4.8: *Histograms produced from a Monte Carlo simulation of plumes generated during pumice cone forming eruptions, forming the shape of the expected 'target' PDFs of these parameters. The gas thrust height results (bottom left) will form the target PDF for this parameter in the energy cone model.*

but instead integrates them into one empirically defined mobility parameter (Malin and Sheridan, 1982; Tierz et al., 2016b). As described earlier, the mobility of the flow can be quantified as the angle of the 'energy line'; the straight line that connects the top of the collapse region to the most distal reach of the flow, in effect describing over what horizontal distance the potential energy is transformed into kinetic energy and finally consumed by effective friction (i.e. how far the density current travels before it stops proportional to the collapse height). The angle of this line from the horizontal reflects the mobility of the flow, where a shallower angle represents a more mobile flow. In modelled flows, the point at which this line intersects the topography represents the flow run-out.

The angle of this line (ϕ) can be calculated as a simple trigonometric function of the horizontal flow distance (l) compared to the vertical drop distance (dh):

$$\phi = tan^{-1}\frac{dh}{l} \tag{4.4}$$

Ideally, one would measure the dh and l of historical PDCs at Aluto and build a PDF of ϕ that could be sampled for iterative energy cone models. However, there are various challenges in doing this: (1) there are no recorded historical eruptions of Aluto, and so there are no direct measurements of dh (in fact, this is also the case for many observed PDC-forming eruptions), (2) in the field, the deposits of previous PDCs are buried, difficult to trace to a source vent, and terminate at the paleolake-edge, meaning accurate values of l cannot be attained.

In the absence of robust measurements at Aluto, I must use PDC mobility data from analogue volcanoes that produce PDCs similar to those at Aluto. As I have already established, the nature of the majority of ignimbrites found at Aluto suggest that they are sourced from column collapse PDCs which have a high particle concentration at their base that suppresses turbulent flow behaviour. There are also occasional fine-grained, cross bedded deposits of dilute PDCs. Some may be sourced from explosive magma-water interactions, and others may represent deposits of the upper dilute turbulent suspension of concentrated PDCs. The FlowDat database (Ogburn, 2012) collates published data of

PDCs, including l, volume and dh. The data chosen for Aluto PDC analogues were filtered to ensure they were representative, whilst also maximising the number of data points to build a robust PDF to sample, and extend beyond the ranges of mobility and collapse height expected to account for unprecedented events in the future. For this reason, the following criteria were applied: (1) Only PDCs sourced from column collapse or pyroclastic fountaining were selected. (2) High-volume ignimbrites from caldera-forming eruptions were excluded, (3) PDCs generated by lateral blasts were excluded. I verified each PDC from the original reference to ensure that they complied with these criteria, and gathered information about their deposits to ascertain whether they were concentrated or dilute. Table 4.2 shows the data extracted from this database and supplemented by some additional sources. After filtering, there are 59 PDC analogues, 54 of which are concentrated PDCs and 5 of which are dilute PDCs. The mobility data are summarised in a series of histograms (Figure 4.9).

The histograms of the filtered PDC mobility data set show that dilute PDCs are more mobile than concentrated PDCs. When taken as a whole, these analogues form a roughly Gaussian distribution of PDC mobility, a feature which has also been recognised by Sheridan and Macías (1995) and Tierz et al. (2016b,a). In the energy cone model, I wish to simulate any potential PDC generated at Aluto. As both concentrated and dilute PDCs have occurred, both must be included in the final mobility PDF. The combined dilute/concentrated PDF shall be used as the PDF for energy cone modelling. However, this presents a sampling bias, as the shape of the PDF will in part be controlled by the proportion of dilute and concentrated PDCs in the database. The proportion of these samples in the data set is strongly skewed towards concentrated PDCs at a ratio of about 1:9. Qualitatively, this is consistent with the deposits at Aluto, where the number of concentrated PDC deposits far outweighs those of dilute PDCs. Unfortunately, there are insufficient data to quantify this relationship. There may also be biases surrounding deposit preservation and deposition between dilute and concentrated PDC deposits at Aluto; owing to their distinct granulometry and run out. Field data therefore, may not accurately represent the true proportion of these flows generated in nature. In the absence of better data, I assume that the proportionality in the analogue database reflects the true global proportionality,

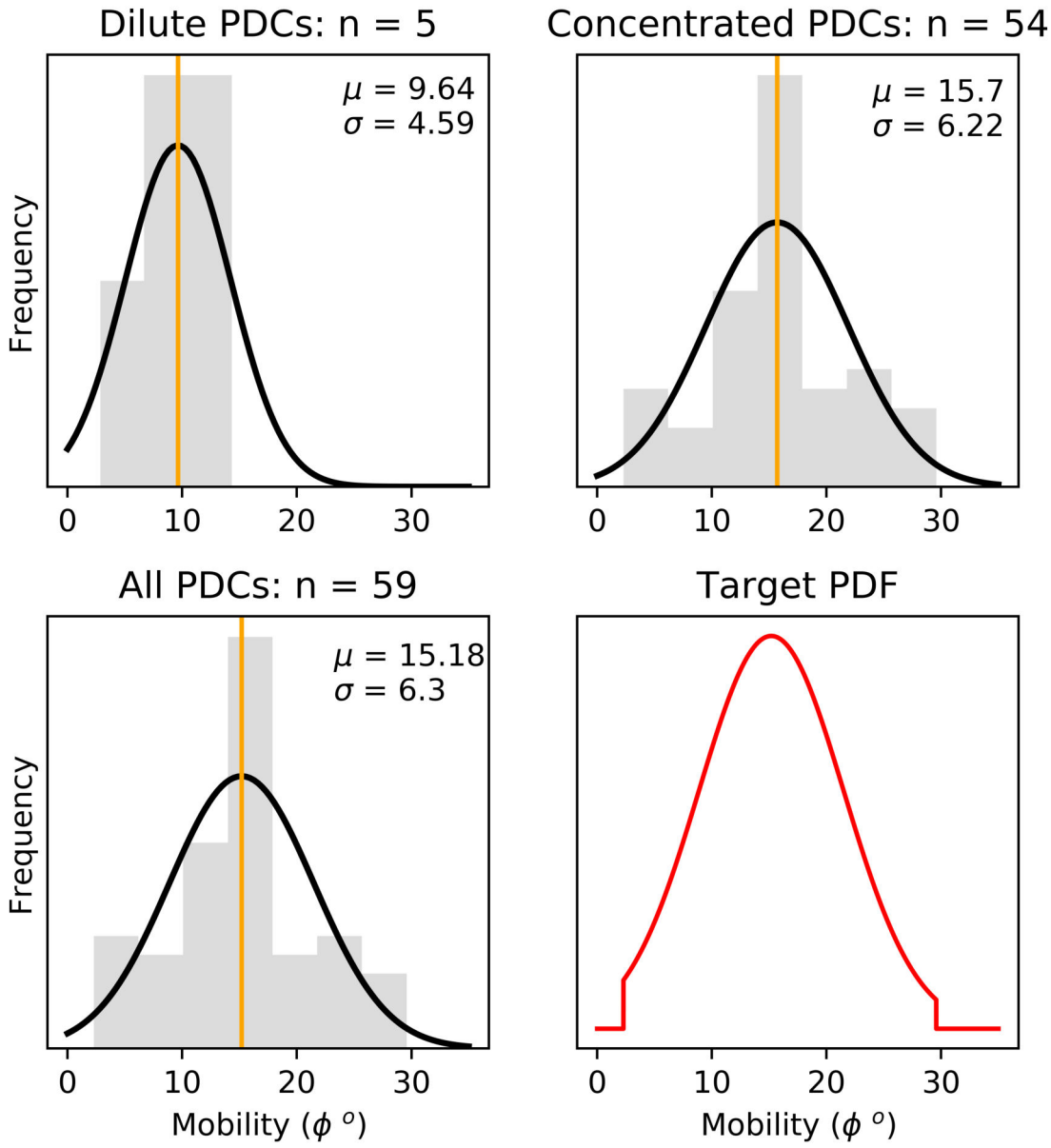

Figure 4.9: *Histograms (dark gray) and best-fit Gaussian PDFs (black) of mobilities of analogue PDCs. As expected, dilute PDCs have a greater average mobility (lower ϕ) than concentrated PDCs. The truncated best fit Gaussian of all PDC mobility data is shown in red, and is the 'target PDF': representing the expected distribution of PDC mobilities at Aluto. Vertical orange lines mark the mean value.*

and so the combined Gaussian distribution of PDC mobility is taken without modification. One feature of these Gaussian PDFs is that they have tails which extend far beyond the analogue data set, and below 0. It is physically inconsistent for a flow to have a mobility of 0° (denoting an infinite mobility). Therefore, I must truncate the PDF at some sensible upper and lower limit in order to remove unrealistic flows associated with the sampling of extreme values in the tails of the PDFs. Following the practice of Tierz et al. (2016b,a), I have chosen to truncate the Gaussian PDF at the integer closest to the lowest and highest mobility represented in the filtered mobility data set. The final mobility PDF used for the energy cone modelling is also presented in Figure 4.9.

Date	Volcano	Type	dh (km)	l (km)	Volume (km^3)	dh/l	Reference
1-Mar-1963	Agung	con	2.500	9	1.00E-02	0.278	(Hayashi and Self, 1992)
1-May-1963	Agung	con	3.300	11.5	1.00E-02	0.287	(Hayashi and Self, 1992)
1929	Akita-Komagatake	con	2.000	6.5		0.308	Tsuya 1930; Kozu 1934
1783	Asamayama (Asama)	con	4.500	8.5		0.529	(Aramaki, 1963)
1783	Asamayama (Asama)	con	4.500	15		0.300	(Aramaki, 1963)
24-Dec-2006	Bezymianny	con	1.761	7.2		0.245	(Carter et al., 2008)
1913	Chokai	con	0.900	10		0.090	(Hayashi and Self, 1992)
1913	Colima	con	2.47	9	1.62E-03	0.274	(Saucedo et al., 2019)
1913	Colima	con	2.48	9.5	1.71E-03	0.261	(Saucedo et al., 2019)
1913	Colima	con	1.6	4.4	1.19E-03	0.364	(Saucedo et al., 2019)
1913	Colima	con	2.35	9	1.08E-03	0.261	(Saucedo et al., 2019)
1913	Colima	con	2.25	7.2	8.64E-04	0.313	(Saucedo et al., 2019)
1913	Colima	con	2.15	7.9	7.11E-04	0.272	(Saucedo et al., 2019)
1913	Colima	con	2.07	6.8	6.12E-04	0.304	(Saucedo et al., 2019)
1913	Colima	con	2.25	7.9	1.19E-04	0.285	(Saucedo et al., 2019)
1913	Colima	con	2.35	8.65	1.82E-03	0.272	(Saucedo et al., 2019)
1913	Colima	con	2.85	13.5	2.84E-02	0.211	(Saucedo et al., 2019)
1913	Colima	con	2.7	12.5	2.25E-01	0.216	(Saucedo et al., 2019)
1913	Colima	con	2.75	13.2	2.38E-02	0.208	(Saucedo et al., 2019)
1913	Colima	con	2.39	10.2	1.22E-02	0.234	(Saucedo et al., 2019)
1913	Colima	con	2.6	15.7	2.83E-02	0.166	(Saucedo et al., 2019)
1913	Colima	con	2.67	15.1	2.94E-02	0.177	(Saucedo et al., 2019)
1913	Colima	con	2.55	9.7	5.82E-03	0.263	(Saucedo et al., 2019)
1913	Colima	con	2.65	14.7	1.76E-02	0.180	(Saucedo et al., 2019)
1913	Colima	con	2.3	9	1.35E-02	0.256	(Saucedo et al., 2019)
1913	Colima	con	2.77	15	2.48E-02	0.185	(Saucedo et al., 2019)
1994	Colima	con	2.85	15.9	2.39E-02	0.179	(Saucedo et al., 2019)
1999	Colima	con	1.56	3.75	5.00E-04	0.416	(Saucedo et al., 2019)
1999	Colima	con	1.48	3.3	8.00E-04	0.448	(Saucedo et al., 2019)
1999	Colima	con	1.44	3	3.60E-04	0.480	(Saucedo et al., 2019)

Date	Volcano	Type	dh (km)	l (km)	Volume (km^3)	dh/l	Reference
2003	Colima	con	1.46	3.5	3.00E-04	0.417	(Saucedo et al., 2019)
2005	Colima	con	1.76	5.1	1.00E-03	0.345	(Saucedo et al., 2019)
1951	Camiguin (Hibok-Hibok)	con	1.500	5.6		0.268	(Macdonald and Alcaraz, 1956)
1968	Mayon	con	2.100	3.7		0.568	(Moore and Sisson, 1981)
1968	Mayon	con	2.100	4.2		0.500	(Moore and Sisson, 1981)
1968	Mayon	con	2.100	4.7		0.447	(Moore and Sisson, 1981)
1968	Mayon	con	2.100	4.5		0.467	(Moore and Sisson, 1981)
1969	Mayon	con	2.600	5	1.50E-03	0.520	(Hayashi and Self, 1992)
22-Jul-1980	Mt. St. Helens	con	1.700	6.5	3.00E-03	0.262	(Moore and Sisson, 1981)
22-Jul-1980	Mt. St. Helens	con	1.200	5.9	3.00E-03	0.203	(Moore and Sisson, 1981)
7-Aug-1981	Mt. St. Helens	con	1.200	5.7	4.00E-03	0.211	(Moore and Sisson, 1981)
19-Feb-75	Ngaurahoe	con	1.400	1.9	1.25E-03	0.737	(Narin and Self, 1978)
6-Jun-1912	Novarupta	con	1.000	25		0.040	(Hayashi and Self, 1992)
1-Apr-1973	Santa Maria (Santiaguito)	con	1.500	4.2		0.357	(Jr et al., 1977)
1-Sep-1973	Santa Maria (Santiaguito)	con	0.900	3		0.300	(Jr et al., 1977)
	Shirouma-Oike	con	1.000	4	3.00E-05	0.250	(Hayashi and Self, 1992)
18-Oct-1997	Soufriere Hills Volcano	con	1.220	4.6	1.41E-04	0.265	(Calder et al., 1999)
18-Oct-1997	Soufriere Hills Volcano	con	1.270	4.4	8.20E-05	0.289	(Calder et al., 1999)
18-Oct-1997	Soufriere Hills Volcano	con	1.050	3	2.00E-05	0.350	(Calder et al., 1999)
18-Oct-1997	Soufriere Hills Volcano	con	1.110	3.3	6.30E-05	0.336	(Calder et al., 1999)
17-Sep-1996	Soufriere Hills Volcano	con	0.946	3	1.23E-02	0.315	(Calder et al., 1999)
10.5 ka	Toluca, Nevado de	con	1.100	7	1.25E-04	0.157	(Arce et al., 2003)
10.5 ka	Toluca, Nevado de	con	1.100	13	1.25E-04	0.085	(Arce et al., 2003)
10.5 ka	Toluca, Nevado de	con	1.100	14	1.25E-04	0.079	(Arce et al., 2003)
10.5 ka	Toluca, Nevado de	con	1.100	13	1.25E-04	0.085	(Arce et al., 2003)
25-Jun-97	Soufriere Hills Volcano	dilute	1.010	6.7	7.91E-04	0.151	(Calder et al., 1999)
26-Dec-97	Soufriere Hills Volcano	dilute	1.200	5	2.50E-03	0.240	(Calder et al., 1999)
Feb-1913	Colima	dilute	2.400	9.4		0.255	(Sulpizio et al., 2015)
10.5 ka	Toluca, Nevado de	dilute	1.100	22	1.25E-04	0.050	(Arce et al., 2003)
10.5 ka	Toluca, Nevado de	dilute	1.100	7	1.25E-04	0.157	(Arce et al., 2003)

Date	Volcano	Type	dh (km)	l (km)	Volume (km^3)	dh/l	Reference

Table 4.2: *Analogue column collapse PDC data used to model future PDCs a Aluto volcano. The data are largely sourced from the FlowDat database (Ogburn, 2012), but are supplemented by data from additional sources. Con = Concentrated base PDC, Dilute = dilute based PDC*

4.2.3 The location of future eruptions at Aluto

A principle parameter that dictates where a PDC might inundate is the location of its source. This controls not only where it is initiated, but also the topography over which the flow traverses. At many volcanoes, a single point source is adequate, as past PDCs have always been generated from an eruption at a single summit vent or a particular lava dome. However, at Aluto, previous eruptions have been sourced from discrete sources across the edifice, in fact 82 geographically distinct eruptive vents have been identified using the LiDAR topographic data set (Figure 4.10). This only represents vents currently visible at the surface, and many will have been buried by the deposits of subsequent eruptions. The deposits of individual pumice cones at Aluto are devoid of intercalating palaeosols, which would suggest that each pumice cone, and thus each vent, is the product of a single eruption. However, some eruptions produce multiple vents, such as the Kertefa Pumice Cone Complex on the NE rim of the caldera. It is unclear, other than from detailed field investigation, whether distinct vents were involved in the same eruption. For simplicity, I assume each vent is the product of a separate eruption. This should be considered a caveat. However, as vents involved in the same eruption are likely to be close together, on the same fissure for example, this should have a relatively minor influence on the final vent opening susceptibility model.

For vent-opening purposes, it is most appropriate to consider post-caldera volcanism at Aluto as a silicic monogenetic field. As is the case for many basaltic monogenetic fields, these vents do not follow an entirely random distribution around the caldera, but are spatially clustered. Many vents are located above underlying structural features such as the caldera ring fault and cross-cutting regional faults (Hutchison et al., 2016c). Similar observations have been made at numerous volcanic fields around the world and the proximity to such structural features is often taken into account in vent opening susceptibility models (Connor and Hill, 1995; Weller et al., 2006; Cappello et al., 2012; Bevilacqua et al., 2015). However, at Aluto the location of many of these underlying structures is inferred from the presence of volcanic vents (Hutchison et al., 2015). It would be somewhat circular to define future vent locations by their proximity to these underlying structures which are

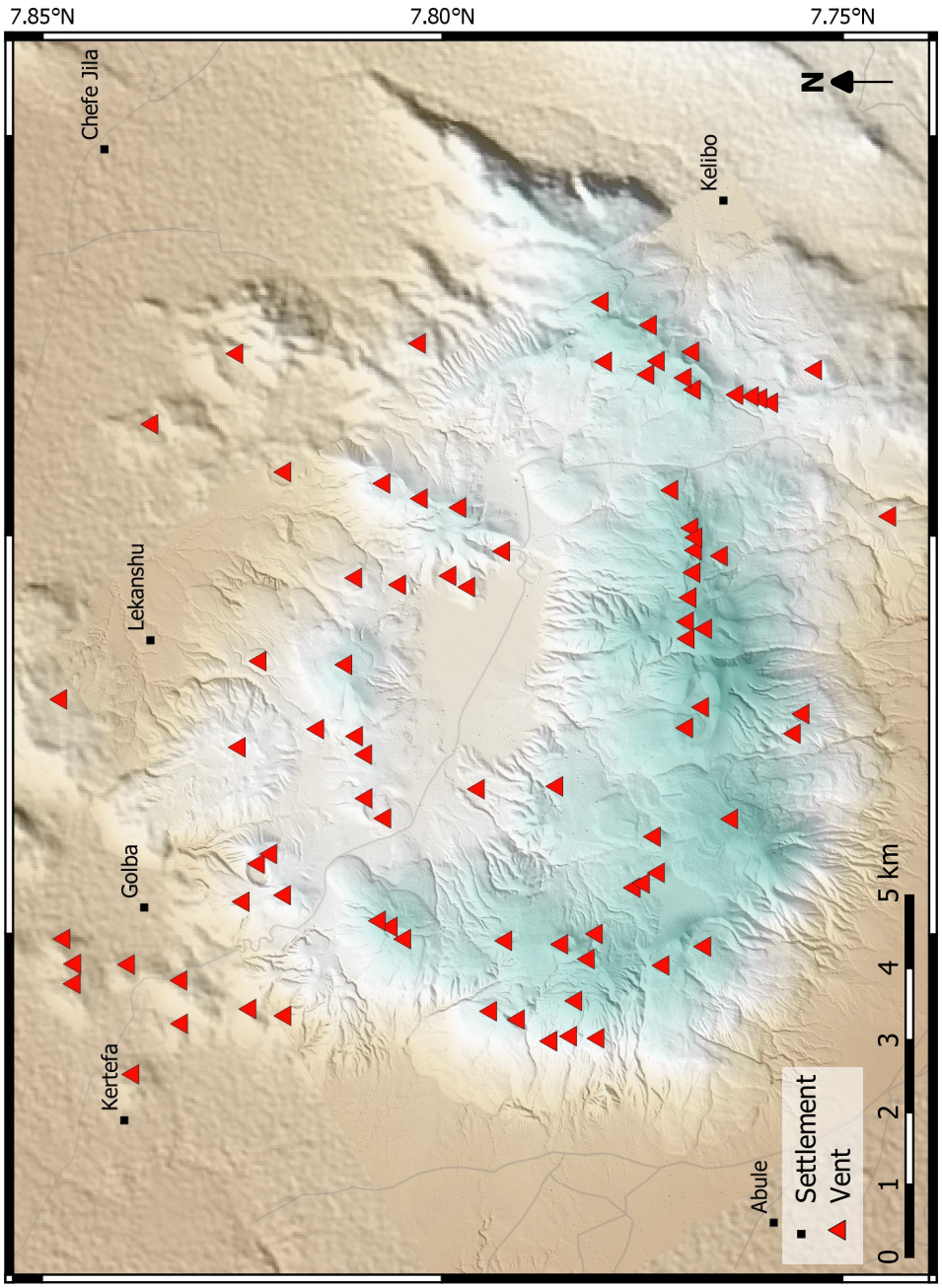

Figure 4.10: *The location of vents across and around Aluto identified from the LiDAR DEM of Hutchison et al. (2014).*

themselves based on the vent locations. Instead, it is more reasonable to establish the probability of future vent locations based on the locations of exposed vents.

We employ a method that has been developed for a monogenetic field in the Yucca mountain region, USA (Connor and Hill, 1995) and has since been adapted and applied to many volcanoes and volcanic fields around the world (Weller et al., 2006; Marti and Felpeto, 2010; Cappello et al., 2012; Bevilacqua et al., 2015). The method assumes the likelihood of an eruption occurring at any location should be proportional to its proximity to vents from previous eruptions. From any past vent, the probability of a new vent opening near it can be characterised by a kernel centred on the past vent. The probability 'decays' at progressively greater distances from the vent in all directions according to the shape of the kernel. When a point in space is close to many past vents, the probability of vent-opening associated with the kernel of each past vent is summed (and in the end normalised). In other words, the probability of an eruption occurring at a particular point is the relative 'spatial intensity' (λ_s) of volcanism at that point.

For this technique to be representative of a particular volcanic field or in our case caldera, the parameters of the kernel must be characteristic of that volcanic field. Typically a Gaussian kernel is used in vent-opening investigations (Weller et al., 2006), and the choice of kernel is thought to have an insignificant influence on the final result compared to the bandwidth of the kernel (Wand and Jones, 1994). To establish a bandwidth, I am interested in how far away future vents are likely to be from past vents, which I assume is related to how far away past vents have tended to be from one another. This is characterised by the nearest neighbour distances of the past vents. I can use these nearest neighbour distances to establish the appropriate bandwidth (h) of the Gaussian kernel.

To do this I find the best-fit Gaussian kernel bandwidth for the cumulative density function (CDF) of the nearest neighbour distances of past vents. I have located past vents across the edifice using the LiDAR-derived DEM of Hutchison et al. (2014), and calculated their nearest neighbour distances. The results of this and the best fit Gaussian kernel is presented in Figure 4.11. The resulting bandwidth is 0.625 km, which for a Gaussian kernel

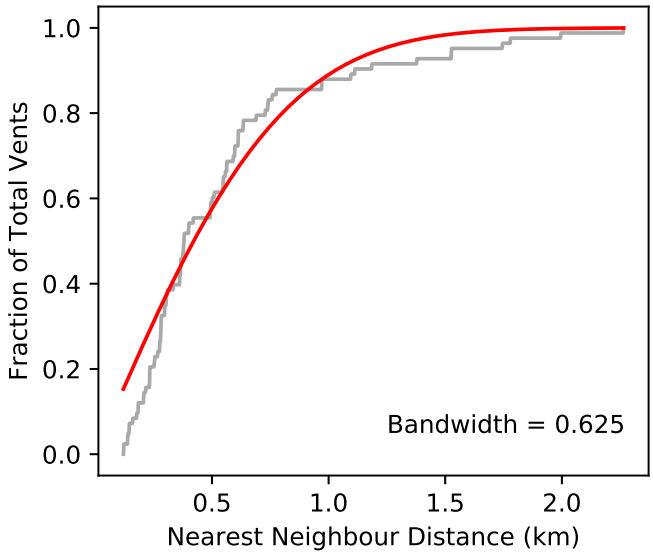

Figure 4.11: *Cumulative distribution function (CDF) of the nearest-neighbour distances of past vents at Aluto (gray) and the best-fit Gaussian CDF to the data (red). The bandwidth of this kernel can be used to characterise how the probability of vent opening decays away from each vent.*

means that 68% of vents are within 0.625 km of another. Locating past vents in such a fashion presents challenges surrounding vents being obscured by later deposits, where the chance of burial is probably related to its proximity to other vents. This produces a biased data set. Unfortunately, this cannot be avoided without being able to identify buried vents. However, generally speaking, it is likely that the more proximal a vent is to another, the greater the probability of its burial and obscuration. This means that the CDF of nearest neighbour distances presented here under-represents the real proportion of vents at lesser distances.

Once the bandwidth is established, the spatial intensity of volcanism at a given point ($\hat{\lambda}_s(x, y)$) can be calculated as Equation 4.5 (Weller et al., 2006):

$$\hat{\lambda}_s(x, y) = \frac{1}{2\pi N h^2} \sum_{i=1}^{N} \exp\left(-\frac{1}{2}\left[\frac{d_i}{h}\right]^2\right) \tag{4.5}$$

where N is the number of past vents, h is the bandwidth of the Gaussian kernel estimated earlier and d_i is the distance between an individual past vent and point (x, y). This process can be repeated in a regular grid across the area of interest to create a vent

opening probability map. Providing the grid of points is sufficiently large, the sum of these probabilities should approach 1. I have chosen 1200 vents where $\hat{\lambda}_s$ will be calculated, with a regular 500 m lat-long spacing, covering a sufficient area for the sum of probabilities at all vents to approach 1 (leaving a residual probability of 1.3×10^{-6} that a vent will open outside the area). The probability associated with the opening of each vent is presented in Figure 4.12. Each of these 1200 vents will be the source of PDCs during energy cone simulations.

4.3 Monte Carlo energy cone PDC simulation

Energy-cone simulation is often employed as a simple method to evaluate the general area that can be invaded by PDCs. The simplicity of the model is appropriate for volcanoes where in depth knowledge of the system is lacking, as only a few parameters are considered, and fewer assumptions need to be made. As the model itself is also computationally simple, it can be run iteratively to fully explore aleatory uncertainties, in a way that a computationally expensive model cannot without statistical emulation (Spiller et al., 2014). The results of the Monte Carlo energy cone simulation are less precise and less grounded in the physics of PDC behaviour, but reflect uncertainties in the inputs, and provide a more useful and accurate answer than only a few complex flow models. The results are quantitative, justifiable and defendable (with clear caveats), making them suitable for risk assessment (Calder et al., 2015).

4.3.1 Methodology

Theory

Based on the energy cone Monte Carlo model, the probability of a PDC invading a particular location $P(PDC_j)$, where j is the location of interest, can be calculated as:

$$P(PDC_j) = \sum_{i=1}^{N} P(PDC_j|vent_i) \times P(vent_i) \tag{4.6}$$

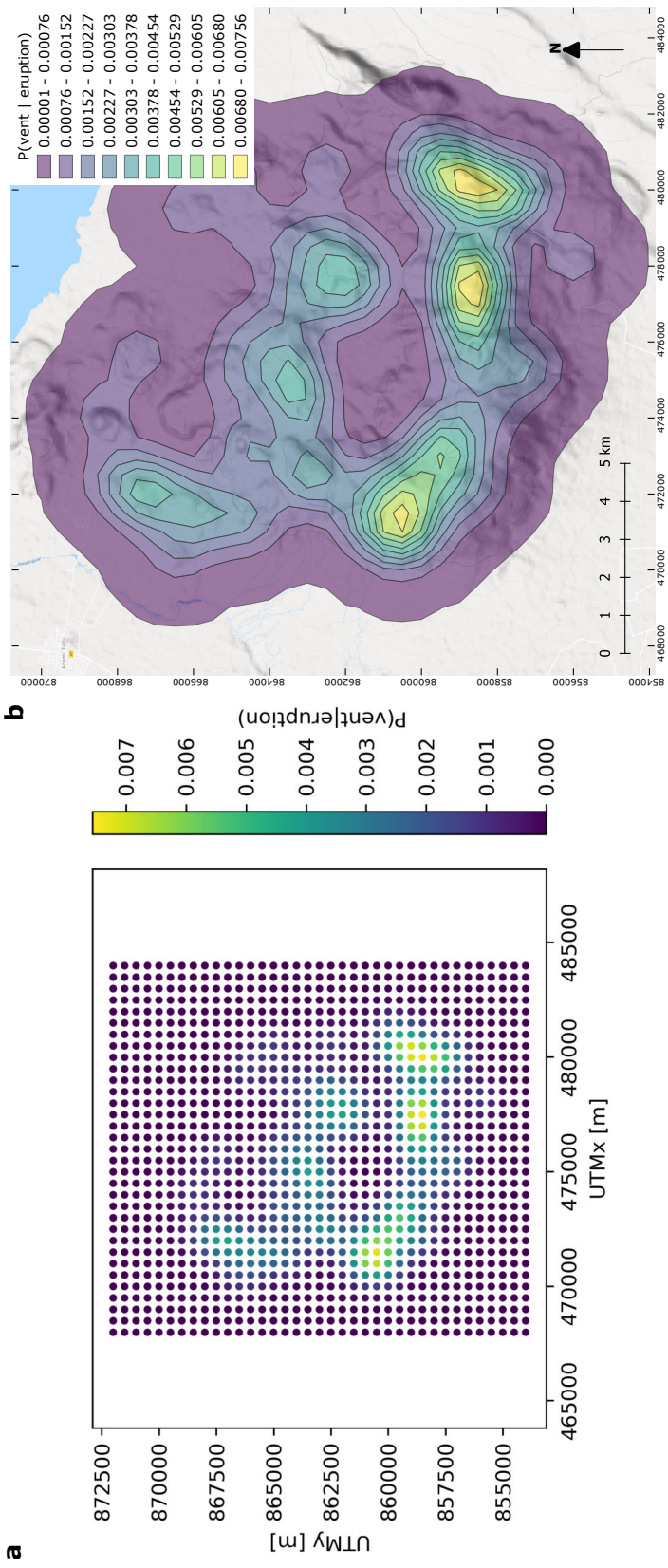

Figure 4.12: *(**a**) Vent opening probability map for each PDC source to be used during Monte Carlo energy cone modelling. (**b**) Contoured vent opening probability using Google terrain base map. Vent opening is most likely around the caldera rim and in particular the southern portion.*

where $vent_i$ is each source vent in the simulation and $P(vent_i)$ is the probability of eruption from source vent i; the value calculated in the vent opening susceptibility section. $P(PDC_j|vent_i)$ (the probability of PDC inundation at point j from vent i) can be calculated as:

$$P(PDC_j|vent_i) = \frac{1}{S} \times \sum_{k=1}^{N} (W_k \times s_k) \tag{4.7}$$

where S is the total number of simulations from $vent_i$, k is the identity of each simulation, s_k is a binary 1 or 0 representing inundation (1) or no inundation (0) during simulation k, and W_k is the weight associated with the input parameters (collapse height (H_0) and mobility (ϕ)) for simulation k. Assuming independence of mobility and collapse height, this weight can be calculated as:

$$W_k = \frac{f1_{H_k} \times f2_{\phi_k}}{g1_{H_k} \times g2_{\phi_k}} \tag{4.8}$$

where $f1$ and $f2$ are the target PDFs of parameters H (collapse height) and ϕ (mobility), respectively, and $g1$ and $g2$ are the sampled (in this case uniform) PDFs of parameters H and ϕ. The values of f and g at H_k and ϕ_k are the infinitesimal probability densities evaluated from the relevant PDF at the value of the parameter used in simulation k. Figure 4.13 shows the 10,000 input combinations of collapse height and PDC mobility used at every one of the 1200 vents in the energy cone model. Each pair is coloured by its respective input parameter weighting (W_k) from Equation 4.8.

Computational methods

The energy cone model at Aluto aims to cover the parameter space outlined in the previous sections: that of PDC source location ($P(vent_i)$), collapse height (H_0) and flow mobility (ϕ). I ran numerous simulations with different combinations of these features to cover the full parameter space and capture the underlying PDFs, 10,000 iterations with sampled combinations of collapse height and flow mobility is generally considered statistically representative (e.g Sandri et al., 2018a; Tierz et al., 2016b,a). As the eruption location is also

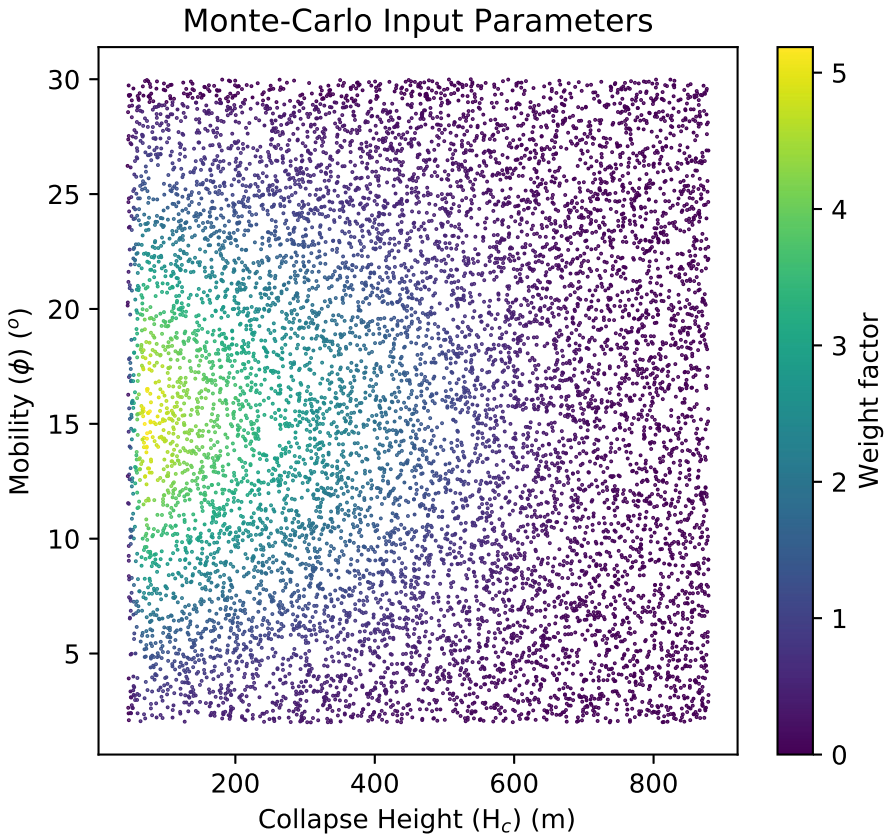

Figure 4.13: *The combinations of input parameters used in the Monte Carlo energy cone simulation at each vent. Points are randomly sampled from uniform distributions within the range of expected values for each parameter, and are weighted according to Equation 4.8. Each input pair is coloured according to its weight.*

uncertain, I ran 10,000 simulations from each of a potential 1200 different sources across the edifice; totalling 12×10^6 simulations. The precision of the result can be approximated as $\frac{1}{\sqrt{n}}$, where n is the number of iterations. This means that with 10,000 simulations per vent, the precision of the Monte Carlo energy cone analysis is approximately 0.01, or 1%. Each simulation was run using input parameters randomly selected from a uniform PDF of collapse height and flow mobility. The output of each simulation is a 2D array (lat/-long) of ones and zeros surrounding the source location, representing inundation (1) and no-inundation (0) by a PDC. Areas which are inundated most often during simulations have the highest probability of inundation (Equation 4.6). The simulations then underwent importance sampling according to the individual combinations of input parameters; ultimately placing greater emphasis on the types of events which are considered more likely than others (Equations 4.7 and 4.8).

To provide flexibility in the emphasis I or future workers wish to apply to particular types of events, it is most efficient to weight the simulations after computation rather than simulating more or fewer events of a particular type. For this reason, the 10,000 combinations of collapse height and flow mobility are randomly selected from *uniform* distributions to ensure an even coverage of the parameter space. The weight I wish to apply to each simulation can then be adapted depending on the distribution of parameters which are considered most representative, whilst maintaining an even coverage of the parameter space. The limits of the uniform distributions are defined by the maximum and minimum expected values from the parameterisation conducted earlier. The weighting factor associated with each parameter in each simulation can be calculated as the ratio between the infinitesimal probability density of the 'target' PDF and the uniform PDF at that parameter value (Equation 4.8); the target PDF being the PDF I think most representative of the true probability distribution of the parameter. Assuming independence of the parameters, a single weighting factor can be obtained by multiplying the weighting factors for each parameter (H_c, ϕ and $\hat{\lambda}_s(x, y)$). As I am conducting an equal number of simulations at each vent, the location parameter is uniformly distributed during computation, the weighting factor applied to each vent is simply the probability of vent opening at that location. By multiplying the 'vent weighting factor' with the 'PDC weighting factor', I obtain the

overall weight for that simulation. This weighting process is summarised in Figure 4.14. Finally, the sum of all weighted simulations at each location, divided by the number of simulations at each vent (10,000), provides a map of inundation probabilities in the event of a PDC of unknown collapse height, mobility or source location. The algorithm developed to produce the probability map from the model outputs is graphically summarised in Figure 4.15. The energy cone model was written in Matlab (Tierz et al., 2016b,a), and adapted for this analysis and run on a 10m DEM resampled from that of Hutchison et al. (2014). The weighting algorithm was developed in Python 3 and the computation took place on the EDDIE cluster at the University of Edinburgh, using the resources of the Edinburgh Compute and Data Facility.

4.4 Exposure to pyroclastic density current hazard

4.4.1 Mapping population and infrastructure exposure around Aluto

Population mapping: Methods

One aspect of risk is the relationship between the footprint of the hazard, and where people reside or work (i.e. exposure). In the following sections, I aim to quantify the exposure around Aluto. One potential approach to is to assess census data. The most recent census in Ethiopia was in 2007 (Central Statistics Agency -Government of Ethiopia and Minnesota Population Center - University of Minnesota, 2007), but was only conducted to a wereda (sometimes spelled *'woreda'*) (local authority) level spatial resolution. The land around Aluto belongs to two weredas, and so this level of precision is insufficient (as the probability of PDC inundation varies from drainage-to-drainage). Another option is to use online databases such as 'WorldPop' or 'LandScan'. WorldPop claims to provide 100 m resolution gridded global population data based on census records, multi-spectral satellite imaging, telecommunications usage data and where data are sparse, random-forest modelling techniques (University of Southampton, 2019; Stevens et al., 2015). LandScan^{TM} claims to provide 1 km gridded global population data. LandScan uses a multilayered dasymetric spatial modelling approach, combining high resolution satellite imagery, the locations of

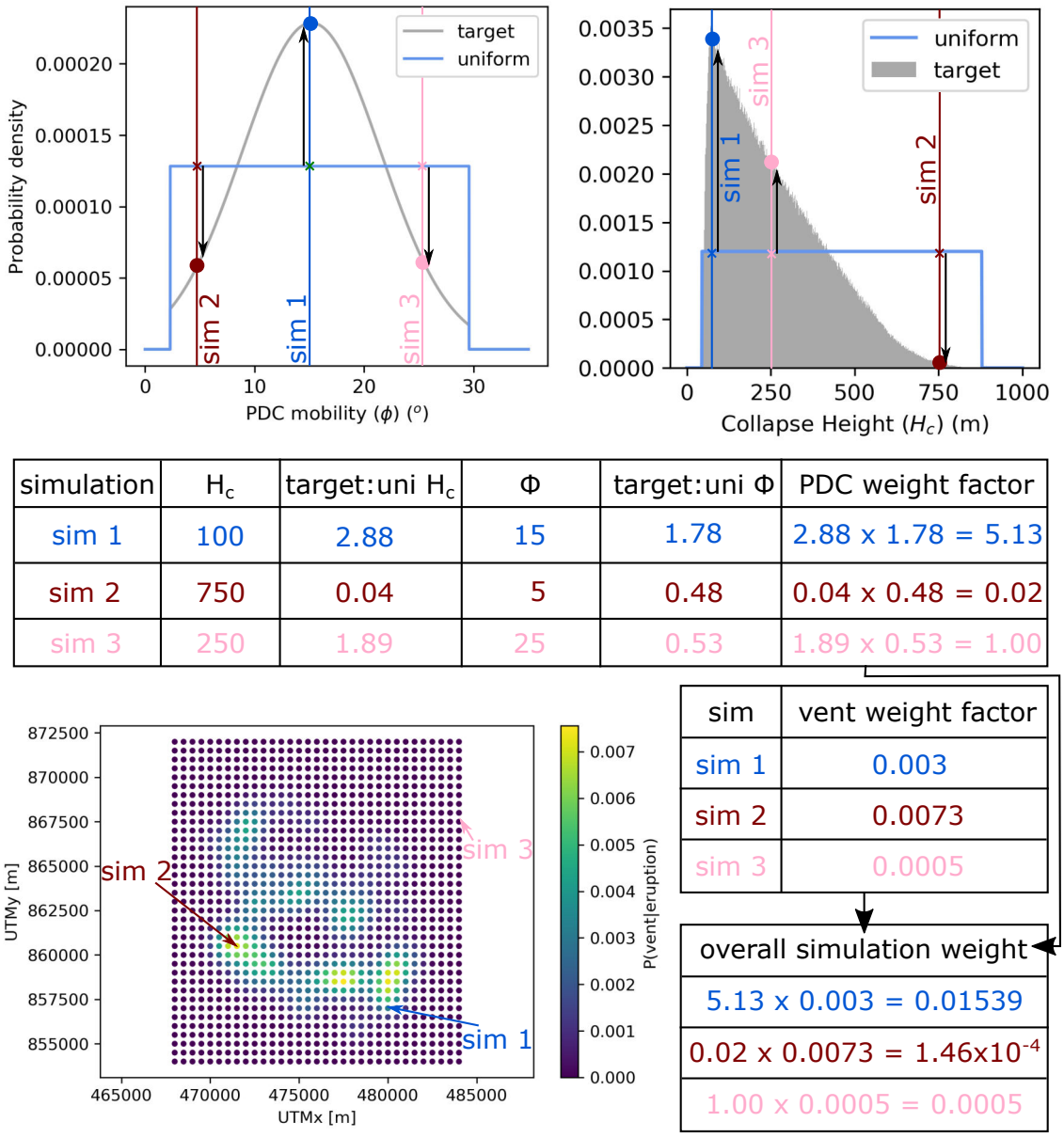

simulation	H_c	target:uni H_c	Φ	target:uni Φ	PDC weight factor
sim 1	100	2.88	15	1.78	2.88 x 1.78 = 5.13
sim 2	750	0.04	5	0.48	0.04 x 0.48 = 0.02
sim 3	250	1.89	25	0.53	1.89 x 0.53 = 1.00

sim	vent weight factor
sim 1	0.003
sim 2	0.0073
sim 3	0.0005

overall simulation weight
5.13 x 0.003 = 0.01539
0.02 x 0.0073 = 1.46×10^{-4}
1.00 x 0.0005 = 0.0005

Figure 4.14: *The method used to calculate the overall weight of each energy cone simulation. The total weight is the product of the individual weights associated with the particular collapse height, mobility, and source vent location of each simulation. The weights of the collapse height and mobility are the ratio between the uniform PDF from which they were randomly sampled, and the 'target' PDF at the value of the parameter in the simulation. The weight associated with the source vent location is simply the probability of vent opening for that location calculated earlier. These weights are then applied to the inundation map arrays for each simulation.*

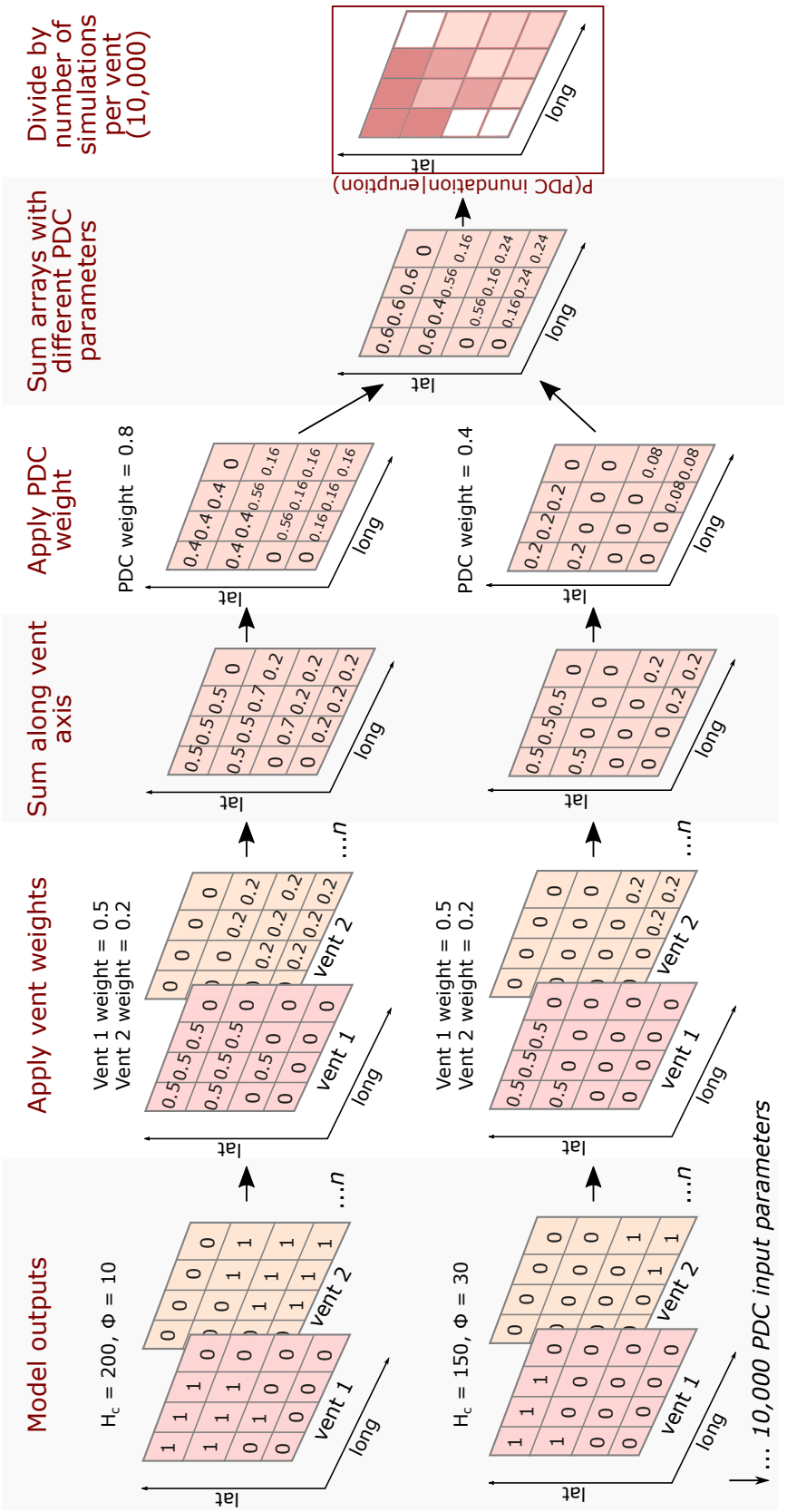

Figure 4.15: *A graphical summary of the algorithm developed in Python 3 to process the model output data and generate a conditional probability map where elements are P(PDC inundation|eruption). The input is a series of 10,000 3D arrays of dimensions (lat:long:vent), where each 3d array represents the model outputs of every vent for one combination of PDC input parameters (H_c and ϕ). The elements within the array inputs are binary, where 1 is PDC inundation, and 0 is no PDC inundation. These elements are then weighted according to the probability associated with the opening of the source vent. The resulting array is then summed (collapsed) along the vent axis, producing a 2D array with the combined inundations of every vent for a given pair of PDC input parameters. The elements in each 2D array are then weighted according to the pair of PDC input parameters that were modelled. The results from all 10,000 input parameter pairs are then summed to create a single 2D array which is then divided by the number of simulations at each vent (10,000) to create a probability map.*

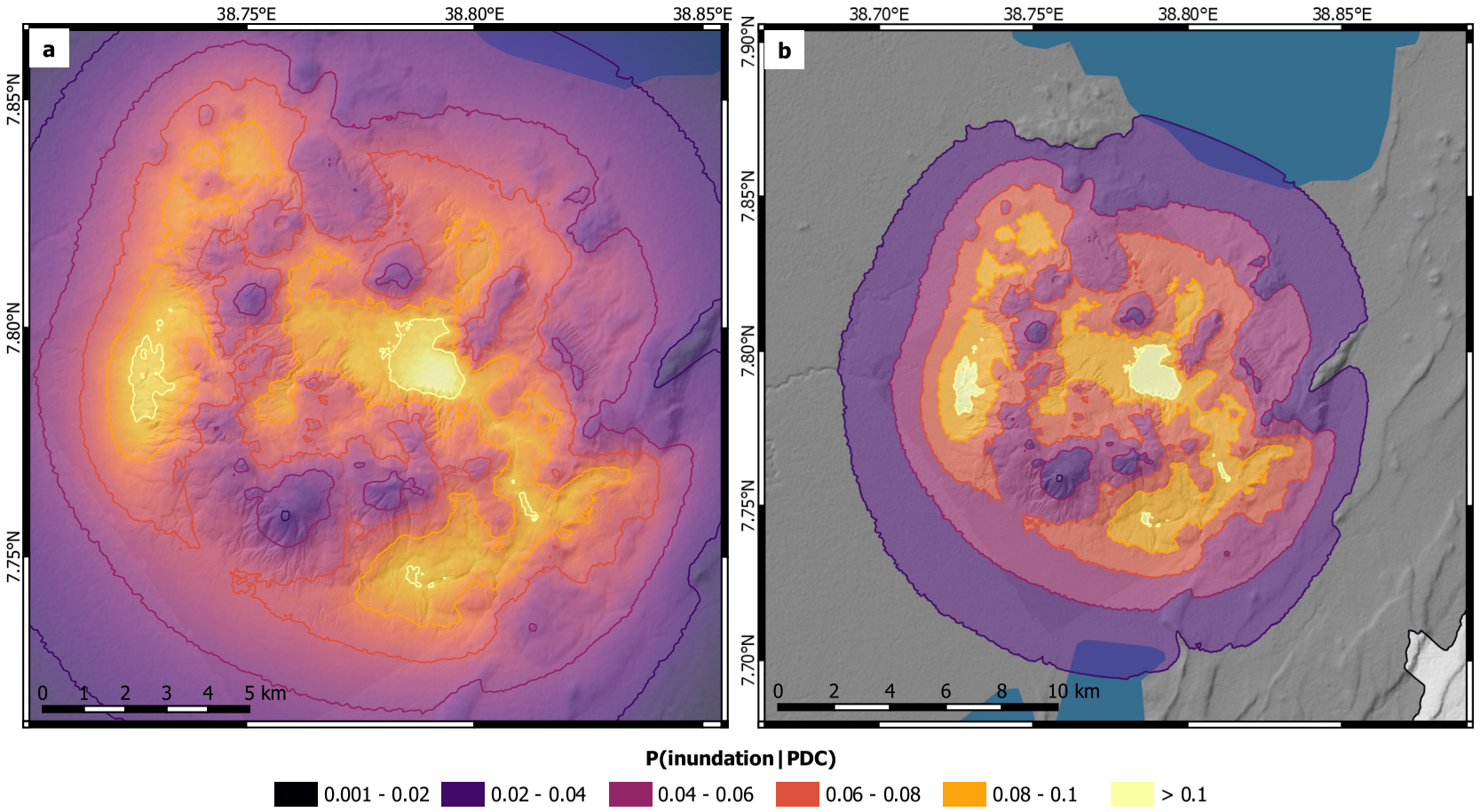

Figure 4.16: *The result of the* 12×10^6 *weighted Monte Carlo energy cone simulations, showing the conditional probability of PDC inundation given the generation of a PDC of unknown collapse-height, mobility and source location at Aluto. (a) A detailed view of the probability of inundation around the caldera. Continuous colour scale with contours; where hotter colours represent greater probabilities. The maximum probability is 0.11. (b) A generalised, large-scale map with categorised probabilities and contours, the colour scale is matched with that in 'a'.*

towns and villages, land cover, slope and roads to assign a probability of whether a cell is populated. This is then calibrated using sub-national census data and a population within the cell is estimated assuming modelled dynamic population change (Oak Ridge National Laboratory, 2019). To attain the highest possible spatial resolution, I also conducted a manual analysis of the population distribution using publicly available remote sensing data. The most granular measure of population achievable by remote sensing is mapping the location of houses combined with an assumed number of people living in each house. This was conducted using the latest satellite imagery provided by Google within QGIS (Google DigitalGlobe). Though the dates of imagery are not uniform across the area of interest, they are all between January 2018 and January 2019, so are considered to be roughly contemporary and the best available (Figure 4.17).

I attempted to automate the process to locate buildings. However, the majority of houses in rural areas have thatched roofs, and as the best aerial imagery was taken during dry seasons (avoiding cloud cover), it coincides with the teff harvest; where residents pile house-sized stacks of straw-coloured teff to dry in large circular mounds by their houses. This made it impossible to automatically distinguish between thatched roofs and nearby stacks of teff without far more complex and time consuming techniques (Figure 4.18). However, these features could be distinguished on a manual, subjective basis by taking into account contextual evidence such as the presence of worn paths and nearby walls. The survey was conducted manually, locating each identifiable building within the roughly 1450 km^2 area of interest surrounding Aluto, with 100% coverage within that area. The boundary of the area was arbitrarily chosen whilst ensuring it was >10 km away from the nearest previously active vent, but also covering the East Ziway volcanic field in case of future volcanic hazard assessments in this area. In rural areas, a building was defined as a structure with a separate roof. In urban areas, roofs were often joined, but the presence of outdoor dividing walls allowed separate residences to be distinguished. Very small structures that were clearly outdoor lavatories or sheds were discounted, but as identification is subjective, it is likely that some such buildings do exist within the data set. Anecdotally, there are very few residences in the urban areas around Aluto that span multiple floors, though this is another potential source of error. The extent of various sites of particular

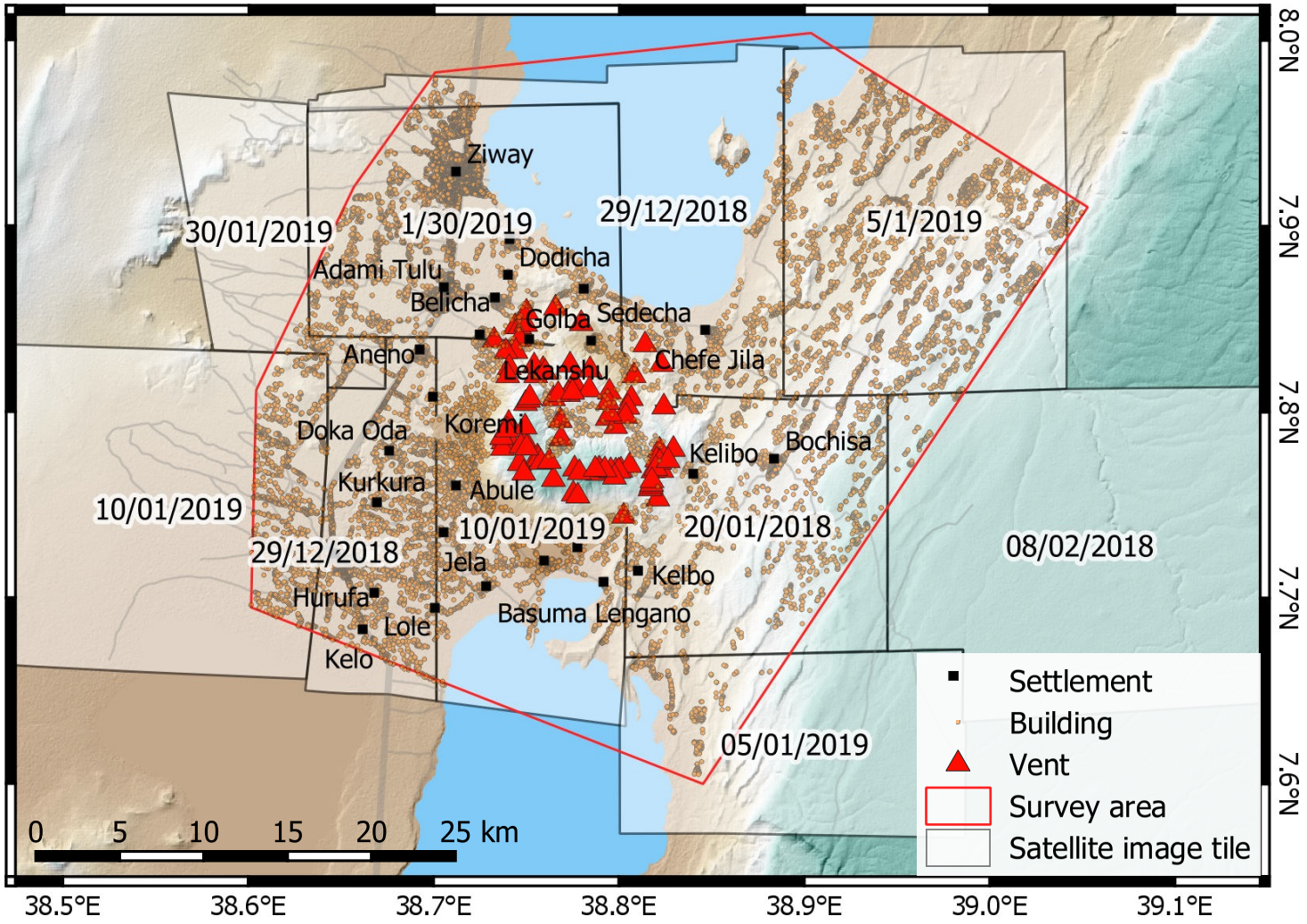

Figure 4.17: *Acquisition dates for satellite imagery used for mapping the distribution of buildings around Aluto in context. The earliest date is January 2018, and the latest January 2019. Orange points are the locations of individual buildings mapped around Aluto (total = 49,459). The red polygon marks the area of investigation for mapping these buildings, over which there is 100% coverage. Imagery source: Google, DigitalGlobe.*

Figure 4.18: *Comparison between (a) piles of teff or 'teff cones', and (b) typical rural huts around aluto. These were challenging to distinguish using aerial imagery, and attempts to automate the process failed. Instead locating buildings was done manually.*

interest (the geothermal power plant, Aluto school and Rose Farm) were identified from the same satellite imagery and traced to produce polygons.

To convert the number of buildings to a population, I need a conversion factor in the form of number of people per building. Anecdotally, residents on Aluto suggested that anywhere between 3 and 10 people live in each building. However, this is likely to vary significantly between households, regions and settlement types (i.e. urban versus rural). The most recent data available to produce robust conversion factors is the 2007 national

population and housing census (Central Statistics Agency -Government of Ethiopia and Minnesota Population Center - University of Minnesota, 2007), and so used to calculate this statistic. A more up-to-date census was planned for 2017 but was postponed indefinitely citing security concerns (Kinfu, 2019). Any future analysis would benefit from use of more up-to-date census data when it becomes available.

The 2007 census was conducted at a wereda level; the two weredas within the area of interest defined in Figure 4.17 are Ziway town, encompassing the urban area of *Ziway town* (sometimes spelled *Zeway*), and the rest of the area encompassed by *Ziway Dugda* (sometimes spelled *Zeway Dugda*). Data were collected at regional centres, requiring members of each household to travel to complete the census. It isn't clear where these centres were but if they were at each wereda office, there would have been one in Ziway, and another in Chefe Jila, 10s of km from many residents. It may be the case that the census under-represents remote, rural settlements and so under-estimates the total population. A wide range of statistics were collected for each wereda, but those pertinent to this work are the total population (P_{total}) and the number of housing units (N_{hu}). Using these two parameters, for each wereda, the average population per housing unit (P_{hu}) is simply defined as:

$$P_{hu} = \left(\frac{P_{total}}{N_{hu}} \right) \tag{4.9}$$

Each housing unit is a building, but not all buildings are housing units. It is challenging to establish how may buildings are lived in (anecdotally, some are abandoned), and how many fulfil other purposes. Dedicated housing for livestock is not typical, the census indicates that in Ziway Dugda, about 64% of households regularly sleep in the same room as their livestock, and 4% of households have no livestock. This means that 32% of households may have need for alternative buildings for their animals. Anecdotally, many households on Aluto keep their livestock in outdoor thorn-pens, and so don't have additional buildings. Therefore, for simplicity, each building is considered a housing unit, and is assigned a number of people according to its wereda and Equation 4.9. I assume that the number people per housing unit presented in the 2007 census is equivalent to that today. Each building in the Ziway town wereda is thus assigned 3.4 people and in the

Wereda	P_{total}	N_{hu}	P_{hu}
Ziway town	43,660	12,876	3.4
Ziway Dugda	120,862	23,631	5.1

Table 4.3: *Table summarising the 2007 population and housing census data for Ziway town and Ziway Dugda; the two weredas near Aluto. P_{total} is the total population, N_{hu} is the total number of housing units, P_{hu} is the number of people per housing unit. Data: Central Statistics Agency -Government of Ethiopia and Minnesota Population Center - University of Minnesota (2007)*

	Manual Analysis			**LandScan**	**WorldPop**	**2007 Census**
Wereda	N_{hu}	P_{hu}	P_{Total}	P_{Total}	P_{Total}	P_{Total}
Ziway Town	11,616	3.4	39,494	66,546	34,654	43,660
Ziway Dugda	47,843	5.1	243,999	223,675	161,914	120,862
Total	*59,459*	*n/a*	*282,009*	*290,221*	*196,568*	*164,522*

Table 4.4: *Table comparing the results of the manual, LandScan, WorldPop and 2007 census population analyses of the weredas surrounding Aluto. N_{hu} is the total number of housing units, P_{hu} is the people per housing unit calculated in Equation 4.9, and P_{total} is the total population. The are disparities between all of the data sets, especially with the 2007 census. However, there is reasonable agreement between the manual and LandScan data sets.*

Ziway Dugda wereda 5.1 people (Table 4.3).

Population mapping: Results

The results of the population distribution analysis are presented in the following section, and the suitability of each data set (Manual analysis, LandScan and WorldPop) for PDC hazard analysis is also critically assessed.

The results of different population analyses in Table 4.4 paint a picture of uncertainty in the true population around Aluto. The 2007 census in particular provides a much smaller estimate than any of the other survey techniques. This is likely to be partly due to the population growth since the census, but also incomplete participation in the census. Of the remaining techniques, LandScan provides the highest estimate, and WorldPop the lowest, with my manual analysis in-between (though closer to the LandScan values). The total population based on counts of buildings and census data (manual analysis), integrated across the area of interest therefore appears consistent, providing a moderate population estimate. For PDC hazard, the resolution of the data set is an important consideration;

PDCs are often topographically constrained, and PDCs at Aluto tend to spread laterally on the scale of km rather than 10s of km. This means that a drainage-to-drainage resolution (ie. 10s to 100s of m) population distribution is essential in order to identify communities at risk. The LandScan data are resolved to 1 km, whilst WorldPop claims 100 m resolution. The manual analysis provides the best possible resolution, but I have gridded it to 100 m for simplicity. Figure 4.19 provides a side-by-side comparison of the same areas covered by the three alternative data sets.

The data sets vary considerably in appearance; the manual analysis and LandScan data appear to be relatively consistent, showing roughly the same distribution of more and less populated areas, albeit to greater or lesser resolution. However, the WorldPop data, despite its high resolution, is less consistent. It appears to resort to random forest modelling of the likely locations of settlements; assuming a circular shape and size, with little accuracy as to the location. The size of settlements appears smaller than is suggested by the manual analysis based on actual building locations, and these are set on a single background population value. Though precise, WorldPop appears not to provide an accurate representation of population distribution, at least around Aluto. To quantify the agreement in population distribution around Aluto reported by different data sets, and to establish the truely accurate maximum resolution of the LandScan and WorldPop data sets, I compared the population values of equivalent pixels. As each data set has a different resolution, I resampled each data set to a consistent grid at a range of resolutions; where the value of each resampled grid cell is the sum of buildings within that grid for each data set. This allows the population over the equivalent locations and areas to be compared. Each was compared to the manual analysis, as this represents the best-resolved and most reliable data set available. The results are shown in scatter plots in Figure 4.20, where the population of equivalent cells of a range of sizes are compared to one another. A graph showing total agreement would perfectly follow the gray 1:1 line provided in each plot.

The plots indicate that WorldPop poorly represents the population distribution below around 5 km resolution, whilst LandScan is better; showing very broad agreement at 1 km resolution. Unsurprisingly, at 100 m resolution, the 1 km LandScan data set poorly repre-

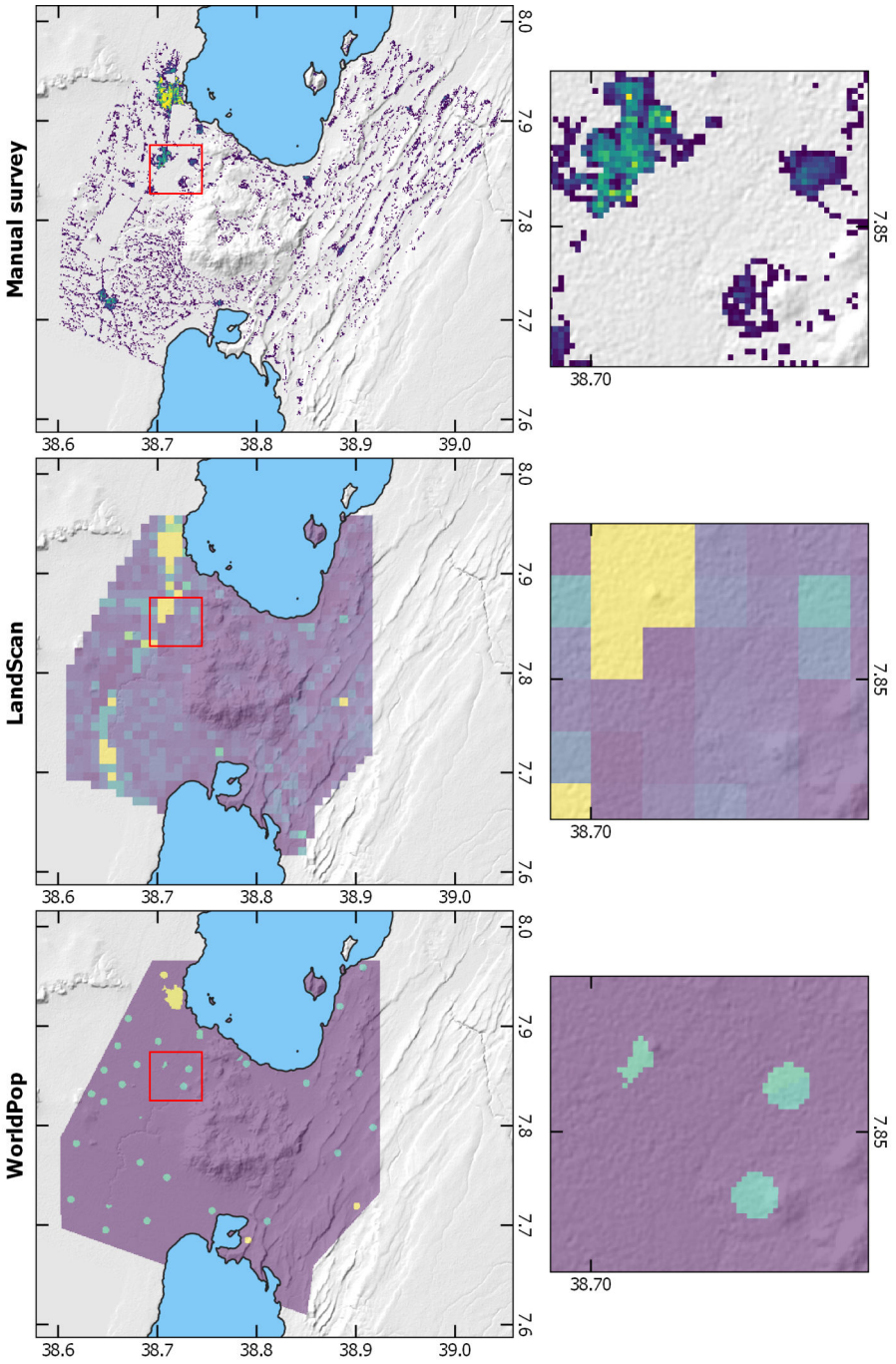

Figure 4.19: *Maps comparing raster population data from my manual analysis, LandScan and WorldPop data sets. The left hand maps show an overview of the data set for the area, and the right hand maps show a magnified inset of the same areas for comparison. The red squares indicate the location of this inset. Though WorldPop claims a 100 m resolution, the accuracy of the population distribution is inferior to both LandScan and the manual analysis. Whilst LandScan appears relatively accurate, it is lower resolution than the manual analysis.*

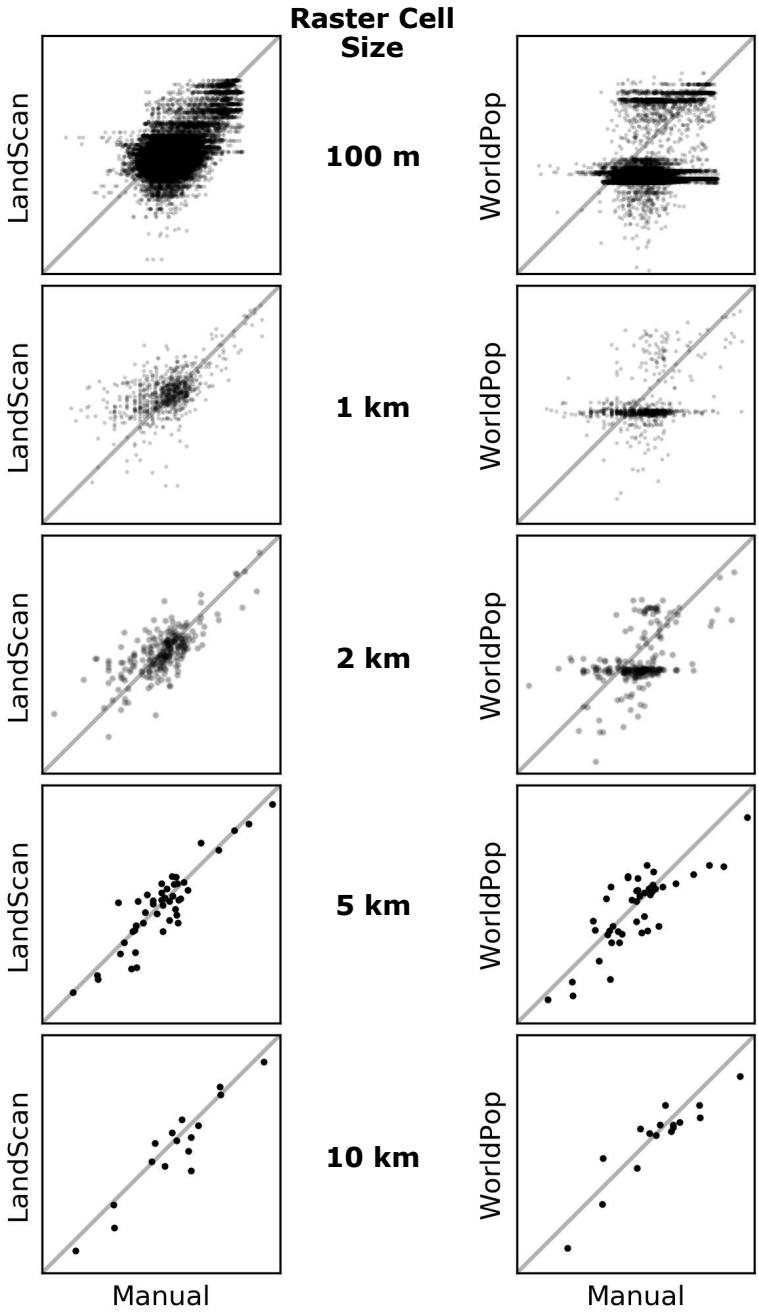

Figure 4.20: *Plots comparing the population of equivalent cells reported by LandScan and WorldPop with the results of the manual analysis. The closer the points to the gray 1:1 line, the better the agreement. This is repeated for a range of cell sizes to assess the degree of spatial agreement between the data sets at different resolutions, effectively showing at what resolution LandScan and WorldPop accurately represents the true population distribution.*

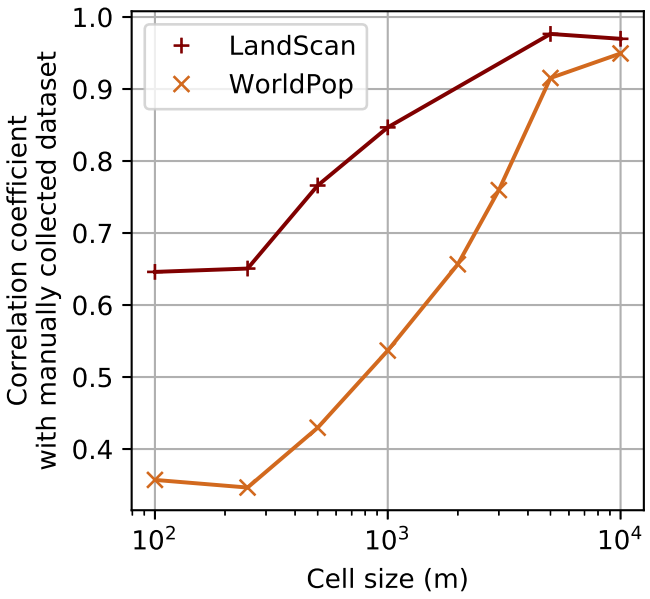

Figure 4.21: *Plot showing the degree of agreement between the LandScan and WorldPop data sets and the manual analysis. Degree of agreement is quantified as the correlation coefficient. The greater the agreement, the more accurately the population distribution is represented in the data set. This plot indicates that agreement improves inversely with the data set resolution. Though the WorldPop data set claims a 100 m spatial resolution, the accuracy of the population distribution at this resolution is very low. LandScan consistently outperforms WorldPop in this regard, despite WorldPop's purported 100 m resolution.*

sents the population distribution. In terms of the accuracy of the population distribution, LandScan consistently outperforms WorldPop at each resolution, with WorldPop agreeing with the manually collected data at only around 5 to 10 km resolution. This can be seen clearly by comparing the correlation coefficients between manual and WorldPop/LandScan data sets at different resolutions (Figure 4.21).

Another factor to investigate is the rate of false positive and negative reports. If the data set fails to report population where it is present, this is a false negative, and can lead to populations being missed-out. If the data set reports population where it is absent, this is a false positive, that leads to a lack of confidence in the data set. False negatives are not present in either data set, as they always report a minimum 'background' population. However, this approach results in a large number of false positives. Table 4.5 shows the number and percentage of cells which are false positive for either data set, and the total

	False Positive				
Data Set	**Cells absolute**	**Cells %**	**Area (km^2)**	**Pop. absolute**	**Pop. % of data set**
LandScan	162	11	162	5,692	2.3
WorldPop	65,247	46	652.5	81,159	44.2

Table 4.5: *Table showing the false positive rate and area for the WorldPop and LandScan data sets. False positive is defined as locations in which population is reported yet is in reality absent. False negatives are never reported in either data set as they always report a baseline population. The population (Pop.) represented by these false positive cells is indicated as an absolute number and as a percentage of the reported population of that data set.*

area and population that these cells represent. The false positive rate is much higher for WorldPop (46%) than for LandScan (11%). This is not necessarily because LandScan is intrinsically more accurate, but because the cell size is larger than WorldPop; so 'background' cells have a greater probability of containing buildings. The significance of this is that in rural areas, where there are truly cells in which no people live, these data sets can contain sizeable regions of false positive population. This effect is less noticeable in coarser resolution data sets, but regardless, reduces the general confidence in the quality of the data set. This false positive population can be sizeable. The fact that 44% of the total population in the WorldPop data set around Aluto reside in false-positive cells suggests that the populations of the 'true-positive' cells are under-estimated. This is probably a manifestation of the excessively small estimated settlement sizes (see Figure 4.19) and perhaps an underestimation of the population within those areas.

The results of these analyses indicate that great care must be taken when selecting the population data set to assess exposure for risk assessment. Even if the purported resolution of the data set is sufficiently precise for the hazard in question, the actual accuracy of the population distribution at this resolution may not be suitable depending on the methods employed to generate it. If the true distribution of the population is not known, or for whatever reason it is not feasible to do a manual survey, the 1 km LandScan data set is preferable to the 100 m WorldPop data set. The fact that such data sets introduce false positive results should also be considered when employing these methods to make risk management decisions. Specifically in this case, the results show that (1) there is broad agreement between the LandScan data and the manually acquired data set, and (2)

that the manually acquired data set sits between the LandScan and WorldPop data sets in terms of integrated population, adding credence to the manually collected data set.

4.4.2 Combining exposure and hazard: risk associated with PDCs from Aluto Volcano

An environmental risk can be defined as the probability of an event ($Hazard$) multiplied by a measure of the potential value or assets at risk ($Exposure$) and the specific circumstances that may exacerbate or mitigate the impact ($Vulnerability$) (Marzocchi et al., 2012); generally expressed as the 'risk equation':

$$Risk = Hazard \times Exposure \times Vulnerability \tag{4.10}$$

The hazard can be defined as the probability of an event capable of causing adverse effects, in this case the probability of PDC inundation. The exposure at Aluto relates to the population, and the presence of key assets such as the school, the geothermal power station and the rose farm. Vulnerability is complex, and there is a plethora of different vulnerabilites at play in any particular community which can vary over space and time. The are many forms of vulnerability, but broadly speaking, two particular classifications of vulnerability are often made (1) physical vulnerability (house strength, road quality etc.) and (2) social vulnerability (health, income, trust in authority, personal experience etc.) (Cutter et al., 2003). Vulnerability is crucial, and apparently small nuances of a community may make the difference between a mitigated and unmitigated disaster. However, as vulnerability has not yet been studied in any detail at Aluto, I simplify the equation to $Risk = Hazard \times Exposure$, with the strong caveat that vulnerability is essential to truly understand the likely impact and be able to mitigate risk effectively.

The impact of pyroclastic density currents on people is binary, where $P(death|inundation) = 1$, and therefore exposure directly relates to impact. For infrastructure, impact may be more complicated; damage is non-binary and relates to the relative strength of the structure and the dynamic pressure and other characteristics of the pyroclastic density current (Baxter

et al., 2005; Spence et al., 2004; Zuccaro et al., 2008). Most buildings around Aluto (including Aluto school), are wattle and daub constructions (95%), usually with thatched roofs (82%), but occasionally with corrugated metal (Central Statistics Agency -Government of Ethiopia and Minnesota Population Center - University of Minnesota, 2007). The geothermal power plant is a modern construction, with more robust materials, but an unknown strength. Buildings are more robust in Ziway town, where 98% of buildings are roofed with corrugated iron. Even so, 61% of buildings are walled with wattle and daub (Central Statistics Agency -Government of Ethiopia and Minnesota Population Center - University of Minnesota, 2007). Whilst building quality is an important consideration for tephra fall hazard which largely depend on roof strength (Spence et al., 2005), no-one should be inside a building likely to be inundated by a PDC. Even if a building is not destroyed, it is likely to be buried, and the temperatures experienced are usually fatal (>200°C) (Baxter et al., 2017). For this reason, and the fact that the energy cone model does not evaluate dynamic pressure, I shall consider a given sites exposure to PDC inundation to equate directly to its destruction and loss of life within it.

The probability of inundation map produced using the Monte Carlo method is at the same resolution as the underlying DEM, in this case 10 m. This is on the scale of individual buildings; the basic unit measured as a proxy for the population. To compare regions in terms of risk to their population, it is useful to down-sample the hazard grid, so that each cell can contain more than one building. The most precautionary approach to down-sample the probability grid is to assign the value of the new larger cell as the highest probability of smaller cells within it. A down-sampled cell size of 500 m by 500 m was chosen to provide a large enough area to encapsulate a large number of buildings, but small enough to retain the spatial variability in probability of PDC inundation within the region, and to be relevant on a drainage-to-drainage scale. The probability of inundation and population maps are presented in Figure 4.22.

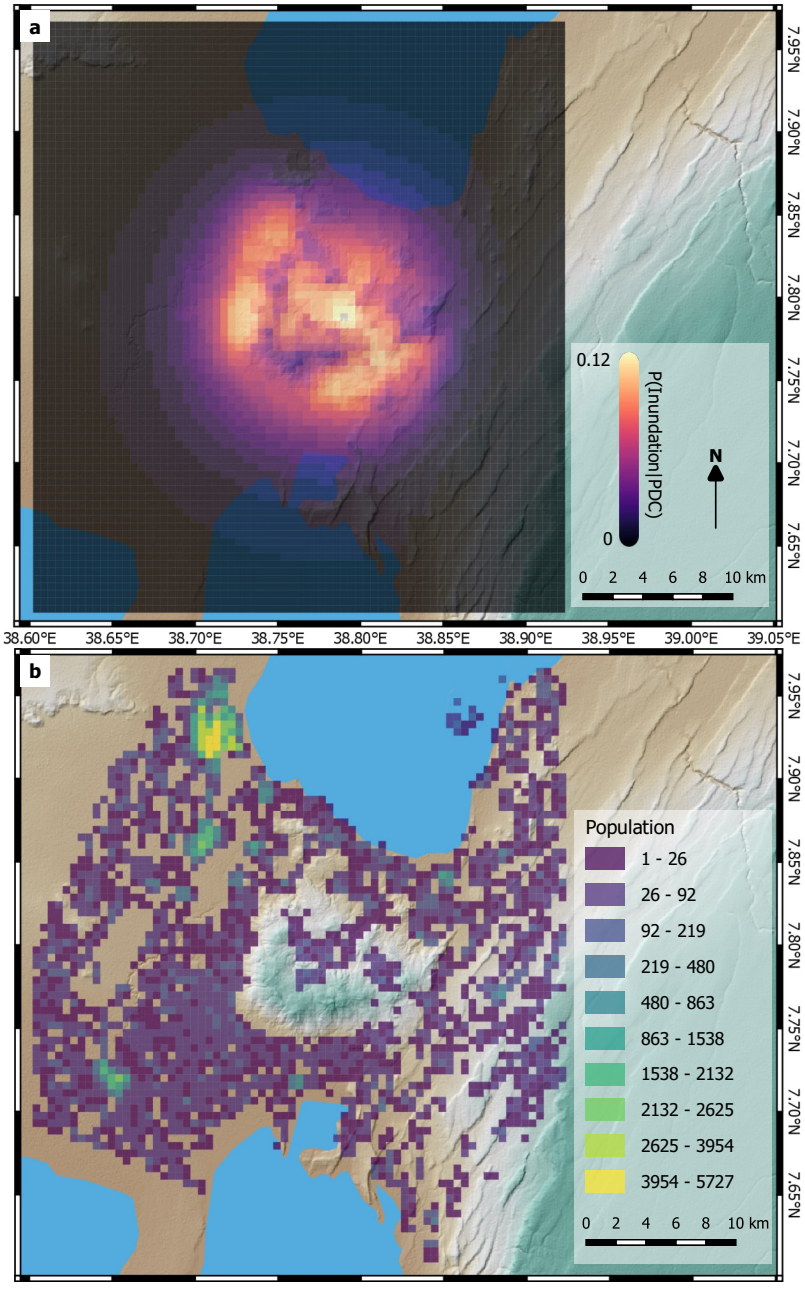

Figure 4.22: *(a) The coarser-resolution probability of PDC inundation map for Aluto volcano. Cell sizes are 500 m × 500 m, and the probability is defined as the maximum probability within the cell area. (b) Integrated population within each cell where population equals the total number of buildings multiplied by the number of people in each building according to the wereda-level census data. This coarser map allows for improved assessment of the risk to population by expanding the cell size beyond the size of individual buildings whilst retaining the variability of probability with space.*

Quantifying the risk to population

Risk, being defined as the impact of an event multiplied by its likelihood of occurring, can be challenging to define in a robust and quantitative way that is easily comprehensible. As decisions are partly made based on perceived risk, it is important that risk is robustly comprehended. A unit of risk that aims to ensure that risk is properly understood is the micromort (Spiegelhalter et al., 2008), a unit devised to allow easy comparison between risks which have the same potential impact (death), but vary significantly in their likelihood. A micromort is a 1-in-1,000,000 probability of sudden death. Such units can be helpful for individual decision making; in the UK for example, 1 micromort equates to 250 mile journey in a car, 15 miles walking, 20 miles cycling or 6 miles on a motorbike; making it clear that from a probability-of-sudden-death standpoint, car journeys are often safer than the alternatives (Spiegelhalter et al., 2008). They can also allow for the characterisation of one's 'background risk', where individuals' background risk is the chance they may die per period of time from any cause. This background risk may be calculated by the average death rate in an area, where death rate is usually defined as deaths per 1000 per year. In 2017, this was 6.67 in Ethiopia, equating to an average background risk of 6670 micromorts per person per year across all age groups (UN et al., 2017). Additional risk, such as living near a volcano, may then be compared to an individual's background, and other risks, which may themselves be perceived as tolerable or intolerable, allowing better informed decisions to be made.

In the case of pyroclastic density current inundation, in most cases, death is sudden, unbiased, and certain, making the micromort an appropriate unit of risk. This means simply that (assuming $P(PDC|eruption) = 1$):

$$micromorts = \frac{P(inundation|PDC)}{1 \times 10^{-6}} \tag{4.11}$$

$$micromorts\ yr^{-1} = micromorts \times \frac{1}{t_r} \tag{4.12}$$

where t_r is the eruption return period in years. An individual living in the most haz-

ardous part of Aluto, where $P(inundation|PDC)$ is 0.11, would experience an additional 516 $micromorts\ yr^{-1}$ risk if t_r was 213 years (the median estimated return period for eruptions of any size at Aluto (Crummy et al. unpublished expert elicitation). Or to put it another way, an additional 7.7 % to their background risk, or about 10× the individual's yearly average risk of death from malaria in Ethiopia (50 $micromorts\ yr^{-1}$) (based on data from WHO (2018)). Such comparisons may be useful for any level of decision-making (individual to regional), and exemplifies how easy it is to underestimate the risk of low-frequency high-impact events, such as a volcanic eruption, by intuition alone. The first analysis performed with the micromort risk metric is an overall population exposure, to gauge how many people, and what proportion of people are currently living at levels of risk around Aluto (Figure 4.23). Hazard is expressed in probability of PDC inundation per year, and probability per 50 year period, a time-frame often used to express hazard (Sandri et al., 2018b; SSHAC, 1997); in part useful because it represents a large proportion of a human lifespan. As the population data is based on stationary buildings rather than mobile people, there is an assumption that an individual's risk accumulates at their place of residence, rather than where they necessarily spend their time. To include this would require more detailed knowledge of people's typical movements throughout the day to higher and lower risk areas, which is beyond the scope of this work. The map presented here may be useful for the planning of new assets around the volcano, indicating which areas, from a PDC hazard perspective, are more favourable than others.

For decision makers, it may be useful to understand how risk is distributed in space in order to prioritise or direct risk-mitigation measures. In order to do this, individual risk (micromort per capita per year) is not appropriate. Instead, the total collective risk experienced in each area is required. This can be done by multiplying the micromorts per person per year by the population in each area. This will highlight areas where there is a high population at great individual risk, and lowlight the areas where the probability of PDC inundation is low, and/or where there is little population exposed. The map showing this is presented in Figure 4.24. The map particularly highlights the settlements of Belicha, O'itu Basuma, Adami Tulu, Chefe Jila, Golba, Kertefa, Lekanshu, Bulbulla and Ziway. A particular strength of this approach is that it balances the risk associated with low-frequency,

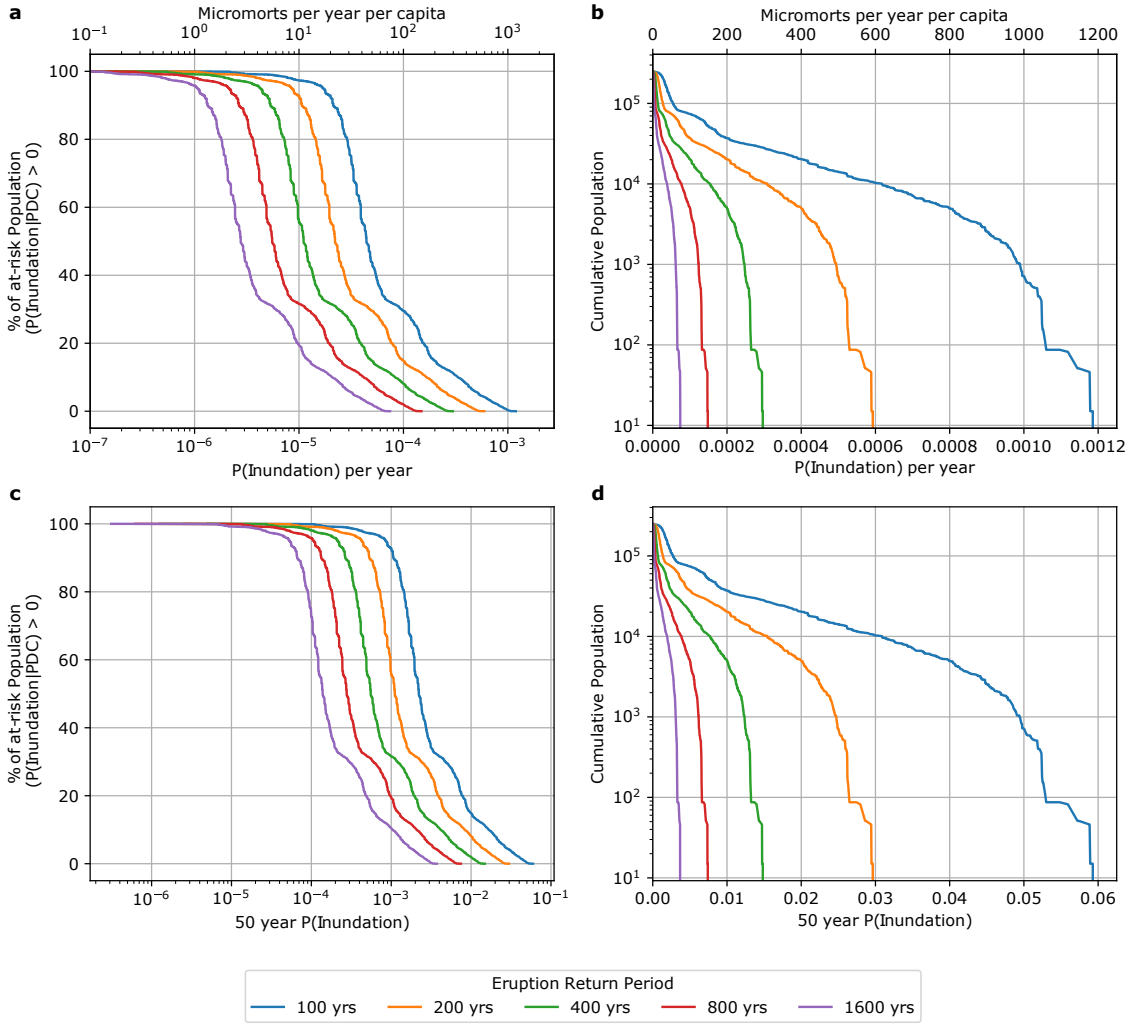

Figure 4.23: *(a) The cumulative percentage of the at-risk population to different risk levels expressed in P(inundation) and micromorts per year per capita, considering a range of possible eruption return periods. The 'at-risk' population is defined as the population where P(inundation) >0. (b) The cumulative absolute population at different risk levels considering a range of possible eruption return periods. For example, assuming a return period of 200 years, around 10% of the at-risk population, or around 20,000 people, live with a >200 micromort per year risk of death from a PDC. (c, d) Equivalent plots expressing probability over 50 years, an common metric of environmental hazards.*

high-impact events with higher-frequency, lower-impact events. This is exemplified by the similar risk in Kertefa and Bulbulla; though the probability of inundation is an order of magnitude higher in Kertefa than Bulbulla (5% vs 0.5%), the potential impact of a PDC inundating Bulbulla would be much greater owing to its far higher population. This means both towns are roughly equivalent in their risk, and should be given an equal weight in any risk mitigation measures. A weakness of the resolution chosen to conduct this analysis is that diffuse populations, that may sum to a large number of people, are overlooked. An example of this is the region around Abule and Jela (SW flank), which hosts a large population, with a relatively high risk of inundation but barely appears on the map. This is because the population around this area is diffuse, and clustered on a scale larger than the cell size. Given a coarser resolution, the area would appear to be at greater risk. This means that the risk-representation of certain types of community depends on a subjective choice of cell size. To avoid this problem, the cell size (or other form of population grouping) should be chosen to reflect the method of risk mitigation. For example, if the mitigation measure was to disseminate hazard information via local churches, mosques or town halls, the risk should be measured over the catchment of each to correctly decide priority. At the other end of the spectrum, if the method was to disseminate information via radio broadcasts, an integrated risk around the whole volcano is sufficient, as in this case the community-to-community variability of risk is irrelevant.

Quantifying the risk to individual sites and key assets

It is also important to quantify the risk to key assets of high human, social, cultural or economic value. The following examples are by no means exhaustive, but are recognised as particular assets at Aluto, subjectively selected for their significance and proximity to the volcano. These are: a school in the center of Aluto caldera, the geothermal power plant within the caldera and the AfriFlora rose farm near Ziway and Adami Tulu. The school is valuable for obvious reasons, but there is clear commercial interest in the geothermal plant and the rose farm. The rose farm is also a major employer in the region, and during the day hosts large numbers of workers. For a more comprehensive evaluation of risk to assets, a combined top-down, bottom-up prioritisation of features would be necessary; that

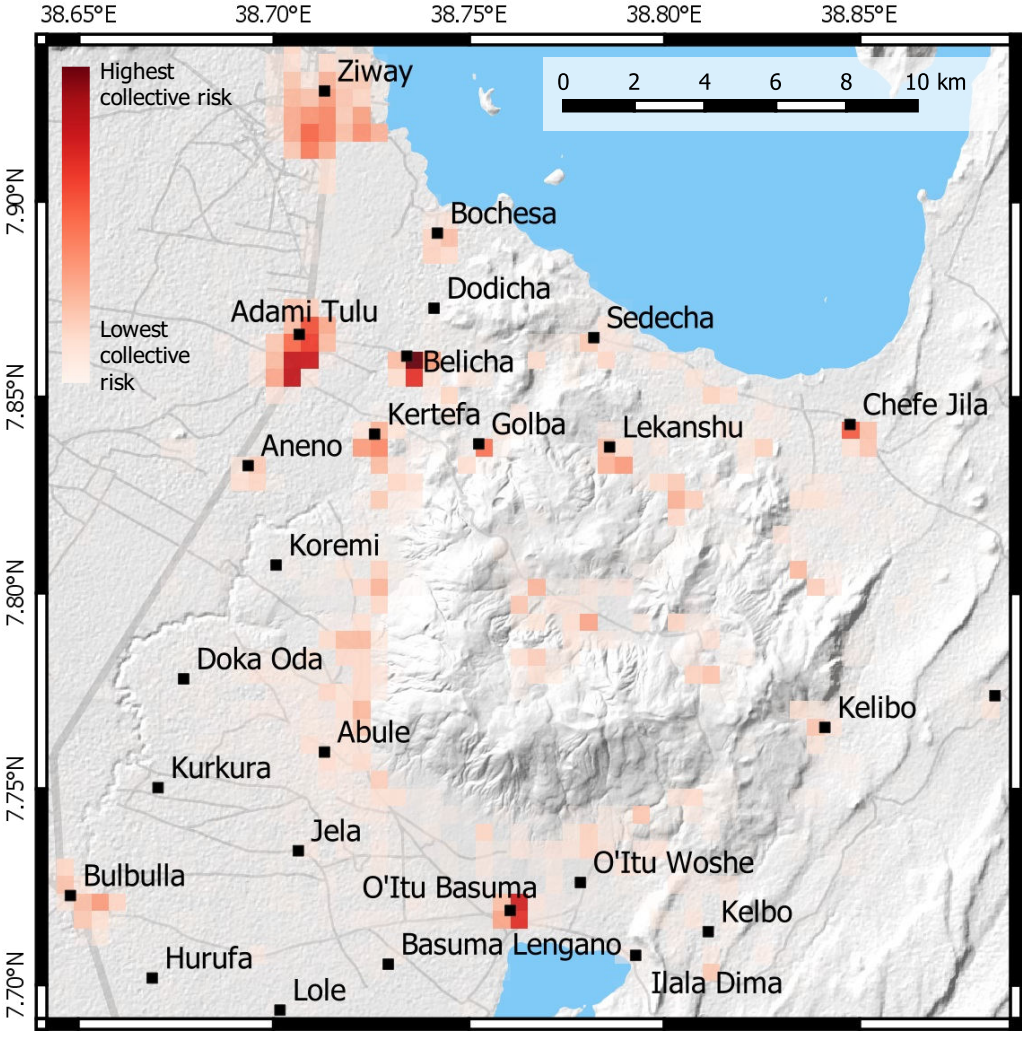

Figure 4.24: *The distribution of risk around the volcano, where risk is expressed as relative collective risk within each cell. Collective risk is the product of the population and micromorts per-capita in each 500 m by 500 m cell. This is displayed in relative (uniform colour scale), rather than absolute terms (numbers), as the absolute number is unimportant.*

is, establishing the most valuable assets according to local authorities and residents alike, including cultural assets that may have no economic value, but are culturally indispensable to the local community.

Single assets can cover broad areas, often larger than individual cell sizes. In this case, all of the assets are larger than the original 100 m^2 cell size. As I am concerned about the probability of *any* part of each asset being inundated by a pyroclastic density current, it makes sense to ascribe the probability of inundation given a PDC for a feature to the cell within that feature most likely to be inundated. The assets were first digitised as shapefiles, and then the highest probability cell within the shapefile was selected to represent the probability of inundation given the generation of a PDC from Aluto ($P(inundation|PDC)_{site}$). Assuming that $P(PDC|eruption) = 1$, the probability of inundation over N years can be calculated as:

$$P(inundation)_{site} = N \times \left(P(inundation|PDC)_{site} \times \frac{1}{t_r} \right) \tag{4.13}$$

To evaluate the probability of inundation for an individual site given the uncertainty surrounding the return period (t_r), I have calculated the yearly probability ($N = 1$) of inundation at each site as a function of the return period (Figure 4.25). For the geothermal power plant the annual probability of inundation by a PDC is 0.06% [0.016, 0.25], for Aluto school it is 0.046% [0.014, 0.098], and for the rose farm it is 0.005% [0.001, 0.022]. The results indicate that the geothermal plant and school have a relatively high yearly probability of inundation by PDC compared to the rose farm. This graph also indicates that the uncertainty in return-period has a greater impact on the potential risk at higher probabilities than lower ones.

It is useful to quickly understand risk at different sites of interest, from those listed above, to the multitude of settlements surrounding Aluto. To do this, I have taken the same approach as for the sites above, and presented the probability of inundation over a 50 year period for selected named settlements around Aluto, including upper and lower 90% confidence intervals of the return period (Figure 4.26). The confidence interval is calculated

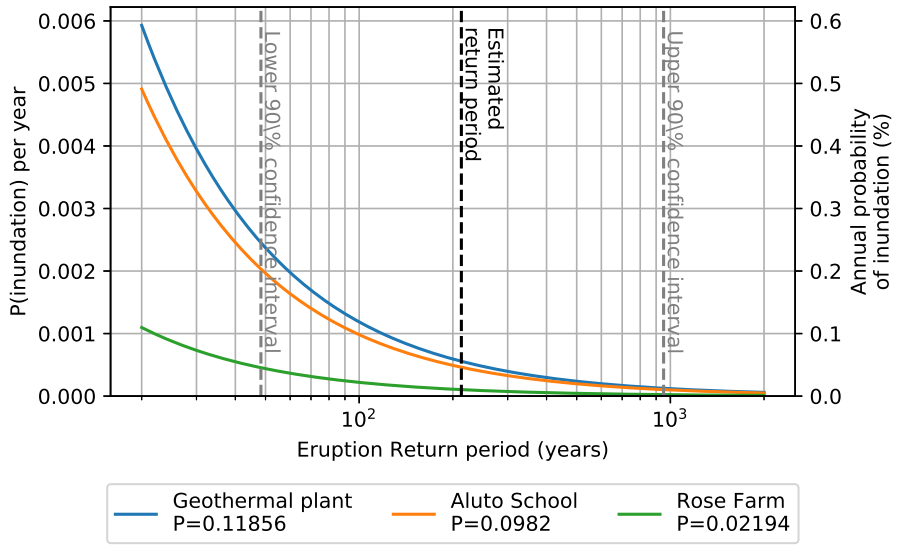

Figure 4.25: *The site-specific yearly probabilities of inundation by a PDC as a function of the eruption return period. Conditional probabilities (P(inundation|PDC)) for each site are presented in the legend.*

from the 5^{th} and 95^{th} percentiles from the PDF of estimated return periods from the expert elicitation (Crummy et al., unpublished). The confidence intervals therefore represent the *variability* of the return period, rather than aleatory or epistemic uncertainty (Roughier et al., 2013). Specifically, these relate to return periods of one eruption every 48, and 951, years.

Acceptability of Risk

The point of calculating the risk of a natural hazard is to aid decision-making for risk mitigation measures, crisis response, development, investment or insurance. Stakeholders making decisions surrounding each of these themes consider varied aspects of the risk, and quantify risk in different ways. For example, investors or insurers may consider the risk of damage to high value infrastructure, whereas those interested in disaster risk reduction may be more concerned about a wider suite of impacts, from human loss of life and livelihoods, to the economic impacts of the destruction of infrastructure. Such stakeholders are likely to use very different metrics for risk. Whilst the micromort is a useful concept for the potential loss of life, it is unable to capture other potential impacts. Even though methods

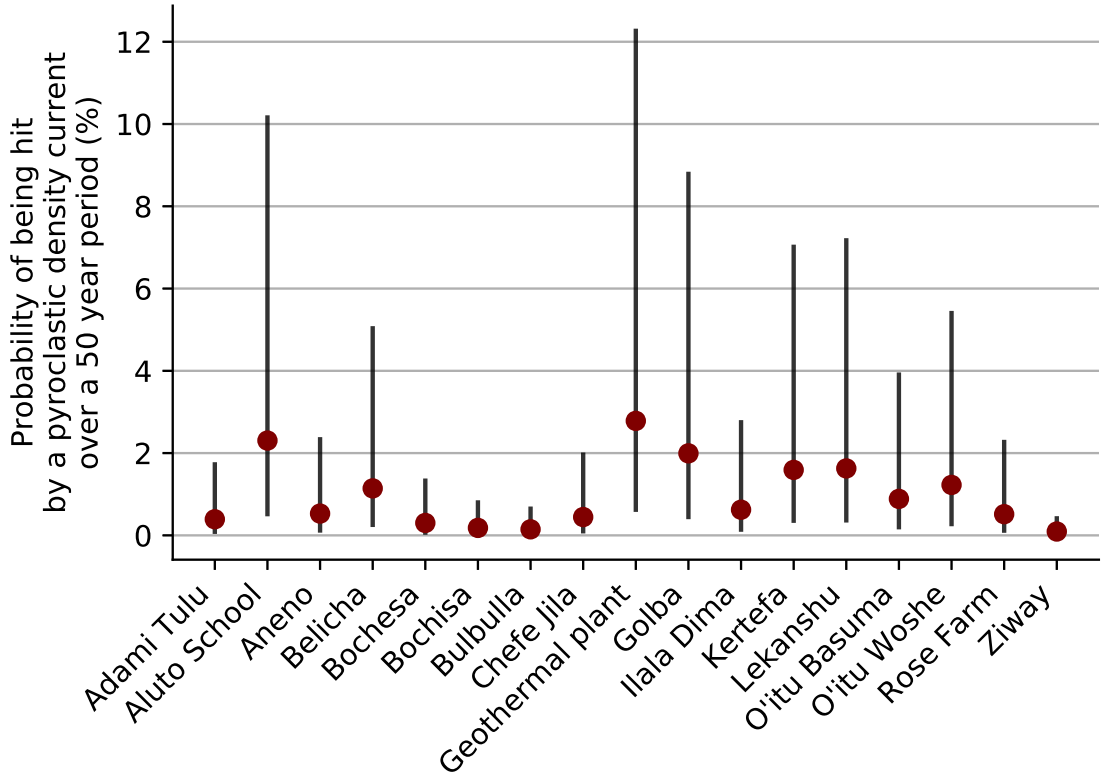

Figure 4.26: *Comparisons of the 50 year probability of PDC inundation at various sites and towns around Aluto volcano including 90% confidence intervals of the return period.*

exist to attempt to combine all impacts into a single metric, these tend to be reductionist and have a monetary basis (to allow literal cost-benefit analysis of risk mitigation methods or investment decisions). This leads to the valuation of human life in monetary terms (known as the Value of a Statistical Life or 'VSL'). This utilitarian method is useful as it allows for objective decision making, but, depending on the method used to calculate VSL, tends to undervalue life compared to societal perceptions (Viscusi and Aldy, 2003), discriminates against those in developing countries where VSL tends to be lower (Viscusi and Aldy, 2003), and does not make moral or religious considerations of those it might affect (Rose, 2008).

An alternative approach is to evaluate different risks separately by their most appropriate method. In the UK, the Health and Safety Executive (HSE) provide guidelines on the acceptability of risk of loss of life in a variety of situations which can be expressed in annual probability of death, or micromorts per year (Health & Safety Executive, 2001). They define risk acceptability in three levels: broadly acceptable, tolerable and unacceptable. The threshold for each of these depends on the relationship between the stakeholder and the risk, and also takes into account public perception of 'dreaded' risks. One such dreaded risk is a 'disaster'; a single event which results in the death of >50 people. Typically, decisions surrounding the tolerability of disaster-risk are made using '$F-N$ curves' (Evans and Verlander, 1997); a plot of N number of fatalities against the frequency of events with $\geq N$ fatalities. Fields are subjectively applied to this plot marking levels of tolerability (ie. a low probability of great loss of life may be tolerable, whilst a high probability would not, and vice versa). This allows events that have the potential for a range in loss of life (such as a volcanic eruption), to be evaluated for their tolerability.

To produce an F-N curve for PDCs at Aluto would require the estimated loss of life during different eruption scenarios, weighted according to their probability. This is an additional complexity to the hazard model, but is possible using a Monte Carlo energy cone approach by recording the potential death toll in each model run. However, an energy cone is likely to significantly overestimate the loss of life during an individual event, as the model calculates roughly circular 'at-risk' areas, which are likely to be significantly larger

		Lower threshold annual probability		
Risk level	**Situation**	**Chance**	**Percent**	**Micromorts**
unacceptable	worker	1 in 1,000	0.1	1000
	public	1 in 10,000	0.01	100
	>50 death event	1 in 5,000	0.5	n/a
tolerable	worker	1 in 1,000,000	0.0001	1
	public	1 in 1,000,000	0.0001	1

Table 4.6: *Table showing the HSE guidelines on the acceptability of risk. Worker risk is defined as the annual risk associated with a job in its entirety. Public risk is defined as risk placed passively, unwillingly or unknowingly upon an individual. A >50 death event is any event which kills more than 50 people in one instance. Tolerability is defined as unacceptable (not acceptable in any instance), tolerable (acceptable only if the benefits outweigh the risk), or for risks lower than this: 'broadly acceptable', as they are of a much smaller magnitude than the annual background risk of death. Data source: Health & Safety Executive (2001).*

than the areas that would be actually inundated. Instead, a more complex model such as Titan2D (Patra et al., 2005) is necessary, and if used to build a statistical emulator, could allow rapid iterative modelling to estimate the loss of life whilst taking aleatory uncertainty into account. This is beyond the scope of this work, and so I shall only evaluate the acceptability of passive individual risk, rather than the risk associated with individual eruptions.

The HSE guidelines (Table 4.6) are designed for the UK, and so their applicability to Ethiopia, where cultural views of risk and acceptability of risk may well be different to those in western cultures, is questionable. However, for the sake of interest, the UK guidelines do provide a benchmark of what might be deemed an acceptable risk in a western context. Due to the current lack of $F - N$ curve for PDCs at Aluto, it is impossible to consider a lower risk threshold according to a 'disaster' scenario. Alternatively, I can suggest what proportion of the population is living at an unacceptable level of risk using the tolerability thresholds associated with passive risks to the public recommended by Health & Safety Executive (2001) (<1 micromort per year = broadly acceptable, >100 micromorts per year = unacceptable) (Figure 4.27). The results of this analysis indicate that only <1 % [0,5] of the at-risk population around Aluto live at a broadly acceptable level of risk. 85 % [55,95] of the population, equating to around 212,000 [137,500, 237,500] people, live at a tolerable risk level. 14% [0, 45], equating to 35,000 [0, 112,500] people, live at an

unacceptable level of risk. It should be noted that 'tolerable risk' does not indicate safety or recommend passivity, in fact, HSE guidelines suggest risks that are 'tolerable', are only such if the benefits outweigh the costs, and that such risks usually necessitate some form of mitigation (Health & Safety Executive, 2001).

4.5 Pyroclastic density current hazard maps for Aluto volcano

Maps are useful tools for communicating spatial data, and can provide a focal point for discussions and decision-making during a crisis or in 'peace-time'. In the following section, I evaluate the ideal traits of an effective hazard map, and put this into practice by creating pyroclastic density current hazard maps for two different stakeholder groups at Aluto volcano.

4.5.1 What makes a good volcanic hazard map?

There is currently no global standard of volcanic hazard maps or methods. Individual maps vary considerably in how they are produced, and their methods for communicating hazard to stakeholders. Regardless of these differences, a good hazard map should be *quantitative*, *accountable* and *defendible* (Calder et al., 2015), in order to help users make robust, well informed decisions that can be held to account. Calder et al. (2015) categorised existing volcanic hazard maps into 5 distinct classes: The most common are *geology-based*, marking the footprints of previous hazard events. An advantage of these maps is that they are evidenced-based, and unique to the volcano. However, they do not necessarily represent a complete catalogue of events, or take into account the possibility of larger events in the future. The next are *integrated-qualitative* maps, which amalgamate knowledge of different potential hazards, which may be based on geology or modelling, and define hazard zones around the volcano. The amalgamation of hazard types into a single set of hazard zones makes communication of the hazard simpler to understand for the non-volcanologist. *Probabilistic hazard maps* represent a single hazard, and quantitatively describe the prob-

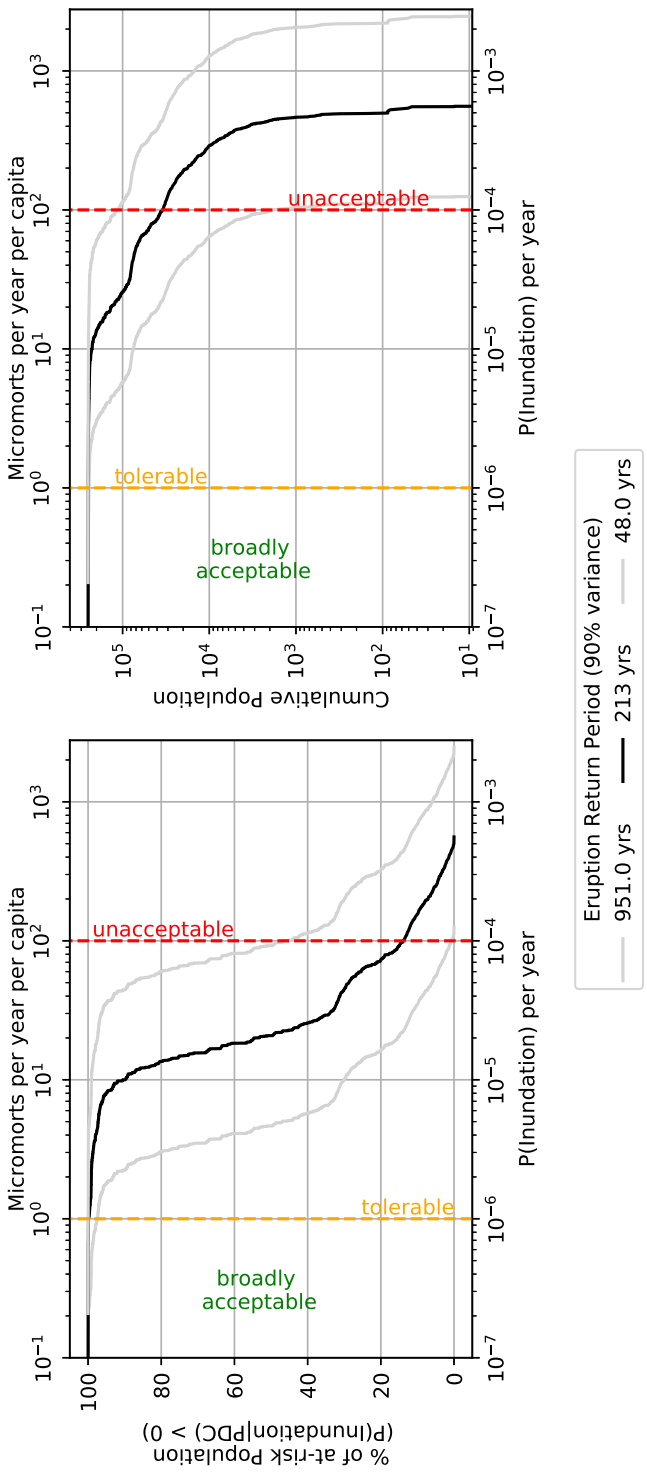

Figure 4.27: *Plots showing the proportion (left) and the absolute number (right) of people living at individual broadly acceptable, tolerable and unacceptable risk of PDCs around Aluto volcano. The black line represents the population at risk considering the return period (213 years) for any sized eruption at Aluto estimated by expert elicitation (Crummy et al. unpublished work) and the 90% confidence interval of the return period. Tolerability thresholds are based on the UK HSE guidelines for fatal risk (Health & Safety Executive, 2001).*

ability of hazard affecting an area. They have the advantage of (assuming the models are well parameterised) a full and robust representation of the range of possible magnitudes of the hazard in question. However, they can often be challenging to understand, do not encompass all hazards, and it is hard to communicate both aleatory and epistemic uncertainties in two-dimensional space without employing multiple maps. The final form are *administrative maps*, which combine hazard information with administrative needs. They can be useful in aiding decision making and planning for a volcanic crisis, but it is often unclear how hazard levels are supported by geological data (Calder et al., 2015).

The type of hazard map should reflect the intended audience; a probabilistic hazard map may be appropriate for authorities or civil protection, but may not be appropriate for communicating hazard rapidly in a crisis to local stakeholders. Additionally, probabilistic hazard maps used for long term planning should reflect this in the units used; a conditional probability of PDC inundation given an eruption is of little use if you are deciding whether an area is likely to be inundated over a particular time period. For qualitative hazard maps, the names and colours of hazard-level zones should be carefully selected to ensure the correct meaning is communicated; does green mean 'safe', or simply the least hazardous of potentially hazardous areas? Without knowledge of the exact end users or their needs at Aluto, I will not attempt to create final operative hazard maps (for one, they will not be written in Amharic or Oromo), but instead provide some examples of what is possible using the probabilistic data I have generated.

The supporting data for these hazard maps are the combined physical and statistical modelling results conducted earlier in this chapter; forming the basis of a *probabilistic hazard map*. This has the benefit of being well justified (through field work, modelling and expert elicitation), quantifiable (with numerical results gathered through physical and statistical modelling) and defendable (with assumptions and caveats well documented in this thesis). However, care must be taken to ensure the magnitude of the hazard is communicated appropriately, and the intended meaning is most efficiently and accurately conveyed. Thompson et al. (2015) conducted structured interviews and questionnaires to assess the ways different methods of presenting hazard information surrounding tephra fall hazard

were understood by different stakeholders. Their findings are summarised in the following thematic sections.

Data Classification

1. Qualitative measures of hazard (i.e. 'high', 'medium' and 'low') were inconsistently interpreted by stakeholders. It is therefore important to include quantitative information alongside qualitative descriptors to ensure accurate and consistent hazard communication.

2. Binned hazard levels, where a single solid colour represents a range of values, was generally disliked by stakeholders who were concerned this failed to accurately convey the gradational nature of hazard levels, and implied a false level of certainty.

3. Maps only displaying a colour gradient to display hazard information were slow to interpret, provided variable accuracy in interpretation, and were disliked by stakeholders.

4. Combined use of a colour gradient and hazard contours was considered the most preferable; combining ease-of-use and accurate hazard communication.

5. Hazard contours should be spaced appropriately for the precision of the model: 10% intervals were preferred over 5% intervals as this was thought to more realistically reflect the uncertainty in the hazard values for the tephra fall analysis in question. *Note: Tephra fall hazard probabilities in this investigation were in the range of 0-65%, PDC hazard at Aluto has a conditional probability of 0-10%, meaning that finer divisions are necessary to convey spatial variation in hazard level. The precision of PDC inundation probabilities from this work are around 1%.*

Colour scheme

1. Sequential colour schemes were preferred by scientists over diverging ones, as diverging colour schemes implied hazard vs no-hazard, whilst sequential colour schemes implied higher hazard vs lower hazard.

2. Diverging colour schemes were preferred by other stakeholders, who had a propensity to seek *risk*, rather than *hazard* information from the map. The diverging colour scheme falsely implied risk, rather than hazard.

3. 'Warm' colour schemes best conveyed specifically *volcanic* hazard, as other colours had connotations of unrelated hazards (ie. blue for flooding). This highlighted the fact many stakeholders are likely to be responsible for interpreting multiple forms of hazard in an area, and desired for them to be easily distinguished.

4. Choosing a colour scheme appropriate and understandable for colour-blind stakeholders is important.

5. The colour scheme should be culturally appropriate to posses the correct connotations. Red, for example, implies danger in many western cultures, but represents joy in Eastern cultures, and life in New Zealand Māori culture.

Use of language and units

1. 'Probability' was the most preferred term, above 'likelihood' or 'chance', as it elicited the greatest level of trust in the numbers presented.

2. Numerical presentation of probability was most preferred in percent (i.e. 10%), over natural frequencies (i.e. 1 in 10), and decimal probability (i.e. 0.1).

3. The authors note that the stakeholders in this study were all well educated and possessed a high level of numeracy. The authors suggest that natural frequencies are often considered the most easily understood by non-scientific stakeholder groups. They agreed with stakeholders and scientists that it was preferable to provide both natural frequencies and percentages side-by-side.

4.5.2 Bringing the pieces together: PDC hazard maps for Aluto

I have produced two PDC hazard maps for Aluto volcano. Small versions are presented in this chapter (Figures 4.28 and 4.29), but full size PDFs can also be found digitally in the electronic appendices, and as larger-format paper maps in the back cover of this thesis.

	Connotations	
Colour	**Amharic**	**Oromo**
White	ash, ice, cotton, milk, paper, heaven	milk, head-scarf, arab, heaven
Black	charcoal, beetle, soot, devil, tar, nigger seed	charcoal, god, hell
Red	blood, cloth, amber, pepper	amber, blood
Yellow	baby diarrhoea, mead	flower, baby diarrhoea
Green	cabbage, leaf, lemon, peace, tranquility	grass, freedom (political)
Blue	bird, god, sky	

Table 4.7: *Table summarising a subset of the findings of Leyew (2016). Listing the connotations of pertinent colours in Amharic and Oromo to assess the cultural appropriateness for each in a volcanic hazard map.*

Following the findings of the work on communication of volcanic hazards presented above, I have made the following considerations when designing the maps:

Choice of colours and gradients

The colours used to represent the probability of flow inundation/death should follow a sequential colour gradient, be suitable for colour-blind users and preferably be perceptually uniform (ie. perceived magnitude is directly proportional to colour). They should also preferably use 'hot' colours that may be immediately associated with a volcano.

In response to the importance of selecting culturally appropriate colours, I have provided a table (Table 4.7) summarising the findings of Leyew (2016); a review of colours and their connotations in 16 Ethiopian languages. I have selected Amharic (the official language of Ethiopia. Spoken around Aluto by educated locals and national and regional authorities) and Oromo (the everyday language of those in living in this part of the Rift Valley). I have selected information on colours most often used in hazard maps.

From this, I have established that although the 'magma' and 'inferno' colour gradients, used previously in this chapter, may be perceptually uniform, suitable for colour blind stakeholders and use 'warm' colours, they are in fact unsuitable. The use of black for lower-hazard areas in both these colour ramps is clearly inappropriate - as this is associated with charcoal, the devil and hell in Amharic and Oromo cultures. Instead, the 'reds'

colour ramp, which uses a pinkish white to red colour gradient may be the most suitable; as white is generally associated with neutral to positive concepts, but red is associated with blood. This colour gradient is also suitable for colour-blind people, is perceptually uniform and uses hot colours making it easily distinguishable from hydrological or other hazards. This is also in keeping with typical practice in western countries, for which red typically denotes warning, caution or danger.

Representation of hazard levels and probability

I have avoided 'low', 'medium' and 'high' hazard levels, as these are highly ambiguous with no standard practice as to what probabilities they quantitatively refer to (Calder et al., 2015; Thompson et al., 2015). Instead I have opted for presenting probability contours in units of percent. These are presented within the legend alongside natural probabilities for greater ease of understanding for stakeholders with less mathematical ability. I have chosen to present conditional probabilities (ie. probability of being hit by a PDC in the event of an eruption), over probabilities over a set time interval because: (1) the values are >1 %, preventing any problems in understanding decimal place value. (2) The concept of *'if this volcano erupts, this is the dangerous area'* seems more intuitive and immediate than *'this is the probability of being hit by a PDC over a 50 year period at this particular place'*. (3) Conditional probabilities here are more statistically robust with lower error, as they do not assume an eruption return period which has a very large error, and makes a steady-state assumption. However, these probabilities are still abstract for an average stakeholder. To overcome this I have related the conditional probabilities on the map with equivalent non-conditional 'everyday' risks which people may be more familiar with; including death from malaria, fire, malnutrition, HIV/AIDS, road traffic accidents and diarrheal diseases. The concept of this infographic is to compare the non-conditional annual risk of living at each level of hazard around the volcano versus the non-conditional annual risk of death from more familiar hazards. The data quantifying these risks are from the World Health Organisation World Health Statistics report from 2017 (WHO, 2017) and the World Malaria report (WHO, 2018), selecting data from Ethiopia. This has the benefit of directly comparing risks for their tolerability to aid individual-level decision making.

Local stakeholder map: Special Considerations

I have developed separate hazard maps for local stakeholders (i.e. non-expert residents, local leaders, business-owners) around the volcano (Figure 4.28), and for regional/national decision-makers. This is because the requirements and education-levels of either community are often very different, necessitating different information, and different ways of presenting the information.

For local stakeholders, individual risk (the risk to the individual stakeholder and their family/school/church/mosque/business) is the basis for individual or family-level decision-making. Individual-level decisions may include: coming up with an plan of where to go in the event of an eruption, whether or not to listen to officials if an evacuation order is given, or whether to take seriously any advice given in advance or in the event of a volcanic crisis. To make these decisions, the individual requires information covering:

1. What are the hazards of being near a volcano when it erupts (bearing in mind there has not been an eruption in living memory)?
2. Which areas are going to be safe or unsafe during an eruption?
3. Is this risk tolerable? Is it risky or unpleasant enough to take action?

To provide answers to these questions, I have included diagrams explaining in basic terms the nature of pyroclastic density currents, why they are hazardous, and their typical behaviour at Aluto. I have only discussed column collapse type PDCs, as I have not seen evidence of dome collapse-type PDCs at Aluto. The map provides information on areas that are most hazardous during an eruption, and the infographic attempts to provide a relative risk indicator for PDC risk at Aluto.

In addition to this, the way that the information is communicated needs to take into account the needs of the stakeholder group. Average adult literacy rates are 49.1% in Ethiopia (male: 57.2%, female: 41.1%) (UNESCO, 2015). Anecdotally, some locals were

clearly well educated, some with degree-level qualifications, but it is clear that there may be a significant proportion of the intended stakeholder group who may be illiterate, and the majority of these are likely to be women (UNESCO, 2015). To account for these special requirements I have minimised the use of words, and provided visualisations of each feature that needs explanation. In reality, an illiterate individual is unlikely to be able to interpret the map without assistance, but the use of visual aids should ease interpretation. Where text is used, I have used plain english and the simplest possible terms.

Regional/National decision-maker map: Special Considerations

Regional/National decision-makers are more concerned with total risk, in order to prioritise funding towards efforts with the greatest reward, be that during a volcanic crisis or in 'peace-time' decision making concerning education programs, town-planning, and passive-risk to critical infrastructure. In order to make these decisions, stakeholders require information on:

1. Which areas are likely to be safe/unsafe from PDCs during a volcanic crisis
2. The total integrated risk to life experienced around the volcano
3. What is the risk, with quantified error, to critical sites and towns from PDCs from Aluto over a given time period?
4. How this risk is currently distributed around the volcano to assist in targeted risk-mitigation?

Regional and national level decision-makers are likely to have a higher level of education than those of farming communities living on Aluto. This allows for the presentation of more scientific information, using graphs with error, and more complex probabilities (such as 50-year risk) to help answer the pertinent questions. However, when decision-makers are making judgements relating to the potential loss of life at Aluto, this still depends on the tolerability of risk at an individual level. For this reason I feel it is still important to include an infographic comparing volcanic risk with other everyday risks. For decision-makers, this

has the added pertinence that they may already be attempting to mitigate these everyday risks, and this might encourage action on comparable volcanic risk. In order to evaluate the risk to life around Aluto, I have provided a graph showing the population exposed to different levels of risk, and a distribution of risk map. I have chosen to provide a relative risk scale for this map. The units are total micromorts per year, but the scale simply indicates relatively high to relatively low risk, as the units themselves are not entirely useful, and are an unnecessary complication. To communicate the risk posed to critical sites and towns, I have presented the 50 year probability (in percent) of each site being impacted by a PDC, based on the median estimate of the return period (213 years), and error bars representing the probability of inundation considering the upper and lower 90% confidence intervals for the return period (48 and 951 years). This efficiently displays the probability, with error, of each location of particular interest, allowing them to be compared side-by-side. The points chosen to represent each critical site or town were chosen as the point within that location with the greatest probability of inundation. Some towns were highly diffuse, without clear boundaries or spatial clustering of buildings (generally to the SW of Aluto). These were omitted from this assessment because selecting a single point for the probability would be arbitrary and somewhat meaningless. This is a drawback of such an analysis, as it fails to include large diffuse populations.

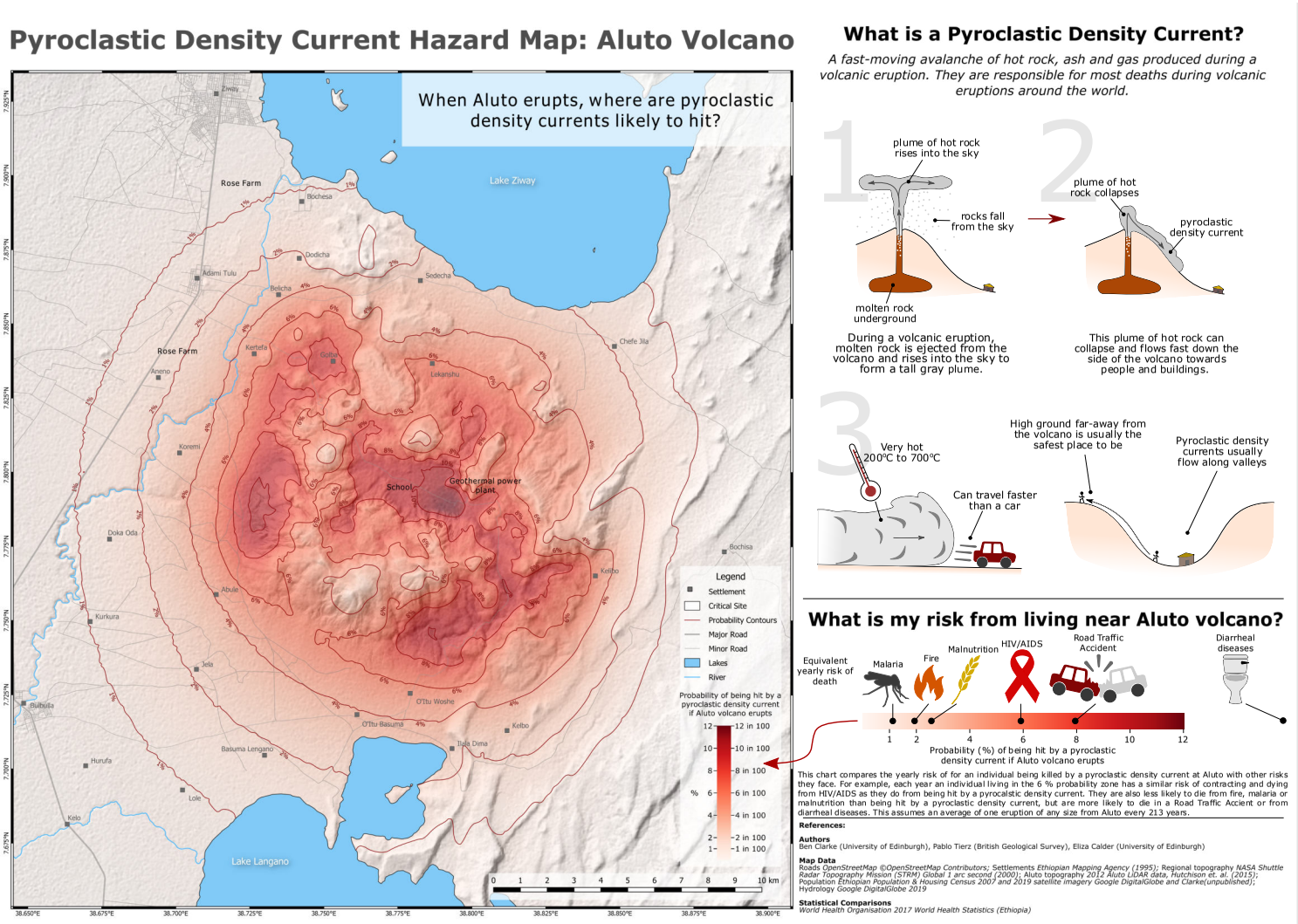

Figure 4.28: *PDC hazard map of Aluto volcano aimed at a non-expert, local-stakeholder group.*

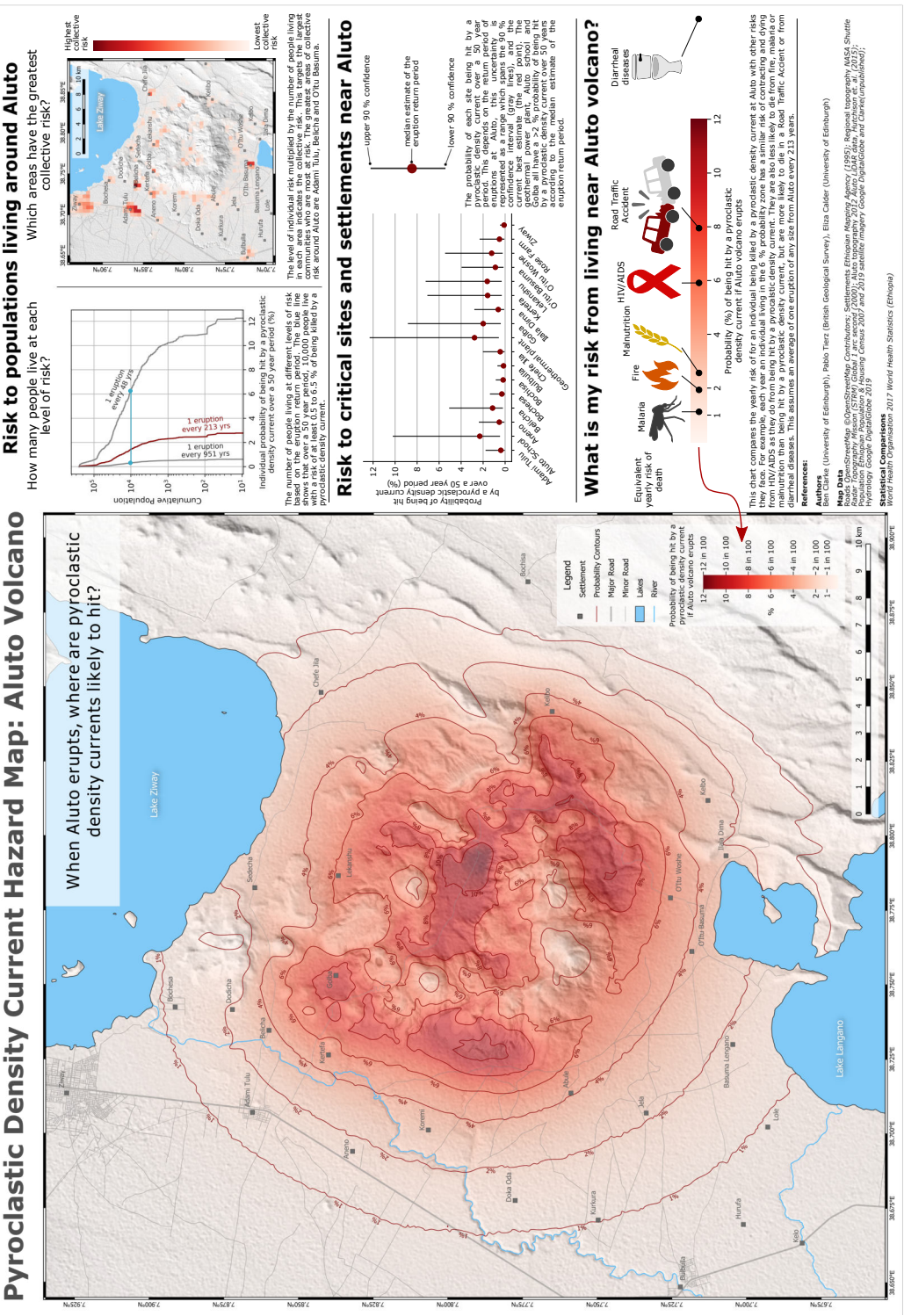

Figure 4.29: *PDC hazard map of Aluto volcano aimed at a local/national decision makers.*

Chapter 5

Summary & Conclusions: The hazardous nature of post-caldera eruptions at Aluto volcano

"We shall not cease from exploration
And the end of all our exploring
Will be to arrive where we started
And know the place for the first time."

T.S. Elliot, Little Gidding Part V

In this thesis, I have investigated and discussed the nature of pumice cone forming eruptions at Aluto volcano, and the hazards and risks associated with them by employing a variety of approaches and techniques. In this chapter, I will summarise this work and tie the findings together as a set of conclusions. Finally, I will provide some recommendations for further work that would help to advance our knowledge of this enigmatic eruption style and the hazards associated with it.

5.1 Summary

In Chapter 2 and 3, I investigated the deposits of post-caldera, pumice cone forming eruptions at Aluto volcano. In chapter 2, I took an in-depth approach to understand the nature of a single pumice cone building deposit and its components. In doing so, I described and provided the first model for the generation of 'pumiceous achneliths' and shed some light on the nature of fragmentation in peralkaline rhyolite magmas. Using insights from these unusual pyroclasts, combined with thermal and ballistic modelling, I established the first-

order depositional processes involved in the formation of pumice cones.

In Chapter 3, I took a broader field-based approach to investigate the deposits of multiple pumice cone eruptions around the volcano. By doing so, and combining this with insights from Chapter 2, I characterised the style of these eruptions, and the processes that lead to the deposits exposed at Aluto today. I also captured aspects of the nature of PDCs and their generation at Aluto, which were used to help parameterise PDC hazard and risk models in Chapter 4. Investigation of these deposits also provided useful information on lahar and debris avalanche hazards that may accompany volcanic eruptions at Aluto.

In the first half of Chapter 4, I quantified probabilistic PDC hazards at Aluto. I first established the likely collapse heights of PDCs at Aluto using a deterministic eruption column model run through a series of Monte-Carlo simulations parameterised using field data, insights from this work and the literature. By doing so, I also estimated the likely range and distribution of eruption column-heights, gas-thrust heights, and intensities displayed by pumice cone forming eruptions at Aluto. Using remote sensing data, and knowledge gained from Chapter 3, I also developed a probabilistic vent-opening model for Aluto, employing kernel density estimation techniques. These insights, combined with selected analogue PDC mobility data, were used to parameterise a Monte-Carlo energy cone PDC model to generate a probabilistic PDC inundation map for Aluto volcano.

In the second half of Chapter 4, I evaluated the exposure to, and risk from PDC hazards at Aluto. I generated new data on the population distribution around Aluto, and identified key sites of interest. In doing so, I also evaluated the appropriateness of commonly-used global population data sets for their use in PDC risk assessment. Combining this exposure data with the probabilistic PDC inundation data, and estimates of eruption return period from an expert elicitation, I evaluated the risk of inundation associated with PDCs at Aluto according to individuals, the collective population, and key sites. Finally, I created two bespoke PDC hazard maps for Aluto volcano designed for different Ethiopian stakeholder groups.

5.2 Conclusions

In the following topical subsections, I list the conclusions drawn from the body of work summarised in the previous section.

5.2.1 Eruptive sequences during pumice cone forming eruptions

1. Pumice cone forming eruptions represent the typical post-caldera eruptive style at Aluto volcano.

2. Pumice cone forming eruptions can occur from single circular vents, or numerous overlapping vents forming a fissure, following underlying faults/dykes. This produces either a cone or a rampart landform.

3. There is no evidence for multiple eruptions emanating from the same vent, meaning that in this respect, pumice cones can be considered monogenetic.

4. Pumice cone forming eruptions undergo a very similar eruptive sequence, albeit over a range of magnitudes.

5. Eruptions begin with an intense, violent-strombolian to sub-plinian eruption column-forming phase, occasionally with the generation of initial column-collapse PDCs.

6. Pumice cones grow during a climactic phase, after the generation of any initial PDCs, through the cumulative deposition from the edge of a relatively stable convecting eruption column. This growth first produces massive deposits and a shallow cone, until, if eruptive conditions persist, the outer cone slope reaches the repose angle of the constituent material. At this point, small granular flows develop down the cone slopes.

7. Later stages of pumice cone growth are characterised by eruption-column unsteadiness, where PDCs are frequently generated between short periods of column re-establishment. These PDCs may be partially responsible for the breaches in the side of many pumice cones.

8. The repeated collapse and re-establishment of eruption columns indicate eruption conditions at this stage hover around the boundary between those associated with a convective and collapsing column.

9. Eruptions finish with the emplacement of a silicic lava flow, though the style of this eruption-phase is unknown. It is unclear whether the effusion of peralkaline rhyolite lava flows more closely resembles the sysn-effusive explosive activity of Cordón Caulle in 2011, or that their potential low viscosity means that they are emplaced in a similar fashion to basaltic lavas. Initial morphometry of peralkaline rhyolite lavas at Corbetti indicates they reside on the viscous end of the lava spectrum (Hunt et al., 2019), which might indicate eruption styles during this phase to be more similar to Cordón Caulle.

10. Though some phreatomagmatic deposits exist on Aluto, they are rare, and might have been a result of the past environment at Aluto. These hazards should not be ignored, as Aluto's rainy seasons produce moderately sized bodies of standing water within the caldera, and the volcano hosts a shallow hydrothermal system.

5.2.2 Eruption dynamics and fragmentation processes

1. Some pumice cone deposits contain 'pumiceous achneliths' (see below) which provide clues to their depositional mechanism and the conduit dynamics of pumice cone forming eruptions.

2. Pumiceous achneliths are fluidal-shaped pyroclasts formed during brittle fragmentation of a low viscosity magma. They maintain fluidity and inflate during flight due to low glass transition temperatures, and depending on their size continue to deform in deposit (DQAs), or freeze in-flight and retain a droplet shape (FQAs).

3. The simultaneous fragmentation and generation of both pumiceous achneliths and more 'typical' angular pumice, indicates that rheology and strain-rate must vary considerably across the conduit during pumice cone forming eruptions, evidencing conduit unsteadiness.

4. Pumiceous achneliths that are large enough to continue deforming in deposit (DQAs), act as depositional chronometers, and thermal modelling indicates deposition must have been rapid ($\ll$ 30 seconds from fragmentation to deposition).

5. The small size of many DQAs (<10 cm), and their distance from the vent, indicates they were not deposited ballistically. The deposit characteristics indicate that pumice-cone hosted DQAs were not emplaced by a PDC. The only remaining explanation that satisfies their short flight-time and distance from the vent is deposition from the edge of an ascending eruption column.

6. Pumice cones at Aluto can therefore be considered to be 'ultraproximal cones' (Riedel et al., 2003), a relatively poorly studied proximal feature of moderate to high intensity eruptions. These cones are though to be generated by column-edge deposition around the vent during moderate to high intensity eruptions that produce convective eruption columns.

7. Modelling of the unstable column phase of pumice cone forming eruptions indicates that eruption column heights just prior to collapse range from 3 to 16 km above the vent (mode = 7.5 km). Gas thrust heights are likely to range from 50 to 800 m above the vent (mode = 100 m).

8. Modelling of the unstable column phase of pumice cone forming eruptions indicate that mass eruption rates just prior to the point of column collapse range from 10^4 to 6×10^6 kg/s (mode = 4×10^4), relating to an eruption intensity of between 7 and 9.75 (mode = 7.75).

5.2.3 The nature of PDCs and other hazards

1. The majority of PDC deposits preserved at Aluto are massive lapilli tuffs, with a wide range of lithic component lithologies that represent the upper basement of the region (above the Bofa basalts). They tend not to contain large blocks of lava. Some cross stratified, fine grained tuffs are also present.

2. Many ignimbrites at Aluto lie above non-ballistic fall deposits, or fall/flow deposit sequences with no intermediate palaeosol.

3. PDCs are therefore most probably generated by the collapse of eruption columns.

4. PDCs generated during pumice cone forming eruptions usually possess a dense basal region, meaning that much of the flow is restricted to drainages. However, the potential of detached, mobile dilute PDCs should not be ignored, and is evidenced by the occasional preservation of their deposits.

5. There is evidence of one on-edifice phreatomagmatic dilute PDC at Awariftu (NE caldera), indicating that such events do occur. This indicates that they might be rare events, or that the deposits are rarely preserved.

6. Poor longitudinal exposure of PDCs means direct quantitative assessments of flow mobility (dh/l) is an unrealistic goal at Aluto. The maximum distance reached by PDCs is also challenging to attain, as many have flowed into a palaeo-lake. Where the end of flows can be found, their source vent is unclear, making the total distance travelled ambiguous.

7. The similarity of Aluto PDC deposits to other massive lapilli tuffs found world wide (e.g. Branney and Kokelaar (2002)) justifies the use of suitable analogue PDCs for flow mobility parameters. These 59 analogues indicate a truncated Gaussian distribution of energy-cone mobilities ranging between 2.5° and 30° ($\mu = 15°$, $\sigma = 6.3°$).

8. Obsidian lava flows, which are generated during the final stages of most pumice cone forming eruptions, are capable of generating small to moderate volume debris avalanches, particularly from loose pumice cone structures.

9. Hyperconcentrated flow and debris flow deposits are common at Aluto, showing that lahars are often generated during and after eruptions. Pumice cone eruptions generate loose (non-welded) deposits, which may be susceptible to re-mobilisation. Rainfall intensities during the modern day rainy seasons at Aluto are comparable to those which most frequently generated lahars on Montserrat, indicating such hazards may be present during future eruptions and the following rainy seasons.

5.2.4 Risk from PDCs around Aluto volcano

1. There is evidence that PDCs are generated during most, if not all pumice cone forming eruptions at Aluto volcano.

2. Due to the monogentic-type spatial distribution of eruptive vents, the vent-opening susceptibility can be estimated through the application of kernel density estimation techniques. The kernel bandwidth is estimated using the nearest neighbour distribution of previously active vents at Aluto, assuming temporal homogeneity.

3. Future pumice cone forming eruptions at Aluto are likely to emanate from the estimated location of Aluto's caldera ring-fault, and in-particular on the SW and SE rim. There is also a higher probability of vent opening in the NW sector of the volcano.

4. Assuming PDCs collapse from the height of the gas thrust region, that they are sourced from the vent, and that they possess a distribution of mobilities obtained from analogue PDC data, the Monte-Carlo energy cone approach provides a reasonable first-order estimation of the PDC inundation probability around the volcano

5. Key caveats to this methodology relate to the over-simplification of PDC flow processes: ignoring channelisation and variable fluidisation, and an absence of a PDC volume constraints. There are also assumptions made during parameterisation that mean some extreme end member parameters are likely to be over/under estimated.

6. Spatially-defined conditional probabilities of PDC inundation (ie. $P(inundation|PDC)$) reach a maximum of 12%. In the current model of 10,000 iterations per vent this is estimated to a precision of $\pm$ 1%.

7. The most likely (>5 % conditional probability) regions to be impacted by PDCs from Aluto are the central caldera region, and the N, NW, and S flanks of the volcano, to a distance of roughly 2 km away from the break in slope at the bottom of the edifice. Lower probabilities (<5 % conditional) extend well beyond the edifice, reaching Ziway and Bulbulla (around 10 km from the edifice).

8. From satellite and census data, there appears to be a significant population living in urban and rural areas within the vicinity of Aluto.

9. The 2007 census data likely underestimates the current population due to incomplete turn-out, location-derived sampling biases, and because it is out of date.

10. WorldPop population data sets largely underestimate the rural population around Aluto, indicate unrealistically small urban area footprints, and contain an erroneous spatial distribution of population in rural areas. Despite their claimed 100 m global population resolution, this only begins to largely agree with the true population distribution at around a 5 km re-sampled spatial resolution. This means it is generally unsuitable for PDC inundation risk assessment.

11. LandScan population data sets provide a much more representative distribution of population around Aluto, and largely agrees with the true distribution at their claimed 1 km resolution. Depending on the nature of the PDCs, population distribution and topography, this may be suitable for first-order assessment of PDC inundation risk.

12. LandScan and WorldPop global population data sets contain false-positive population in rural areas. This is most prevalent in the WorldPop data set.

13. Many settlements lie within the reach of modelled PDCs at Aluto. Assuming expert elicitation-derived eruption return periods (213yr [951yr, 48yr]): 20,000 [0, 80,000] people live at >1 % non-conditional probability of being killed by a PDC over a 50 year period. Such probabilities are comparable to the individual non-conditional national-average risk of death from malaria, fire, malnutrition, HIV/AIDS and road traffic accidents in Ethiopia. Living within the riskiest areas of Aluto carries a 0.2% smaller yearly risk (0.05) than death from a diarrheal disease (0.07), and around 10 times the risk of death from malaria.

14. The 90% confidence interval of PDC inundation is based on the confidence interval of the return period. The uncertainty associated with PDC inundation over a time period is greatest where there the PDC inundation probability is highest. In other words, the inundation uncertainty is greatest in the highest risk regions of the volcano.

15. The school located in Aluto caldera carries a 2.3% [0.5%, 10%] probability of being inundated by a PDC over a 50 year period.

16. The geothermal power plant on Aluto, which currently represents around US$218 million of investment and aims to supply 70-80 Mw of power supporting the national Ethiopian grid, has a 2.78% [0.62%, 12.3%] probability of being hit by a PDC over a 50 year period.

17. The AfriFlora Sher rose farm, which provides much of the employment in the area and during the daytime has hundreds of people on site, has a 0.52% [0.11%, 2.27%] probability of being hit by a PDC over a 50 year period.

18. The settlements of Golba, Kertefa, Lekanshu, O'itu Woshe and O'itu Basuma carry the greatest risk of PDC inundation. Though some diffuse settlements, particularly on the SW flank of Aluto carry similar risks but are poorly identified in the collective risk analysis due to their wide geographic spread.

19. Though the probability of PDC inundation at the most populous (but distal) settlements (Adami Tulu, Bulbulla and Ziway) is low (<1.5 % conditional probability), their high population density means their collective risk is similar to smaller settlements much closer to the volcano (Figure 4.24).

5.3 Recommendations for further work

The work presented in this thesis is amongst the first to study pumice cone forming eruptions from peralkaline rhyolite volcanoes, and as a consequence there are a considerable number of questions left unanswered, and work yet to do. In this section, I suggest a few pertinent exercises which might benefit our knowledge of these eruptions, and the hazards and risks they pose.

5.3.1 The nature of pumice cone forming eruptions

1. *The global applicability of pumice cone eruption styles and sequences at Aluto:* Aluto shows clear and consistent eruption styles and sequences during pumice cone forming eruptions, but are these insights true for pumice cones elsewhere? Studies of pumice cones at Pantelleria and Mayor Island suggest such eruptions might be more strombolian in style. Is this the case, or are they misinterpreted? Pumice cones represent

the most frequent style of eruption at peralkaline rhyolite calderas, so understanding the full range of potential eruption styles is essential to understand the risk they pose globally. This work would necessitate similar fieldwork to that carried out at Aluto, but at a wider range of field sites where pumice cones are present. This is likely to be a lengthy and expensive undertaking, requiring extensive fieldwork in many regions. The work would be valuable, in that it may establish robust eruption scenarios for peralkaline rhyolite volcanoes worldwide, and help to define the best eruption analogues to use for probabilistic hazard analyses.

2. *The eruption dynamics of ultraproximal cone forming eruptions:* What are the physical processes that lead to the generation of ultraproximal cones? How does sedimentation take place, and how might cone geometry and granulometry relate to the duration, intensity, granulometry and dynamics of the eruption column? What features of the eruption column and dynamics can we deduce from the nature of ultraproximal cones? There are a variety of approaches one could take to answer this question of linking deposit to process, which can be done in the field and through numerical modelling. One possible method is to investigate a variety of pumice cones with a range of morphologies (in terms of volume, height to crater diameter ratio, and slope angle), and investigate the proximal to distal isopach and isopleth distributions of their tephras. These can then be inverted to establish eruption column heights and intensities, which may be compared to the pumice cone morphologies to establish if there is a link between the proximal deposit morphology and useful parameters of the eruption dynamics. The challenge here is finding suitable sites where the proximal to distal deposits are traceable. Having amongst the greatest number density of pumice cones globally, the Main Ethiopian Rift is likely to be a good candidate, though similarities in magma composition make correlation hard. This might benefit from work at Pantelleria and Mayor Island, where there are fewer pumice cones (thus fewer tephras to confuse), and potentially a greater variation in magma composition. However, working on relatively small volcanic islands does mean field investigations are limited in lateral extent, though in both cases, ocean drill cores may be available. Another option is to investigate other ultraproximal cones, such as those mentioned

at the end of Chapter 3, each of these examples is in a terrestrial setting, and for many of these eruptions detailed distal isopach and isopleth data already exist, and only investigation of the proximal and ultraproximal deposits might be necessary, thus minimising cost. The question might also benefit from numerical modelling. Numerical modelling of eruption columns is relatively commonplace, but generally focuses on distal tephra dispersal from an umbrella cloud. A plume model that also considers mass loss from the edge of an ascending eruption column would be necessary. The model may be used to explore the parameter space (mass eruption rate, componentry, gas mass fraction, duration) necessary to produce ultraproximal cones. Comparison of the expected deposit morphologies and granulometries from the model with real world pumice cones could validate the model, and link the eruption dynamics to the final cone morphology and granulometry. Including the thermal evolution of pyroclasts in this model could also more precisely link the eruption conditions to the degree of welding or presence of pumiceous achneliths in the deposit. A numerical modelling approach is likely to be cheaper than a primarily field based approach, but does still require investigation of some ultraproximal pumice cone deposits for model validation. To an extent, the model validation of cone geometry could also take place using high resolution digital terrain models, but care would need to be taken to ensure that ultraproximal cones such as pumice cones aren't confused with basaltic scoria cones. The validation of any granulometric model outputs would require field investigation. The potential benefit of this work would be to provide a much quicker method for determining eruption conditions from the geometry and granulometry of ultraproximal deposits. This would allow many more data points, of greater accuracy, to provide a more robust parameterisation for probabilistic hazard models not only at pumice cones, but in any volcanic system that produces ultraproximal cones.

3. *The rheological evolution of peralkaline rhyolite magmas during ascent and fragmentation:* The processes at play during ascent and fragmentation of peralkaline rhyolites in the conduit remain somewhat mysterious. Chapter 2 reveals that there is significant variability in the rheology and strain rate across pumice cone conduits, resulting in the presence of simultaneously erupted pumice and pumiceous achneliths.

The eruptions are unsteady, which may be a direct result of this variability in rheology and strain rate in the conduit. By understanding this process further, we might better understand the nature of the explosive-effusive transition, a key goal of modern physical volcanology. Peralkaline rhyolite systems are currently not considered in most experimental work on fragmentation, but their unusual composition and rheology may mean that they provide an important test case for processes currently supposed for more typical magma compositions. Inclusion of these magmas in ongoing and planned investigations should be considered. Additionally, there are important features of peralkaline rhyolite magmas which we don't yet fully understand: in particular, the rheological evolution of peralkaline rhyolite magmas as they ascend in a volcanic system. The viscosity of peralkaline rhyolite melts, for example, is strongly dependent on their oxidation state and water content, with particularly rapid changes at <1 wt% H_2O. Establishing the H_2O solubility with temperature and pressure, in addition to how the oxidation state changes during ascent, is an essential step to understand this process. Ultimately, these rheological changes are what may control the eruption style of peralkaline rhyolites. The benefit of understanding this may be to better predict the behaviour of a future eruption, and the likely hazards involved. This investigation would be primarily experimental, firstly evaluating the solubility of H_2O in peralkaline rhyolite melt at a range of temperature and pressures, and secondly, evaluating the rheological properties (viscosity, fragility, glass transition temperature) of peralkaline rhyolite melt at different oxidation states.

4. *Emplacement processes and eruption dynamics of peralkaline rhyolite lava flows:* Currently, we have very few constraints on how explosive the lava emplacement phase of pumice cone eruptions is. Is it similar to Cordòn Caulle, where lava flow effusion was accompanied by synchronous explosive activity, or is the process more similar to purely effusive basaltic lava flows? This could be solved using detailed and targeted field investigation of silicic lavas at Aluto, particularly to search for evidence of tuffisite formation, intercalated pumice lapilli, or clastogenic regions. There are a number of sites around Aluto which provide the necessary cross sections through these lavas, though there may be challenges surrounding the accessibility of these

exposures, as they tend to form cap-rock at the top of gorges. Accessible peralkaline rhyolite lavas also occur at Corbetti. An important consideration when determining the emplacement process of these lavas is their rheology during eruption and emplacement. A particularly pertinent feature at Aluto is the influence of granophyre growth on the bulk flow rheology. This could be studied through laboratory and desk-based investigations; focusing on (1) an experimental petrological approach to understand the thermodynamic conditions required for the growth and quenching of granophyres in peralkaline rhyolites. This could be complemented by differential scanning calorimetry to determine the cooling rates and glass transition temperatures of natural peralkaline rhyolite obsidians. This would inform (2) numerical modelling of the influence of graphophyre growth during lava emplacement. This could be complemented with remote sensing work, using high resolution digital terrain models to extract rheological properties of silicic lavas from their morphology. The benefits of this would be three-fold: firstly, understanding the eruption processes of these lavas would indicate whether explosive eruption hazards such as tephra fall and PDCs are likely to continue through the final phase of pumice cone eruptions. If they are similar to other rhyolite eruptions, such as Cordón Caulle, there may also be cause to consider such eruptions as suitable analogues, refining analogue data sets. Secondly, the processes of silicic lava flow emplacement are somewhat ambiguous, and most current understanding is based upon metaluminous rhyolites from the western United States, with some more recent investigations in Chile. Broadening this study to different compositions in a different geological and geochemical setting may provide some useful insights in understanding the broader processes of silicic lava emplacement. Finally, the influence of crystal growth on magma rheology is of great interest to the volcanological community, and is central to the question of the explosive-effusive transition, and mechanisms of magmatic fragmentation. Any numerical techniques developed to model the influence of crystal growth on magma rheology, particularly as this evolves through time, would be directly applicable to many other streams of investigation currently taking place in the physical volcanology community.

5.3.2 Volcanic Risk

1. *The combined spatial and temporal clustering of pumice cone eruptions at Aluto:* Clearly, there have been many pumice cone eruptions at Aluto, but their distribution in time is poorly constrained, mostly due to a lack of date-able material. Work on lake tephras suggests they may be temporally clustered, but as there are few samples, they cannot be tied to particular vents. The lack of date-able material is difficult to overcome, however, understanding whether proximal vents are associated with the same eruption might provide an indication of whether proximal eruptions are temporally clustered (i.e. are small areas of the volcano particularly active at the same time?). As I have demonstrated at the KPCC, this does not necessitate date-able material, just detailed fieldwork. The benefit of knowing this is that if an eruption occurs at one location, it may be the initiation of a new spatio-temporal cluster, and the probability of vent opening for the next eruption can be adjusted assuming it will be proximal to the last event (i.e. in the same cluster). This would require extensive additional fieldwork at Aluto, targeting vent clusters, and determining whether there is a significant time gap between the deposits from each vent within the cluster. In reality, the impact of this is limited, as it only proves useful for determining the location of the eruption after the next at Aluto. It provides no indication of the location of the next spatial cluster, and only asserts that the subsequent event may be more likely to occur close to the last.

2. *Multihazard volcanic risk at Aluto:* Only PDCs have been considered in this thesis, but considerable disruption, and crop, livestock and building damage can result from tephra fall. Tephra fall may also increase the physical vulnerability to PDC hazards by reducing people's mobility, and capacity to recover after the event. For a better understanding of the potential impact of an eruption of Aluto, a combined PDC and tephra fall hazard assessment should be undertaken. Fall and flow hazards/risk should be communicated in a joined-up fashion. This could be done through statistical application of tephra dispersion models, co-parameterised with the PDC model. For example, the PlumeRise model used to determine collapse height for PDCs also produced estimates of mass eruption rate and column height. These could be used,

in combination with current data on wind fields at Aluto, and estimates of eruption duration, to parameterise tephra dispersion models. These could be conducted in a similar Monte Carlo fashion to the way PDCs were treated in this thesis. The eruption return period is estimated by expert elicitation and lake tephras, and the location of the vent can be determined using the same model used for PDC hazards in this thesis. Provided sufficient high performance computing resources are available, this would produce a probabilistic tephra fall hazard map, requiring no additional field work, and could be done using existing data and well established models.

3. *Lahars at Aluto:* Lahar deposits are quite common at Aluto. What conditions are likely to trigger lahars, how long after an eruption are they likely to occur, which deposits are most prone to forming lahars, and what topographic circumstances are most susceptible to their initiation and inundation? What is the risk associated with lahars at Aluto? This is a broad question, and largely reflects a global deficit in the knowledge surrounding lahar initiation, rather than any particular nuance of Aluto. However, lahars are still a hazard at Aluto, and methods do exist to assess lahar hazard. This could be conducted remotely, combining remotely sensed topographic data sets with climatic data and a physical lahar model, whilst making assumptions of the initiation conditions. A problem with such assessment is that it strongly depends on the location of loose material after an eruption, and so is contingent on vent opening, tephra dispersal and PDC inundation, leading to large uncertainties. Lahar hazard modelling may be best conducted in the event of a volcanic crisis, when the priors are better established and uncertainty is reduced.

4. *Open-source energy cone modelling:* Currently the energy cone model is written in Matlab code, and so is proprietary, limiting access to potential end-users. Re-writing in an open-source high level (user friendly and well supported) programming language such as Python may be beneficial to accessibility. It would also be beneficial to integrate parameterisation and analysis, perhaps including the ability to visualise in open-source GIS packages such as QGIS. A porting of the Matlab code to Python would be relatively simple, cheap, and fairly rapid, though an integration into QGIS may take longer and require greater expertise. However, as I argue below, a simple

translation to Python may miss an opportunity to greatly improve the methodology:

5. *Rapid, computationally efficient Monte-Carlo energy cone modelling:* An individual energy cone model is quick to run, meaning that a Monte-Carlo approach is achievable. However, for Aluto, 12 million simulations were necessary taking roughly 4 core-years of processing time (1 month actual time on one of the UKs best-resourced High Performance Computing (HPC) systems). This effectively means that (1) the approach, though generally considered 'simple and accessible', actually necessitates access to HPC for realistic processing timescales. (2) Energy cone modelling is not rapid enough to be employed in the event of an ensuing volcanic crisis. A project that would be of great benefit would be to redevelop the energy cone model from a computer-science mindset. The current code works in a highly intuitive, yet inefficient, manner. Ultimately, the problem can be reduced to that of rapidly determining which cells on a digital elevation model intersect a given 3D cone; a problem which is solved almost instantaneously in graphics engines. Instead, the current Matlab model interpolates a profile at every n^{th} degree of azimuth, and at each projects an energy line from the collapse source and determines where the line intersects the interpolated profile; taking a number of seconds for each cone. If the run time could be reduced to days or hours rather than weeks, the energy cone method could provide the most rapid probabilistic PDC hazard assessment available.

6. *Vulnerability assessments:* So far, the PDC risk assessment at Aluto has only considered exposure, and not the wide variety of vulnerabilities associated with people and infrastructure around Aluto. This is essential for a realistic view of the potential impacts of an eruption at Aluto, and might help to identify effective risk mitigation strategies. This would be a multidisciplinary investigation led by social scientists, local stakeholders and volcanologists, to determine what the local vulnerabilities might be, consider how they influence the risk, and how risk might be mitigated in the light of this.

7. *Hazard map appraisal:* Currently, the hazard map developed in this thesis is designed using volcano hazard map principles established in New Zealand, and published information regarding colour choice and language for Ethiopia. The best way of as-

certaining whether the hazard map is suitable and effective for Ethiopian audiences would be to survey the target groups. This could be done informally by asking existing contacts in Ethiopia, or ideally using a social science approach with qualitative questionnaires and/or interviews, to determine (1) how well information is currently communicated, (2) what information stakeholder groups actually desire in a PDC hazard map for Aluto and (3) what suggestions they have surrounding design choices such as colour, style, language and data representation. This would require time in-country with a number of people from the relevant target groups (local residents and decision makers), and expertise in questionnaire design and interview techniques.

5.4 Final Remarks

The principal outcome of this work is a much improved understanding of post-caldera peralkaline rhyolite pumice cone forming eruptions. Prior to this work, few attempts have been made to investigate pumice cones, and those that did have found them to form during low intensity eruptions, with minimal hazardous effects in all but the most proximal regions around the vent (Orsi et al., 1989; Houghton et al., 1985). Regardless of whether these interpretations are correct, this has led to a general assumption that pumice cones, which represent one of the most conspicuous and frequent products of eruptions at many Ethiopian volcanoes, are relatively benign. Somewhat incongruously, investigations along the Ethiopian rift have revealed many widespread and voluminous pyroclastic fall deposits, and frequent PDC deposits that suggest more intense and greater magnitude eruptions are common. This work demonstrates that pumice cones may be responsible for these deposits. Pumice cones are deposited during relatively intense eruptions that are capable of generating convective eruption columns that first disperse tephra through the atmosphere, then collapse to form pyroclastic density currents. Though the most voluminous pyroclastic deposits in the Ethiopian rift are related to caldera collapse events (Hutchison et al., 2016b), many of the smaller, but still potentially worrying events, are likely to be sourced from pumice cone vents. These eruptions are hazardous, and there is an increasing exposure to these hazards around volcanoes in the Main Ethiopian Rift (Vye-Brown et al., 2016). Continued population growth, and the development of geothermal

and other infrastructure around these volcanoes is increasing the risk Ethiopia faces from its volcanoes. The lack of a major explosive eruption, or, for that matter, any eruption, in the Main Ethiopian Rift in living memory might also be encouraging a false sense of security (Vye-Brown et al., 2016). Such risk might be largely mitigated by in-country capacity building, from physical monitoring, to volcanological and sociological expertise and planning. However, volcanic risk must be balanced with the needs and other risks faced by one of Africa's fastest growing countries. As the previous section has laid out, there is much yet to learn about these enigmatic volcanoes, their magmas and their eruptions, but hopefully this work provides an initial, realistic assessment of PDC hazards at Aluto, as well as providing a framework for the probable course of future pumice cone forming eruptions in the Main Ethiopian Rift.

Bibliography

B. Abebe, V. Acocella, T. Korme, and D. Ayalew. Quaternary faulting and volcanism in the Main Ethiopian Rift. *Journal of African Earth Sciences*, 48(2-3):115–124, 2007. ISSN 08995362. doi: 10.1016/j.jafrearsci.2006.10.005.

V. Acocella, T. Korme, F. Salvini, and R. Funiciello. Elliptic calderas in the Ethiopian Rift: Control of pre-existing structures. *Journal of Volcanology and Geothermal Research*, 119 (1-4):189–203, 2002. ISSN 0377-0273. doi: 10.1016/S0377-0273(02)00342-6.

AfriFlora and Sher Ethiopia. AfriFlora - About Us, 2017. URL `https://afriflora.nl/en/about-us/`.

A. Aiuppa, D. R. Baker, and J. D. Webster. Halogens in volcanic systems. *Chemical Geology*, 263(1-4):1–18, 2009. ISSN 00092541. doi: 10.1016/j.chemgeo.2008.10.005. URL `http://dx.doi.org/10.1016/j.chemgeo.2008.10.005`.

F. Alfano, C. Bonadonna, A. C. Volentik, C. B. Connor, S. F. Watt, D. M. Pyle, and L. J. Connor. Tephra stratigraphy and eruptive volume of the May, 2008, Chaitén eruption, Chile. *Bulletin of Volcanology*, 73(5):613–630, 2011. ISSN 02588900. doi: 10.1007/s00445-010-0428-x.

S. Aramaki. Geology of Asama Volcano. *J. Fac. Sci. Univ. Tokyo, Soc. II*, 14:229–443, 1963.

J. L. Arce, J. L. Macías, and L. Vázquez-Selem. The 10.5 ka Plinian eruption of Nevado de Toluca volcano, Mexico: Stratigraphy and hazard implications. *Bulletin of the Geological Society of America*, 115(2):230–248, 2003. ISSN 00167606. doi: 10.1130/0016-7606(2003)115⟨0230:TKPEON⟩2.0.CO;2.

I. Arganda-Carreras, V. Kaynig, C. Rueden, K. W. Eliceiri, J. Schindelin, A. Cardona, and H. S. Seung. Trainable Weka Segmentation: A machine learning tool for microscopy pixel classification. *Bioinformatics*, 33(15):2424–2426, 2017. ISSN 14602059. doi: 10.1093/bioinformatics/btx180.

W. Aspinall, M. Auker, T. Hincks, S. Manhony, F. Nadim, J. Pooley, and R. Sparks. Volcano hazard and risk exposure in GFDRR priority countries and risk mitigation measures: Volcano Risk Study 0100806001R, 2011.

A. Baasner, B. Schmidt, and S. Webb. Compositional dependence of the rheology of halogen (F, Cl) bearing aluminosilicate melts. *Chemical Geology*, 346:172–

183, 2013. ISSN 00092541. doi: 10.1016/j.chemgeo.2012.09.020. URL http://linkinghub.elsevier.com/retrieve/pii/S0009254112004445.

N. Bagdassarov and D. Dingwell. Thermal properties of vesicular rhyolite. *Journal of Volcanology and Geothermal Research*, 60(2):179–191, 1994. ISSN 03770273. doi: 10.1016/0377-0273(94)90067-1.

D. K. Bailey and R. Macdonald. Fluorine and chlorine in peralkaline liquids and the need for magma generation in an open system. *Mineralogical Magazine*, 40(312):405–414, 1975. ISSN 0026-461X. doi: 10.1180/minmag.1975.040.312.10.

F. Barberi, R. Santacroce, and J. Varet. Silicic peralkaline volcanic rocks of the afar depression (Ethiopia). *Bulletin Volcanologique*, 38(2):755–790, 1974. ISSN 14320819. doi: 10.1007/BF02596907.

J. Barclay, J. E. Johnstone, and A. J. Matthews. Meteorological monitoring of an active volcano: Implications for eruption prediction. *Journal of Volcanology and Geothermal Research*, 150(4):339–358, 2006. ISSN 03770273. doi: 10.1016/j.jvolgeores.2005.07.020.

P. Baxter, S. Jenkins, R. Seswandhana, J.-C. Komorowski, K. Dunn, D. Purser, and B. Voight. Human survival in volcanic eruptions: Thermal injuries in pyroclastic surges, their causes, prognosis and emergency management. *Burns*, 43(5):1051–1069, 2017. ISSN 0305-4179. doi: http://dx.doi.org/10.1016/j.burns.2017.01.025. URL http://www.elsevier.com/locate/burns%0Ahttp://ovidsp.ovid.com/ovidweb.cgi?T=JS&PAGE=reference&D=emexb&NEWS=N&AN=614542795.

P. J. Baxter, R. Boyle, P. Cole, A. Neri, R. Spence, and G. Zuccaro. The impacts of pyroclastic surges on buildings at the eruption of the Soufrière Hills volcano, Montserrat. *Bulletin of Volcanology*, 67(4):292–313, 2005. ISSN 02588900. doi: 10.1007/s00445-004-0365-7.

M. C. Benage, J. Dufek, W. Degruyter, D. Geist, K. Harpp, and E. Rader. Tying textures of breadcrust bombs to their transport regime and cooling history. *Journal of Volcanology and Geothermal Research*, 274:92–107, 2014. ISSN 03770273. doi: 10.1016/j.jvolgeores.2014.02.005. URL http://dx.doi.org/10.1016/j.jvolgeores.2014.02.005.

M. Benvenuti and I. P. Martini. Analysis of terrestrial hyperconcentrated flows and their deposits. *Flood and Megaflood Processes and Deposits: Recent and Ancient Examples*, pages 167–193, 2002. ISSN 00370746. doi: 10.1002/9781444304299.ch10.

M. Benvenuti, S. Carnicelli, G. Belluomini, N. Dainelli, S. Di Grazia, G. A. Ferrari, C. Iasio, M. Sagri, D. Ventra, B. Atnafu, and S. Kebede. The Ziway-Shala lake basin (main Ethiopian rift, Ethiopia): A revision of basin evolution with special reference to the Late Quaternary. *Journal of African Earth Sciences*, 35(2):247–269, 2002a. ISSN 08995362. doi: 10.1016/S0899-5362(02)00036-2.

M. Benvenuti, S. Carnicelli, G. Belluomini, N. Dainelli, S. Di Grazia, G. A. Ferrari, C. Iasio, M. Sagri, D. Ventra, B. Atnafu, and S. Kebede. The Ziway-Shala lake basin (main Ethiopian rift, Ethiopia): A revision of basin evolution with special reference to the Late

Quaternary. *Journal of African Earth Sciences*, 35(2):247–269, 2002b. ISSN 08995362. doi: 10.1016/S0899-5362(02)00036-2.

A. Bevilacqua, R. Isaia, A. Neri, S. Vitale, W. P. Aspinall, M. Bisson, F. Flandoli, P. J. Baxter, A. Bertagnini, T. Esposti Ongaro, E. Iannuzzi, M. Pistolesi, and M. Rosi. Quantifying volcanic hazard at Campi Flegrei caldera (Italy) with uncertainty assessment: 1. Vent opening maps. *Journal of Geophysical Research: Solid Earth*, 120 (4):2309–2329, 4 2015. ISSN 21699313. doi: 10.1002/2014JB011775. URL `http://doi.wiley.com/10.1002/2014JB011775`.

G. Biagioli, A. Bevilacqua, T. Esposti Ongaro, and M. de' Michieli Vitturi. PyBox : a Python tool for simulating the kinematics of Pyroclastic density currents with the box-model approach Reference and User ' s Guide Phenomenological aspects of PDCs, 2019.

J. Biggs, I. D. Bastow, D. Keir, and E. Lewi. Pulses of deformation reveal frequently recurring shallow magmatic activity beneath the Main Ethiopian Rift. *Geochemistry, Geophysics, Geosystems*, 12(9):1–11, 2011. ISSN 15252027. doi: 10.1029/2011GC003662.

C. Bonadonna, G. C. Mayberry, E. S. Calder, R. S. J. Sparks, C. Choux, P. Jackson, A. M. Lejeune, S. C. Loughlin, G. E. Norton, W. I. Rose, G. Ryan, and S. R. Young. Tephra fallout in the eruption of Soufrière Hills Volcano, Montserrat. *Geological Society, London, Memoirs*, 21(1):483–516, 2002. ISSN 0435-4052. doi: 10.1144/GSL.MEM.2002.021.01.22. URL `http://mem.lyellcollection.org/lookup/doi/10.1144/GSL.MEM.2002.021.01.22`.

F. L. Bonali, C. Corazzato, and A. Tibaldi. Identifying rift zones on volcanoes: An example from La Réunion island, Indian Ocean. *Bulletin of Volcanology*, 73(3):347–366, 2011. ISSN 02588900. doi: 10.1007/s00445-010-0416-1.

Y. Bottinga and D. Weill. Densities of liquid silicate systems calculated from partial molar volumes of oxide components. *Science*, 269:169–182, 1970.

M. Braddock, J. Biggs, I. M. Watson, W. Hutchison, D. M. Pyle, and T. A. Mather. Satellite observations of fumarole activity at Aluto volcano, Ethiopia: Implications for geothermal monitoring and volcanic hazard. *Journal of Volcanology and Geothermal Research*, 341:70–83, 2017. ISSN 03770273. doi: 10.1016/j.jvolgeores.2017.05.006. URL `http://dx.doi.org/10.1016/j.jvolgeores.2017.05.006`.

M. J. Branney. Eruption and depositional facies Whorneyside Tuff English Lake District. *Geological Society Of America Bulletin*, 103(July):886–897, 1991.

M. J. Branney and P. Kokelaar. *Pyroclastic density currents and the sedimentation of ignimbrites*, volume 27. Geological Society of London Special Publications, 2002. ISBN 1862390975.

E. C. Breard, J. Dufek, and G. Lube. Enhanced Mobility in Concentrated Pyroclastic Density Currents: An Examination of a Self-Fluidization Mechanism. *Geophysical Research Letters*, 45(2):654–664, 2018. ISSN 19448007. doi: 10.1002/2017GL075759.

R. J. Brown, M. J. Branney, C. Maher, and P. Dávila-Harris. Origin of accretionary lapilli within ground-hugging density currents: Evidence from pyroclastic couplets on Tenerife. *Bulletin of the Geological Society of America*, 122(1-2):305–320, 2010. ISSN 00167606. doi: 10.1130/B26449.1.

D. Buchanan. A model for fuel-coolant interactions. *Journal of Physics D: Applied Physics*, 7:1441–1457, 1974.

D. Buttsworth. A finite difference routine for the solution of transient one dimenasional heat conduction problems with curvature and temperature-dependent thermal properties: OUEL Report Numer 2130/97. Technical report, 1997.

E. S. Calder, P. D. Cole, W. B. Dade, T. H. Druitt, R. P. Hoblitt, H. E. Huppert, L. Ritchie, R. Sparks, and S. R. Young. Mobility of pyroclastic flows and surges at the Soufriere Hills volcano, Montserrat. *Geophysical Research Letters*, 26(5):537–540, 1999.

E. S. Calder, K. Wagner, and S. E. Ogburn. Volcanic hazard maps. In S. C. Loughlin, R. Sparks, S. Brown, S. Jenkins, and C. Vye-brown, editors, *Global volcanic hazards and risk*, chapter 20. Cambridge University Press, Cambridge, 1 edition, 2015. ISBN 9781316276273. doi: 10.1017/CBO9781316276273.022. URL `https://doi.org/10.1017/CBO9781316276273.022`.

B. Capaccioni and F. Cuccoli. Spatter and welded air fall deposits generated by fire-fountaining eruptions: Cooling of pyroclasts during transport and deposition. *Journal of Volcanology and Geothermal Research*, 145(3-4):263–280, 2005. ISSN 03770273. doi: 10.1016/j.jvolgeores.2005.02.001.

A. Cappello, M. Neri, V. Acocella, G. Gallo, A. Vicari, and C. Del Negro. Spatial vent opening probability map of Etna volcano (Sicily, Italy). *Bulletin of Volcanology*, 74(9): 2083–2094, 2012. ISSN 02588900. doi: 10.1007/s00445-012-0647-4.

A. J. Carter, O. Girina, M. S. Ramsey, and Y. V. Demyanchuk. ASTER and field observations of the 24 December 2006 eruption of Bezymianny Volcano, Russia. *Remote Sensing of Environment*, 112(5):2569–2577, 2008. ISSN 00344257. doi: 10.1016/j.rse.2007.12.001.

J. M. Castro, C. I. Schipper, S. P. Mueller, A. S. Militzer, A. Amigo, C. S. Parejas, and D. Jacob. Storage and eruption of near-liquidus rhyolite magma at Cordón Caulle, Chile. *Bulletin of Volcanology*, 75(4):1–17, 2013. ISSN 02588900. doi: 10.1007/s00445-013-0702-9.

J. M. Castro, I. N. Bindeman, H. Tuffen, and C. Ian Schipper. Explosive origin of silicic lava: Textural and δD-H2O evidence for pyroclastic degassing during rhyolite effusion. *Earth and Planetary Science Letters*, 405:52–61, 2014. ISSN 0012821X. doi: 10.1016/j.epsl.2014.08.012. URL `http://dx.doi.org/10.1016/j.epsl.2014.08.012`.

Central Statistics Agency -Government of Ethiopia and Minnesota Population Center - University of Minnesota. Ethiopia - Population and Housing Census 2007 - IPUMS Subset, 2007. URL `http://microdata.worldbank.org/index.php/catalog/2747`.

B. Clarke, E. S. Calder, F. Dessalegn, K. Fontijn, J. A. Cortés, M. Naylor, I. Butler, W. Hutchison, and G. Yirgu. Fluidal pyroclasts reveal the intensity of peralkaline rhyolite pumice cone eruptions. *Nature Communications*, 10(1):1–10, 2019. ISSN 2041-1723. doi: 10.1038/s41467-019-09947-8. URL `http://www.nature.com/articles/s41467-019-09947-8`.

P. D. Cole, A. Neri, and P. J. Baxter. *Hazards from Pyroclastic Density Currents*. Elsevier Inc., second edi edition, 2015. ISBN 9780123859389. doi: 10.1016/b978-0-12-385938-9.00054-7. URL `http://dx.doi.org/10.1016/B978-0-12-385938-9.00054-7`.

B. Connor and E. Hill. Three nonhomogeneous Poisson models for the probability of basaltic volcanism: Application to the Yucca Mountain region, Nevada. *Journal of Geophysical Research*, 100(B6):107–117, 1995.

C. Corazzato and A. Tibaldi. Fracture control on type, morphology and distribution of parasitic volcanic cones: An example from Mt. Etna, Italy. *Journal of Volcanology and Geothermal Research*, 158(1-2):177–194, 2006. ISSN 03770273. doi: 10.1016/j.jvolgeores.2006.04.018.

G. Corti. Continental rift evolution: From rift initiation to incipient break-up in the Main Ethiopian Rift, East Africa. *Earth-Science Reviews*, 96(1-2):1–53, 2009. ISSN 00128252. doi: 10.1016/j.earscirev.2009.06.005. URL `http://dx.doi.org/10.1016/j.earscirev.2009.06.005`.

A. Costa. Viscosity of high crystal content melts: Dependence on solid fraction. *Geophysical Research Letters*, 32(22):1–5, 2005. ISSN 00948276. doi: 10.1029/2005GL024303.

S. L. Cutter, B. J. Boruff, and W. L. Shirley. Social vulnerability to environmental hazards. *Social Science Quarterly*, 84(2):242, 2003. URL `https://onlinelibrary-wiley-com.ezproxy.lib.monash.edu.au/doi/pdf/10.1111/1540-6237.8402002`.

M. Davì, R. De Rosa, P. Donato, and R. Sulpizio. The Lami pyroclastic succession (Lipari, Aeolian Islands): A clue for unravelling the eruptive dynamics of the Monte Pilato rhyolitic pumice cone. *Journal of Volcanology and Geothermal Research*, 201(1-4):39–52, 2011. ISSN 03770273. doi: 10.1016/j.jvolgeores.2010.09.010. URL `http://dx.doi.org/10.1016/j.jvolgeores.2010.09.010`.

D. Di Genova, C. Romano, K. U. Hess, A. Vona, B. T. Poe, D. Giordano, D. B. Dingwell, and H. Behrens. The rheology of peralkaline rhyolites from Pantelleria Island. *Journal of Volcanology and Geothermal Research*, 249:201–216, 2013. ISSN 03770273. doi: 10.1016/j.jvolgeores.2012.10.017. URL `http://dx.doi.org/10.1016/j.jvolgeores.2012.10.017`.

D. Di Genova, C. Romano, D. Giordano, and M. Alletti. Heat capacity, configurational heat capacity and fragility of hydrous magmas. *Geochimica et Cosmochimica Acta*, 142:314–333, 2014. ISSN 00167037. doi: 10.1016/j.gca.2014.07.012. URL `http://dx.doi.org/10.1016/j.gca.2014.07.012`.

D. B. Dingwell and S. L. Webb. Structural relaxation in silicate melts and non-Newtonian melt rheology in geologic processes. *Physics and Chemistry of Minerals*, 16(5):508–516, 1989. ISSN 03421791. doi: 10.1007/BF00197020.

D. B. Dingwell, C. M. Scarfe, and D. J. Cronin. The effect of fluorine on viscosities in the system sodium monoxide-aluminum oxide-silicon dioxide: implications for phonolites, trachytes and rhyolites. *American Mineralogist*, 70(1-2):80–87, 1985. ISSN 0003004X.

D. B. Dingwell, K. U. Hess, and C. Romano. Extremely fluid behavior of hydrous peralkaline rhyolites. *Earth and Planetary Science Letters*, 158(1-2):31–38, 1998. ISSN 0012821X. doi: 10.1016/S0012-821X(98)00046-6.

D. B. Dingwell, Y. Lavallée, K. U. Hess, A. Flaws, J. Marti, A. R. Nichols, H. A. Gilg, and B. Schillinger. Eruptive shearing of tube pumice: Pure and simple. *Solid Earth*, 7(5): 1383–1393, 2016. ISSN 18699529. doi: 10.5194/se-7-1383-2016.

G. A. Douillet, D. A. Pacheco, U. Kueppers, J. Letort, E. Tsang-Hin-Sun, J. Bustillos, M. Hall, P. Ramón, and D. B. Dingwell. Dune bedforms produced by dilute pyroclastic density currents from the August 2006 eruption of Tungurahua volcano, Ecuador. *Bulletin of Volcanology*, 75(11):1–20, 2013. ISSN 02588900. doi: 10.1007/s00445-013-0762-x.

T. Dullforce, D. Buchanan, and R. Peckover. Self-triggering of small-scale fuel-coolant interactions : 1. Experiments. *Journal of Physics D: Applied Physics*, 9:1295–1303, 1976.

C. Ebinger. Continental break-up: The East African perspective. *Astronomy and Geophysics*, 46(2):16–2, 2005. ISSN 1366-8781. doi: 10.1111/j.1468-4004.2005.46216.x. URL `https://academic.oup.com/astrogeo/article-lookup/doi/10.1111/j.1468-4004.2005.46216.x`.

A. Einstein. *Eine neue bestimmung der molekuldimensionen*. PhD thesis, Universitat Zurich, 1906.

A. W. Evans and N. Q. Verlander. What is wrong with criterion FN-lines for judging the tolerability of risk? *Risk Analysis*, 17(2):157–168, 1997. ISSN 02724332. doi: 10.1111/j.1539-6924.1997.tb00855.x.

M. Fazzini, C. Bisci, and P. Billi. Landscapes and Landforms of Ethiopia. In P. Billi, editor, *Landscapes and Landforms of Ethiopia*, chapter 3, pages 65–87. Springer Science & Buisness Media, 1 edition, 2015. ISBN 978-94-017-8025-4. doi: 10.1007/978-94-017-8026-1. URL `http://link.springer.com/10.1007/978-94-017-8026-1`.

D. J. Ferguson, J. MacLennan, I. D. Bastow, D. M. Pyle, S. M. Jones, D. Keir, J. D. Blundy, T. Plank, and G. Yirgu. Melting during late-stage rifting in Afar is hot and deep. *Nature*, 499(7456):70–73, 2013. ISSN 00280836. doi: 10.1038/nature12292. URL `http://dx.doi.org/10.1038/nature12292`.

L. Field, J. Blundy, R. A. Brooker, T. Wright, and G. Yirgu. Magma storage conditions beneath Dabbahu Volcano (Ethiopia) constrained by petrology, seismicity and satellite geodesy. *Bulletin of Volcanology*, 74(5):981–1004, 2012. ISSN 02588900. doi: 10.1007/s00445-012-0580-6.

L. Field, J. Blundy, A. Calvert, and G. Yirgu. Magmatic history of Dabbahu, a composite volcano in the Afar Rift, Ethiopia. *Bulletin of the Geological Society of America*, 125 (1-2):128–147, 2013. ISSN 00167606. doi: 10.1130/B30560.1.

J. Fierstein, B. F. Houghton, C. J. Wilson, and W. Hildreth. Complexities of plinian fall deposition at vent: An example from the 1912 Novarupta eruption (Alaska). *Journal of Volcanology and Geothermal Research*, 76(3-4):215–227, 1997. ISSN 03770273. doi: 10.1016/S0377-0273(96)00081-9.

R. V. Fisher and H.-U. Schmincke. *Pyroclastic Rocks*. Springer-Verlag, Berlin, 1 edition, 1984. ISBN 3540513418.

K. Fontijn, G. G. Ernst, C. Bonadonna, M. A. Elburg, E. Mbede, and P. Jacobs. The ˜4-ka Rungwe Pumice (South-Western Tanzania): A wind-still Plinian eruption. *Bulletin of Volcanology*, 73(9):1353–1368, 2011. ISSN 02588900. doi: 10.1007/s00445-011-0486-8.

K. Fontijn, K. McNamara, A. Zafu Tadesse, D. M. Pyle, F. Dessalegn, W. Hutchison, T. A. Mather, and G. Yirgu. Contrasting styles of post-caldera volcanism along the Main Ethiopian Rift: Implications for contemporary volcanic hazards. *Journal of Volcanology and Geothermal Research*, 356:90–113, 2018. ISSN 03770273. doi: 10.1016/j.jvolgeores.2018.02.001. URL `https://doi.org/10.1016/j.jvolgeores.2018.02.001`.

A. N. Ford Versypt and R. D. Braatz. Analysis of finite difference discretization schemes for diffusion in spheres with variable diffusivity. *Computers and Chemical Engineering*, 71:241–252, 2014. ISSN 00981354. doi: 10.1016/j.compchemeng.2014.05.022. URL `http://dx.doi.org/10.1016/j.compchemeng.2014.05.022`.

R. Fusillo. *Understanding the volcanic history of Corbetti caldera (Main Ethiopian Rift). An integrated study of the stratigraphic reconstruction and the geochemical characterization of the deposits*. PhD thesis, University of Bristol, 2018.

F. Geotti-Bianchini and J. Loherngel. The thermal conductivity of float glass at room temperature. *Glastechnische Berichte*, 66(2):25–29, 1993.

A. Gioncada and P. Landi. The pre-eruptive volatile contents of recent basaltic and pantelleritic magmas at Pantelleria (Italy). *Journal of Volcanology and Geothermal Research*, 189(1-2):191–201, 2010. ISSN 03770273. doi: 10.1016/j.jvolgeores.2009.11.006. URL `http://dx.doi.org/10.1016/j.jvolgeores.2009.11.006`.

D. Giordano, C. Romano, D. B. Dingwell, B. Poe, and H. Behrens. The combined effects of water and fluorine on the viscosity of silicic magmas. *Geochimica et Cosmochimica Acta*, 68(24):5159–5168, 2004. ISSN 00167037. doi: 10.1016/j.gca.2004.08.012.

D. Giordano, J. K. Russell, and D. B. Dingwell. Viscosity of magmatic liquids: A model. *Earth and Planetary Science Letters*, 271(1-4):123–134, 2008. ISSN 0012821X. doi: 10.1016/j.epsl.2008.03.038.

M. Gleeson, M. Stock, D. M. Pyle, T. A. Mather, W. Hutchison, G. Yirgu, and J. Wade. Constraining magma storage conditions at a restless volcano in the Main Ethiopian Rift using phase equilibria models. *Journal of Volcanology and GEothermal Research*, 337:44–61, 2017. ISSN 03770273. doi: 10.1016/j.jvolgeores.2017.02.026. URL `http://dx.doi.org/10.1016/j.jvolgeores.2017.02.026`.

A. H. Graettinger, G. A. Valentine, I. Sonder, P. S. Ross, J. D. White, and J. Taddeucci. Maar-diatreme geometry and deposits: Subsurface blast experiments with variable explosion depth. *Geochemistry, Geophysics, Geosystems*, 15(3):740–764, 2014. ISSN 15252027. doi: 10.1002/2013GC005198.

A. H. Graettinger, G. A. Valentine, I. Sonder, P. S. Ross, and J. D. White. Facies distribution of ejecta in analog tephra rings from experiments with single and multiple subsurface explosions. *Bulletin of Volcanology*, 77(8):1–12, 2015. ISSN 14320819. doi: 10.1007/s00445-015-0951-x.

R. W. Griffiths and J. H. Fink. Solidifying Bingham extrusions: A model for the growth of silicic lava domes. *Journal of Fluid Mechanics*, 347:13–36, 1997. ISSN 00221120. doi: 10.1017/S0022112097006344.

G. A. R. Gualda, M. S. Ghiorso, R. V. Lemons, and T. L. Carley. Rhyolite-MELTS: A modified calibration of MELTS optimized for silica-rich, fluid-bearing magmatic systems. *Journal of Petrology*, 53(5):875–890, 2012. ISSN 00223530. doi: 10.1093/petrology/egr080.

N. Harris. The role of fluorine and chlorine in the petrogenesis of a peralkaline complex from Saudi Arabia. *Chemical Geology*, 31:303–310, 1981. ISSN 03008207. doi: 10.3109/03008207409152259.

R. Hay, W. Hildreth, and R. Lambe. Globule Ignimbrite of Mount Suswa, Kenya. *Geological Society of America Special Papers*, 180:167–175, 1979.

J. Hayashi and S. Self. A comparison of pyroclastic flow and debris avalanche mobility. *Journal of Geophysical Research*, 97:9063–9071, 1992.

Health & Safety Executive. *Reducing Risks: Protecting People - HSE's decision making process*. Stationary Office, Norwich, 1 edition, 2001. ISBN 0717621510.

K.-U. Hess, D. B. Dingwell, and S. Webb. The influence of H2O on the viscosity of a haplogranitic melt. *American Mineralogist*, 80:297–304, 1995. ISSN 0003004X. doi: 10.2138/am-1996-9-1014.

T. Hewett, J. Fay, and D. Hoult. Laboratory experiments of smokestack plumes in a stable atmosphere. *Atmospheric Environment (1967)*, 5(9):767–789, 9 1971. ISSN 00046981. doi: 10.1016/0004-6981(71)90028-X. URL `https://linkinghub.elsevier.com/retrieve/pii/000469817190028X`.

W. Hildreth and R. E. Drake. Volcan Quizapu, Chilean Andes. *Bulletin of Volcanology*, 54:93–125, 1992.

C. Hofmann, V. Courtillot, G. Feraud, P. Rochette, G. Yirgu, E. Ketefo, and R. Pik. Timing of the Ethiopian flood basalt event and implications for plume birth and global change. *Nature*, 389(October):838–841, 1997. doi: 10.1038/nature03031.1.

S. Horn and H.-U. Schmincke. Volatile emission during the eruption of Baitoushan Volcano (China/North Korea) ca. 969 AD. *Bulletin of Volcanology*, 61:537–555, 2000. URL `papers2://publication/uuid/58D7CA0F-187D-41BF-BC70-4CBDB52DA0FE`.

B. F. Houghton and C. J. Wilson. A vesicularity index for pyroclastic deposits. *Bulletin of Volcanology*, 51:451–462, 1989.

B. F. Houghton, C. J. Wilson, and S. Weaver. Strombolian deposits at Mayor Island: "Basaltic" eruption styles displayed by a peralkaline rhyolitic volcano. *New Zealand Geological Survey record*, 8:42–51, 1985.

J. Hübert, K. Whaler, and S. Fisseha. The Electrical Structure of the Central Main Ethiopian Rift as Imaged by Magnetotellurics: Implications for Magma Storage and Pathways. *Journal of Geophysical Research: Solid Earth*, 123(7):6019–6032, 2018. ISSN 21699356. doi: 10.1029/2017JB015160.

E. C. Hughes, D. A. Neave, K. J. Dobson, P. J. Withers, and M. Edmonds. How to fragment peralkaline rhyolites: Observations on pumice using combined multi-scale 2D and 3D imaging. *Journal of Volcanology and Geothermal Research*, 336:179–191, 2017. ISSN 03770273. doi: 10.1016/j.jvolgeores.2017.02.020. URL `http://dx.doi.org/10.1016/j.jvolgeores.2017.02.020`.

J. A. Hunt, A. Zafu, T. A. Mather, D. M. Pyle, and P. H. Barry. Spatially Variable CO2 Degassing in the Main Ethiopian Rift: Implications for Magma Storage, Volatile Transport, and Rift-Related Emissions. *Geochemistry, Geophysics, Geosystems*, 18(10): 3714–3737, 2017. ISSN 15252027. doi: 10.1002/2017GC006975.

J. A. Hunt, D. M. Pyle, and T. A. Mather. The Geomorphology, Structure, and Lava Flow Dynamics of Peralkaline Rift Volcanoes From High-Resolution Digital Elevation Models. *Geochemistry, Geophysics, Geosystems*, 20(3):1508–1538, 2019. ISSN 15252027. doi: 10.1029/2018GC008085.

H. E. Huppert and J. E. Simpson. The slumping of gravity currents. *Journal of Fluid Mechanics*, 99(4):785–799, 1980. ISSN 14697645. doi: 10.1017/S0022112080000894.

W. Hutchison. *Past, present and future volcanic activity at restless calderas in the Main Ethiopian Rift*. PhD thesis, University of Oxford, 2015.

W. Hutchison, D. M. Pyle, T. A. Mather, J. Biggs, and G. Yirgu. 2012 Aluto LiDAR data, 2014. URL `https://figshare.com/articles/2012_Aluto_LiDAR_data/1261646`.

W. Hutchison, T. A. Mather, D. M. Pyle, J. Biggs, and G. Yirgu. Structural controls on fluid pathways in an active rift system: A case study of the Aluto volcanic complex. *Geosphere*, 11(3):542–562, 2015. ISSN 1553040X. doi: 10.1130/GES01119.1.

W. Hutchison, J. Biggs, T. A. Mather, D. M. Pyle, E. Lewi, G. Yirgu, S. Caliro, G. Chiodini, L. E. Clor, and T. P. Fischer. Causes of unrest at silicic calderas in the East African Rift: New constraints from InSAR and soil-gas chemistry at Aluto volcano, Ethiopia. *Geochemistry Geophysics Geosystems*, 17:2825–2834, 2016a. ISSN 0012821X. doi: 10.1002/2014GC005684.Key.

W. Hutchison, R. Fusillo, D. M. Pyle, T. A. Mather, J. D. Blundy, J. Biggs, G. Yirgu, B. E. Cohen, R. A. Brooker, D. N. Barfod, and A. T. Calvert. A pulse of mid-Pleistocene rift volcanism in Ethiopia at the dawn of modern humans. *Nature Communications*, 7:

1–12, 2016b. ISSN 20411723. doi: 10.1038/ncomms13192. URL http://dx.doi.org/10.1038/ncomms13192.

W. Hutchison, D. M. Pyle, T. A. Mather, G. Yirgu, J. Biggs, B. E. Cohen, D. N. Barfod, and E. Lewi. The eruptive history and magmatic evolution of Aluto volcano: new insights into silicic peralkaline volcanism in the Ethiopian rift. *Journal of Volcanology and Geothermal Research*, 328:9–33, 2016c. ISSN 03770273. doi: 10.1016/j.jvolgeores.2016.09.010. URL http://dx.doi.org/10.1016/j.jvolgeores.2016.09.010.

F. Iddon, C. Jackson, W. Hutchison, K. Fontijn, D. M. Pyle, T. A. Mather, G. Yirgu, and M. Edmonds. Mixing and Crystal Scavenging in the Main Ethiopian Rift Revealed by Trace Element Systematics in Feldspars and Glasses. *Geochemistry, Geophysics, Geosystems*, 20(1):230–259, 2019. ISSN 15252027. doi: 10.1029/2018GC007836.

D. Inman. Measures for describing the size distribution of sediments. *Journal of Sedimentary Petrology*, 22(3):125–145, 1952.

International Civil Aviation Organization and Langley Aeronautical Laboratory. Report 1235: Standard atmosphere tables and data for altitudes to 65,800 feet. Technical report, 1955.

International Energy Agency. World Energy Outlook 2015. Technical report, International Energy Agency, 2015.

S. Jenkins, J. C. Komorowski, P. J. Baxter, R. Spence, A. Picquout, F. Lavigne, and Surono. The Merapi 2010 eruption: An interdisciplinary impact assessment methodology for studying pyroclastic density current dynamics. *Journal of Volcanology and Geothermal Research*, 261:316–329, 2013. ISSN 03770273. doi: 10.1016/j.jvolgeores.2013.02.012. URL http://dx.doi.org/10.1016/j.jvolgeores.2013.02.012.

R. W. Johnson. Volcanic globule rock from Mount Suswa, Kenya. *Bulletin of the Geological Society of America*, 79(5):647–652, 1968. ISSN 00167606. doi: 10.1130/0016-7606(1968)79[647:VGRFMS]2.0.CO;2.

E. Jones, E. Oliphant, P. Peterson, and others. SciPy: Open source scientific tools for Python, 2001. URL http://www.scipy.org/.

W. I. R. Jr, N. K. Grant, G. A. Hahn, I. M. Lange, J. L. Powell, J. Easter, and J. M. Degraff. The Evolution of Santa María Volcano , Guatemala. *JSTOR*, 85(1):63–87, 1977.

K. Kelfoun and T. H. Druitt. Numerical modeling of the emplacement of Socompa rock avalanche, Chile. *Journal of Geophysical Research: Solid Earth*, 110(12):1–13, 2005. ISSN 21699356. doi: 10.1029/2005JB003758.

J. M. Kendall, G. W. Stuart, C. J. Ebinger, I. D. Bastow, and D. Keir. Magma-assisted rifting in Ethiopia. *Nature*, 433(7022):146–148, 2005. ISSN 00280836. doi: 10.1038/nature03161.

K. Keranen and S. L. Klemperer. Discontinuous and diachronous evolution of the Main Ethiopian Rift: Implications for development of continental rifts. *Earth and Planetary Science Letters*, 265(1-2):96–111, 2008. ISSN 0012821X. doi: 10.1016/j.epsl.2007.09.038.

Y. Kinfu. In-depth analysis: The postponement of the 4th Ethiopian census: Was it justified and what next?, 4 2019. URL `https://addisstandard.com/in-depth-analysis-the-postponement-of-the-4th-ethiopian-census-was-it-justified-and-what-next/`.

M. Klawonn, B. F. Houghton, D. A. Swanson, S. A. Fagents, P. Wessel, and C. J. Wolfe. Constraining explosive volcanism: Subjective choices during estimates of eruption magnitude. *Bulletin of Volcanology*, 76(2):1–6, 2014. ISSN 02588900. doi: 10.1007/s00445-013-0793-3.

S. Kleinbeck, M. Schäper, S. A. Juran, E. Kiesswetter, M. Blaszkewicz, K. Golka, A. Zimmermann, T. Brüning, and C. Van Thriel. Odor thresholds and breathing changes of human volunteers as consequences of sulphur dioxide exposure considering individual factors. *Safety and Health at Work*, 2(4):355–364, 2011. ISSN 20937997. doi: 10.5491/SHAW.2011.2.4.355.

R. L. Korotev. A self-consistent compilation of elemental concentration data for 93 geochemical reference samples. *Geostandards Newsletter*, 20(2):217–245, 1996. ISSN 01505505. doi: 10.1111/j.1751-908X.1996.tb00185.x.

P. Lahitte, P. Y. Gillot, and V. Courtillot. Silicic central volcanoes as precursors to rift propagation: The Afar case. *Earth and Planetary Science Letters*, 207(1-4):103–116, 2003. ISSN 0012821X. doi: 10.1016/S0012-821X(02)01130-5.

A. L. Lamb, M. J. Leng, M. U. Mohammed, and H. F. Lamb. Holocene climate and vegetation change in the Main Ethiopian Rift Valley, inferred from the composition (C/N and δ13C) of lacustrine organic matter. *Quaternary Science Reviews*, 23(7-8): 881–891, 2004. ISSN 02773791. doi: 10.1016/j.quascirev.2003.06.010.

G. Lanzo, P. Landi, and S. G. Rotolo. Volatiles in pantellerite magmas: A case study of the Green Tuff Plinian eruption (Island of Pantelleria, Italy). *Journal of Volcanology and Geothermal Research*, 262:153–163, 2013. ISSN 03770273. doi: 10.1016/j.jvolgeores.2013.06.011. URL `http://dx.doi.org/10.1016/j.jvolgeores.2013.06.011`.

C. Le Turdu, J.-J. Tiercelin, B. E. Gilbert, Y. Travi, K.-E. Lezzar, R. Jean-Paul, F. Gasse, R. Bonnefille, M. Decoubert, B. Gensous, V. Jeudy, E. Tamrat, M. U. Mohammed, K. Martens, B. Atnafu, T. Chernet, D. Williamson, and M. Taieb. The Ziway–Shala lake basin system, Main Ethiopian Rift: influence of volcanism, tectonics, and climatic forcing on basin formation and sedimentation. *Palaeogeography, Palaeoclimatology, Palaeoecology*, 150(3-4):135–177, 1999. URL `http://www.eah.org.et/docs/Ziway-Shallalakes.pdf`.

D. R. Lentz and A. D. Fowler. A dynamic model for graphic quartz-feldspar intergrowths in granite pegmatites in the southwestern Grenville Province. *Canadian Mineralogist*, 30:571–585, 1992.

Z. Leyew. The Description of Colour Terms in Ethiopian Languages. *Eastern Africa Social Science Research Review*, 32(2):53–86, 2016. doi: 10.1353/eas.2016.0008.

R. Lloyd, J. Biggs, M. Wilks, A. Nowacki, J. M. Kendall, A. Ayele, E. Lewi, and H. Eysteinsson. Evidence for cross rift structural controls on deformation and seismicity at a continental rift caldera. *Earth and Planetary Science Letters*, 487:190–200, 2018. ISSN 0012821X. doi: 10.1016/j.epsl.2018.01.037. URL https://doi.org/10.1016/j.epsl.2018.01.037.

S. C. Loughlin, C. Vye-brown, R. Sparks, S. Brown, J. Barclay, E. S. Calder, E. Cottrell, G. Jolly, J.-C. Komorowski, C. Madeville, C. Newhall, J. Palma, S. Potter, and G. Valentine. Global volcanic hazards and risk, Summary background paper for the UN_ISDR Global assessment report on disaster risk reduction 2015. Technical report, 2015.

D. J. Lowe. Tephrochronology and its application: A review. *Quaternary Geochronology*, 6(2):107–153, 2011. ISSN 18711014. doi: 10.1016/j.quageo.2010.08.003.

J. B. Lowenstern and G. Mahood. New data on magmatic H2O contents of pantellerites, with implications for petrogenesis and eruptive dynamics at Pantelleria. *Bulletin of Volcanology*, 54:78–83, 1991.

G. A. Macdonald and A. Alcaraz. Nuees ardentes of the 1948-1953 eruption of Hibok-Hibok. *Bulletin of Volcanology*, 18(1):169–178, 1956.

R. Macdonald, G. R. Davies, C. M. Bliss, P. T. Leat, and D. K. Bailey. Geochemistry of High-silica Peralkaline Rhyolites , Naivasha, Kenya Rift Valley. *Journal of Petrology*, 28 (1970):979–1008, 1987.

G. Mahood. Pyroclastic rocks and calderas associated with strongly peralkaline magmatism. *Journal of Geophysical Research*, 89(B10):8540–8552, 1984.

M. C. Malin and M. F. Sheridan. Computer-Assisted Mapping of Pyroclastic Surges. *Science*, 217(4560):637–640, 8 1982. ISSN 0036-8075. doi: 10.1126/science.217.4560.637. URL http://www.sciencemag.org/cgi/doi/10.1126/science.217.4560.637.

J. Marti and A. Felpeto. Methodology for the computation of volcanic susceptibility. An example for mafic and felsic eruptions on Tenerife (Canary Islands). *Journal of Volcanology and Geothermal Research*, 195(1):69–77, 2010. ISSN 03770273. doi: 10.1016/j.jvolgeores.2010.06.008. URL http://dx.doi.org/10.1016/j.jvolgeores.2010.06.008.

U. Martin and K. Németh. How Strombolian is a " Strombolian " scoria cone ? Some irregularities in scoria cone architecture from the Transmexican Volcanic Belt, near Volcan Ceboruco, (Mexico) and Al Haruj (Libya). *Journal of Volcanology and Geothermal Research*, 155:104–118, 2006. doi: 10.1016/j.jvolgeores.2006.02.012.

W. Marzocchi, A. Garcia-Aristizabal, P. Gasparini, M. L. Mastellone, and A. D. Ruocco. Basic principles of multi-risk assessment: A case study in Italy. *Natural Hazards*, 62(2): 551–573, 2012. ISSN 0921030X. doi: 10.1007/s11069-012-0092-x.

L. G. Mastin. A simple calculator of balistic trajectories for blocks ejected during volcnaic eruptions. Technical report, 2001.

L. G. Mastin. Plots of Wind Patterns of the World's Volcanoes: U.S. Geological Survey data release, 2017.

F. Mazzarini, N. Le Corvec, I. Isola, and M. Favalli. Volcanic field elongation, vent distribution, and tectonic evolution of a continental rift: The Main Ethiopian Rift example. *Geosphere*, 12(3):706–720, 2016. ISSN 1553040X. doi: 10.1130/GES01193.1.

T. R. McGetchin, M. Settle, and B. A. Chouet. Cinder cone growth modeled after Northeast Crater, Mount Etna, Sicily. *Journal of Geophysical Research*, 79(23):3257–3272, 1974. ISSN 01480227. doi: 10.1029/JB079i023p03257. URL `http://doi.wiley.com/10.1029/JB079i023p03257`.

K. McNamara, K. V. Cashman, A. C. Rust, K. Fontijn, F. Chalié, E. L. Tomlinson, and G. Yirgu. Using Lake Sediment Cores to Improve Records of Volcanism at Aluto Volcano in the Main Ethiopian Rift. *Geochemistry, Geophysics, Geosystems*, 19(9):3164–3188, 2018. ISSN 15252027. doi: 10.1029/2018GC007686.

J. G. Moore and T. W. Sisson. The 1980 Eruptions of Mount St Helens, Washington. *US Geological Survey Professional Papers*, 1981.

G. B. Morgan and D. London. Process of granophyre crystallization in the long mountain granite, Southern Oklahoma. *Bulletin of the Geological Society of America*, 124(7-8): 1251–1261, 2012. ISSN 00167606. doi: 10.1130/B30569.1.

B. R. Morton. Buoyant plumes in a moist atmosphere. *Journal of Fluid Mechanics*, 2(2): 127–144, 1956. doi: /10.1017/S0022112057000038.

A. Namiki and M. Manga. Transition between fragmentation and permeable outgassing of low viscosity magmas. *Journal of Volcanology and Geothermal Research*, 169(1-2): 48–60, 2008. ISSN 03770273. doi: 10.1016/j.jvolgeores.2007.07.020.

I. A. Narin and S. Self. Explosive Eruptions and Pyroclastic Avalanches from Ngaurahoe in February 1975. *Journal of Volcanology and Geothermal Research*, 3:39–60, 1978.

NASA. NASA Shuttle Radar Topography Mission Global 1 arc second V003, 2014.

National Park Service. Valley of Ten Thousand Smokes and the 1912 Novarupta-Katmai Eruption, 2018. URL `https://www.nps.gov/katm/learn/nature/valley-of-ten-thousand-smokes.htm`.

D. A. Neave, G. Fabbro, R. A. Herd, C. M. Petrone, and M. Edmonds. Melting, differentiation and degassing at the pantelleria volcano, Italy. *Journal of Petrology*, 53(3): 637–663, 2012. ISSN 00223530. doi: 10.1093/petrology/egr074.

Oak Ridge National Laboratory. LandScan: Documentation, 2019. URL `https://landscan.ornl.gov/documentation/#inputData`.

S. Ogburn. FlowDat: Mass flow database v2.2, 2012. URL `https://vhub.org/groups/massflowdatabase`.

S. E. Ogburn and E. S. Calder. The relative effectiveness of empirical and physical models for simulating the dense undercurrent of pyroclastic flows under different emplacement conditions. *Frontiers in Earth Science*, 5(November), 2017. ISSN 22966463. doi: 10.3389/feart.2017.00083.

OpenStreetMap. Planet dump retrieved from https://planet.osm.org, 2019. URL https://www.openstreetmap.org.

G. Orsi, L. Ruvo, and C. Scarpati. The Serra della Fastuca Tephra at Pantelleria: Physical parameters for an explosive eruption of peralkaline magma. *Journal of Volcanology and Geothermal Research*, 39(1):55–60, 1989. ISSN 03770273. doi: 10.1016/0377-0273(89)90020-6.

G. M. Paola. Geology of the Corbetti Caldera area (Main Ethiopian Rift Valley). *Bulletin Volcanologique*, 35(2):497–506, 1971. ISSN 0258-8900. doi: 10.1007/BF02596970. URL http://www.springerlink.com/index/10.1007/BF02596970.

A. K. Patra, A. C. Bauer, C. C. Nichita, E. B. Pitman, M. F. Sheridan, M. Bursik, B. Rupp, A. Webber, A. J. Stinton, L. M. Namikawa, and C. S. Renschler. Parallel adaptive numerical simulation of dry avalanches over natural terrain. *Journal of Volcanology and Geothermal Research*, 139(1-2):1–21, 2005. ISSN 03770273. doi: 10.1016/j.jvolgeores.2004.06.014.

A. Peccerillo, M. Barberio, G. Yirgu, D. Ayalew, M. Barbieri, and T. Wu. Relationships between Mafic and Peralkaline Silicic Magmatism in Continental Rift Settings: a Petrological, Geochemical and Isotopic Study of the Gedemsa Volcano, Central Ethiopian Rift. *Journal of Petrology*, 44(11):2003–2032, 2003. ISSN 1460-2415. doi: 10.1093/petrology/egg068. URL https://academic.oup.com/petrology/article-lookup/doi/10.1093/petrology/egg068.

A. Peccerillo, C. Donati, A. P. Santo, A. Orlando, G. Yirgu, and D. Ayalew. Petrogenesis of silicic peralkaline rocks in the Ethiopian rift: Geochemical evidence and volcanological implications. *Journal of African Earth Sciences*, 48(2-3):161–173, 2007. ISSN 08995362. doi: 10.1016/j.jafrearsci.2006.06.010.

T. C. Pierson and K. M. Scott. Downstream Dilution of a Lahar: Transition From Debris Flow to Hyperconcentrated Streamflow. *Water Resources Research*, 21(10):1511–1524, 1985. ISSN 19447973. doi: 10.1029/WR021i010p01511.

R. Pik, C. Deniel, C. Coulon, G. Yirgu, C. Hofmann, and D. Ayalew. The northwestern Ethiopian Plateau flood basalts: classification and spatial distribution of magma types. *Journal of Volcanology and Geothermal Research*, 81(1-2):91–111, 1998. ISSN 03770273. doi: 10.1016/S0377-0273(97)00073-5.

H. Pinkerton and S. J. Sparks. Field measurements of the rheology of lava. *Nature*, 276 (November):383–385, 1978.

L. Pioli, E. Erlund, E. Johnson, K. Cashman, P. Wallace, M. Rosi, and H. Delgado Granados. Explosive dynamics of violent Strombolian eruptions: The eruption of Parícutin Volcano 1943-1952 (Mexico). *Earth and Planetary Science Letters*, 271(1-4):359–368, 2008. ISSN 0012821X. doi: 10.1016/j.epsl.2008.04.026.

M. Pistolesi, R. Cioni, C. Bonadonna, M. Elissondo, V. Baumann, A. Bertagnini, L. Chiari, R. Gonzales, M. Rosi, and L. Francalanci. Complex dynamics of small-moderate volcanic

events: the example of the 2011 rhyolitic Cordón Caulle eruption, Chile. *Bulletin of Volcanology*, 77(1), 2015. ISSN 14320819. doi: 10.1007/s00445-014-0898-3.

M. Polacci. Constraining the dynamics of volcanic eruptions by characterization of pumice textures. *Annals of Geophysics*, 48(4-5):731–738, 2005. ISSN 15935213.

L. A. Porritt, J. K. Russell, and S. L. Quane. Pele's tears and spheres: Examples from Kilauea Iki. *Earth and Planetary Science Letters*, 333-334:171–180, 2012. ISSN 0012821X. doi: 10.1016/j.epsl.2012.03.031. URL http://dx.doi.org/10.1016/j.epsl.2012.03.031.

G. Postma. An analysis of the variation in delta architecture. *Terra Review*, 2:124–130, 1990. doi: 10.1111/j.1365-3121.1990.tb00052.x.

D. M. Pyle. The thickness, volume and grainsize of tephra fall deposits. *Bulletin of Volcanology*, 51:1–15, 1989.

D. M. Pyle. *Sizes of Volcanic Eruptions*. Elsevier Inc., second edi edition, 2015. ISBN 9780123859389. doi: 10.1016/b978-0-12-385938-9.00013-4. URL http://dx.doi.org/10.1016/B978-0-12-385938-9.00013-4.

V. Rapprich, V. Žáček, K. Verner, V. Erban, T. Goslar, Y. Bekele, F. Legesa, T. Hroch, and P. Hejtmánková. Wendo Koshe Pumice: The latest Holocene silicic explosive eruption product of the Corbetti Volcanic System (Southern Ethiopia). *Journal of Volcanology and Geothermal Research*, 310:159–171, 2016. ISSN 03770273. doi: 10.1016/j.jvolgeores.2015.12.008.

RCMRD. Africa Water Bodies, 2015.

A. Richter. Drilling contract signed for 70 MW geothermal development in Ethiopia, 2019. URL http://www.thinkgeoenergy.com/drilling-contract-signed-for-70-mw-geothermal-development-in-ethiopia/.

C. Riedel, G. G. Ernst, and M. Riley. Controls on the growth and geometry of pyroclastic constructs. *Journal of Volcanology and Geothermal Research*, 127(1-2):121–152, 2003. ISSN 03770273. doi: 10.1016/S0377-0273(03)00196-3.

T. O. Rooney, W. K. Hart, C. M. Hall, D. Ayalew, M. S. Ghiorso, P. Hidalgo, and G. Yirgu. Peralkaline magma evolution and the tephra record in the Ethiopian Rift. *Contributions to Mineralogy and Petrology*, 164(3):407–426, 2012. ISSN 00107999. doi: 10.1007/s00410-012-0744-6.

N. Rose. The value of life: somatic ethics & the spirit of biocapital. *Daedalus*, 137(1): 36–48, 2008. ISSN 0899-2363. doi: 10.1215/08992363-2144697.

J. Roughier, S. Sparks, and L. J. Hill. *Risk and Uncertainty Assessment for*. Cambridge University Press, 1 edition, 2013. ISBN 9781107006195.

C. A. Rychert, J. O. Hammond, N. Harmon, J. Michael Kendall, D. Keir, C. Ebinger, I. D. Bastow, A. Ayele, M. Belachew, and G. Stuart. Volcanism in the Afar Rift sustained by decompression melting with minimal plume influence. *Nature Geoscience*, 5(6):406–409, 2012. ISSN 17520894. doi: 10.1038/ngeo1455. URL http://dx.doi.org/10.1038/ngeo1455.

F. Samrock, A. Kuvshinov, J. Bakker, A. Jackson, and S. Fisseha. 3-D analysis and interpretation of magnetotelluric data from the Aluto-Langano geothermal field, Ethiopia. *Geophysical Journal International*, 202(3):1923–1948, 2015. ISSN 1365246X. doi: 10.1093/gji/ggv270.

L. Sandri, P. Tierz, A. Costa, and W. Marzocchi. Journal of Geophysical Research : Solid Earth in the Neapolitan Area (Southern Italy). *Journal of Geophysical Research: Solid Earth*, 123:1–27, 2018a.

L. Sandri, P. Tierz, A. Costa, and W. Marzocchi. Probabilistic Hazard From Pyroclastic Density Currents in the Neapolitan Area (Southern Italy). *Journal of Geophysical Research: Solid Earth*, 123(5):3474–3500, 5 2018b. ISSN 21699313. doi: 10.1002/2017JB014890. URL `http://doi.wiley.com/10.1002/2017JB014890`.

R. Saucedo, J. L. Macías, M. F. Sheridan, M. I. Bursik, and J. C. Komorowski. Modeling of pyroclastic flows of Colima Volcano, Mexico: Implications for hazard assessment. *Journal of Volcanology and Geothermal Research*, 139(1-2):103–115, 2005. ISSN 03770273. doi: 10.1016/j.jvolgeores.2004.06.019.

R. Saucedo, J. L. Macías, J. C. Gavilanes-Ruiz, M. I. Bursik, and V. Vargas-Gutiérrez. *Pyroclastic Density Currents at Volcán de Colima*. Springer, 2019. ISBN 9783642259104. doi: 10.1007/978-3-642-25911-1{_}11.

C. Schaschke. *Steam Tables*. Oxford University Press, 1 edition, 2014. ISBN 9780199651450.

W. Schiesser. Heat conduction in cylindrical and spherical coordinates. *The numerical method of lines*, page 326, 1991. ISSN 1875-869X. doi: 10.3233/HAB-2010-0222.

C. I. Schipper, J. M. Castro, B. M. Kennedy, B. W. Christenson, A. Aiuppa, B. Alloway, P. Forte, G. Seropian, and H. Tuffen. Halogen (Cl, F) and sulphur release during explosive, effusive, and intrusive phases of the 2011 rhyolitic eruption at Cordón Caulle volcano (Chile). *Volcanica*, 2(1):73–90, 2019.

H.-U. Schmincke. Froth flows and globule flows in Kenya. *Naturwissenschaften*, page 510, 1972. ISSN 00442968. doi: 10.1524/zkri.1961.115.5-6.460.

H.-U. Schmincke. Volcanological aspects of peralkaline silicic welded ash-flow tuffs. *Bulletin Volcanologique*, 38(3):594–636, 1975a.

H.-U. Schmincke. Volcanological aspects of peralkaline silicic welded ash-flow tuffs. *Bulletin Volcanologique*, 38(3):594–636, 1975b.

D. Schultz. *Eloquent Science*. American Meterological Society, Boston, 1 edition, 2009. ISBN 978-1-935704-03-4. doi: 10.1007/978-1-935704-03-4.

M. F. Sheridan and J. Macías. Estimation of risk probability for gravity-driven pyroclastic flows at Volcan Colima, Mexico. *Journal of Volcanology and Geothermal Research*, 66 (1-4):251–256, 1995. ISSN 03770273. doi: 10.1016/0377-0273(94)00058-O.

M. F. Sheridan, B. Hubbard, M. I. Bursik, M. Abrams, C. Siebe, J. L. Macías, and H. Delgado. Gauging short-term volcanic hazards at popocatepetl. *Eos*, 82(16), 2001. ISSN 23249250. doi: 10.1029/01EO00097.

G. M. Smith, R. Williams, P. J. Rowley, and D. R. Parsons. Investigation of variable aeration of monodisperse mixtures: implications for pyroclastic density currents. *Bulletin of Volcanology*, 80(8):1–12, 2018. ISSN 14320819. doi: 10.1007/s00445-018-1241-1.

Y. K. Sohn and S. K. Chough. The Udo tuff cone, Cheju Island, South Korea: transformation of pyroclastic fall into debris fall and grain flow on a steep volcanic cone slope. *Sedimentology*, 40(4):769–786, 1993. ISSN 13653091. doi: 10.1111/j.1365-3091.1993.tb01359.x.

R. Sparks. The dynamics of bubble formation and growth in magmas: a review and analysis. *Journal of Volcanology and Geothermal Research*, 3:1–37, 1978. ISSN 1424-8220. doi: 10.3390/s16071032.

R. Sparks. *Volcanic Plumes*. Wiley, Chichester, 1 edition, 1997. ISBN 0471939013.

R. S. Sparks and H. Pinkerton. Effect of degassing on rheology of basaltic lava. *Nature*, 276(5686):385–386, 1978. ISSN 00280836. doi: 10.1038/276385a0.

R. J. Spence, P. J. Baxter, and G. Zuccaro. Building vulnerability and human casualty estimation for a pyroclastic flow: A model and its application to Vesuvius. *Journal of Volcanology and Geothermal Research*, 133(1-4):321–343, 2004. ISSN 03770273. doi: 10.1016/S0377-0273(03)00405-0.

R. J. S. Spence, I. Kelman, P. J. Baxter, G. Zuccaro, and S. Petrazzuoli. Residential building and occupant vulnerability to tephra fall. *Natural Hazards and Earth System Sciences*, 5:477–494, 2005.

D. Spiegelhalter, M. Pearson, O. Smith, A. Garay-Arevalo, and I. Short. Understanding Uncertainty, 2008. URL `https://understandinguncertainty.org/`.

E. T. Spiller, M. J. Bayarri, J. O. Berger, E. S. Calder, A. K. Patra, E. B. Pitman, and R. L. Wolpert. Automating Emulator Construction for Geophysical Hazard Maps. *SIAM/ASA Journal on Uncertainty Quantification*, 2(1):126–152, 2014. doi: 10.1137/120899285.

SSHAC. Recommendations for probabilistic seismic hazard hazard analysis: Guidance on uncertainty and use of experts. NUREG/CR-6372. Technical report, U.S Nuclear Regulatory Commission, 1997.

D. S. Stamps, E. Calais, E. Saria, C. Hartnady, J. M. Nocquet, C. J. Ebinger, and R. M. Fernandes. A kinematic model for the East African Rift. *Geophysical Research Letters*, 35(5):1–6, 2008. ISSN 00948276. doi: 10.1029/2007GL032781.

F. R. Stevens, A. E. Gaughan, C. Linard, and A. J. Tatem. Disaggregating census data for population mapping using Random forests with remotely-sensed and ancillary data. *PLoS ONE*, 10(2):1–22, 2015. ISSN 19326203. doi: 10.1371/journal.pone.0107042. URL `http://dx.doi.org/10.1371/journal.pone.0107042`.

R. Sulpizio, L. Capra, D. Sarocchi, R. Saucedo, J. C. Gavilanes-Ruiz, and N. R. Varley. Predicting the block-and-ash flow inundation areas at Volcán de Colima (Colima, Mexico) based on the present day (February 2010) status. *Journal of Volcanology and Geothermal Research*, 193(1-2):49–66, 2010. ISSN 03770273. doi: 10.1016/j.jvolgeores.2010.03.007. URL http://dx.doi.org/10.1016/j.jvolgeores.2010.03.007.

R. Sulpizio, P. Dellino, D. M. Doronzo, and D. Sarocchi. Pyroclastic density currents: State of the art and perspectives. *Journal of Volcanology and Geothermal Research*, 283:36–65, 2014a. ISSN 03770273. doi: 10.1016/j.jvolgeores.2014.06.014. URL http://dx.doi.org/10.1016/j.jvolgeores.2014.06.014.

R. Sulpizio, E. Zanella, J. L. Macías, and R. Saucedo. Deposit temperature of pyroclastic density currents emplaced during the El Chichón 1982 and Colima 1913 eruptions. *Geological Society, London, Special Publications*, 396(1):35–49, 2014b. ISSN 0305-8719. doi: 10.1144/sp396.5.

R. Sulpizio, E. Zanella, J. L. Macías, and R. Saucedo. Deposit temperature of pyroclastic density currents emplaced during the El Chichón 1982 and Colima 1913 eruptions. *Geological Society, London, Special Publications*, 396(1):35–49, 2015. ISSN 0305-8719. doi: 10.1144/sp396.5.

J. M. Sumner. Formation of clastogenic lava flows during fissure eruption and scoria cone collapse: The 1986 eruption of Izu-Oshima Volcano, eastern Japan. *Bulletin of Volcanology*, 60(3):195–212, 1998. ISSN 02588900. doi: 10.1007/s004450050227.

J. M. Sumner and M. J. Branney. The emplacement history of a remarkable heterogeneous, chemically zoned, rheomorphic and locally lava-like ignimbrite: 'TL' on Gran Canaria. *Journal of Volcanology and Geothermal Research*, 115(1-2):109–138, 2002. ISSN 03770273. doi: 10.1016/S0377-0273(01)00311-0.

J. Taddeucci, M. Edmonds, B. Houghton, M. R. James, and S. Vergniolle. *Hawaiian and Strombolian Eruptions*. Elsevier Inc., second edi edition, 2015. ISBN 9780123859389. doi: 10.1016/b978-0-12-385938-9.00027-4. URL http://dx.doi.org/10.1016/B978-0-12-385938-9.00027-4.

F. Tedesse. Ethiopia: Aluto-Langano Geothermal Expansion Comes to Life, 2018. URL https://allafrica.com/stories/201803200882.html.

M. Teklemariam and S. Kebede. Strategy for geothermal resource exploration and development in Ethiopia. In *Proceedings: World Geothermal Congress, Bali, Indonesia*, Bali, 2010. ISBN 0172-4622. doi: 10.1055/s-2007-971115. URL http://www.geothermal-energy.org/pdf/IGAstandard/WGC/2010/0155.pdf.

R. Thomas and R. Sparks. Cooling of tephra during fallout from eruption columns. *Bulletin of Volcanology*, 54:542–553, 1992.

M. A. Thompson, J. M. Lindsay, and J. C. Gaillard. The influence of probabilistic volcanic hazard map properties on hazard communication. *Journal of Applied Volcanology*, 4(1), 2015. ISSN 21915040. doi: 10.1186/s13617-015-0023-0.

S. Thorarinsson. The Crater Groups in Iceland. *Bulletin of Volcanology*, 14:3–44, 1953.

S. Thorarinsson, S. Steinthorsson, T. Einarsson, H. Kristmannsdottir, and N. Oskarsson. The eruption on Heimaey, Iceland. *Nature*, 241:327–375, 1973. ISSN 00280836. doi: 10.1038/246421a0.

T. Thordarson and S. Self. The Lake (Skaftar Fires) and Grimsvotn eruptions in 1783-1785. *Bulletin of Volcanology*, 55:233–263, 1993.

P. Tierz, L. Sandri, A. Costa, R. Sulpizio, L. Zaccarelli, M. A. D. Vito, and W. Marzocchi. Uncertainty Assessment of Pyroclastic Density Currents at Mount Vesuvius (Italy) Simulated Through the Energy Cone Model. In K. Riley, P. Webley, and M. Thompson, editors, *Natural Hazard Uncertainty Assessment: Modeling and Decision Support*, pages 125–145. John Wiley & Sons, Inc., 1st edition, 2016a. ISBN 9781119028116. doi: 10.1002/9781119028116.ch9.

P. Tierz, L. Sandri, A. Costa, L. Zaccarelli, M. A. Di Vito, R. Sulpizio, and W. Marzocchi. Suitability of energy cone for probabilistic volcanic hazard assessment: validation tests at Somma-Vesuvius and Campi Flegrei (Italy). *Bulletin of Volcanology*, 78:79, 2016b. ISSN 14320819. doi: 10.1007/s00445-016-1073-9. URL http://dx.doi.org/10.1007/s00445-016-1073-9.

H. Tuffen, M. R. James, J. M. Castro, and C. I. Schipper. Exceptional mobility of an advancing rhyolitic obsidian flow at Cordón Caulle volcano in Chile. *Nature Communications*, 4:1–7, 2013. ISSN 20411723. doi: 10.1038/ncomms3709. URL http://dx.doi.org/10.1038/ncomms3709.

UN, Eurostat, and World Bank. Death rate, crude (per 1,000 people), 2017. URL https://data.worldbank.org/indicator/SP.DYN.CDRT.IN?end=2017&locations=GB-ET&most_recent_value_desc=false&start=1960&view=chart.

UNDP. Human Development Reports - Ethiopia. Technical report, UN, 2018. URL http://hdr.undp.org/en/countries/profiles/ETH.

UNESCO. Adult literacy rate, population 15+ years (both sexes, male, female), 2015. URL http://data.uis.unesco.org/Index.aspx?DataSetCode=EDULIT_DS&popupcustomise=true&lang=en#.

University of Southampton. WorldPop - Methods, 2019. URL https://www.worldpop.org/.

C. Valentin, J. Poesen, and Y. Li. Gully erosion: Impacts, factors and control. *Catena*, 63 (2-3):132–153, 2005. ISSN 03418162. doi: 10.1016/j.catena.2005.06.001.

J. W. Vallance and R. M. Iverson. *Lahars and Their Deposits*. Elsevier, second edi edition, 2015. ISBN 9780123859389. doi: 10.1016/B978-0-12-385938-9.00037-7. URL http://linkinghub.elsevier.com/retrieve/pii/B9780123859389000377.

J. W. Vallance and S. B. Savage. Particle Segregation in Granular Flows Down Chutes. In *IUTAM Symposium on Segregation in Granular Flows. Solid Mechanics and Its Applications*, pages 31–51. Springer, 2000. ISBN 978-94-015-9498-1. doi: 10.1007/978-94-015-9498-1{_}3. URL http://link.springer.com/10.1007/978-94-015-9498-1_3.

W. K. Viscusi and J. E. Aldy. The value of a statistical life: A critical review of market estimates throughout the world. *Journal of Risk and uncertainty*, 27(1):5–76, 2003.

C. Vye-Brown, R. S. J. Sparks, E. Lewi, G. Mewa, A. Asrat, S. C. Loughlin, K. Mee, and T. J. Wright. Ethiopian volcanic hazards: a changing research landscape. *Geological Society, London, Special Publications*, 420(1):355–365, 2016. ISSN 0305-8719. doi: 10.1144/sp420.16.

W. Wagner and A. Pruss. Revised Release on the {IAPWS} Formulation 1995 for the Thermodynamic Properties of Ordinary Water Substance for General and Scientific Use. *J. Phys. Chem. Ref. Data*, 31(2):387–535, 2002. doi: 10.1158/0008-5472.CAN-09-0634.

R. Waitt and USGS. Photograph of Mount Tawawera, 1986. URL http://www.volcano.si.edu/world/volcano.cfm?vnum=0401-05=&volpage=photos&photo=016016,PublicDomain,https://commons.wikimedia.org/w/index.php?curid=5333057.

G. P. Walker and R. Croasdale. Characteristics of some basaltic pyroclastics. *Bulletin Volcanologique*, 35(2):303–317, 1971. ISSN 0366483X. doi: 10.1007/BF02596957.

G. P. L. Walker. Structure, and origin by injection of lava under surface crust, of tumuli, lava rises, lava-rise pits, and lava-inflation clefts in Hawaii. *Bulletin of Volcanology*, 53(7):546–558, 9 1991. ISSN 0258-8900. doi: 10.1007/BF00298155. URL http://link.springer.com/10.1007/BF00298155.

G. P. L. Walker, S. Self, and L. Wilson. Tawawera 1886, New Zealand - A basaltic plinian fissure eruption. *Journal of Volcanology and Geothermal Research*, 21:61–78, 1984.

M. P. Wand and M. C. Jones. *Kernel Smoothing*. Champan & Hall, London, 1 edition, 1994. ISBN 9780412552700.

J. D. Webster, R. P. Taylor, and C. Bean. Pre-eruptive melt composition and constraints on degassing of a water-rich pantellerite magma, Fantale volcano, Ethiopia. *Contributions to Mineralogy and Petrology*, 114(1):53–62, 1993. ISSN 00107999. doi: 10.1007/BF00307865.

J. N. Weller, A. J. Martin, C. B. Connor, L. J. Connor, and A. Karakhanian. Modelling the spatial distribution of volcanoes: an example from Armenia. In H. M. Mader, S. G. Coles, C. B. Connor, and L. J. Connor, editors, *Statistics in Volcanology*, chapter 7, pages 77–87. Geological Society of London Special Publications, London, 1 edition, 2006. doi: 10.1144/iavcei001.7.

J. D. White. Impure coolants and interaction dynamics of phreatomagmatic eruptions. *Journal of Volcanology and Geothermal Research*, 74(3-4):155–170, 1996. ISSN 03770273. doi: 10.1016/S0377-0273(96)00061-3.

WHO. World Health Statistics 2017. Technical report, Switzerland, 2017. URL https://www.who.int/gho/publications/world_health_statistics/2017/en/.

WHO. World malaria report 2018. Technical report, 2018.

M. C. Wilding, R. Macdonald, J. E. Davies, and A. E. Fallick. Volatile characteristics of peralkaline rhyolites from Kenya: an ion microprobe, infrared spectroscopic and hydrogen isotope study. *Contributions to Mineralogy and Petrology*, 114(2):264–275, 1993. ISSN 00107999. doi: 10.1007/BF00307761.

M. Wilks, J. M. Kendall, A. Nowacki, J. Biggs, J. Wookey, Y. Birhanu, A. Ayele, and T. Bedada. Seismicity associated with magmatism, faulting and hydrothermal circulation at Aluto Volcano, Main Ethiopian Rift. *Journal of Volcanology and Geothermal Research*, 340:52–67, 2017. ISSN 03770273. doi: 10.1016/j.jvolgeores.2017.04.003. URL http://dx.doi.org/10.1016/j.jvolgeores.2017.04.003.

R. Williams. *Emplacement of radial pyroclastic density currents over irregular topography.* PhD thesis, University of Leicester, 2010.

C. Wilson and W. Hildreth. The Bishop Tuff: New Insights From Eruptive Stratigraphy. *The Journal of Geology*, 105(4):407–440, 1997. ISSN 0022-1376. doi: 10.1086/515937. URL https://www.journals.uchicago.edu/doi/10.1086/515937.

L. Wilson, R. S. J. Sparks, T. C. Huang, and N. D. Watkins. The control of volcanic column heights by eruption energetics and dynamics. *Journal of Geophysical Research: Solid Earth*, 83(B4):1829–1836, 1978. doi: 10.1029/jb083ib04p01829.

L. Wilson, R. S. J. Sparks, and G. P. L. Walker. Explosive volcanic eruptions – IV. The control of magma properties and conduit geometry on eruption column behaviour. *Geophysical Journal International*, 63(1):117–148, 10 1980a. ISSN 0956-540X. doi: 10.1111/j.1365-246X.1980.tb02613.x. URL https://academic.oup.com/gji/article-lookup/doi/10.1111/j.1365-246X.1980.tb02613.x.

L. Wilson, S. J. Sparks, and L. Walker. Explosive volcanic eruptions - IV. The control of magma properties and conduit geometry on eruption column behaviour. *Geophysical Journal International*, 63(1):117–148, 1980b.

K. H. Wohletz. Mechanisms of hydrovolcanic pyroclast formation: grain-size, scanning electron microscopy, and experimental studies. *Journal of Volcanology and Geothermal Research*, 17:31–63, 1983.

G. Woldegabriel, J. L. Aronson, and R. C. Walter. Main Ethiopia Rift Geology, geochronology, and rift basin development in the central sector of the Main Ethiopian Rift. *Geological Society of America Bulletin*, 102(April):439–458, 1990. doi: 10.1130/0016-7606(1990)102⟨0439:GGARBD⟩2.3.CO;2. URL http://www.geosociety.org/pubs/copyrt.htm#gsa.

C. A. Wood. Morphometric evolution of cinder cones. *Journal of Volcanology and Geothermal Research*, 7(3-4):387–413, 1980. ISSN 03770273. doi: 10.1016/0377-0273(80)90040-2.

M. J. Woodhouse, A. J. Hogg, J. C. Phillips, and R. S. Sparks. Interaction between volcanic plumes and wind during the 2010 Eyjafjallajökull eruption, Iceland. *Journal of Geophysical Research: Solid Earth*, 118(1):92–109, 2013. ISSN 21699356. doi: 10.1029/2012JB009592.

A. Woods. The fluid dynamics and thermodynamics of eruption columns. *Bulletin of Volcanology*, 50:169–193, 1988.

World Bank. Ethiopia Geothermal Development Project, 2016. URL `http://www.worldbank.org/projects/P133613?lang=en`.

H. M. Wright, K. V. Cashman, M. Rosi, and R. Cioni. Breadcrust bombs as indicators of Vulcanian eruption dynamics at Guagua Pichincha volcano, Ecuador. *Bulletin of Volcanology*, 69(3):281–300, 2007. ISSN 02588900. doi: 10.1007/s00445-006-0073-6.

H. M. N. Wright and R. F. Weinberg. Strain localization in vesicular magma: Implications for rheology and fragmentation. *Geology*, 37(11):1023–1026, 2009. ISSN 00917613. doi: 10.1130/G30199A.1.

J. J. Wylie, K. R. Helfrich, B. Dade, J. R. Lister, and J. F. Salzig. Flow localization in fissure eruptions. *Bulletin of Volcanology*, 60(6):432–440, 1999. ISSN 02588900. doi: 10.1007/s004450050243.

B. Zimanowski, G. Fröhlich, and V. Lorenz. Quantitative experiments on phreatomagmatic explosions. *Journal of Volcanology and Geothermal Research*, 48(3-4):341–358, 1991. ISSN 03770273. doi: 10.1016/0377-0273(91)90050-A.

M. Zimova and S. L. Webb. The combined effects of chlorine and fluorine on the viscosity of aluminosilicate melts. *Geochimica et Cosmochimica Acta*, 71(6):1553–1562, 2007. ISSN 00167037. doi: 10.1016/j.gca.2006.12.002.

T. Zingg. *Beitrag zur Schotteranalyse*. PhD thesis, ETH Zurich, 1935.

G. Zuccaro, F. Cacace, R. J. Spence, and P. J. Baxter. Impact of explosive eruption scenarios at Vesuvius. *Journal of Volcanology and Geothermal Research*, 178(3):416–453, 2008. ISSN 03770273. doi: 10.1016/j.jvolgeores.2008.01.005. URL `http://dx.doi.org/10.1016/j.jvolgeores.2008.01.005`.

Appendix A

Corbetti: Hawassa North Shore

Corbetti is an actively deforming (Biggs et al., 2011; Lloyd et al., 2018) peralkaline rhyolite silicic caldera in the MER (Paola, 1971). It lies south along the rift from Aluto, around 7 km NW of Hawassa city between the lakes Hawassa and Shala. In many ways, Corbetti closely resembles Aluto, with post-caldera pumice cones and obsidian lava flows within the caldera region (Fontijn et al., 2018; Hunt et al., 2019). Volcanic vents at Corbetti occur across the whole caldera, but tend to be focused around two centres, Chabbi (the term for 'obsidian' in Oromo) and Urji (Paola, 1971). These edifices are thought to sit on an east-west structure which provides a permeable pathway for magma (Acocella et al., 2002; Lloyd et al., 2018). Volcanism at Corbetti also extends beyond the caldera and towards the northern shore of lake Hawassa. The lake edge is littered with features that resemble phreatomagmatic tuff cones and obsidian lavas. There is a sizeable exposure to volcanic hazard in this region (Figure A.1): Hawassa city, for example, is expanding NW towards Corbetti; with new residential areas and factories. A new airport is also under construction on the NW shore of lake Hawassa, with new roads and infrastructure built around the north of the lake connecting it to Hawassa city on the eastern shore. This infrastructure has been built close to multiple tuff cones, pyroclastic deposits and silicic lava flows. There is thus a clear impetus to understand the nature of extra-caldera, lake-edge volcanism associated with Corbetti volcano. Road cuts, wadis and lake-edge sections provide an insight into the range of processes that occur in this region. The following appendix aims to report on the volcanology of this area. However, these insights are based on only 3 days of field exploration around Hawassa's northern shore, and so significant uncertainties surround the

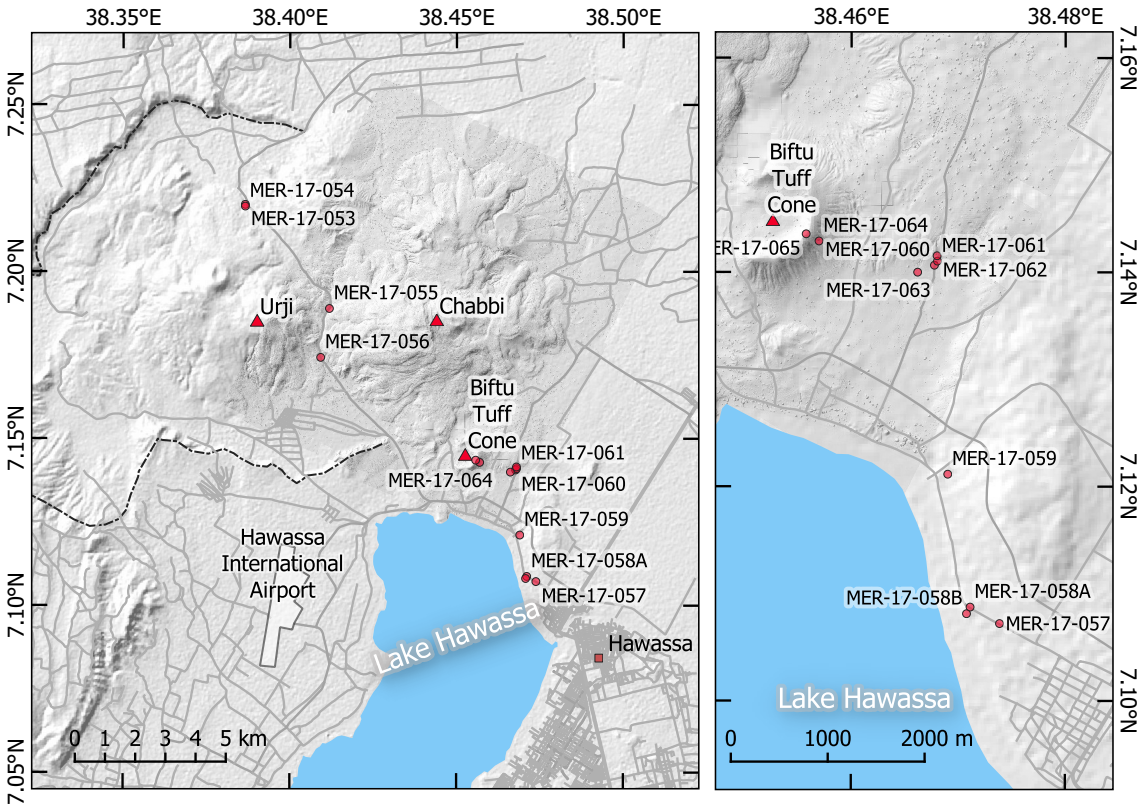

Figure A.1: *Map showing the context of the lake Hawassa northern shore localities, and their proximity to major infrastructure and Hawassa city.*

lateral correlation of eruption units and the attribution of each to particular vents, other than that they are sourced from the Corbetti volcanic system. There is still a substantial amount of work required to unpick the complex volcanic history of this region, which is why this investigation resides in the appendices of this thesis. However, the field work has provided some valuable insights into the hazards posed to this exposed region, and might form a starting point for future work in the area. The field localities and overview of Hawassa's north shore is shown in Figure A.1.

A.1 Volcanic features of the North Hawassa shore

The volcanic features of the northern shore of lake Hawassa have been initially identified using the DEM of Hunt et al. (2019). They comprise numerous silicic lava flows, remnants

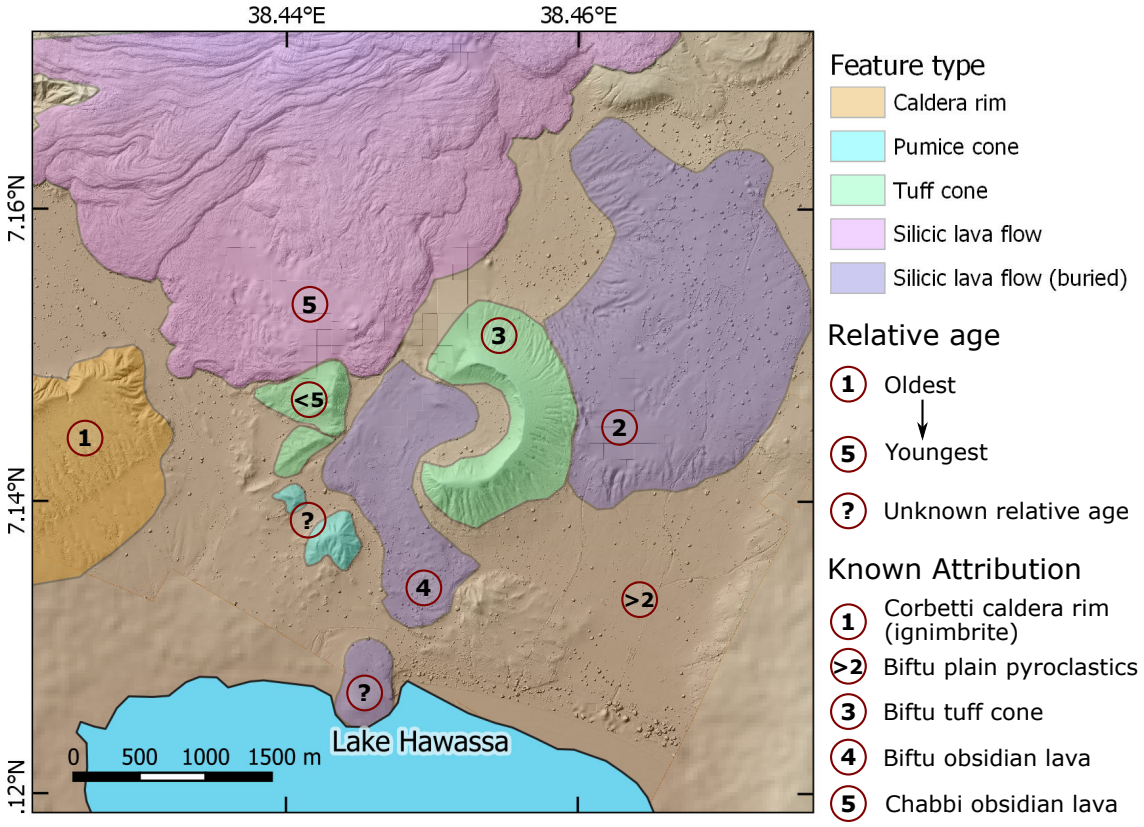

Figure A.2: *An overview of the different volcanic features of the northern shore of lake Hawassa, their relative ages and any known attributions. The DEM is sourced from Hunt et al. (2019). Relative ages are derived from geomorphological features such as the diversion of lava flows around structures, superposition, and the muting of lava flow topography by overlying pyroclastic deposits. The relative age relationships are consistent with those suggested by Rapprich et al. (2016)*

of tuff cones, pumice cones, and assorted pyroclastics and reworked pyroclastics that form much of the flat ground in the area. These features, with their relative ages derived from geomorphological relationships, field relations and existing literature, are presented in Figure A.2. In the following sections, I present the field observations and insights from Biftu tuff cone, and the pyroclastics forming the NE shore of lake Hawassa.

A.1.1 Biftu tuff cone

The Biftu tuff cone sits on the Northern shore of lake Hawassa, overlooking small settlements and visible from Hawassa city and Hawassa international airport (Figure A.1). The steep sided cone (22° exterior, 30° interior) rises 120 m above the surrounding plain,

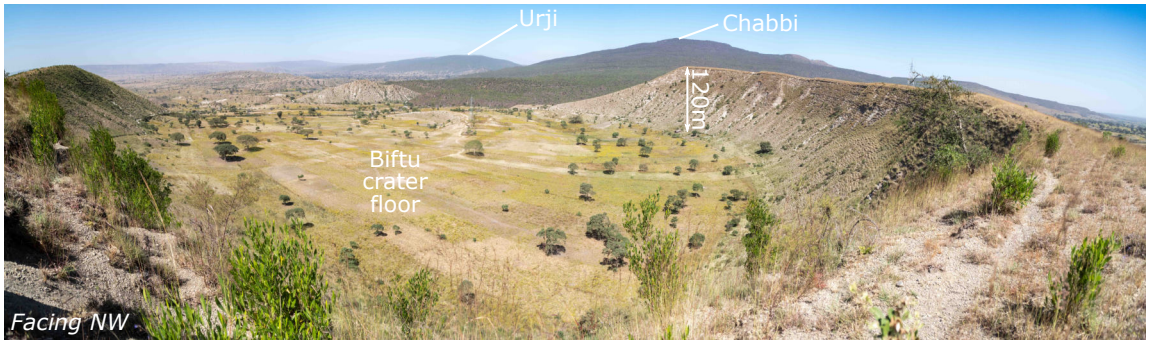

Figure A.3: *A panoramic view of Biftu tuff cone taken from the eastern crater rim. The main eruptive centres at Corbetti (Chabbi and Urji) are visible on the horizon. The youngest of Chabbi's obsidian lava flows can be seen flowing into the crater in the far NW of Biftu cone.*

measuring 950 m from rim-to-rim. A view of the Biftu crater is shown in Figure A.3. Emanating from the cone, flowing westwards before diverting south, is a lava flow that has been partially buried. Though exposures of the flow weren't found, considering the cone itself comprises silicic pumice, it seems reasonable to assume that this lava flow is also silicic. There is very little exposure of the cone itself, save for a few gully sections on the eastern outer flank. The deposits of this section (MER-17-64) are shown in Figure A.4.

The first deposit in this section (B1) is a poorly sorted, clast supported angular pumice and lithic breccia. The lithic population is highly heterogeneous, including porphyritic obsidian and a variety of altered volcanics. There is also a coarse ashy matrix. This description is equally appropriate for deposits B3 and B5 in the same section. The angularity and clast supported nature of these deposits is typical of a fall and the poor sorting is feasibly a result of ultraproximal deposition, consistent with the proximity of these deposits to their vent. Poor to very poor sorting (inman sorting 1 - 2 $\sigma\phi$), is very typical of cone deposits (Riedel et al., 2003; Sohn and Chough, 1993), and relates to the chaotic and mixed depositional mechanisms of ballistic and column-edge fall. Experimental work on the growth of tuff cones has also invoked 'ballistic curtains' (Graettinger et al., 2015), where discrete explosions produce a poorly sorted mixture of pyroclasts that deposit mostly close to the vent through a combination of fall and density-current processes. Moving distally, such deposits rapidly thin, and eventually grade into individual ballistics. Interbedded with these units is a series of particularly ash-rich, diffusely cross bedded units (B2, B4

and B6). These are matrix supported, with occasional lapilli sized clasts of rounded pumice and angular lithics, of a similar assortment to those seen in units B1, B3 and B5. Unit B2 has been sieved, the results of which can be found in Appendix C.2 under sample number MER-17-64B. In some places there are clear bomb sags, where laminations of ash form a concave depression. In some cases, the depression is occupied by a large ballistic, clearly the culprit of the sag. In other instances, there is no large clast present, indicating that the ballistic was subsequently removed by an over-riding current, and the depression filled with ash. These are the deposits of proximal dilute pyroclastic density currents, within the reach of ballistics. The fine ashy nature of these deposits indicate a high fragmentation efficiency. The units in this succession are relatively thinly interbedded, with a pulsatory change in deposit character on a scale of 10s of cm. This implies a highly unsteady eruptive process. There is also a lava flow that emanates from Biftu tuff cone towards the west and then south, indicating the eruption ended in a similar fashion to pumice cones at Aluto. The presence of abundant fine ash, dilute PDC deposits, pulsatory highly chaotic deposits, tuff-cone morphology and proximity to lake Hawassa point towards a phreatomagmatic origin. Stranded shore lines are visible in the LiDAR dataset, indicating that lake levels at Hawassa, as they are in the Ziway Shala lake basin (Benvenuti et al., 2002a) are currently decreasing. It is plausible that Biftu represents a phreatomagmatic monogentic rhyolitic eruption during a higher stand of lake Hawassa. Biftu may therefore represent what happens when a monogenetic rhyolitic 'pumice cone' eruption occurs in shallow water.

The age of the Biftu tuff cone is uncertain, but from geomorphological relationships is clearly older than the most recent Chabbi obsidian (named CO6 in Rapprich et al. (2016), labelled '1' in Figure A.2) and younger than the buried lava flow to its eastern flank (named COX in Rapprich et al. (2016), labelled '2' in Figure A.2). Rapprich et al. (2016) suggest that Biftu and the other monogenetic cones are slightly older or synchronous with the sub-plinian Wendo Koshe Younger Pumice (WKYP) eruption (from Urji) at 396 ± 38 BC, though there is still great uncertain surrounding the precise field relations.

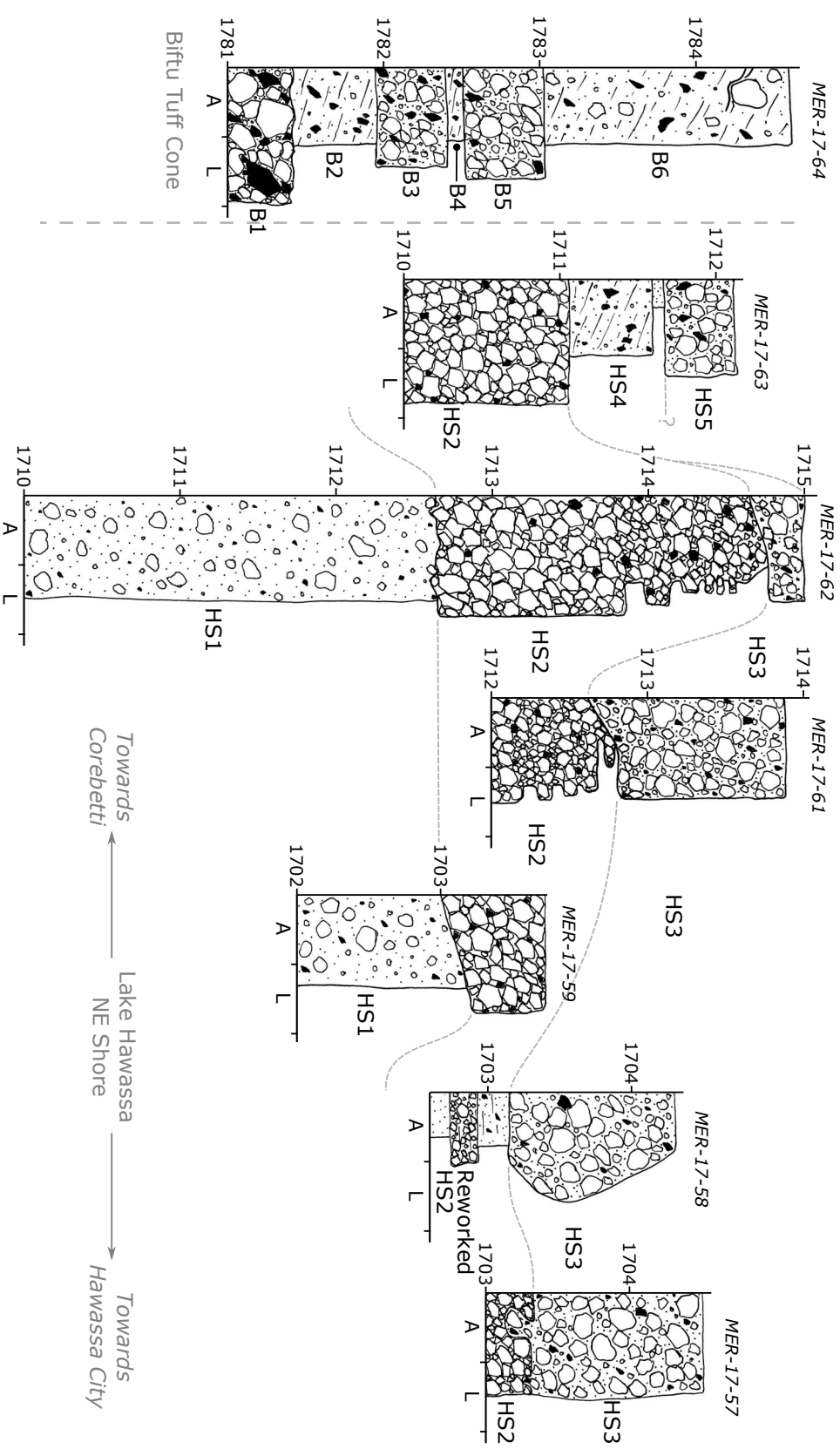

Figure A.4: *Fence diagram showing the stratigraphic relationships along the Hawassa North Shore region including Biftu tuff cone. The relationship between the Biftu deposits and the other pyroclastics is unknown.*

A.1.2 Hawassa shore pyroclastics

Pyroclastic Stratigraphy

To the east of Biftu tuff cone lies a flat plain incised by road-cuts and wadis. In current geological maps of this area, the plain is simply described as comprising 'polygenetic sediments' (Rapprich et al., 2016), 'lacustrine deposits' (Paola, 1971) or 'alluvial deposits' (Fusillo, 2018). Though superficially true, it ignores the presence of multiple, primary pyroclastic units underneath the thin veneer of reworked material, that are traceable on a km scale. The stratigrpahy of the area is shown in Figure A.4. The oldest exposed unit is HS1, a distinct fine ash matrix-rich massive lapilli tuff with coarse lapilli sized pumices and small dense obsidian fragments. It can be best seen at MER-17-62, and is at least 2.5 m thick (base not exposed), but it can be seen as far away as MER-17-59, 2.2 km SE towards Hawassa with a 1 m minimum thickness. HS1 has been sieved, the results of which can be found in Appendix C.2 under sample number MER-17-62A. On top of this, without an intermediate palaeosol, is HS2, an angular pumice lapilli fall deposit with small angular fragments of obsidian. At MER-17-62, the unit is 2 m thick. Its lower section is massive, but at around half way up becomes highly pulsatory between coarse and fine lapilli grade material on a 5-10 cm scale. There is a general decrease in the pumice size towards the top of the unit. The lack of reworking in this unit suggests that it was deposited sub-aerially. HS2 can be found at every field site we investigated in the NE shore of lake Hawassa. In most of these locations, the unit is capped by HS3, a matrix to near-clast supported massive lapilli tuff, with small fragments of porphyritic obsidian. HS3 has been sieved, the results of which can be found in Appendix C.2 under sample number MER-17-61D. The unit can be traced around 4 km SSE along the lake shore from MER-17-62, where it forms a small cliff at the edge of the lake. At MER-17-63, just west of the other localities and closer to Biftu tuff cone, HS4, a fine grained, diffusely cross bedded tuff with angular obsidians and small rounded pumices sits on top of the HS2 fall unit. Above this is a thin massive ash fall, perhaps a co-ignimbrite ash associated with the underlying ignimbrite. Finally, the stratigraphically highest unit we investigated is HS5, a reworked pumice and ash rich eruption unit which appears largely soilified.

Volcanological Interpretation

The HS1 mLT was deposited from a pyroclastic density current. The lack of large blocks of lava and almost exclusive presence of juvenile material suggests that the PDC may have been sourced from a column-collapse event. There is no palaeosol between HS1 and HS2, indicating there was not an extended period of repose. This, and the lack of reworking at the top of HS1, implies they may have been the product of the same eruption. Eruption unit HS2 represents a stable column-forming eruption, generating a steady, massive tephra fall unit. As the eruption progressed it became less steady, generating the bedded fall at the top of the unit. The decrease in grain size, if not caused by a change in wind direction, might relate to a weakening, shortening eruption column, consistent with the increased unsteadiness. The presence of ignimbrite HS3 above this suggests that the eruption column collapsed, producing a relatively mobile PDC that blanketed the area.

A.1.3 Source of the Biftu and Hawassa north shore pyroclastics

As the Biftu deposits form the edifice of the tuff cone itself, they are clearly associated with the Biftu vent. Their phreatomagmatic origin implies they were erupted during a relatively high stand of lake Hawassa, where waters reached at least 1725 masl.

However, the attribution of the deposits exposed on the NE shore and plain is unclear. Considering they include PDC deposits, they are relatively proximal to their source, indicating that they were generated somewhere in the Corbetti complex, probably south of (and including) the topographic barriers of Chabbi and Urji. The deposits appear to be deposited onto dry land, with no noticeable reworking down to an altitude of around 1703 masl. This indicates that they were deposited at a low stand of lake Hawassa, meaning they cannot have been sourced from the phreatomagmatic Biftu tuff cone eruption. Neither are they from the WKYP eruption, as the HS2 pumice fall deposits contain obsidian lithics, which are almost absent from the WKYP eruptive deposits (Fontijn et al., 2018). Eruption unit HS4 is a dilute PDC deposit close to Biftu, which strongly resembles those on the flanks of Biftu tuff cone itself. If HS4 is sourced from Biftu, its superposition on

HS2 indicates that the HS1 to HS3 deposits pre-date the Biftu tuff cone eruption. There are many potential sources for these deposits, though their precise attribution remains unclear, and requires additional field investigation.

A.2 Volcanic hazards from volcanism on Hawassa's Northern shore

The deposits on the northern shore of lake Hawassa indicate the region has been the site of numerous volcanic eruptions in the past. On at least two occasions the region has been blanketed by PDCs from post-caldera eruptions from the Corbetti complex. Deposits of these PDCs reach the edge of the outskirts (as of 2017) of Hawassa, but with already increasing development over this area it seems inevitable that Hawassa will expand over this region which is clearly susceptible to PDC inundation from Corbetti. Biftu tuff cone indicates that phreatomagmatic activity may also be of concern on the northern shore of lake Hawassa, though the lake edge is further away from Corbetti than it was during the Biftu eruption, eruptions have clearly occurred in the same location as the present day lake edge (Figure A.2). Such eruptions are likely to be highly explosive, generating dilute (and therefore mobile) PDCs, and finally obsidian lava flows, that may endanger population and infrastructure in the region.

Volcanism in this particular region deserves greater attention, as it contains some of the most valuable infrastructure close to Corbetti. In particular, finding the source of the eruption that produced HS1 to HS3 would be of benefit. Improving the chronostratigraphic framework of the region may also help to contextualise these deposits, and determine how frequent such events might be. Much of this will require additional field work. Though samples exist, geochemical correlation and distinction of deposits at Corbetti has not been particularly fruitful, as glasses from different eruptions are often geochemically indistinguishable (Fontijn et al., 2018; McNamara et al., 2018). However, there is good exposure around the NE shore, with small scale quarrying activities and road cuts providing valuable opportunities to trace deposits laterally. This work shows that PDCs, not just tephra fall,

threaten Hawassa city.

Appendix B

Catalogues

B.1 Localities

Locality	Volcano	Sub-area	Lat	Long	Type	Photos	Samples
MER-15-047	Aluto	Central	7.7728	38.8087	Description		
MER-15-048	Aluto	Humo gorge	7.7942	38.7652	Description, Log, Sample	0813 - 0817	15-048 A,B,C,D,E
MER-15-049	Aluto	Humo gorge	7.7938	38.7643	Description, Log, Sample	0818 - 0820	15-094 A,B,C,D,E,F
MER-15-050	Aluto	Humo gorge	7.7917	38.7623	Description	0821	
MER-15-051	Aluto	Humo gorge	7.7909	38.7626	Description, Sample	0822 - 0827	15-051 A,B
MER-15-054	Aluto	Gabiben	7.8053	38.7675	Description, Sample		15-054 A
MER-15-055	Aluto	Gabiben	7.8081	38.7669	Description, Sample		15-055 A,B
MER-15-056	Aluto	Gabiben	7.8091	38.7671	Description, Log	0830 - 0846	
MER-15-057	Aluto	Central	7.8134	38.7719	Description		
MER-15-058	Aluto	Central	7.8138	38.7750	Description		
MER-15-059	Aluto	Central	7.8201	38.7805	Description, Log	0848	
MER-15-060	Aluto	Awariftu	7.8183	38.8027	ELIZA CALDER		
MER-15-061	Aluto	Awariftu	7.8177	38.8033	ELIZA CALDER		
MER-15-062	Aluto	Awariftu	7.8177	38.8059	ELIZA CALDER		
MER-15-063	Aluto	Awariftu	7.8175	38.8075	ELIZA CALDER		
MER-15-064	Aluto	Awariftu	7.8160	38.8063	ELIZA CALDER		
MER-15-065	Aluto	Awariftu	7.8128	38.8048	ELIZA CALDER		
MER-17-001	Aluto	Central	7.7970	38.7912	Description, Sample	5409 - 5421	17-001 A,B
MER-17-002	Aluto	Central	7.7982	38.7928	Description, Sample	5424 - 5431	17-002 A
MER-17-003	Aluto	Central	7.8044	38.7664	Description, Sample	5443	17-003 A
MER-17-004	Aluto	Gabiben	7.8093	38.7669	Description		
MER-17-005	Aluto	Gabiben	7.8099	38.7672	Description, Sample	5460 - 5463	17-005 A
MER-17-006	Aluto	Gabiben	7.8053	38.7674	Description, Log	5467 - 5478	
MER-17-007	Aluto	Kertefa	7.8219	38.7495	Description, Sample	5479 - 5488	17-007 A
MER-17-008	Aluto	Humo gorge	7.7994	38.7700	Description	5487	
MER-17-009	Aluto	Humo gorge	7.7976	38.7681	Description, Log		
MER-17-010	Aluto	Humo gorge	7.7961	38.7663	Description		
MER-17-011	Aluto	Humo gorge	7.7937	38.7646	Description		
MER-17-012	Aluto	Humo gorge	7.7910	38.7626	Description, Log	5488 - 5491	
MER-17-013	Aluto	Humo gorge	7.7907	38.7626	Description, Log	5492 - 5494	

Locality	Volcano	Sub-area	Lat	Long	Type	Photos	Samples
MER-17-014	Aluto	Quarry	7.7933	38.7956	Description, Log	5495 - 5500	
MER-17-015	Aluto	Quarry	7.7936	38.7959	Description, Sample		17-015 A
MER-17-016	Aluto	Chefe Jila	7.8601	38.7640	Description, Log, Sample	5523 - 5526	17-016 A,B
MER-17-017	Aluto	Far east road	7.7452	38.8005	Description, Log	5528 - 5529	
MER-17-018	Aluto	Far east road	7.7518	38.8076	Description	5530 - 5534	
MER-17-019	Aluto	Quarry	7.7937	38.7964	Description, Sample	5542 - 5544	17-019 A
MER-17-020	Aluto	Quarry	7.7941	38.7957	Description, Sample	5545 - 5546	17-020 A
MER-17-021A	Aluto	Kertefa Wadi	7.8187	38.7511	Description, Log	5648 - 5650	
MER-17-021B	Aluto	Kertefa Wadi	7.8186	38.7513	Description, Log	5678 -5679	17-021 A,B
MER-17-021C	Aluto	Kertefa Wadi	7.8172	38.7518	Description, Log	5652 - 5657	
MER-17-022	Aluto	Central	7.7999	38.7968	Description		
MER-17-023	Aluto	Kalosanga	7.7413	38.7888	Description, Log, Sample	5685 - 5689	17-023 A
MER-17-024	Aluto	Kalosanga	7.7404	38.7893	Description, Log, Sample	5690 - 5693	17-024 A
MER-17-025	Aluto	Kalosanga	7.7400	38.7896	Description, Log	5694 - 5696	
MER-17-026	Aluto	Kalosanga	7.7390	38.7898	Description	5698 - 5703	
MER-17-027	Aluto	Kalosanga	7.7377	38.7895	Description	5704	
MER-17-028	Aluto	Kalosanga	7.7350	38.7896	Description	5705 - 5706	
MER-17-029	Aluto	Jidduu	7.7347	38.7827	Description, Log, Sample	5715 - 5716	17-29 A,B,C,D
MER-17-030	Aluto	Chopa	7.7369	38.7820	Description, Log	5717 - 5718	
MER-17-031	Aluto	Chopa	7.7385	38.7806	Description, Log, Sample	5719 - 5726	17-31 A,B
MER-17-032	Aluto	Chopa	7.7415	38.7819	Description, Sample	5727 - 5728	17-32 A
MER-17-033	Aluto	Awariftu	7.8068	38.7989	Description, Log, Sample	5752 - 5763	17-33 A,B
MER-17-034	Aluto	Awariftu	7.8071	38.8004	Description, Log, Sample	5764 - 5768	17-34 A
MER-17-035	Aluto	Awariftu	7.8093	38.8013	Description, Log, Sample	5776 - 5778	17-35 A
MER-17-036	Aluto	Awariftu	7.8110	38.8033	Description, Log		17-36 A
MER-17-037	Aluto	Awariftu	7.8090	38.8008	Sample		17-37 A
MER-17-038	Aluto	Humo gorge	7.7994	38.7714	Description	5805 - 5808	
MER-17-039	Aluto	Humo gorge	7.7997	38.7705	Description, Log	5809 - 5813	
MER-17-040A	Aluto	Humo gorge	7.7956	38.7658	Description	5814 - 5815	
MER-17-040B	Aluto	Humo gorge	7.7987	38.7684	Description	5820 - 5830	

Locality	Volcano	Sub-area	Lat	Long	Type	Photos	Samples
MER-17-041	Aluto	Humo gorge	7.7983	38.7684	Description, Log	5831 - 5832	
MER-17-042	Aluto	Humo gorge	7.7976	38.7681	Description, Log		
MER-17-043	Aluto	Humo gorge	7.7941	38.7681	Description, Log, Sample	5838	17-43 A
MER-17-044	Aluto	Humo gorge	7.7977	38.7733	Description, Log, Sample	5840	17-44 A
MER-17-045	Aluto	Humo gorge	7.7960	38.7729	Description, Log, Sample		17-45 A
MER-17-046	Aluto	Humo gorge	7.7936	38.7706	Description, Log	5843	
MER-17-047	Aluto	Humo gorge	7.7914	38.7693	Description, Log, Sample	5844	17-47 A
MER-17-048	Aluto	Humo gorge	7.7929	38.7714	Description	5849	
MER-17-049	Aluto	Humo gorge	7.8000	38.7715	Sample		17-49 A
MER-17-050	Corbetti	Sheshamene	7.2251	38.5545	Description, Sample	5861	17-50 A
MER-17-051	Corbetti	Sheshamene	7.2888	38.4201	Description		
MER-17-052	Corbetti	Sheshamene	7.2910	38.3866	Description, Log		
MER-17-053	Corbetti	Central	7.2201	38.3866	Description	5867	
MER-17-054	Corbetti	Central	7.2196	38.3866	Description, Log	5871	
MER-17-055	Corbetti	Central	7.1890	38.4119	Description, Log	5886	
MER-17-056	Corbetti	Central	7.1743	38.4093	Description, Log	5887 - 5888	
MER-17-057	Corbetti	Lake Hawassa	7.1072	38.4739	Description, Log, Sample	5910 - 5913	17-57 A
MER-17-058A	Corbetti	Lake Hawassa	7.1088	38.4711	Description, Log, Sample	5914 - 5915	17-58 A
MER-17-058B	Corbetti	Lake Hawassa	7.1081	38.4708	Description	5924 - 5925	
MER-17-059	Corbetti	Lake Hawassa	7.1212	38.4690	Description, Log	5929	
MER-17-060	Corbetti	Lake Hawassa	7.1407	38.4678	Description, Log	9530	
MER-17-061	Corbetti	Biftu	7.1410	38.4680	Description, Log, Sample	5931 - 5935	17-61 A,B,C,D
MER-17-062	Corbetti	Biftu	7.1415	38.4680	Description, Log, Sample	5937	17-62 A,B
MER-17-063	Corbetti	Biftu	7.1400	38.4662	Description, Log		
MER-17-064	Corbetti	Biftu	7.1429	38.4570	Description, Log, Sample	5941 - 5943	17-64 A,B
MER-17-065	Corbetti	Biftu	7.1436	38.4558	Description	5945 - 5951	
MER-17-066	Aluto	Kertefa	7.8273	38.7480	Description, Log, Sample	5962 - 5965	17-66 A,B
MER-17-067	Aluto	Kertefa	7.8268	38.7480	Description, Log, Sample	5967	17-67 A,B
MER-17-068	Aluto	Kertefa	7.8252	38.7490	Description, Log, Sample	5968 - 5983	17-68
MER-17-069A	Aluto	Awariftu	7.8110	38.8035	Description, Log, Sample	6033 - 6039	17-68 A,B,C,D

Locality	Volcano	Sub-area	Lat	Long	Type	Photos	Samples
MER-17-069B	Aluto	Awariftu	7.8142	38.8047	Description		
MER-17-070	Aluto	Awariftu	7.8142	38.8054	Description, Log, Sample	6041	17-70 A
MER-17-071	Aluto	Awariftu	7.8144	38.8042	Description, Log	6047 - 6048	
MER-17-072	Aluto	Awariftu	7.8154	38.8038	Description, Log	6049	
MER-17-073	Aluto	Awariftu	7.8176	38.8034	Description, Log		
MER-17-074	Aluto	Jidduu	7.7327	38.7846	Description, Log	6309	
MER-17-075A	Aluto	Jidduu	7.7337	38.7845	Description, Log	6310	
MER-17-075B	Aluto	Jidduu	7.7350	38.7841	Description	6311 - 6312	
MER-17-076A	Aluto	Chopa	7.7391	38.7821	Description, Log	6314 - 6318	
MER-17-076B	Aluto	Chopa	7.7396	38.7825	Description, Log	6319 - 6320	
MER-17-076C	Aluto	Chopa	7.7396	38.7827	Description		
MER-17-077	Aluto	Chopa	7.7404	38.7826	Description, Log	6321 - 6342	
MER-17-078	Aluto	Chopa	7.7375	38.7817	Description, Log	6344	
MER-17-079	Aluto	Chopa	7.7358	38.7820	Description	6345	
MER-17-080	Aluto	Chopa	7.7330	38.7736	Description, Log, Sample	6346 - 6347	17-80 A
MER-17-081	Aluto	Gemedo	7.7350	38.7737	Description, Log	6349 - 6355	
MER-17-082	Aluto	Gemedo	7.7356	38.7734	Description, Log	6357	
MER-17-083	Aluto	Gemedo	7.7362	38.7734	Description, Log		
MER-17-084	Aluto	Gemedo	7.7359	38.7733	Description	6360	
MER-17-085	Aluto	Kertefa	7.8254	38.7487	Description, Log	6367 - 6368	
MER-17-086	Aluto	Kertefa	7.8252	38.7485	Description, Log	6369 - 6387	
MER-17-087	Aluto	Kertefa	7.8251	38.7492	Description, Log	6404 - 6397	

Table B.1: *The localities investigated throughout the fieldwork in Ethiopia and the data associated with each. Photos are available from Ben Clarke on request. Samples are all prefixed with 'MER-'. For details on samples, see Appendix B.2.*

B.2 Samples

Sample	Volcano	Sub-area	Lat	Long	Stratigraphic Unit	Description
MER-17-001A	Aluto	Central	7.7970	38.7912	Pumice cone mPbr	Bulk mPbr (missing >64mm)
MER-17-001B	Aluto	Central	7.7970	38.7912	Pumice cone mPbr	Large DQA
MER-17-002A	Aluto	Gabiben	7.7982	38.7928	Phase 3 lava flow	Obsidian dense
MER-17-003A	Aluto	Gabiben	7.8044	38.7664	Phase 3 lava flow	Obsidian dense
MER-17-005A	Aluto	Gabiben	7.8100	38.7673	Phase 2 crater	Bulk, crater top
MER-17-007A	Aluto	Kertefa	7.8219	38.7495	K2	Obsidian, various
MER-17-015A	Aluto	Quarry	7.7936	38.7959	Pumice cone mPbr	Pumice and pumiceous achneliths
MER-17-016A	Aluto	Chefe Jila	7.8601	38.7640	n/a	Flow deposit, phreatomagmatic?
MER-17-016B	Aluto	Chefe Jila	7.8601	38.7640	n/a	Flow deposit, phreatomagmatic?
MER-17-019A	Aluto	Quarry	7.7937	38.7964	Pumice cone rsPbr	Bulk rsPbr (small volume)
MER-17-020A	Aluto	Quarry	7.7941	38.7957	Pumice cone rsPbr	Pumice & pumiceous achneliths
MER-17-021A	Aluto	Kertefa Wadi	7.8187	38.7511	SK8	Bulk ignimbrite
MER-17-021B	Aluto	Kertefa Wadi	7.8187	38.7511	SK9	Ignimbrite (juvenile material)
MER-17-021C	Aluto	Kertefa Wadi	7.8187	38.7511	SK7	Bulk
MER-17-021D	Aluto	Kertefa Wadi	7.8187	38.7511	SK7	Bulk
MER-17-023A	Aluto	Kalosanga	7.7413	38.7888	K1	Bulk ignimbrite
MER-17-024A	Aluto	Kalosanga	7.7404	38.7893	K2	Ignimbrite pumices
MER-17-029A	Aluto	Jidduu	7.7347	38.7827	J10	Pumices
MER-17-029B	Aluto	Jidduu	7.7347	38.7827	J10	Mixed pumices
MER-17-031A	Aluto	Chopa	7.7385	38.7806	C1	Ignimbrite pumices
MER-17-031B	Aluto	Chopa	7.7385	38.7806	C3	Ignimbrite pumices
MER-17-032A	Aluto	Chopa	7.7415	38.7819	C1	Ignimbrite pumices & obsidian
MER-17-033A	Aluto	Awariftu	7.8068	38.7989	A15	Pumice & pumiceous achneliths
MER-17-033B	Aluto	Awariftu	7.8068	38.7989	A20	mPbr pumices
MER-17-034A	Aluto	Awariftu	7.8071	38.8004	A13	Bulk PDC (partially sieved)
MER-17-035A	Aluto	Awariftu	7.8093	38.8013	A15	Bulk mPbr (partially sieved)
MER-17-036A	Aluto	Awariftu	7.8110	38.8033	A7	Bulk ignimbrite (partially sieved)
MER-17-037A	Aluto	Awariftu	7.8090	38.8008	Awariftu lava	Obsidian dense
MER-17-43A	Aluto	Humo gorge	7.7941	38.7681	H24	Bulk ignimbrite
MER-17-44A	Aluto	Humo gorge	7.7977	38.7733	H2	Bulk mPbr

Sample	Volcano	Sub-area	Lat	Long	Stratigraphic Unit	Description
MER-17-45A	Aluto	Humo gorge	7.7960	38.7729	H6	rsPbr pumices
MER-17-47A	Aluto	Humo gorge	7.7914	38.7693	H6	Bulk rsPbr
MER-17-49A	Aluto	Humo gorge	7.8000	38.7715	H8	Bulk ignimbrite
MER-17-50A	Corbetti	Shashamane	7.2251	38.5545	n/a	Bulk ignimbrite & accretionary lapilli
MER-17-57A	Corbetti	Lake Hawassa	7.1072	38.4739	HS3	Bulk ignimbrite
MER-17-58A	Corbetti	Lake Hawassa	7.1088	38.4711	HS3	Ignimbrite pumices & lithics
MER-17-061A	Corbetti	Biftu	7.1410	38.4680	HS2	Fall pumices & lithics
MER-17-061B	Corbetti	Biftu	7.1410	38.4680	HS2	Fall pumices & lithics
MER-17-061C	Corbetti	Biftu	7.1410	38.4680	HS2	Fall pumices & lithics
MER-17-061D	Corbetti	Biftu	7.1410	38.4680	HS2	Fall pumices & lithics
MER-17-062A	Corbetti	Biftu	7.1415	38.4680	HS1	Bulk ignimbrite
MER-17-062B	Corbetti	Biftu	7.1415	38.4680	HS1	Ignimbrite pumices & lithics
MER-17-064A	Corbetti	Biftu	7.1429	38.4570	B1	Ignimbrite pumices & lithics
MER-17-064B	Corbetti	Biftu	7.1429	38.4570	B2	Bulk ignimbrite
MER-17-066A	Aluto	Kertefa	7.8273	38.7480	K5 (lower fall)	Fall pumices & lithics
MER-17-066B	Aluto	Kertefa	7.8273	38.7480	K5 (upper PDC)	Bulk ignimbrite
MER-17-067A	Aluto	Kertefa	7.8271	38.7480	K11	Bulk ignimbrite
MER-17-067B	Aluto	Kertefa	7.8271	38.7480	K11 (indurated)	Indurated ignimbrite
MER-17-068A	Aluto	Kertefa	7.8252	38.7490	K4	Fall pumices
MER-17-069A	Aluto	Awariftu	7.8110	38.8035	A10	Bulk ignimbrite
MER-17-069B	Aluto	Awariftu	7.8110	38.8035	A7	Bulk ignimbrite
MER-17-069C	Aluto	Awariftu	7.8110	38.8035	A3	Bulk fall (small volume)
MER-17-069D	Aluto	Awariftu	7.8110	38.8035	A2	Bulk ignimbrite
MER-17-070A	Aluto	Awariftu	7.8142	38.8054	A2	Ignimbrite pumiceous achneliths
MER-17-080A	Aluto	Chopa	7.7330	38.7736	C1	Ignimbrite pumices & lithics
MER-15-048A	Aluto	Humo gorge	7.7942	36.7652	H12	Ignimbrite breadcrusted pumice
MER-15-048B	Aluto	Humo gorge	7.7942	36.7652	H12	Ignimbrite obsidian vesicular
MER-15-048C	Aluto	Humo gorge	7.7942	36.7652	H12	Ignimbrite obsidian dense
MER-15-048D	Aluto	Humo gorge	7.7942	36.7652	H12	Ignimrbite matrix
MER-15-048E	Aluto	Humo gorge	7.7942	36.7652	H12	Ignimrbite breadcrust bomb

Sample	Volcano	Sub-area	Lat	Long	Stratigraphic Unit	Description
MER-15-049A	Aluto	Humo gorge	7.7938	38.7643	H13	Ignimbrite matrix
MER-15-049B	Aluto	Humo gorge	7.7938	38.7643	H13	Ignimbrite obsidian vesicular
MER-15-049C	Aluto	Humo gorge	7.7938	38.7643	H13	Ignimbrite pumices
MER-15-049D	Aluto	Humo gorge	7.7938	38.7643	H13	Ignimbrite denser pumices
MER-15-049E	Aluto	Humo gorge	7.7938	38.7643	H15	Ignimbrite matrix
MER-15-049F	Aluto	Humo gorge	7.7938	38.7643	H15	Ignimbrite pumices
MER-15-051A	Aluto	Humo gorge	7.7909	38.7626	H18	Ignimbrite pumices
MER-15-051B	Aluto	Humo gorge	7.7909	38.7626	H19	mPbr pumices
MER-15-054A	Aluto	Gabiben	7.8053	38.7675	n/a	Obsidian breadcrust bomb interior
MER-15-054B	Aluto	Gabiben	7.8053	38.7675	n/a	Obsidian bomb chunk
MER-15-055A	Aluto	Gabiben	7.8081	38.7669	Phase 3 lava flow	Xstal rich obsidian
MER-15-055B	Aluto	Gabiben	7.8081	38.7669	n/a	Obsidian bomb w. tuffisite
MER60-1	Aluto	Awariftu	7.8183	38.8027	Eliza calder	Bulk ignimbrite
MER60-2	Aluto	Awariftu	7.8183	38.8027	Eliza calder	Ignimbrite pumices
MER60-3	Aluto	Awariftu	7.8183	38.8027	Eliza calder	Bulk
MER60-4	Aluto	Awariftu	7.8183	38.8027	Eliza calder	Bulk ignimbrite (partially sieved)
MER60-5	Aluto	Awariftu	7.8183	38.8027	Eliza calder	Ignimbrite pumices
MER60-6	Aluto	Awariftu	7.8183	38.8027	Eliza calder	?
MER61-8	Aluto	Awariftu	7.8177	38.8033	Eliza calder	Bulk ignimbrite
MER61-9	Aluto	Awariftu	7.8177	38.8033	Eliza calder	Ignimbrite matrix
MER61-10	Aluto	Awariftu	7.8177	38.8033	Eliza calder	Bulk ignimbrite (xST)
MER61-11	Aluto	Awariftu	7.8177	38.8033	Eliza calder	?
MER61-12	Aluto	Awariftu	7.8177	38.8033	Eliza calder	?
MER62-13	Aluto	Awariftu	7.8177	38.8059	Eliza calder	mPbr woody pumice
MER62-14	Aluto	Awariftu	7.8177	38.8059	Eliza calder	mPbr pumiceous achneliths
MER62-15	Aluto	Awariftu	7.8177	38.8059	Eliza calder	mPbr pumiceous achneliths
MER62-16	Aluto	Awariftu	7.8177	38.8059	Eliza calder	Bulk mPbr
MER62-17	Aluto	Awariftu	7.8177	38.8059	Eliza calder	Obsidian elongated vesicles
MER62-18	Aluto	Awariftu	7.8177	38.8059	Eliza calder	Obsidian bomb
MER64-19	Aluto	Awariftu	7.8160	38.8063	Eliza calder	Bulk ignimbrite

Sample	Volcano	Sub-area	Lat	Long	Stratigraphic Unit	Description
MER64-20	Aluto	Awariftu	7.8160	38.8063	Eliza calder	?
MER64-21	Aluto	Awariftu	7.8160	38.8063	Eliza calder	Bulk ignimbrite
MER64-22	Aluto	Awariftu	7.8160	38.8063	Eliza calder	Bulk PDC
MER65-23	Aluto	Awariftu	7.8128	38.8048	Eliza calder	Bulk mPbr w. pumicous achneliths
MER65-24	Aluto	Awariftu	7.8128	38.8048	Eliza calder	mPbr lapilli

Table B.2: *Table detailing the samples collected fromt eh two field seasons in the Main Ethiopian Rift. mPbr = massive pumice breccia, rsPbr = repose slope pumice breccia, xST = cross stratified tuff. Where stratigraphy is listed as 'Eliza Calder', the field data resides in her notebooks, due to my absence at these localities, I have chosen not to attempt to integrate her stratigraphy with mine.*

Appendix C

Data

Data sets used in this thesis are provided in the electronic appendices. Where the data format permits, data are also provided in print format in the following sections. Due to the volume of images, scanning electron microscope (SEM) (backscatter and secondary-electron) data are provided in digital format only. 3D models of pumiceous achneliths, built using XCT data are provided online via Figshare at this address: `https://figshare.com/s/310bc3f3ae076b17fc82`, and an annotated 3D model of an flight quenched pumiceous achnelith can be found at: `https://skfb.ly/6JVzI`.

C.1 Geochemical Data

Clast	Type	SiO_2	TiO_2	Al_2O_3	$FeO_{(t)}$	MnO	MgO	CaO	Na_2O	K_2O	P_2O_5	SO_2	F	Cl	Total
L	tP	73.98	0.24	8.83	5.50	0.25	-	0.26	6.01	4.29	-	0.02	0.44	0.20	98.89
L	tP	73.91	0.24	8.80	5.48	0.24	-	0.21	6.02	4.46	0.01	0.02	0.43	0.20	98.51
L	tP	73.57	0.24	9.16	5.51	0.24	-	0.22	6.04	4.38	0.01	0.01	0.48	0.19	98.41
L	tP	74.03	0.24	9.14	5.46	0.25	0.04	0.18	5.63	4.31	0.01	0.01	0.48	0.20	97.57
L	tP	73.83	0.24	9.06	5.51	0.25	0.04	0.29	5.99	4.12	-	0.01	0.46	0.20	97.72
L	tP	73.87	0.24	9.01	5.45	0.25	0.02	0.17	6.04	4.31	-	0.01	0.43	0.19	99.53
Q	mvP	73.58	0.24	9.13	5.49	0.25	-	0.15	6.21	4.40	-	0.01	0.35	0.19	99.98
Q	mvP	73.92	0.24	8.71	5.50	0.26	-	0.21	6.29	4.32	0.01	0.01	0.36	0.20	99.21
Q	mvP	73.89	0.24	9.18	5.48	0.25	-	0.20	5.92	4.27	-	0.01	0.36	0.19	99.46
Q	mvP	73.53	0.24	9.32	5.46	0.25	0.02	0.24	5.93	4.47	-	0.01	0.33	0.20	98.84
Q	mvP	73.89	0.25	8.83	5.56	0.26	0.02	0.29	5.97	4.38	-	0.02	0.35	0.19	98.84
Q	mvP	73.84	0.23	8.45	5.55	0.25	0.01	0.24	6.30	4.56	0.01	0.01	0.38	0.19	98.39
Q	mvP	71.53	0.15	11.49	4.52	0.17	0.01	0.09	6.79	4.90	-	-	0.24	0.12	99.79
Q	mvP	73.55	0.25	9.04	5.47	0.24	0.03	0.23	6.38	4.24	0.01	0.01	0.35	0.19	99.57
Q	mvP	74.00	0.24	8.76	5.61	0.25	0.02	0.21	6.00	4.28	0.01	0.02	0.39	0.20	98.05
Q	mvP	73.72	0.23	9.05	5.49	0.25	0.04	0.20	6.14	4.34	-	-	0.35	0.20	99.46
Q	mvP	73.74	0.24	8.96	5.50	0.25	0.01	0.25	6.10	4.44	0.02	0.01	0.32	0.19	99.72
O	OBB	74.22	0.24	8.74	5.56	0.26	0.04	0.20	5.92	4.28	0.01	0.01	0.33	0.20	100.28
O	OBB	73.67	0.24	8.90	5.55	0.25	-	0.23	6.19	4.40	0.01	0.00	0.37	0.20	99.86
O	OBB	73.59	0.23	9.31	5.57	0.25	-	0.24	6.00	4.25	0.01	0.01	0.36	0.20	100.43
O	OBB	74.09	0.25	8.86	5.64	0.25	-	0.17	5.89	4.27	0.01	0.01	0.35	0.20	99.29
O	OBB	73.62	0.24	9.06	5.58	0.24	-	0.24	6.07	4.39	-	0.02	0.35	0.20	99.94
O	OBB	73.77	0.25	8.96	5.65	0.25	-	0.21	5.90	4.47	0.01	0.01	0.33	0.20	100.16
O	OBB	73.86	0.23	8.79	5.59	0.26	0.04	0.20	6.03	4.44	0.00	0.01	0.36	0.20	99.70
O	OBB	73.55	0.25	9.22	5.57	0.26	0.02	0.19	6.10	4.27	0.01	0.01	0.37	0.19	100.25
O	OBB	73.87	0.24	8.80	5.57	0.24	-	0.24	6.08	4.37	0.01	0.01	0.37	0.20	99.88
O	OBB	73.84	0.24	9.25	5.53	0.25	-	0.21	6.01	4.09	0.01	-	0.37	0.20	100.61
O	OBB	73.70	0.24	9.32	5.59	0.25	0.02	0.20	5.86	4.26	0.01	0.02	0.33	0.19	98.68
O	OBB	73.19	0.24	9.33	5.58	0.25	-	0.20	6.17	4.47	0.02	0.01	0.35	0.20	98.45
O	OBB	73.65	0.25	9.35	5.52	0.25	-	0.22	6.06	4.19	-	0.02	0.33	0.19	99.15

Clast	Type	SiO_2	TiO_2	Al_2O_3	$FeO_{(t)}$	MnO	MgO	CaO	Na_2O	K_2O	P_2O_5	SO_2	F	Cl	Total
O	OBB	74.24	0.24	8.89	5.48	0.25	0.03	0.12	5.87	4.34	0.01	0.01	0.32	0.19	99.25
O	OBB	73.67	0.24	9.09	5.56	0.25	0.03	0.19	5.99	4.43	0.02	0.01	0.32	0.20	98.64
O	OBB	73.11	0.24	9.30	5.61	0.25	-	0.18	6.30	4.44	0.01	0.01	0.36	0.19	98.01
O	OBB	73.55	0.24	9.05	5.53	0.24	0.02	0.21	6.13	4.46	-	0.01	0.37	0.20	98.64
O	OBB	73.71	0.24	8.81	5.57	0.25	-	0.15	6.53	4.20	-	0.01	0.33	0.19	99.68
O	OBB	73.12	0.25	9.41	5.51	0.24	0.05	0.23	6.17	4.46	-	0.01	0.36	0.19	99.62
O	OBB	73.35	0.24	9.01	5.62	0.25	-	0.20	6.31	4.43	-	0.01	0.37	0.20	98.38
N	DQA	73.46	0.24	9.25	5.51	0.25	0.03	0.19	6.30	4.16	0.01	0.01	0.39	0.19	98.77
N	DQA	73.25	0.24	9.13	5.50	0.24	-	0.23	6.28	4.48	0.02	0.01	0.45	0.20	98.68
N	DQA	73.06	0.25	9.25	5.59	0.25	0.06	0.17	6.31	4.46	0.01	0.02	0.38	0.20	98.26
N	DQA	73.72	0.24	8.79	5.58	0.25	0.01	0.20	6.23	4.38	0.02	0.02	0.36	0.20	98.77
N	DQA	74.09	0.23	9.10	5.44	0.24	-	0.17	5.90	4.26	0.01	0.01	0.39	0.19	100.60
N	DQA	73.84	0.24	8.66	5.43	0.24	0.04	0.19	6.21	4.49	0.01	0.01	0.44	0.20	99.50
N	DQA	73.82	0.25	8.89	5.50	0.24	0.01	0.20	6.12	4.36	-	0.01	0.41	0.19	99.16
N	DQA	73.88	0.24	9.00	5.49	0.24	0.02	0.18	6.05	4.31	-	0.01	0.39	0.19	99.76
N	DQA	74.13	0.23	8.86	5.46	0.25	-	0.15	6.07	4.27	-	0.01	0.40	0.19	100.47
N	DQA	73.38	0.24	9.09	5.43	0.23	-	0.16	6.37	4.46	0.01	0.01	0.43	0.20	99.80
N	DQA	74.09	0.24	8.63	5.48	0.25	0.02	0.19	6.04	4.40	0.01	0.01	0.44	0.19	98.73
N	DQA	73.31	0.24	9.31	5.44	0.25	-	0.25	6.14	4.47	0.01	0.01	0.42	0.19	99.93
M	DQA	73.80	0.23	8.71	5.50	0.24	0.02	0.27	6.33	4.32	0.01	0.01	0.36	0.20	99.36
M	DQA	73.94	0.24	8.84	5.41	0.23	-	0.08	6.23	4.44	-	0.01	0.38	0.20	99.63
M	DQA	74.21	0.24	8.71	5.47	0.25	-	0.16	5.96	4.39	0.01	0.01	0.41	0.20	99.24
M	DQA	73.54	0.24	9.02	5.41	0.24	-	0.27	6.39	4.29	0.01	0.01	0.39	0.19	99.65
M	DQA	73.44	0.25	9.27	5.58	0.26	-	0.22	6.17	4.24	0.01	0.01	0.40	0.21	98.54
M	DQA	74.10	0.24	8.66	5.53	0.26	0.02	0.18	5.85	4.54	-	0.02	0.39	0.20	97.06
M	DQA	74.09	0.24	8.87	5.38	0.25	0.04	0.22	6.01	4.29	0.01	0.02	0.40	0.19	100.05
M	DQA	73.06	0.25	9.57	5.49	0.26	0.04	0.26	6.07	4.38	-	0.01	0.40	0.20	98.06
M	DQA	73.73	0.24	9.13	5.45	0.24	-	0.15	6.15	4.25	0.01	0.01	0.45	0.20	97.59
M	DQA	73.10	0.24	9.37	5.51	0.25	0.02	0.26	6.27	4.40	0.01	0.01	0.37	0.20	98.86
P	DQA	74.17	0.25	8.90	5.53	0.24	0.02	0.20	5.72	4.37	0.01	0.01	0.38	0.20	99.96

Clast	Type	SiO_2	TiO_2	Al_2O_3	$FeO_{(t)}$	MnO	MgO	CaO	Na_2O	K_2O	P_2O_5	SO_2	F	Cl	Total
P	DQA	73.82	0.24	9.10	5.56	0.25	-	0.25	6.00	4.25	-	-	0.32	0.19	99.89
P	DQA	74.23	0.25	8.73	5.46	0.23	0.02	0.23	6.01	4.28	0.01	-	0.34	0.20	98.87
P	DQA	73.56	0.24	9.28	5.53	0.24	0.03	0.19	5.99	4.37	0.01	0.01	0.34	0.20	99.47
P	DQA	74.15	0.25	8.89	5.43	0.25	0.01	0.27	5.88	4.28	0.01	0.01	0.37	0.20	99.50
P	DQA	74.13	0.24	8.97	5.46	0.24	0.03	0.18	5.82	4.38	0.01	0.01	0.34	0.19	100.04
P	DQA	73.98	0.23	8.82	5.54	0.24	0.03	0.21	5.95	4.44	0.01	0.01	0.35	0.20	100.46
P	DQA	73.68	0.25	9.00	5.51	0.24	0.02	0.22	6.09	4.42	0.01	0.02	0.34	0.20	100.57
P	DQA	73.85	0.24	9.12	5.43	0.24	-	0.22	6.06	4.27	-	0.01	0.37	0.20	99.97
P	DQA	73.99	0.25	8.85	5.52	0.24	-	0.20	5.89	4.51	-	-	0.36	0.20	99.95
P	DQA	74.21	0.24	8.90	5.51	0.25	-	0.21	5.97	4.20	-	0.01	0.35	0.20	99.04
P	DQA	73.45	0.23	9.13	5.50	0.26	0.02	0.22	6.17	4.45	-	0.02	0.33	0.20	99.30
P	DQA	73.49	0.24	9.19	5.47	0.24	0.01	0.31	6.11	4.32	-	0.01	0.41	0.19	99.30
P	DQA	73.53	0.23	9.17	5.40	0.25	0.04	0.13	6.32	4.40	-	0.01	0.32	0.20	98.63
P	DQA	73.84	0.24	9.08	5.44	0.23	0.02	0.22	5.96	4.39	-	0.01	0.38	0.19	99.89
P	DQA	73.64	0.25	9.07	5.53	0.25	-	0.19	6.20	4.34	-	0.01	0.35	0.20	98.60
P	DQA	73.61	0.22	9.10	5.56	0.23	-	0.15	6.39	4.18	0.01	-	0.36	0.19	99.59
P	DQA	73.60	0.24	9.23	5.49	0.25	-	0.19	6.18	4.26	0.01	0.01	0.36	0.19	99.46
P	DQA	73.79	0.24	8.92	5.55	0.25	-	0.18	6.12	4.36	0.01	0.01	0.38	0.20	97.78
P	DQA	73.79	0.25	8.94	5.58	0.23	-	0.18	5.94	4.47	0.01	0.01	0.40	0.20	96.25

Table C.1: *Electron microprobe analysis data from various juvenile pyroclastic components of bulk mPbr sample MER-62-16. All values are reported as weight % oxide, and measured against a Lipari obsidian standard. Conditions Na, Mg, Al, K, Ca, Si: accelerating voltage 15 KeV; beam current 1 nA; beam size 14 μm. Conditions F, Cl, P, S, Ti, Fe, Mn: accelerating voltage 15 KeV; beam current 80 nA; beam size 12 μm. Each separate clast is defined by a unique letter. Clast types: tP = tube pumice; mvP = microvesicular pumice; OBB = obsidian breadcrust bomb; DQA = deposit quenched pumiceous achnelith. A '-' represents concentrations below detectable limits.*

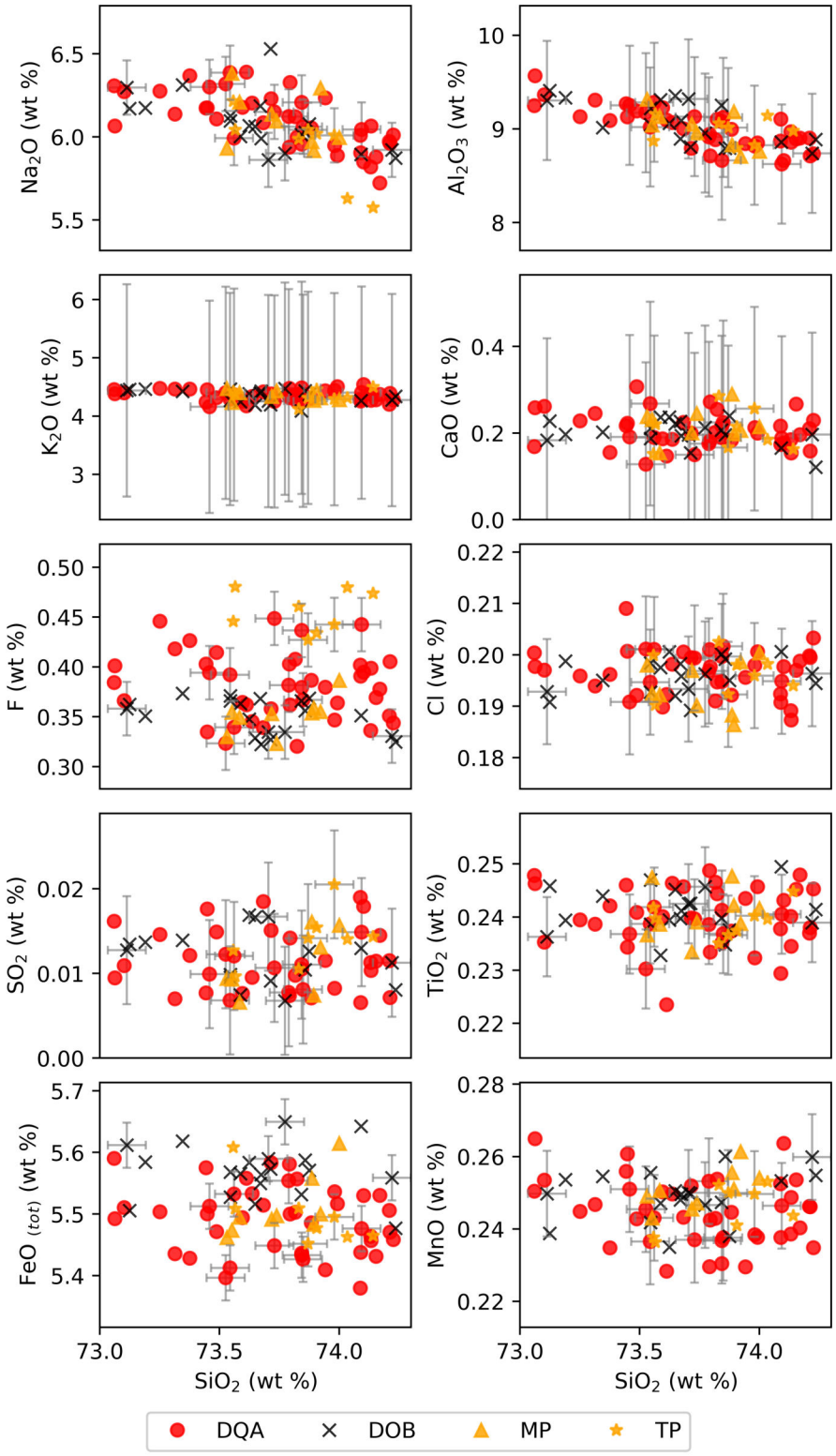

Figure C.1: *Harker plots comparing deposit components:* ***DQA*** *deposit quenched achnelith,* ***DOB*** *dense obsidian bread crust bomb,* ***MP*** *microvesicular pumice and* ***TP*** *tube pumice. Error bars represent ± 1 standard deviation of the standard data for each element. Sample: MER62-16.*

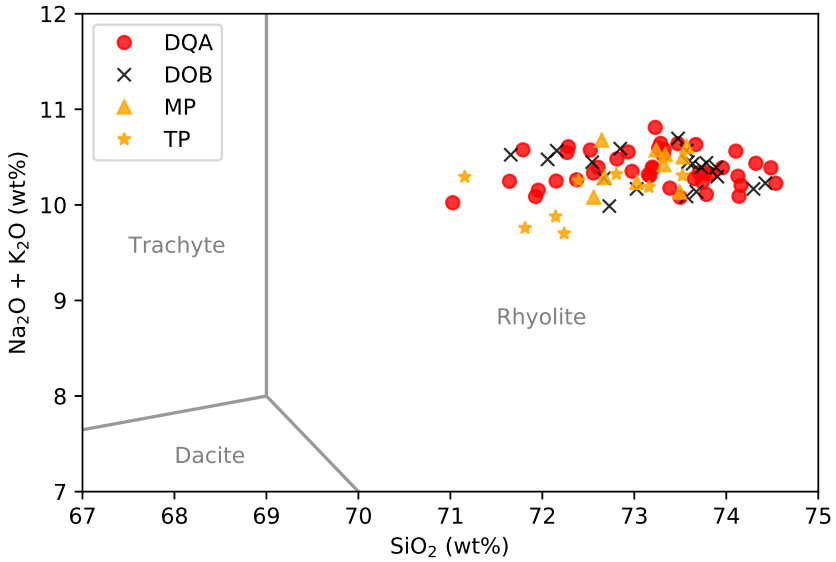

Figure C.2: *Total alkali – silica classification of deposit components:* ***DQA*** *deposit quenched achnelith,* ***DOB*** *dense obsidian bread crust bomb,* ***MP*** *microvesicular pumice and* ***TP*** *tube pumice. Sample: MER62-16.*

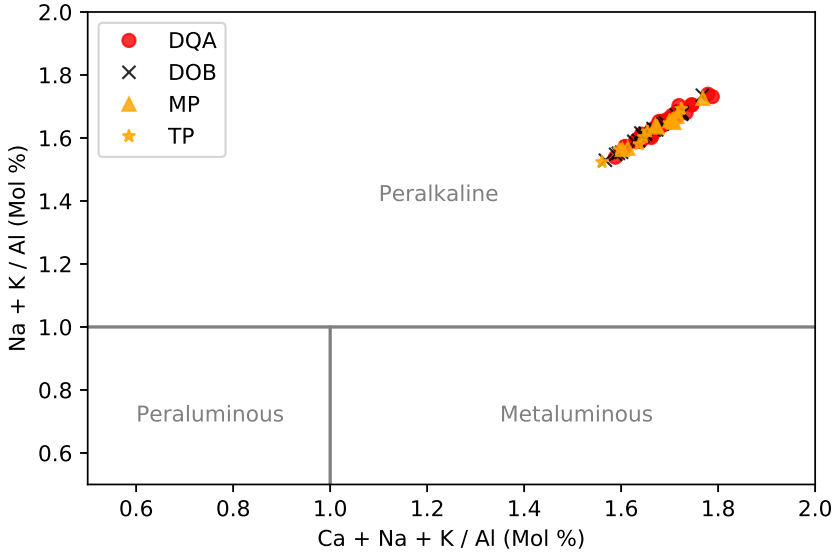

Figure C.3: *Peralkaline classification of deposit components:* ***DQA*** *deposit quenched achnelith,* ***DOB*** *dense obsidian bread crust bomb,* ***MP*** *microvesicular pumice and* ***TP*** *tube pumice. Sample: MER62-16.*

C.2 Granulometry Data

Sample	Phi	mm	Mass (g)	Pumice (%)	Lithic (%)
MER-17-35A	-5	32	240.0	100	
	-4	16	440.0	100	
	-3	8	420.0	81	19
	-2	4	520.0		
	-1	2	869.5	84	16
	0	1	568.4		
	1	0.5	282.3		
	2	0.25	126.2		
	3	0.125	76.8		
	4	0.0625	74.3		
	5	0.03125	202.4		
MER-17-36A	-5	32	0.0		
	-4	16	0.0		
	-3	8	0.0		
	-2	4	0.0		
	-1	2	217.3	45	55
	0	1	196.3		
	1	0.5	158.5		
	2	0.25	114.9		
	3	0.125	73.8		
	4	0.0625	53.4		
	5	0.03125	61.1		
MER-17-69A	-5	32	0.0		
	-4	16	7.2	100	
	-3	8	81.0	10	90
	-2	4	241.3	21	79
	-1	2	355.6	27	73
	0	1	317.3		
	1	0.5	266.2		
	2	0.25	174.5		
	3	0.125	107.2		
	4	0.0625	72.5		
	5	0.03125	100.8		
MER-17-69B	-5	32	0.0		
	-4	16	425.3	6	94
	-3	8	576.8	27	73
	-2	4	466.0	4	96
	-1	2	401.1	32	68
	0	1	314.1		
	1	0.5	240.1		
	2	0.25	157.4		
	3	0.125	98.4		

Sample	Phi	mm	Mass (g)	Pumice (%)	Lithic (%)
	4	0.0625	29.0		
	5	0.03125	83.1		
MER-17-19A	-5	32	196.9	100	
	-4	16	395.4	88	12
	-3	8	257.6	73	27
	-2	4	143.3	73	27
	-1	2	111.4	73	27
	0	1	96.4		
	1	0.5	71.5		
	2	0.25	44.5		
	3	0.125	32.4		
	4	0.0625	26.5		
	5	0.03125	78.9		
MER-17-61D	-5	32	0.0		
	-4	16	11.1	100	
	-3	8	60.3	95	6
	-2	4	209.7	90	10
	-1	2	353.7	92	8
	0	1	418.1		
	1	0.5	361.8		
	2	0.25	180.7		
	3	0.125	116.9		
	4	0.0625	122.2		
	5	0.03125	345.4		
MER-17-23A	-5	32	144.3	63	37
	-4	16	177.6	97	3
	-3	8	258.1	71	29
	-2	4	273.2	63	37
	-1	2	285.8	42	58
	0	1	288.2		
	1	0.5	283.2		
	2	0.25	251.0		
	3	0.125	182.5		
	4	0.0625	128.0		
	5	0.03125	403.2		
MER-17-64B	-5	32	0.0		
	-4	16	0.0		
	-3	8	2.7	48	52
	-2	4	15.9	83	17
	-1	2	53.9	81	19
	0	1	58.4		
	1	0.5	48.1		
	2	0.25	38.3		
	3	0.125	43.0		
	4	0.0625	60.9		

Sample	Phi	mm	Mass (g)	Pumice (%)	Lithic (%)
	5	0.03125	142.3		
MER-17-62A	-5	32	150.9		
	-4	16	0.0		
	-3	8	48.4	78	22
	-2	4	100.8	70	30
	-1	2	164.4	70	30
	0	1	215.6		
	1	0.5	300.7		
	2	0.25	348.0		
	3	0.125	400.3		
	4	0.0625	360.3		
	5	0.03125	545.4		
MER-17-69C	-5	32	227.5		
	-4	16	647.2	33	67
	-3	8	238.8	71	29
	-2	4	15.4	69	31
	-1	2	4.9	41	59
	0	1	3.0		
	1	0.5	3.5		
	2	0.25	4.3		
	3	0.125	4.3		
	4	0.0625	3.8		
	5	0.03125	7.3		
MER-17-69D	-5	32	0.0		
	-4	16	261.5		
	-3	8	262.9	11	89
	-2	4	561.3	26	74
	-1	2	351.6	28	72
	0	1	364.9		
	1	0.5	398.7		
	2	0.25	347.7		
	3	0.125	246.3		
	4	0.0625	130.2		
	5	0.03125	160.5		
MER-17-34A	-5	32	0.0		
	-4	16	662.6	19	81
	-3	8	868.0	9	91
	-2	4	396.5	37	63
	-1	2	161.7	31	69
	0	1	166.9		
	1	0.5	138.7		
	2	0.25	92.8		
	3	0.125	57.1		
	4	0.0625	30.2		

Sample	Phi	mm	Mass (g)	Pumice (%)	Lithic (%)
	5	0.03125	52.7		
MER-17-20A	-5	32	86.6	100	
	-4	16	144.5	100	
	-3	8	57.3	84	16
	-2	4	43.8	68	32
	-1	2	39.3	59	41
	0	1	25.4		
	1	0.5	18.7		
	2	0.25	12.8		
	3	0.125	9.1		
	4	0.0625	7.0		
	5	0.03125	13.2		
MER62-16	-5	32	1002.1	96	4
	-4	16	668.6	96	4
	-3	8	418.5	92	8
	-2	4	235.1	91	9
	-1	2	96.1	95	5
	0	1	53.0		
	1	0.5	32.5		
	2	0.25	23.5		
	3	0.125	25.0		
	4	0.0625	19.0		
	5	0.03125	14.5		
MER65-23	-5	32	84.1	100	
	-4	16	119.2	90	10
	-3	8	54.7	85	15
	-2	4	49.6	80	20
	-1	2	36.9	78	22
	0	1	28.7		
	1	0.5	22.7		
	2	0.25	17.2		
	3	0.125	16.8		
	4	0.0625	18.1		
	5	0.03125	24.3		

Table C.2: *Table showing the granulometry data from a variety of pyroclastic deposits collected during the two field campaigns. The phi sizes between -1 and 5 represent a subsample of the whole bulk sample investigated partially in the field, however, the masses reported here have been recalculated so that they are proportional to the total bulk sample. Lithic/Pumice percentages are reported where available, and were never assessed below a grain size of 1mm. Pumiceous achneliths were grouped with pumice.*

Sample	Median	Mean	Sorting	Skewness	Kurtosis
MER-17-35A	-1.77	-1.71	2.26	0.03	-1.69
MER-17-36A	0.25	0.5	1.84	0.14	1.21
MER-17-69A	-0.41	-0.17	2.1	0.11	0.53
MER-17-69B	-2.14	-1.71	2.31	0.19	0.62
MER-17-19A	-3.53	-4.24	0.68	-1.04	-1.98
MER-17-61D	0.12	0.51	2.32	0.17	0.15
MER-17-23A	-0.37	-0.17	3.44	0.06	0.14
MER-17-64B	2.28	0.69	1.62	-0.98	0.33
MER-17-62A	1.98	1.51	2.69	-0.17	0.61
MER-17-69C	-4.56	-2.23	1.47	1.59	-1.75
MER-17-69D	-0.75	-0.51	2.76	0.09	0.47
MER-17-34A	-3.2	-2.59	1.87	0.33	0.32
MER-17-20A	-3.95	-2.76	0.53	2.25	-2.38
MER62-16	-4.62	-0.46	2.22	1.87	-1.51
MER65-23	-3.48	-3.21	0.64	0.42	-2.28

Table C.3: *Table showing the Inman parameters calculated for each of the sieved samples. The Inman parameters are defined in Inman (1952), and listed in Equations C.1, C.2, C.3, C.4 and C.5.*

The median grain size (Md_ϕ) is defined by Equation C.1 from Inman (1952):

$$Md_\phi = \phi_{50} \tag{C.1}$$

The mean grain size (M_ϕ) is defined by Equation C.2 from Inman (1952):

$$M_\phi = \frac{1}{2} \times (\phi_{16} + \phi_{84}) \tag{C.2}$$

Sorting (σ_ϕ) is the dispersion of grain sizes; defined by Equation C.3 from Inman (1952):

$$\sigma_\phi = \frac{1}{2} \times (\phi_{84} + \phi_{16}) \tag{C.3}$$

Skewness (α_ϕ) is the asymmetry of the distribution, defined by Equation C.4 from Inman (1952):

$$\alpha_\phi = \frac{M_\phi - Md_\phi}{\sigma_\phi} \tag{C.4}$$

Kurtosis, or 'peakedness' (β_ϕ), is defined by Equation C.5, from Inman (1952):

$$\beta_\phi = \frac{\frac{1}{2} \times (\phi_{95} - \phi_5) - \sigma_\phi}{\sigma_\phi} \tag{C.5}$$

where ϕ_x is defined by the phi value (ϕ) at the x'th percentile of the cumulative mass distribution. These distributions are shown in Figure C.4.

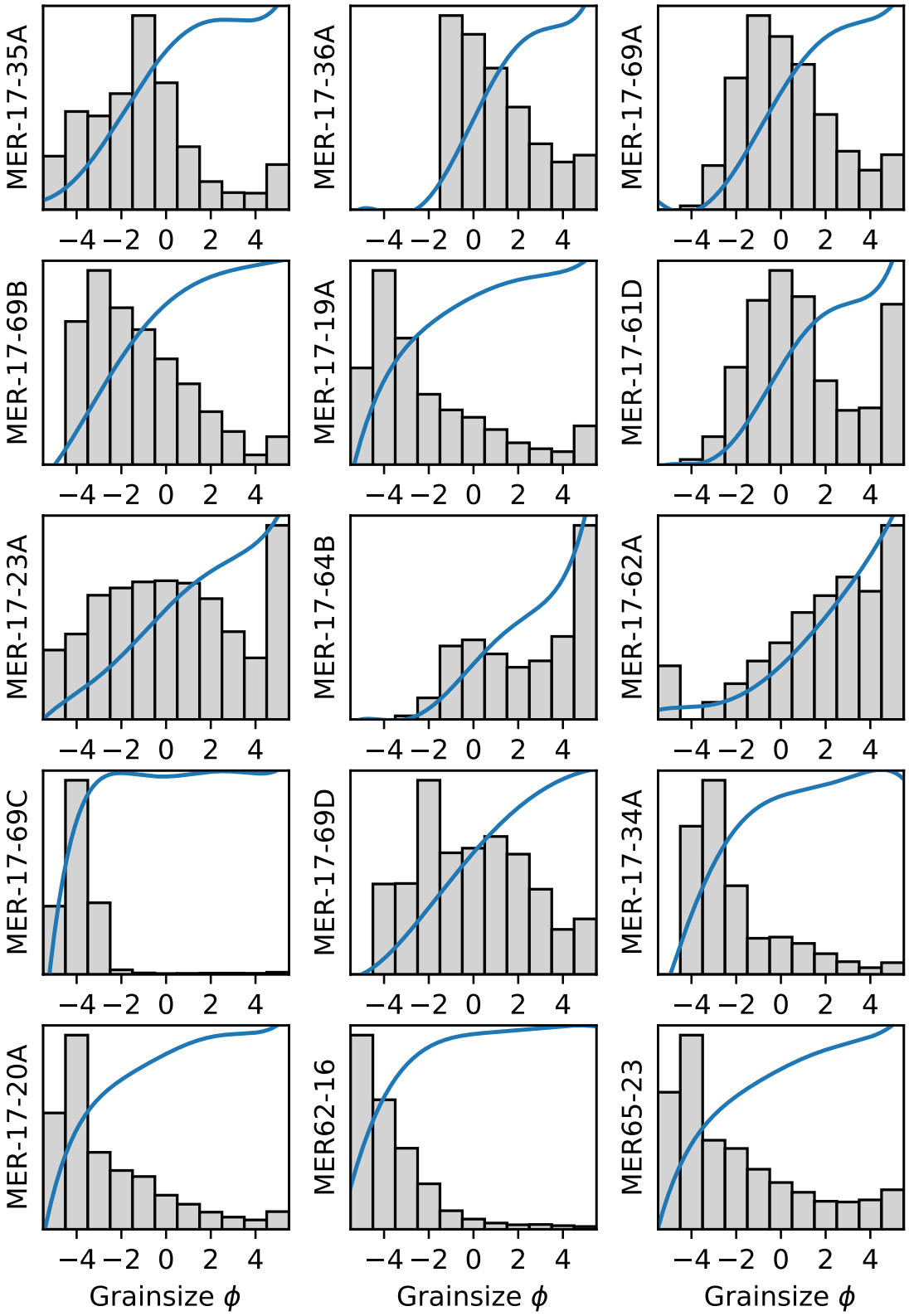

Figure C.4: *Histograms showing the granulometry of the sieved samples. Proportions are by mass, and the blue curves are polynomials of the cumulative size fractions.*

Appendix D

Code

D.1 Magmatic melt viscosity modelling

The viscosity model was developed for use in Chapter 2 in order to rapidly compare the modelled viscosities of melts with distinct compositions over a range of water contents. Here is an example of the model for a single composition over a range of water contents. The model can be used for magmatic liquids within the calibrated range in Giordano et al. (2008), in addition to Pantellerites. The model is written in Python 3 and is also available digitally as a Jupyter Notebook by using the following link: `https://doi.org/10.5281/zenodo.3333608`

Features

- Calculates the viscosity of a silicate melt from the input weight percent oxide geochemistry and water concentration
- Iterates the viscosity calculation over a range of hypothetical water contents
- Viscosity is calculated using the VFT equation from Giordano et al. (2008). If the melt is peralkaline, model coefficients from Di Genova et al. (2013) are automatically applied

Load Libraries

```
import numpy as np
import matplotlib.pyplot as plt
from math import log10, floor
import pandas as pd
from matplotlib.ticker import (MultipleLocator, FormatStrFormatter,
                               AutoMinorLocator, ScalarFormatter)
```

Define functions for processing and analysing geochemical inputs

```
def calculate_coefficients(wt_pc,WATER):
    # define oxide sequence
    comp = ['sio2', 'tio2', 'al2o3', 'fe2o3', 'feo', 'mno', 'mgo', 'cao', '
    na2o', 'p2o5', 'k2o', 'f2o', 'water']
```

```
    # assign molar mass to each oxide
    molar_mass = [60.08, 79.88, 101.96, 159.96, 71.85, 70.94, 40.3, 56.08,
    61.99, 283.886, 94.2, 53.99621, 18.02]
    # add the iterable water concentration (in weight percent) to the
    analytical chemistry
    wt_pc.append(WATER)

    # ---- Create a Pandas dataframe to process the data ready for analysis
    df = pd.DataFrame()
    df['elements'] = comp
    df['wt_pc'] = wt_pc
    df['molar_mass'] = molar_mass
    # Normalise the data set, including water, and convert to molar percent
    df['norm_wt'] = (df['wt_pc']/(sum(df['wt_pc']))) * 100
    df['norm_mol'] = df['norm_wt'] / df['molar_mass']
    df['mol_pc'] = (df['norm_mol'] / (sum(df['norm_mol']))) * 100

    # assign molar percent to each analyte and water
    sio2   = df.loc[0,'mol_pc']
    tio2   = df.loc[1,'mol_pc']
    al2o3  = df.loc[2,'mol_pc']
    fe2o3  = df.loc[3,'mol_pc']
    feo    = df.loc[4,'mol_pc']
    mno    = df.loc[5,'mol_pc']
    mgo    = df.loc[6,'mol_pc']
    cao    = df.loc[7,'mol_pc']
    na2o   = df.loc[8,'mol_pc']
    p2o5   = df.loc[9,'mol_pc']
    k2o    = df.loc[10,'mol_pc']
    f2o    = df.loc[11,'mol_pc']
    water  = df.loc[12,'mol_pc']

    # Assess geochemistry and assign peralkaline/non-peralkaline model
    coefficients
    A = -4.55

    if (na2o + k2o) > al2o3: # if it's peralkaline, apply di Genvoa
    pantellerite coefficeints
        b3 = 10528.64
        b4 = -4672.21
        c3 = 172.27
        c4 = 89.75
        B = b3 + b4 *(log10(1+water))
        C = c3 + c4 *(log10(1+water))

    else: # for all other compositions apply the standard coefficient
    calculations according to Giordano et al.
        V = water + f2o
        FM = feo + fe2o3 + mno + mgo
        TA = tio2 + al2o3
        NK = na2o + k2o
        b1 = sio2 + tio2
        b2 = al2o3
        b3 = feo + fe2o3 + mno + p2o5
        b4 = mgo
        b5 = cao
```

```
        b6 = na2o + V
        b7 = V + np.log(1 + water)
        b11 = (sio2 + tio2) * FM
        b12 = (sio2 + TA) * (NK + water)
        b13 = al2o3 * NK
        c1 = sio2
        c2 = TA
        c3 = FM
        c4 = cao
        c5 = NK
        c6 = np.log(1 + V)
        c11 = (al2o3 + FM + cao) * (NK + V)
        k_b1 = 159.6
        k_b2 = -173.3
        k_b3 = 72.1
        k_b4 = 75.7
        k_b5 = -39
        k_b6 = -84.1
        k_b7 = 141.5
        k_b11 = -2.43
        k_b12 = -0.91
        k_b13 = 17.6
        k_c1 = 2.75
        k_c2 = 15.7
        k_c3 = 8.3
        k_c4 = 10.2
        k_c5 = -12.3
        k_c6 = -99.5
        k_c11 = 0.3

        B = (b1*k_b1) + (b2*k_b2) + (b3*k_b3) + (b4*k_b4) + (b5*k_b5) + (b6*k_b6) + (b7*k_b7) + (b11*k_b11) + (b12*k_b12) + (b13*k_b13)
        C = (c1*k_c1) + (c2*k_c2) + (c3*k_c3) + (c4*k_c4) + (c5*k_c5) + (c6*k_c6) + (c11*k_c11)

    coefficients = [A,B,C]
    return coefficients

# ---- Calculate the viscosity according the coefficients provided
def calculate_viscosity(T,A,B,C):
    viscosity = 10**(A + (B / (T - C)))
    return viscosity
```

Example Geochemistry

```
#Aluto_pantellerite (values in weight percent oxide)
sio2   = 73.78
tio2   = 0.24
al2o3  = 9.06
fe2o3  = 5.5
feo    = 0
mno    = 0.25
mgo    = 0.05
cao    = 0.2
na2o   = 6.03
p2o5   = 0.01
k2o    = 4.34
```

```
f2o     = 0.38
chemistry = [sio2, tio2, al2o3, fe2o3, feo, mno, mgo, cao, na2o, p2o5, k2o,
    f2o]
```

Perform and visualise the analysis

```
#---- Define modelling conditions
lower_t = 250 # lower temperature in Celcius
upper_t = 1200 # upper temperature in Celcius
T_absolute = 273.15 # for conversion to Kelvin
# set temperature range based on user input
T_span = np.linspace(lower_t+T_absolute, upper_t+T_absolute, 100)
# define range of water contents to investigate
water_range = [0.1, 1, 2, 3, 4]

#---- Perform analysis and plot results
fig, ax = plt.subplots()

for WATER in water_range:
    coef = calculate_coefficients(chemistry,WATER) # calculate coefficients
    chemistry = chemistry[:-1] # remove the water value ready for the next
    loop
    A = coef[0]
    B = coef[1]
    C = coef[2]
    temp = []
    visc = []

    for T in T_span:
        y = calculate_viscosity(T,A,B,C)
        temp.append(T)
        visc.append(y)

    ax.plot(temp,visc, label=str(np.round(WATER,2)) + ' wt% H$_2$O')

# ---- Define viscosity axis display range from 1 to T$_g$
ymin = (1)  # Log Pa s
ymax = (10**12) # Log Pa s

minorLocator = MultipleLocator(50)
majorLocator = MultipleLocator(200)
majorFormatter = FormatStrFormatter('%d')

ax.set_ylim(ymin,ymax)
ax.set_xlim((lower_t+T_absolute),(upper_t+T_absolute))
ax.set_xlabel("Temperature (K)")
ax.set_ylabel("Viscosity (Pa s)")
ax.set_yscale('log')
ax.xaxis.set_minor_locator(minorLocator)
ax.xaxis.set_major_formatter(majorFormatter)
ax.xaxis.set_major_locator(majorLocator)
ax.legend()
plt.show()
```

D.2 Transient cooling of a spherical pyroclast

The model presented here is the exemplar base case of that used to solve the thermal evolution of pumiceous achneliths in Chapter 2. The code is written in Python 3 and a digital Jupyter Notebook version can be accessed via Github/Zenodo using the following link: `https://doi.org/10.5281/zenodo.2616499`.

Features

- Uses method of lines to solve the problem
- Discretisation from Ford Versypt and Braatz (2014)
- Radiative and convective outer boundary
- Spherically symmetric
- 'odeint' deals with the time discretisation

Load libraries

```
import numpy as np
from scipy.integrate import odeint
import matplotlib.pyplot as plt

T_absolute = 273.17
```

Set parameters

```
N = 101         # number of points to discretize
L = 0.01/2      # Radius of sample [d/2]
por = 0         # porosity
v = 30          # average velocity [m/s^-1]
T_0 = 25.       # Ambient Temperature [degC]

AD = 0.95       # air density [g/m^-3]
au = 0.000017 # air viscoisty [Pa.s]
Ka = 0.024      # thermal conductivity of air [W/m/K]
Km = 1.224      # thermal conductivity pantellerite glass [W/m/K]
md = 2470000  # density of melt [g/m^-3]
cpm = 1.42      # Heat capacity pantellerite melt [J/K/g]
vd = 590        # density of gas in vesicles [g/m^-3]
cps = 2         # heat capacity of gas in vesicles ie.steam [J/K/g]

# Reynolds number
Re = (v*(L*2)*AD) / au
# Nusselt number
Nu = 2 + (0.25+((3/10000)*Re)**1.6)**(1/2)
# Heat transfer coefficient
h_c = (Nu*Ka)/(L*2)
# bulk density of foam [g/m^-3]
fd = (vd*por) + (md*(1-por))
# Conductivity of foam taking porosity into account [W/m/K]
k = Km*(1-por)/(1+por)
```

```
# Heat capacity of foam [J/K/g]
cpf = ((por*cps*vd) + ((1-por)*cpm*md))/fd
# Thermal diffusivity taking porosity into account [m^2/s]
kappa = k/(fd*cpf)
# Black body emissivity [W/m^2/K^4]
gamma = 5.669e-8

X = np.linspace(0, L, N) # position along radius
dr = L / (N - 1)         # Spatial step size
```

Solve problem

```
def odefunc(u, t):
dudt = np.zeros(X.shape)
dudt[0] = 6*kappa/dr**2 *(u[1]-u[0]) # constant at boundary condition
dudt[-1] += 2.* h_c*kappa/k * (T_0 - u[-1])/dr
dudt[-1] += 2.* gamma*kappa/k * ((T_0+T_absolute)**4 - (u[-1]+T_absolute)**4)
    /dr

# now for the internal nodes
for i in range(1, N-1):
dudt[i] = kappa * ((i+1)*u[i + 1] - 2*i*u[i] + (i-1)*u[i - 1])/ (i*dr**2)

return dudt

init = 750.0 * np.ones(X.shape) # initial temperature

tspan = np.linspace(0.0, 60.0, 100) #{"begin time", "end time", "number of
    intervals"}
sol = odeint(odefunc, init, tspan)
```

Plot temperature-radius-time 3D surface

```
%matplotlib inline

from mpl_toolkits.mplot3d import Axes3D
fig = plt.figure()
ax = fig.add_subplot(111, projection='3d')

SX, ST = np.meshgrid(X, tspan)
ax.plot_surface(SX, ST, sol, cmap='jet')
ax.set_xlabel('R from Center m')
ax.set_ylabel('time s')
ax.set_zlabel('T DegC')
ax.view_init(elev=40, azim=60) # adjust view
```

D.3 Vent opening model

The Python 3 model used to assign the probability of each PDC source location is provided below. It is a vent opening susceptibility model based on the method described in Weller et al. (2006). A digital version, including the supporting data files from Aluto required to run it, are provided digitally via GitHub/Zenodo at: `https://doi.org/10.5281/zenodo.3334360`

Features

- Calculates the probability of at least 1 vent opening over a grid of specified locations around the volcano or volcanic field based on the location of previously active vents
- Based on the model described in Weller et al. (2006), used to evaluate vent opening probabilities of a basaltic monogenetic field in Armenia
- Assumes each vent at Aluto represents a single monogenetic vent from a distinct eruption
- Calculates the nearest neighbour distances of vents and finds a best-fit Gaussian kernel to develop a characteristic kernel bandwidth describing how far vents tend to be away from one another
- Applies the kernel to each vent, and according to the normalised sum of kernel values at each grid point calculates the spatial intensity of volcanism at that point (ie. the probability that that point will be the location of a future vent)

Import Libraries

```
import matplotlib.pyplot as plt
import csv
import numpy as np
from scipy.special import erf
import matplotlib.mlab as mlab
import pandas as pd
from scipy.optimize import curve_fit
```

Import Aluto Data

```
vent = pd.read_csv('/aluto_vents.csv')# import csv of existing vent locations
fishnet = pd.read_csv('/vent_loc.csv') # import csv of input features (points
    at which to assess probability)
```

Calculate Nearest Neighbour Distances of Vents

```
x_mv1 = vent.x_mv.values # set x location values from vent csv
y_mv1 = vent.y_mv.values # set y location values from vent csv

x_mv2 = x_mv1 # create copy of x values
y_mv2 = y_mv1 # create copy of y values

#create empty fields for dx and dy
```

```
dx=[]
dy=[]

#calculate difference in x and y coordinates between every vent. Append these to lists.
for i in range(0,len(vent)):
    for j in range(0,len(vent)):
        dx.append(np.abs(x_mv1[i] - x_mv2[j]))
        dy.append(np.abs(y_mv1[i] - y_mv2[j]))

dist = np.hypot(dx,dy) # calculate distance between vents
by_vent = np.reshape(dist,(len(vent),-1)) # split union of vent distances into vent distances per vent
m_by_vent = np.ma.masked_equal(by_vent, 0.0, copy=False) # mask zero values in array
near = np.amin(m_by_vent, axis=1) # extract nearest (min) distance within each by_vent
nearkm = near*0.001 # convert to km
```

Compute the best-fit Gaussian kernel of the cumulative nearest neighbour distances

```
#----------Define function that describes best-fit curve

def func_gauss(kernel,band):
    return erf(kernel/(np.sqrt(2)*band))

#----------Calculate cumulative density distribution of distance to nearest neighbour vent and find best fit-curve

freq = np.histogram(nearkm,bins=1000) # bin near distance data
cum_freq = np.cumsum(freq[0]) # calculate cumulative frequency of near distance bins
cum_frac = cum_freq/max(cum_freq) # calculate cumulative frequency as fraction of total vents
cum_frac = np.insert(cum_frac,0,0) # add zero value to beggining of cum_frac array to account for binning

xdata = freq[1] # define x data
ydata = cum_frac # define y data

popt, pcov = curve_fit(func_gauss, xdata, ydata) # find curve defined by function that best matches cumulative density distribution

#----------Plot result

plt.plot(xdata,ydata, label='Cumulative density distribution of user data')
plt.plot(xdata, func_gauss(xdata, *popt), 'r-', label="Bandwidth = "+ str(popt)+ " km")
plt.xlabel("Nearest Neighbour Distance (km)")
plt.ylabel("Fraction of Total Vents")
plt.title("Bandwidth = " +str(popt))
plt.show()
```

Calculate the vent opening probability based on the bandwidth of the gaussian kernel

```
#-------------Extract x and y coordinates from near and input CSVs

x_mf = fishnet.x_mf.values
x_mv = vent.x_mv.values

y_mf = fishnet.y_mf.values
y_mv = vent.y_mv.values

#-------------create empty fields for dx and dy
dx=[]
dy=[]

#-------------calculate distance between every input and near feature. Append these to lists.
for i in range(0,len(x_mf)):
    for j in range(0,len(x_mv)):
        dx.append(np.abs(x_mf[i] - x_mv[j]))
        dy.append(np.abs(y_mf[i] - y_mv[j]))

dist = np.hypot(dx,dy) # calculate distance between input and near features
neardist = dist*0.001 # convert to km

#-------------calculate vent opening probability at every input feature (fishnet point)

h = popt # set fixed bandwidth as Gaussian best-fit kernel bandwidth estimated in previous step
z = np.exp(-0.5*(neardist/h)**2) # calculate z for every input-near distance
by_fishnet = np.reshape(z,(len(fishnet),-1)) # split list of z values into chunks where each chunk contains all z values associated with each input feature
sumz = np.sum(by_fishnet, axis = 1) # sum z values in each chunk.
intensity = (sumz*(1/(2*np.pi*len(vent)*h**2)))/(4) # calculate spatial intensity for every input feature final division takes into account 500m point spacing but 1 km analysis size ((1km / spacing) ^2)

#-------------create dataframe of probabilities at each input location
d = {'xUTM' :x_mf, 'yUTM' :y_mf, 'Prob' :intensity}
df_prob = pd.DataFrame(d)

#-------------Visualise the results
plt.scatter(x_mf, y_mf, c=intensity, cmap='viridis', s=7, marker='o')
plt.axis('equal')
plt.colorbar(label='P(vent|eruption)')
plt.xlabel('UTMx [m]')
plt.ylabel('UTMy [m]')

#plt.scatter(x_mv, y_mv, c='white', s=2, marker='^')
plt.ticklabel_format(axis='both', style='sci')#, scilimits=(-2,2))
plt.show()
```

D.4 Energy cone model

The energy cone model is written in Matlab and adapted from the code employed in Tierz et al. (2016b) and Tierz et al. (2016a). The code is presented here as two functions, the of which evaluates the model considering an individual set of input parameters (collapse height, mobility and vent location). The second function iterates the first over the range of input parameters. The functions are ultimately called though a bash script to run in a high performance computing setting. In the case of this work, the bash script called these functions to run as an array job on the EDDIE cluster at the University of Edinburgh Compute and Data Facility. In such a job, the task is divided into chunks (sets of input parameters to evaluate), which commence on any available nodes across the EDDIE cluster. The bash script is not included in this thesis. The output of the models are '.mat' files, which in reality are '.hdf5' files, where data are stored as a 3D array in the form (y location, x location, vent index). The files are named with an index number (in this case 1:10,000), each relating to a unique combination of collapse height and PDC mobility. The matlab code, and the files required to run it, are available in the electronic appendices.

Function to run energy cone model

```
1
2  function dum = energy_cone(Darea,deltaH0,phi,ivent,inputID)
3
4  %This script performs EC simulations and assigns 1 (point invaded by PDCs)
5  %and 0 (point not invaded by PDCs) values to the points inside the DEM.
6  %Note that the script is a function that needs to be called in Matlab,
7  %Using the input parameters indicated above:
8  %Darea: 'pointer' to the Matlab file where the DEM is stored
9  %deltaH0: value of eruption-column collapse height, measured from the top of
10 % the volcano to the collapse height (note line 151)
11 %phi: value of the effective friction coefficient, expressed as the angle
12 % of the energy line from the horizontal (phi = theta_f = arctan(H/L),
13 % using the notation of Sheridan, 1979)
14 %ivent: index of the vent from which to evaluate the energy cone
15 %inputID: variable used to to automatically write files with unique
       identifiers
16
17 out_suffix='var'; %suffix to label inputs in file output
18
19 % load DEM
20 if Darea==5 % load Aluto 30m DEM
21     load /topo_vents_Alu_30m_last.mat
22     DEMr=gridx(2)-gridx(1);
23 end
24
25 [mescx, mescy]=meshgrid(gridx,gridy);
26
27 % assignement
28 nx=length(gridx);
29 ny=length(gridy);
30
31 batchl=length(deltaH0); %a variable just used to go through the loop
32       %as well as to store the files using the
```

```
      %correct identifier
display(deltaH0)
display(phi)

%loop to compute the N couples of values H0-Phi
for input=1:batchl

    % convert phi to radians
    phi(input)=phi(input)*pi/180;

  vent=[alon2(ivent) alat2(ivent)];

        icol=find(abs(gridx-vent(1))<DEMr);
        irow=find(abs(gridy-vent(2))<DEMr);
        d=hypot(mescx(irow,icol)-vent(1),mescy(irow,icol)-vent(2));
        mind=min(min(d));
        [ii, jj]=find(d==mind);
        vpt=[gridx(icol(jj)) gridy(irow(ii)) gridz(irow(ii),icol(jj))];

        H0=vpt(3)+deltaH0(input);

        % maximum distance
        dmax=H0./tan(phi(input));

        % iterate over every 1/20 of a degree of azimuth
        th=(0:1/20:(360-(1/20)))*2*pi/360;
        rh=DEMr:DEMr:dmax;
        v=zeros(length(rh),length(th));

        [mescth, mescrh]=meshgrid(th,rh);
        [px, py]=pol2cart(mescth,mescrh);
        px=px+vpt(1);
        py=py+vpt(2);
        pz=interp2(mescx,mescy,gridz,px,py);
        for ith=1:length(th)
            for irh=1:length(rh)
                H=(dmax-rh(irh))*tan(phi(input));
                deltaH=H-pz(irh,ith);
                if deltaH>0
                    v(irh,ith)=sqrt(2*9.81*deltaH);
                else
                    break
                end
            end
        end

        % create array, assign to 'dum' variable as output of function
        mescv=griddata(px,py,v,mescx,mescy);

        %% dum = 0 --> no pflow
        dum=int8(zeros(ny,nx));
        ind=mescv>0.0001;
        %% dum =1 --> pflow!
        dum(ind)=int8(1);


```

```
    % print vent index and inputs index to check progress
    disp(ivent)
    disp(inputID)
end
end
```

Function to call and iterate energy cone model

```
function call_energy_cone(i)

    % load arrays containing input data
    load '/hclist10k.mat'; % collapse heights
    load '/philist10k.mat'; % effective friction angles
    load '/topo_vents_Alu_30m_last.mat'; % vent locations and DEM

    hclist = hclist10k;
    philist = philist10k;

    % define which vents to iterate over
    minvent = 1; % start on vent number
    maxvent = 1200; % end on vent number

    % create empty int8 array to fill with the results in the form (x:y:vent)
    results_array = int8(zeros(length(gridy),length(gridx),2));

    % iterate over input indexes
    for i = 1:10000
        % for each set of inputs, iterate over every vent
        for vent = minvent:maxvent
                %run model function with i'th input parameters
                dum = energy_cone(5,hclist(i), philist(i), vent, i);
                % write the results to a 3D array
                results_array(:,:,vent) = int8(dum);
                % store as a 8bit integer array
                results_array = int8(results_array);
        end

        % save result, naming file by input index identifier
        save (sprintf('/invasion_input%d.mat', i), 'results_array', '-v7.3')
    end
```

D.5 Energy cone data processing

The output of the energy cone model is a series of arrays as separate files, each containing the results of an individual pair of collapse height and PDC mobility, iterated over every vent as a 3D array in the form (y location, x location, vent index). The first function is to weight the results of each vent according to the probability of that vent opening, then flatten the array, summing along the vent axis, and then to weight the 2D array according to the collapse height and PDC mobility. The result of this first function is a 2D array of weighted values associated with every vent for a particular combination of input parameters. This array can then be fed into the second function, which adds all these arrays together to a single 2D array representing the final probability map. This is then converted to a geographically defined geoTiff in the final function. The code is written in Python 3, and a Jupyter notebook can be found in the electronic appendices. As the code requires the specific Matlab model outputs to operate, the code is not hosted on GitHub.

Weight & flatten energy cone model outputs

```
1
2  def array_processing_stage1(inputs, vw, iw, weightcode):
3      # inputs = number of input to process (ie. 1-10,000)
4      # vw = vent weighting in the form of pandas dataframe of vent weights for
        each input
5      # iw = input weighting in the form of pandas dataframe of input weights
       for each input
6      # weightcode = number to distinguish this particular weighting procedure,
        must change each time different weights or methods are applied, must be
       a corresponding output folder
7
8      ######----------IMPORT----------##########
9
10     # find the correct folder based on the input value
11     str_inputs = str(inputs)
12     len_num = len(str_inputs)
13
14     if len_num < 4:
15         folder = '0k'
16     else:
17         first_num = str_inputs[0]
18         folder = first_num + 'k'
19
20     # identify the file and filepath associated with this input
21     input_idx = inputs-1 # index of the input is 1 less than the input number
        as python starts counting from 0
22     #filename = '/invasion_input' + str(inputs) + '.mat'
23     filename = '/'+ folder + '/invasion_input' + str(inputs) + '.mat'
24
25
26     # import that file as a dask array in 1200 chunks
27     f = h5py.File(filename)
28     data = da.from_array(f["results_array"], chunks=(1200, 1305, 1305))
29
30     ######----------PROCESSING-------############
31
```

```
    # use the einsum function to multiply the vw with the vents and the output is the sum of vent weighted elements
    with dask.config.set(scheduler='threads'):
        collapsed = da.einsum('ijk, i -> jk', data, vw['Prob'][:1200]).compute()

    #apply the input weighting
    # find weighting for this array according to input index
    input_weight = iw['input_factor'][input_idx]
    # multiply the elements by input weight
    collapsed = collapsed * input_weight
    # transpose the lat:long so they are the correct way around
    collapsed = collapsed.T

    ######----------EXPORT-----------############

    #save this in a compressed HDF5 file format (about 50-100kb for 2d array shape (1305:1305))
    savefilename = '/processed'+str(weightcode)+'/'+folder+'/input_'+str(inputs)+'_p'+str(weightcode)+'.h5'

    with h5py.File(savefilename, 'w') as h5f:
        h5f.create_dataset('dataset1', data=collapsed, compression='gzip', compression_opts=9)

    ######----------PROGRESS CHECK------############

    #Create some outputs to check progress
    print('.........................')
    print('Done Input' ,inputs)

#load in the input weights as a dataframe
input_filename =  '/input_weights.csv' #define input weight file
iw = dd.read_csv(input_filename).compute() # load input weights into a pandas dataframe

#load in the vent weights as a dataframe
vw = dd.read_csv('/vent_prob_1200vents.csv').compute()

#########-ITERATE FUNCTION OVER FILES-############

weightcode = 1

for inputs in range(1,10000):
    array_processing_stage1(inputs, vw, iw, weightcode)
```

Combine flattened weighted arrays

```
def combine_arrays(start_input, end_input, weightcode, nvents, niterations):

    #function used to find folder that each file is stored in
    def find_folder(filenumber):
        str_inputs = str(filenumber)
        len_num = len(str_inputs)

        if len_num < 4:
            folder = '0k'
```

```
        elif filenumber % 1000 == 0:
            folder = str(int(str_inputs[0]) - 1) + 'k'
        else:
            first_num = str_inputs[0]
            folder = first_num + 'k'
        return folder

    # function to import HDF5, and convert to a numpy array
    def hdf5_to_array(filename):
        with h5py.File(filename) as h5f:
            f = h5py.File(filename)
            dataset_name = list(f.keys())
            result = np.array(f[dataset_name[0]])
        return result

    # function to save a numpy array as a compressed HDF5
    def array_to_hdf5(array):
        cumfilename = '/processed'+str(weightcode)+'/cumulative_starting_' +
    str(start_input) + '_ending_' + str(end_input) + '.h5'
        with h5py.File(cumfilename, 'w') as h5f:
            h5f.create_dataset('dataset1', data=array, compression='gzip',
    compression_opts=9)
        return

    # create list to store any files that have been skipped in the
    compilation
    skipped_files = []

    #initialise the cumulative array by saving the start array as the
    cumulative array
    start_file = '/processed'+ str(weightcode)+'/' + find_folder(start_input)
    + '/input_' + str(start_input) + '_p'+str(weightcode)+'.h5'
    start_array = hdf5_to_array(start_file) #import start array

    cumfilename = '/processed'+str(weightcode)+'/cumulative_starting_' + str(
    start_input) + '_ending_' + str(end_input) + '.h5'

    # load the cumulative array
    cumulative_array = start_array

    for file in range(start_input, end_input+1):

        # find the filename of the next array to be added to the cumulative
    array
        next_file = '/processed'+str(weightcode)+'/' + find_folder(file) + '
    \\input_' + str(file) + '_p'+str(weightcode)+'.h5'

        #---------IF THE FILE DOESNT EXIST, START THE NEXT LOOP!
        next_file_list = glob.glob('/processed'+ str(weightcode)+'/' +
    find_folder(file) + '/*')
        if next_file not in next_file_list:
            skipped_files.append(next_file)
            print('.............................')
            print('File not here, skipping to next!')
            continue

```

```
        #import this as an array
        next_array = hdf5_to_array(next_file)

        #add the arrays together
        cumulative_array = cumulative_array + next_array

        print('.......................')
        print('Added Input ' + str(file))

    nsims = (nvents * niterations) - (len(skipped_files) * nvents)

    # finally normalise the probabilties by the number of simulations used to
     calculate them
    cumulative_array = cumulative_array / niterations # nsims
    cumulative_array = np.flip(cumulative_array, axis = 0) # flip the y axis
    so north is up
    array_to_hdf5(cumulative_array) #save to hdf5

    # report some variables to check processing is OK
    return cumulative_array, skipped_files, nsims

###--- RUN THE FUNCTION OVER THE WHOLE DATA SET ---###

weightcode = 1
results = combine_arrays(1,10000, weightcode, 1200, 10000)
```

Georeference the probability map as a geoTIFF

```
import csv
from osgeo import gdal
from osgeo import gdal_array
from osgeo import osr

#--- create array for georeferencing to UTM format (zone 37N)

# import x and y UTM values for the array
yname = '/grid_y.csv'
xname = '/grid_x.csv'

# function to read in csv data to lists
def csv_to_float_list(filename):
    with open(filename, 'r', encoding='utf8') as f:
        reader = csv.reader(f)
        values = list(reader)

    values = values[0]
    values[0] = values[0][1:]
    for i in range(0,len(values)):
        values[i] = float(values[i])

    return values

# create an array of UTM values
lat = np.flip(np.array(csv_to_float_list(yname)))
lon = np.array(csv_to_float_list(xname))
lonG, latG = np.meshgrid(lon,lat)
array = result
```

```
30
31 #--- apply the probability data to this array
32
33 xmin,ymin,xmax,ymax = [lon.min(),lat.min(),lon.max(),lat.max()]
34 nrows,ncols = np.shape(result)
35 xres = (xmax-xmin)/float(ncols)
36 yres = (ymax-ymin)/float(nrows)
37 geotransform=(xmin,xres,0,ymax,0, -yres)
38 # That's (top left x, w-e pixel resolution, rotation (0 if North is up),
39 #         top left y, rotation (0 if North is up), n-s pixel resolution)
40
41 name = '/probmap_p2.tif'
42
43 output_raster = gdal.GetDriverByName('GTiff').Create(name,ncols, nrows, 1 ,
       gdal.GDT_Float32)  # Open the file
44 # Specify its coordinates
45 output_raster.SetGeoTransform(geotransform)
46 # Establish its coordinate encoding
47 srs = osr.SpatialReference()
48 # This one specifies coordinate system
49 srs.ImportFromEPSG(32637)
50
51 # Exports the coordinate system
52 output_raster.SetProjection( srs.ExportToWkt() )
53 # Writes my array to the raster
54 output_raster.GetRasterBand(1).WriteArray(result)
55
56 output_raster.FlushCache()
```